

AFFDL-TR-74-133

**AERODYNAMICALLY INDUCED PRESSURE
OSCILLATIONS IN CAVITIES - PHYSICAL
MECHANISMS AND SUPPRESSION CONCEPTS**

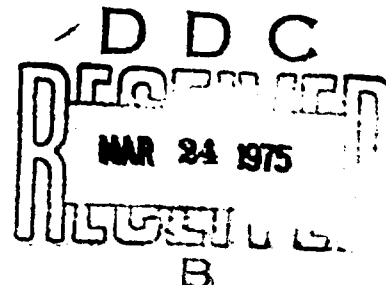
BOLT BERANEK AND NEWMAN INC.

**Reproduced From
Best Available Copy**

TECHNICAL REPORT AFFDL-TR-74-133

FEBRUARY 1975

Distribution limited to U.S. Government agencies; test and evaluation; statement applied 7 November 1974. Other requests for this document must be referred to AF Flight Dynamics Laboratory, (FY), Wright-Patterson Air Force Base, Ohio 45433.



**AIR FORCE FLIGHT DYNAMICS LABORATORY
AIR FORCE SYSTEMS COMMAND
WRIGHT-PATTERSON AIR FORCE BASE, OHIO 45433**

AD B 002701

NOTICE

When Government drawings, specifications, or other data are used for any purpose other than in connection with a definitely related Government procurement operation, the United States Government thereby incurs no responsibility nor any obligation whatsoever; and the fact that the government may have formulated, furnished, or in any way supplied the said drawings, specifications, or other data, is not to be regarded by implication or otherwise as in any manner licensing the holder or any other person or corporation, or conveying any rights or permission to manufacture, use, or sell any patented invention that may in any way be related thereto.

Copies of this report should not be returned unless return is required by security considerations, contractual obligations, or notice on a specific document.

AFFDL-TR-74-133

AERODYNAMICALLY INDUCED PRESSURE
OSCILLATIONS IN CAVITIES - PHYSICAL
MECHANISMS AND SUPPRESSION CONCEPTS

Hanno H. Heller

Donald B. Bliss

BOLT BERANEK AND NEWMAN INC.

Distribution limited to U.S. Government agencies; test and evaluation; statement applied 7 November 1974. Other requests for this document must be referred to AF Flight Dynamics Laboratory, (FY), Wright-Patterson AFB, Ohio 45433.

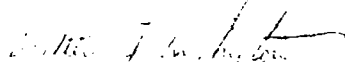
FOREWORD

This report was prepared by Bolt Beranek and Newman Inc., Cambridge, Massachusetts, for the Aero-Acoustics Branch, Vehicle Dynamics Division, Air Force Flight Dynamics Laboratory, Wright Patterson Air Force Base, Ohio under contract F33615-73-C-3075. The work described herein is a part of the Air Force System Command continuing program to establish methods of predicting and controlling the aero-acoustic environment of flight vehicles. The work was directed under Project 1471, "Aero-Acoustic Problems in Flight Vehicles, Task 147102 Aero-Acoustics."

The authors are grateful to Mr. Davey L. Smith (AFFDL/FYA), Task Engineer, and Mr. Leonard L. Shaw of AFFDL for their cooperation and assistance in the course of this research program. We also appreciate the efforts of Mr. Raymond Karabinus, Mr. Calvin Lovell, and the staff of the Flight and Wind Tunnel Division of the NASA Lewis Research Center, where the large-scale wind tunnel tests were performed.

This report concludes the work on Contract F33615-73-C-3075, which covered a period from April 1973 to November 1974. The manuscript was released by the authors on November 1974.

This report has been reviewed and is approved.


WALTER J. MYKYTOW
Asst. for Research & Technology
Vehicle Dynamics Division

ABSTRACT

This report presents the results of an analytical and experimental research program to (1) improve the understanding of the physical mechanisms that control the occurrence of pressure fluctuations in long and shallow rectangular cavities, exposed to high-speed external flow, and (2) devise and evaluate devices that would either substantially reduce the amplitude of such pressure fluctuations, or totally suppress the occurrence of pressure fluctuations.

During this investigation, the understanding of the complex interaction of the external shear layer and the cavity internal fluid medium, which constitutes the generating mechanism of high-intensity periodic pressure fluctuations, was substantially furthered. Both the analysis and investigation of the physical mechanisms were aided through extensive shallow-water flow simulation experiments.

Large-scale experiments, using the NASA Lewis Research Center 8 x 6 ft Supersonic Wind Tunnel, were conducted to substantiate some of the analytical predictions and to study in detail the aeroacoustic behavior of cavities in the length-to-depth ratio range of 2.3 to 5.5, and the Mach number range of 0.8 to 2.0. Detailed information was obtained on the normalized levels of the first three resonant modes in the cavity for a range of cavity length-to-depth ratios and freestream Mach numbers.

Several concepts for pressure oscillation suppression were developed and evaluated in wind tunnel experiments. The most promising concept utilizes a slanted trailing edge, which stabilizes the free shear flow above the cavity, thus effectively suppressing discrete-tone generation.

TABLE OF CONTENTS

	page
1. INTRODUCTION	1
2. PAST RESEARCH EFFORTS AND PROBLEM DEFINITION	3
2.1 Overview	3
2.2 Excitation Mechanisms	3
2.3 Oscillation Mechanism for Shallow Cavities	4
2.4 Onset Mechanism	5
3. PHYSICAL MECHANISMS	7
3.1 Introduction	7
3.2 Steady-Flow Considerations	7
3.3 Oscillation Phenomena	10
3.3.1 Wave Motion in a Cavity	10
3.3.2 External Radiation Pattern	15
3.4 Physical Model	18
4. ANALYSIS	23
4.1 Introduction	23
4.2 Analytical Model for Cavity Oscillation	23
4.2.1 General Considerations	23
4.2.2 Real Flow Effects	24
4.2.3 A Simple Analytical Model	25
4.3 Wave Motion of a Shear Layer Above a Boundary	27
4.4 Wave Solution Synthesization	36
4.5 Discussion of Results	41
4.6 Frequency Prediction	51
5. EXPERIMENTAL CONSIDERATIONS	55
5.1 Scope of Experimental Studies	55
5.2 Experimental Techniques: Small-Scale Studies	56
5.2.1 Exploratory Studies: Wall-Jet Flow Facility	56
5.2.2 Exploratory Studies: Water Table Facility	61
5.3 Experimental Techniques: Large-Scale Studies	61
5.3.1 Wind Tunnel Facility	61
5.3.2 Cavity Model	65
5.3.3 Instrumentation	65
5.3.4 Data Acquisition and Reduction	72

TABLE OF CONTENTS (Cont.)

	page
6. TEST RESULTS: BASIC CAVITY	79
6.1 Flow Visualization	79
6.2 Boundary Layer Characteristics	89
6.3 Mean Pressure	89
6.4 Cavity Temperature	93
6.5 Fluctuating-Pressure Data	93
6.5.1 Spectra	93
6.5.2 Resonant Frequencies	101
6.5.3 Effect of L/D Ratio on Frequencies	104
6.5.4 Levels	105
6.5.5 Mode Shapes	108
6.5.6 Broadband Noise	122
6.5.7 Consecutive Cavities	124
6.6 Aerodynamic Mean Drag	128
6.7 Wake Flow Characteristics	135
6.8 Prediction Approaches	139
6.8.1 Frequency Prediction	139
6.8.2 Level Prediction: Resonant Frequencies ...	140
6.8.3 Level Prediction: Broadband Noise	140
6.8.4 Mode Shape Prediction	140
7. TEST RESULTS: OSCILLATION SUPPRESSION	143
7.1 Conceptual Consideration	143
7.2 Unsuccessful Concepts	143
7.3 Successful Concepts	146
7.3.1 Shear Layer Stabilization	146
7.3.2 Neutralization of Mass-Exchange Process ...	155
7.4 Consecutive Cavities	155
7.5 Drag Induced by Suppression Devices	172
7.6 Evaluation of Suppression Devices	172
7.6.1 Acoustic Effectiveness	172
7.6.2 Implementation into Aircraft Design	174
7.6.3 Effects on Aircraft Performance	175
8. CONCLUSIONS	177
8.1 Principal Results	177
8.2 Oscillation Phenomenon	177
8.3 Analytical Work	178
8.4 Experimental Results	179
8.4.1 Basic Cavity	179
8.4.2 Oscillation Suppression	180

TABLE OF CONTENTS (Cont.)

	page
APPENDIX A: PSEUDOPISTON ANALYSIS	183
A.1 Overview	183
A.2 Analytical Model for the Pseudopiston Process	183
A.2.1 Simple Mass Flow Model	183
A.2.2 Thermodynamic Mass Addition Model	184
A.3 Discussion of Mass Flow, Shear Layer Deflection, and Pseudopiston Motion	190
APPENDIX B: TABLES OF ROOTS	197
APPENDIX C: AERODYNAMIC FLOW STABILIZATION THROUGH A SLANTED TRAILING EDGE	203
APPENDIX D: FLOW STABILIZATION THROUGH DETACHED TRAILING-EDGE COWL	209
BIBLIOGRAPHY	211

LIST OF FIGURES

FIGURE	page
1. Typical steady-flow condition	8
2. Impossible steady-state flow conditions	8
3. Typical pressure oscillation cycle. (3) mass removal stops; (4) mass addition starts; (12) mass addition ends; (13) mass removal starts	12
4. Wave diagram based on water table experiment	14
5. Stages of trailing-edge flow impingement (a and b), and leading-edge flow separation (c and d) within oscillation cycle	16
6. Typical cavity external radiation patterns	17
7. Mass addition and removal process by shear layer deflection at the cavity trailing edge	20
8. Waves on a shear layer above a boundary	28
9. General spatial configuration of roots	34
10. Map of roots A, B, and C in the K-plane	35
11. Pseudopiston analogy	37
12. Magnitude of unsteady pressure fluctuations as function of distance from the leading edge	43
13. Magnitude of longitudinal velocity fluctuations as function of distance from the leading edge ...	44
14. Magnitude of unsteady shear layer displacement as function of distance from the leading edge ...	44
15. Magnitude of the ratio of shear layer deflection and longitudinal velocity fluctuation (pseudo- piston velocity) as function of distance from the leading edge	45
16. Phase of the ratio of shear layer deflection and longitudinal velocity fluctuation	45

LIST OF FIGURES (Cont.)

FIGURE	page
17. Magnitude of the impedance of a pseudopiston as function of its distance from the leading edge ..	46
18. Phase of the impedance shown in Fig. 17	46
19. Magnitude of an impedance based on shear layer displacement as function of distance from the leading edge	47
20. Phase of the impedance shown in Fig. 19	47
21. Magnitude of unsteady pressure fluctuations as function of distance from the leading edge	49
22. Comparison of semiempirically derived length-to-depth ratio dependence of resonant frequencies with experimental data	54
23. Small-scale wall-jet facility	57
24. Location of experimental cavity under a wall-jet flow	58
25. Experimental setup for drag measurements	60
26. Setup for water table flow visualization experiments	62
27. NASA Lewis 8 x 6 ft wind tunnel. Mach number dependence of unit Reynolds number, re per foot, freestream dynamic pressure q_∞ , and total pressure P_o	63
28. NASA Lewis 8 x 6 ft wind tunnel. Mach number dependence of freestream static pressure and corresponding altitude simulation	64
29. Large-scale cavity model dimensions	66
30. Cavity model with sideplate removed	67
31. Cavity model with leading-edge and trailing-edge extensions	68

LIST OF FIGURES (Cont.)

FIGURE		page
32.	Cavity model with remote-controlled trailing-edge rods and upstream delta-wing spoilers	69
33.	Cavity model in test section of NASA Lewis 8 x 6 ft wind tunnel	70
34.	Closeup of installed cavity model	71
35.	Instrumentation for steady-flow quantity measurements	73
36.	Fluctuating-pressure sensor locations	74
37.	Data acquisition schematic	75
38.	Data reduction schematic	77
39.	Water table visualization of oscillation cycle under simulated external supersonic flow $M_\infty = 1.5$	80-84
40.	Water table visualization of higher order modes in cavity	86
41.	Smoke visualization of resonating cavity under subsonic external flow	87
42.	Shadowgraph visualization of resonating cavity at subsonic flow speeds	88
43.	Velocity profile at cavity leading edge	90
44.	Mach number dependence of boundary layer displacement thickness at cavity leading edge	91
45.	Normalized static pressure distribution along cavity floor	92
46.	Mach number dependence of average normalized static pressure	94
47.	Mach number dependence of recovery factor	95

LIST OF FIGURES (CONT.)

FIGURE		page
48.	Leading-edge bulkhead spectra, cavity length 5 ft.	97
49.	Pressure level spectra at various locations in and near the cavity at $K_{eq} = 0.5$; cavity length $L = 5$ ft, $L/D = 1.3$	99
50.	Pressure level spectra in and near the cavity at $K_{eq} = 1.5$, cavity length 5 ft, $L/D = 2.3$	100
51.	Narrowband analysis of leading-edge and trailing-edge bulkhead sensor signals	102
52.	Streamal frequencies of cavity modes as function of Mach number	103
53.	Length-to-depth ratio dependence of nondimensional resonant mode frequencies for $K_{eq} = 0.22$.	106
54.	Comparison of Mach number dependences of resonant mode levels: leading-edge area	107
55.	Comparison of Mach number dependences of resonant mode levels: trailing-edge area	109
56.	Mach number dependence of normalized mode-2 levels, Cavity leading-edge bulkhead region: $L/D = 4$	110
57a.	Mach number dependence of normalized mode-1 levels at leading-edge bulkhead for various L/D ratios	111
57b.	Mach number dependence of normalized mode-2 levels at leading-edge bulkhead for various L/D ratios	112
57c.	Mach number dependence of normalized mode-3 levels at leading-edge bulkhead for various L/D ratios	113
57d.	Mach number dependence of normalized mode-1 levels at trailing-edge bulkhead for various L/D ratios	114

LIST OF FIGURES (Cont.)

FIGURE		page
57e.	Mach number dependence of normalized mode-2 levels at trailing-edge bulkhead for various L/D ratios	115
57f.	Mach number dependence of normalized mode-3 levels at trailing-edge bulkhead for various L/D ratios	116
58.	Typical mode shape trace across cavity span	117
59.	Comparison of mode shapes for cavities with various length-to-depth ratios: $M_\infty = 0.8$	118
60.	Comparison of mode shapes for cavities with various length-to-depth ratios: $M_\infty = 1.0$	119
61.	Derivation of broadband noise spectra	123
62.	Envelope of all nondimensional broadband spectra in 1/3-octave bands	125
63.	Consecutive cavities	126
64.	Spectra in consecutive cavities: $L = 17.5$ in., $L/D = 2.9$	127
65.	Normalized mode levels in consecutive cavities .	129
66.	Water table visualization of resonating consecutive cavities under simulated external supersonic flow $M_\infty = 1.5$	130-131
67.	Typical trace of flow-induced cavity drag $L = 5.5$ in., $L/D = 2.2$. Laminar inflow	132
68.	Length-to-depth ratio dependence of cavity drag coefficient for $M_\infty < 0.6$	134
69.	Velocity profiles downstream of cavity	136
70.	Comparison of upstream and downstream velocity profiles at $M_\infty = 1$	138

LIST OF FIGURES (Cont.)

FIGURE	page
71. Comparison of measured and predicted mode shapes.	141
72. Perspective representation of unsuccessful suppression concepts	144
73. Perspective representation of successful suppression concepts	147
74. Boundary layer spoilers	148
75. Trailing-edge slant (a) without and (b) with upstream spoilers	149
76. Detached trailing-edge cowl and trailing-edge slant	150
77a. Effect of upstream spoilers at 45° angle of attack on leading-edge bulkhead pressure signal: $M_\infty = 0.9$; $L/D = 2.3$	151
77b. Effect of upstream spoilers at 45° angle of attack on leading-edge bulkhead pressure signal: $M_\infty = 0.9$; $L/D = 4.0$	152
77c. Effect of upstream spoilers at 45° angle of attack on leading-edge bulkhead pressure signal: $M_\infty = 0.9$; $L/D = 5.1$	153
78. Effect of upstream spoilers at 45° angle of attack on leading-edge bulkhead pressure signal: $M_\infty = 1.5$; $L/D = 2.3$	154
79a. Effect of trailing-edge slant with and without upstream spoilers on leading-edge bulkhead pressure signal: $M_\infty = 0.8$; $L/D = 2.3$	156
79b. Effect of trailing-edge slant on leading-edge bulkhead pressure signal: $M_\infty = 0.8$; $L/D = 4.0$..	157
79c. Effect of trailing-edge slant on leading-edge bulkhead pressure signal: $M_\infty = 0.8$; $L/D = 5.1$..	158
80a. Effect of trailing-edge slant with and without upstream spoilers on leading-edge bulkhead pressure signal: $M_\infty = 1.2$; $L/D = 2.3$	159

LIST OF FIGURES (Cont.)

FIGURE		page
80b.	Effect of trailing-edge slant on leading-edge bulkhead pressure signal: $M_\infty = 1.2$; $L/D = 4.0$..	160
80c.	Effect of trailing-edge slant on leading-edge bulkhead pressure signal: $M_\infty = 1.2$; $L/D = 5.1$..	161
81a.	Effect of trailing-edge slant with and without upstream spoilers on leading-edge bulkhead pressure signal: $M_\infty = 1.5$; $L/D = 2.3$	162
81b.	Effect of trailing-edge slant on leading-edge bulkhead pressure signal: $M_\infty = 1.5$; $L/D = 4.0$..	163
81c.	Effect of trailing-edge slant on leading-edge bulkhead pressure signal: $M_\infty = 1.5$; $L/D = 5.1$..	164
82a.	Effect of trailing-edge slant in combination with a detached cowl on leading-edge bulkhead pressure signal: $M_\infty = 0.8$; $L/D = 2.3$	165
82b.	Effect of trailing-edge slant in combination with a detached cowl on leading-edge bulkhead pressure signal: $M_\infty = 0.8$; $L/D = 4.0$	166
82c.	Effect of trailing-edge slant in combination with a detached cowl on leading-edge bulkhead pressure signal: $M_\infty = 0.8$; $L/D = 5.1$	167
83a.	Effect of trailing-edge slant in combination with a detached cowl on leading-edge bulkhead pressure signal: $M_\infty = 1.5$; $L/D = 2.3$	168
83b.	Effect of trailing-edge slant in combination with a detached cowl on leading-edge bulkhead pressure signal: $M_\infty = 1.5$; $L/D = 4.0$	169
83c.	Effect of trailing-edge slant in combination with a detached cowl on leading-edge bulkhead pressure signal: $M_\infty = 1.5$; $L/D = 5.1$	170
84.	Effect of triangular spoilers and trailing-edge slants on pressure levels at the leading edge of the upstream cavity of a double cavity system ...	171

LIST OF FIGURES (Cont.)

FIGURE		page
85.	Flow-induced cavity drag when suppression devices are employed	173
86.	Simple mass flow model	185
87.	Two equivalent representations of the thermo-dynamic mass addition model	185
88.	Comparison of the time behavior of the shear layer displacement, the mass flow rate, and the pseudopiston motion	191
89.	Stagnation-point flow with constant vorticity ...	205
90a.	Flow over a conventional cavity	207
90b.	Flow over a cavity with a slanted trailing edge .	207
91.	Water table visualization of stabilized flow through detached trailing-edge cowl	210

SECTION 1

INTRODUCTION

Cavities and cut-outs in structural surfaces of aircraft that are exposed to high-speed external flow can give rise to intense pressure fluctuations. The amplitude of these fluctuations can be of such magnitude that they affect the structural integrity of nearby aircraft components, of sensitive instrumentation, or, at the very least, interfere with crew performance, communication, and comfort. In fact, levels close to 180 dB at resonant frequencies can easily occur at transonic flight speeds.

Substantial effort has already gone into the study of cavity pressure oscillations,* resulting in some understanding of the physical mechanisms and the complex interaction of the cavity external shear layer and the cavity internal fluid medium, which is responsible for the generation of the highly periodic pressure fluctuations.

In 1970, the aeroacoustic characteristics of narrow and shallow rectangular cavities in the Mach number range from 0.8 to 3.0 were investigated by Heller, Holmes, and Covert (1970). The main result of this study was an improvement of an analytical expression (first developed by J.F. Rossiter in 1966) that relates nondimensional resonance frequencies and freestream Mach number. However, only an upper bound for resonance amplitudes could be derived. At that time, the phenomena were still understood too poorly to predict reliably the occurrence of discrete pressure oscillations and their energy distribution within the cavity.

In 1972, the U.S. Air Force conducted extensive flight tests using an RF-4C aircraft with a modified SUU 41 test pod. Results became available on the aeroacoustic environment of shallow cavities in the Mach number range from 0.6 to 1.3 for realistic flight environments (Smith *et al.*, 1974). It seemed that the previously assumed upper-bound level for resonant modes was generally too high. Furthermore, it was realized that each resonant mode must be considered individually

*An Air Force Technical Report (Heller *et al.*, 1970) describes previous relevant research and provides some 50 references.

for prediction purposes, since each mode shows a different level dependence on the freestream Mach number.

This lack of thorough physical understanding has also hampered the development and implementation of devices that would either substantially reduce the oscillation amplitudes, or, ideally, suppress the occurrence of resonant oscillations altogether.

In view of these facts, an analytical and experimental research program was initiated to (1) further improve the understanding of the mechanisms that control pressure oscillations in flow-exposed cavities, (2) investigate onset and feedback mechanisms, and (3) devise techniques to control the onset/feedback mechanisms in order to eliminate the occurrence of oscillations or to reduce their intensity.

This report discusses the research program and its results.

SECTION 2

PAST RESEARCH EFFORTS AND PROBLEM DEFINITION

2.1 Overview

One of the first experimental studies investigating flow-induced oscillations in a simulated weapon bay environment was performed by Karamacheti (1955). Discrete-frequency acoustic radiation from the cavity was observed at both subsonic and supersonic external flow speeds. Karamacheti noted that acoustic intensities were higher when the boundary layer upstream of the cavity was laminar.

Later studies of the unsteady environment in and around rectangular cavities were conducted by Gibson (1958), Ingard and Dear (1958), Leopold and Baker (1959), Plumblee *et al.* (1962), Quinn (1963), East (1966), Rossiter (1966), Spee (1966), White and McGregor (1970), Covert (1970), Heller *et al.* (1970), Bilanin and Covert (1973), and Smith *et al.* (1974). The Mach number range covered in these studies is 0.1 to 5.0, and the cavities had length-to-depth ratios (L/D) between 0.12 and 10. In general, these studies showed that all but the shallowest cavities resonated at discrete frequencies.

2.2 Excitation Mechanisms

Cavities are often classified as being shallow ($L/D > 1$) or deep ($L/D < 1$). Covert (1970) explained this distinction in terms of the effect of the image vorticity required to satisfy the cavity's rigid wall boundary conditions. The image vorticity on the floor of a shallow cavity tends to excite longitudinal modes, whereas the image vorticity in the fore and aft bulkheads of deep cavities tends to excite depth modes. Using an acoustic monopole distribution to model the pressure environment in an oscillating cavity, Bilanin (1973) also found that the cavity tends to respond in the direction of greatest dimension.

Several physically motivated models have been studied to identify the mechanism of oscillation for shallow cavities. Plumblee *et al.* (1962) hypothesized that the environment inside the cavity must follow the characteristic acoustic response of the cavity (a result which, however, appears to hold only for deep cavities). The mathematical problem consisted of solving for the radiation impedance of the cavity opening. However, the shear layer spanning the cavity is capable of sustaining

wave motion, and it is likely to be unstable. Howe (1970) theoretically examined the transmission of an acoustic pulse through a plane vortex sheet and showed that a grossly inaccurate description of the radiation field could result unless the analysis considers the vortex sheet dynamics.

Experimental results of Karamcheti (1955) and Heller *et al.* (1970) have cast doubt on the assumption that the forcing mechanisms which drive the cavity are provided by fluctuations in the turbulent boundary layer. Cavity oscillations are most intense when the boundary layer upstream is laminar. Thickening the boundary layer has the effect of reducing oscillation intensity (Heller, 1970). Rossiter (1966) also concurs, pointing out that when a small spoiler is placed upstream of the cavity it reduces oscillation intensities.

Since excitation frequencies of shallow cavities do not agree with the acoustic modal frequencies of the enclosure, investigators have sought an excitation mechanism that is not strongly dependent on the detailed acoustics in the shallow cavity. Rossiter (1966) suggested such a mechanism based on feedback similar to that used by Powell (1961) to describe the production of edgelines. Using a shadowgraph, Rossiter observed that periodic density fluctuations travel downstream over the cavity mouth. These fluctuations were assumed to be vortices shed from the leading edge of the cavity. The shadowgraphs also show acoustic waves in the cavity whose primary source is near the trailing edge. Assuming that the vortices were shed when an acoustic disturbance reached the leading edge of the cavity, and that acoustic disturbances were generated when the vortices reached the cavity's trailing edge, he was able to determine a frequency relation at which oscillation might occur. Although this frequency relation requires two empirically determined constants, with a suitable choice of constants a reasonable agreement with experimental data can be obtained over a moderate Mach number range. Heller *et al.* (1970) improved this result by correcting the sound speed in the cavity.

2.3 Oscillation Mechanism for Shallow Cavities

Pressure oscillation in shallow cavities was believed to result from the unstable shear layer, which spans the cavity, being forcibly displaced by disturbances that are generated at or near the cavity's trailing edge. These disturbances were thought to arise from the interaction of the oscillating shear layer with the trailing edge; this constitutes a source mechanism.

Although these disturbances should force the shear layer along the entire cavity length, models that assumed coupling to occur only at the leading edge of the cavity have given good predictions for allowable frequencies of oscillation. Thus, the shear layer is most sensitive to perturbations at the leading edge, where it is thinnest. An explanation is that an acoustic disturbance reflecting from the forward bulkhead causes a pressure doubling, while disturbances in the external flow, if present, are not reflected, and a pressure jump across the shear layer must be balanced by deflecting the shear layer.

Recently, Bilanin and Covert (1973) analyzed a model of the excitation mechanism suggested by Rossiter. In their model, the complicated flow process at the trailing edge of the cavity was modeled with an acoustic monopole. The pressure field of the monopole is used to drive the shear layer spanning the cavity, which yields an eigenvalue relation for excitation frequency. For shallow cavities, the acoustic field in the cavity can be adequately represented by a single monopole at the cavity's trailing edge. The effect of the cavity floor was to influence the instability of the shear layer by changing both the phase velocity (this, in turn, changes the excitation frequency) and the amplification rate of the shear layer displacement. Coupling of the acoustic cavity with the shear layer without considering forcing from the external flow limits the validity of the model to $M > 1$. Analytic results were in excellent agreement with experimental data.

2.4 Onset Mechanism

Although the above feedback mechanism, as suggested by Rossiter and modeled by Bilanin, estimated possible excitation frequencies, it did not predict whether, in fact, any of these will occur. Selection of the excited frequency was thought to be based on a gain criteria; i.e., the frequency or frequencies at which a cavity responds must correspond to the mode or modes receiving sufficient gain along the feedback loop.

To illustrate this idea, let us suppose that for a given geometry and external velocity the possible frequencies of oscillation are estimated using the above feedback model. The shear layer is then forced at the leading edge with a periodic pressure fluctuation with frequency corresponding to a possible excitation frequency. The shear layer is displaced, and vorticity waves propagate aft and interact with the trailing edge of the cavity, which cause a pressure disturbance to be generated. Upon reaching the leading edge of the cavity, this pressure disturbance

will have the same phase as the forcing pressure (the frequency chosen is a possible excitation frequency), but the amplitude of the disturbance will not, in general, equal the forcing amplitude. If the returning pressure disturbance is of smaller amplitude than that of the forcing pressure ($\text{gain} < 1.0$), it can be anticipated that this mode cannot sustain oscillation. However, if the returning disturbance is of greater amplitude than the forcing ($\text{gain} > 1.0$), the oscillation amplitude will be increased until nonlinear effects have reduced the gain to unity. The amplitude at which a cavity will oscillate is that amplitude at which the gain is unity: i.e., when the energy addition to the feedback loop from the external flow just balances the energy losses through viscosity and radiation. If other possible frequencies of excitation can meet this gain criteria, then the excitation of simultaneous discrete frequencies, as observed in practice, is possible.*

Covert (1970) examined the oscillation phenomenon as a problem in hydrodynamic stability. He suggested that while the external flow is capable of supplying energy to the enclosure, the cavity is capable of dissipating energy through viscosity and radiation. If the rate of energy supply is less than the rate at which energy can be dissipated from the cavity, oscillation cannot occur ($\text{gain} < 1$). As the external flow velocity is increased, a point is reached where energy supply equals cavity energy dissipation ($\text{gain} = 1$). This velocity is termed the critical or onset velocity. Further increases in external flow velocity result in sustained cavity oscillation. A stability analysis of the vortex sheet across the cavity opening supports this description of onset. However, Covert's model did not predict excitation frequencies for shallow cavities since it did not adequately model the interaction of the shear layer with the trailing edge.

*In Secs. 3 and 4, a physical model of cavity pressure oscillation will be discussed that deviates in several important aspects from the "Rossiter Model."

SECTION 3

PHYSICAL MECHANISMS

3.1 Introduction

In this chapter, a detailed, but essentially qualitative, description of steady and unsteady cavity flow phenomena is presented. This description provides physical insight that will be helpful in understanding and interpreting the analytical efforts and experimental results. Such an understanding is also required to appreciate the operation of oscillation suppression devices.

3.2 Steady-Flow Considerations

Although we are primarily concerned with unsteady effects, it is worthwhile to consider briefly the somewhat hypothetical case of steady flow over a cavity. This flow is steady only in an overall sense, since shear layer turbulence is included in the discussion. Figure 1 is a sketch of a steady cavity flow. If the flow were supersonic, then a steady wave structure at the leading and trailing edges would also be present.

The flow separates at the sharp leading edge of the cavity, and a shear layer grows downstream. At the rear bulkhead, the flow stagnates and splits. Part of the shear layer enters the cavity, and the rest passes over the cavity trailing edge and continues downstream as part of the downstream boundary layer. In the laminar flow case, the dashed line across the cavity mouth (see Fig. 1) denotes the streamline that divides the flow which enters the cavity from that which does not. The same fluid always remains in the cavity. The fluid that is entrained from the cavity by the shear layer over the cavity mouth is returned to the cavity by the trailing-edge stagnation process. The same is essentially true when the shear layer is turbulent, although there will actually be some change in which fluid elements occupy the cavity. This exchange of fluid occurs because of the turbulent diffusion across the dividing streamline. On the average, however, the process remains as illustrated in the figure.

It can be concluded that this must be the flow configuration for the steady case. The shear layer always entrains fluid; therefore, there must always be a stagnation on the rear bulkhead to return this fluid to the cavity. A similar argument establishes that the entire shear layer does not enter the cavity. Figure 2 illustrates this point. It is important

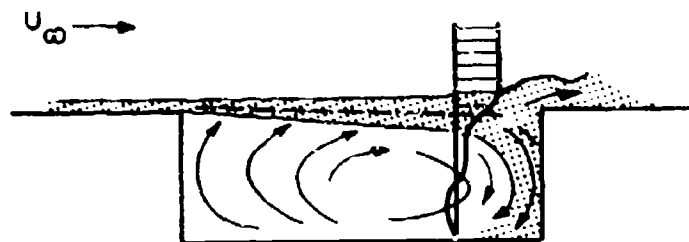


FIG. 1. TYPICAL STEADY-FLOW CONDITION.

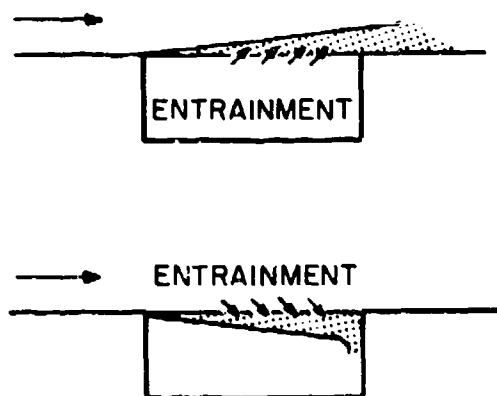


FIG. 2. IMPOSSIBLE STEADY-STATE FLOW CONDITIONS.

that the cavity must maintain a mass flow balance, particularly when we consider oscillation suppression devices. The ultimate goal of these devices is to make the cavity flow steady. As will be seen, this idea of a mass flow balance is also important to our understanding of the mass addition and mass removal process at the trailing edge of an oscillating cavity.

In a steady cavity, there must always be a flow recirculation because of shear stresses across the cavity mouth, and the necessity of mass entrainment by the shear layer and its return to the cavity at the trailing edge. The magnitude of the entrainment by the shear layer fixes the level of this recirculation. This entrainment also controls the location of the stagnation streamline within the shear layer.

The presence of this (sometimes substantial) recirculation within the cavity affects the unsteady phenomena. Flow recirculation acts to change the motion of waves within the cavity and alters the character and the dynamics of the shear layer. This recirculation flow is essentially a vortex flow contained within the cavity and bounded by its side walls. The sidewall boundary layers provide considerable damping to the recirculation flow; they cause secondary flows to be set up within the recirculation vortex, which leads to fluid exchange between regions with high and low angular momentum. This is a familiar process in viscous rotating flow boundary layers. It is possible, therefore, that the presence of side walls contributes as much resistance to flow recirculation as the cavity floor and front and rear bulkheads. Since the level of flow recirculation affects the shear stress at the cavity mouth, it can be concluded that cavity width will affect the cavity drag. Since the presence of flow recirculation affects unsteady cavity behavior, this behavior must be dependent to some extent on cavity width.

Of course, the cavity width affects the shear layer characteristics directly in addition to influencing flow recirculation. Other factors that are important to the shear layer properties are the upstream boundary layer thickness, the flow Mach number, and the Reynolds number.

Two requirements must be met to achieve a steady cavity flow: a steady-flow solution must be possible; and it must be stable to disturbances. To find a steady solution means that the mass flow balance requirement must be satisfied, and that, simultaneously, the shear layer must assume a shape for which it is in force equilibrium everywhere: i.e., the internal

and external flow static pressure must balance across the shear layer. For a rectangular cavity, it is questionable whether a steady solution is even possible. This point is discussed later in connection with a particular cavity configuration that suppresses oscillations.

3.3 Oscillation Phenomena

The physical character and underlying mechanisms of flow-induced cavity oscillation are described below. This description was partially inspired by a water table simulation of a supersonic flow over a cavity (see Sec. 6.1 and Heller et al., 1973). The available literature on the subject (see Sec. 2), particularly flow visualization photographs of the phenomena in air, was also valuable.

3.3.1 Wave Motion in a Cavity

The water table simulation study reveals that unsteady motion of the shear layer leads to periodic mass addition and removal at the cavity trailing edge. In a shallow cavity (i.e., in practice, a length-to-depth ratio of two or greater), this mass addition and removal produces an effect that is similar to replacing the cavity rear bulkhead with an oscillating piston. In fact, this similarity has been demonstrated experimentally using the water table. Therefore, the effect of mass addition and removal at the rear bulkhead is sometimes referred to as the "pseudopiston" effect. This effect generates forward traveling waves in the cavity that reflect from the front bulkhead and become rearward traveling waves. The resulting wave structure in the cavity forces the shear layer in an unsteady manner. This shear layer motion is responsible for the trailing-edge mass addition and removal that produced the cavity wave structure, thus closing the feedback loop. The energy to sustain this process is drawn from the external flow.

Using movies* of the water table simulation of cavity oscillations, it is possible to study in detail a typical oscillation cycle. Figure 3 presents a series of 18 sketches which delineate the stages of such a cycle. These sketches, which were derived from motion picture frames separated by equal time intervals, show the essential features of the phenomenon, i.e., the shape of the shear layer and the location of pressure waves. The sketches are numbered in the order of

*Reproductions of a sequence of flow simulation movie frames appear in Sec. 6.

their sequence and arranged in lettered rows in Fig. 3. Each row can be viewed as a typical state in the oscillation cycle; an explanation is presented below corresponding to each lettered row. The choice of a starting point for the cycle is arbitrary and it is necessary to review the entire process to understand completely the conditions at the beginning.

A. The pressure wave from the previous trailing-edge disturbance reaches the front of the cavity and reflects. Another such wave already reflected off the front wall approaches the rear of the cavity. The shear layer is above the trailing edge, so the external flow cannot interact with the trailing edge to produce disturbances. Some fluid leaves the cavity at the rear.

B. The shear layer waveform travels rearward reducing the height of the shear layer above the trailing edge, which causes a new compression wave to form at the rear as the flow interacts with the trailing edge and fluid is added to the cavity. The front compression wave has reflected off the leading edge and moves rearward nearly in phase with the shear layer displacement. The previous rearward wave has reached the trailing edge.

C. The wave reflected off the front wall continues to move rearward in phase with the shear layer displacement. The shear layer, which is now below the trailing edge at the rear of the cavity, forms a new forward traveling compression wave as the external flow impinges on the back of the cavity.

D. The newly generated forward traveling compression wave and the reflected, rearward traveling compression wave meet and interact near the cavity center.

E. After interaction, the waves continue in their respective directions. The external part of the forward traveling wave moves into the supersonic flow causing it to be tipped more than the external flow Mach angle. The rearward wave moves in the same direction as the external flow and travels at subsonic speed relative to it. This subsonic relative speed explains why the rearward traveling wave stops at the shear layer. At the rear, the shear layer reaches the trailing-edge height.

F. The shear layer is now above the trailing-edge height. The wave generated at the trailing edge approaches the front of the cavity. The reflected wave nears the rear of the cavity. The next step is the same as A as the oscillation cycle repeats.

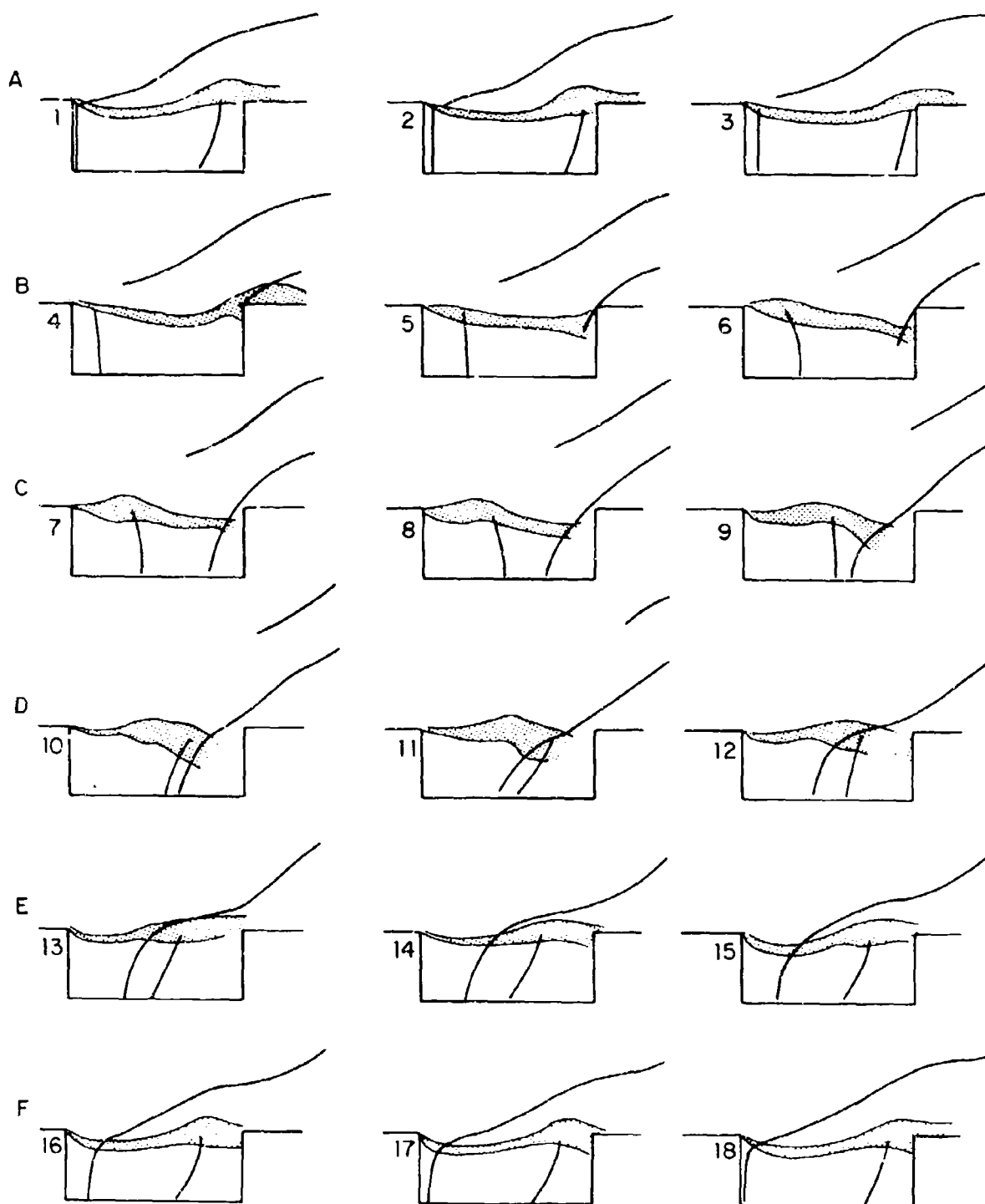


FIG. 3. TYPICAL PRESSURE OSCILLATION CYCLE. (3) Mass Removal Stops; (4) Mass Addition Starts; (12) Mass Addition Ends; (13) Mass Removal Starts.

The water table simulation shown here applies to supersonic flow. It is believed, however, that the process is essentially the same for subsonic flow, particularly as regards the internal wave structure. In the subsonic case, the forward traveling wave will still be supersonic relative to the external flow. The other aspects of the external wave system will have been changed or will be absent. Photographs of the subsonic case in air also indicate a tendency for the downstream traveling shear layer disturbances to roll up into vortices (see Sec. 6).

Figure 4 is a wave diagram for the cavity derived from the water table simulation. Some of the irregularities of the wave motion are caused by the optics of the system and the difficulty in properly locating the wave positions in the region where they cross. An important feature of the diagram is the staggered arrangement of the pattern, which is caused by the difference in the phase speeds of the upstream and downstream waves. The upstream wave (moving toward the leading edge) travels faster than the downstream wave (moving toward the trailing edge). This difference between wave speeds results from the complicated interaction of the shear layer motion and the internal wave system. Essentially, the shear layer appears "stiffer" to the upstream wave (supersonic relative to the external flow) than to the downstream wave (subsonic relative to the external flow). This interaction between the cavity wave structure and the shear layer will be discussed further in subsequent sections.

Because the upstream wave is supersonic relative to the external flow, it radiates an external wave. Thus, energy is radiated away, and the upstream wave can be expected to decay as it travels forward. Similarly, since the downstream wave produces a shear layer disturbance that is subsonic relative to the external flow, it can be expected to draw energy from the mean flow and amplify as it travels rearward.

Therefore, the wave pattern in a cavity is a modal structure formed essentially from the two waves traveling in opposite directions with slightly different wavelengths and spatial amplification rates. The spatial envelope of both waves will expand towards the cavity trailing edge. The results of the water table simulation correspond essentially to a first mode of oscillation, i.e., only one wavefront of each type in the cavity and one pressure node. Real cavities in air often exhibit higher modes: in fact, the second mode usually dominates. These modes are seldom seen naturally in the water table experiment, probably because of high damping.

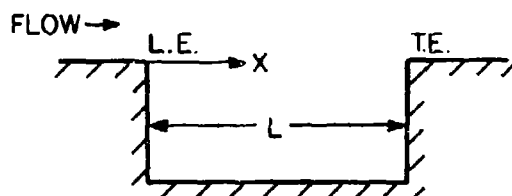
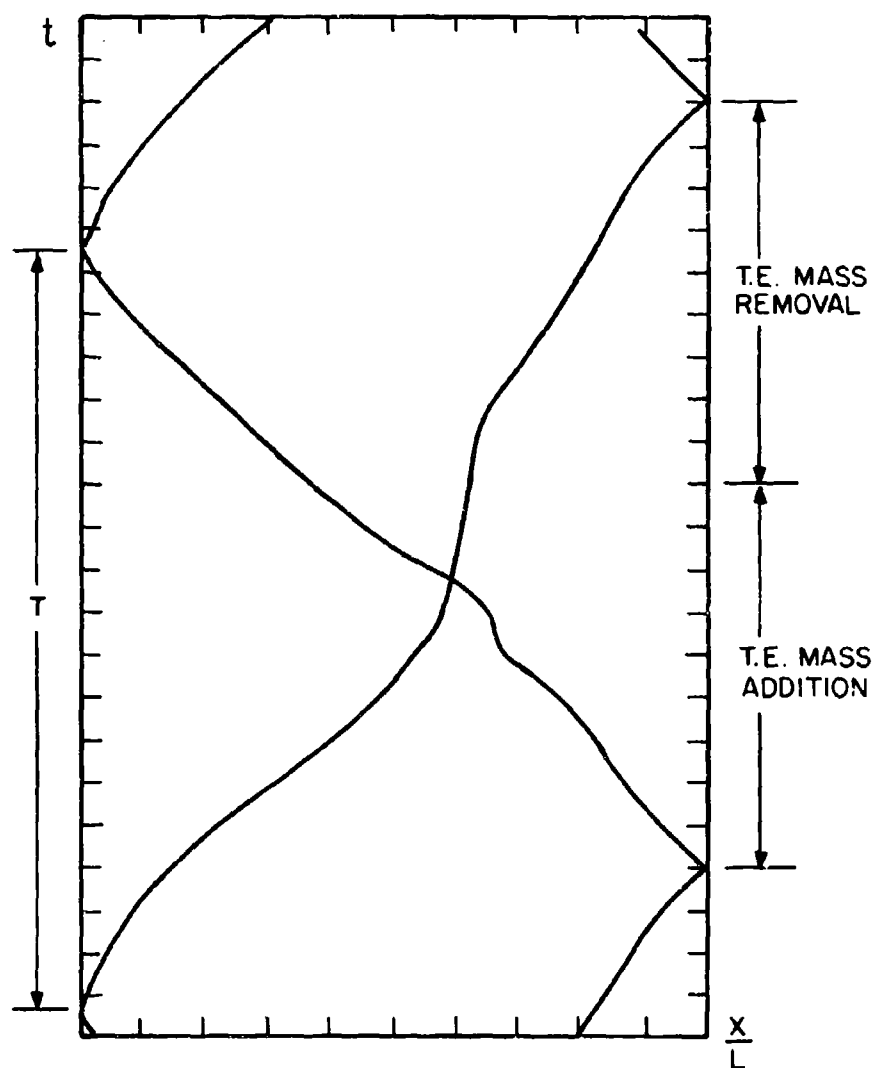


FIG. 4. WAVE DIAGRAM BASED ON WATER TABLE EXPERIMENT.

3.3.2 External Radiation Pattern

From water table simulation results and the Schlieren photographs available in the literature, it is possible to construct a picture of the external radiation pattern of an oscillating cavity. This picture is consistent with the internal wave structure described above.

Consider a supersonic flow over a cavity. Figure 5 shows the expected wave patterns at the leading and trailing edges of the cavity for different shear layer positions. When the shear layer is deflected downward at the trailing edge, three basic waves can be expected (Fig. 5a). As described previously, one of these waves is the upstream traveling wave and its corresponding shear layer disturbance, which trails a traveling wave into the external flow. The second of these waves is a quasi-steady "bow-wave," which is caused by the supersonic external flow interacting with the relatively blunt trailing-edge region. The third wave is an oblique shock that occurs when the flow readjusts just behind the cavity trailing edge. When the shear layer is above the trailing edge, as when a downstream wave is arriving, there seems to be no significant external wave system (see Fig. 5b). It must be recalled that the shear layer disturbance associated with this wave moves at a subsonic speed relative to the external flow.

At the leading edge, the picture is simpler (Fig. 5c and d). As an upstream wave approaches the leading edge, the shear layer is bent downward and there is an expansion wave at the edge as well as the upstream traveling compression wave. After the upstream wave is reflected to become a downstream traveling wave, the external portion trails away since the downstream wave is subsonic relative to the external flow. At this time, the shear layer is deflected upward and a leading-edge oblique shock occurs.

This sequence of occurrences can be compared with observed radiation patterns (see McGregor, 1969, and Rossiter, 1966) to arrive at Fig. 6a, for supersonic flow. Figure 6b is a similarly derived sketch at high-speed subsonic and transonic external flow. In this case, the radiation caused by the leading- and trailing-edge oblique waves is absent. Although the primary contributor to the subsonic flow radiation pattern is the external portion of the upstream traveling wave, another wave is also seen. This wave is caused by direct external radiation from the unsteady shear layer impingement at the trailing edge. Because the flow is subsonic, this wave can also move upstream.

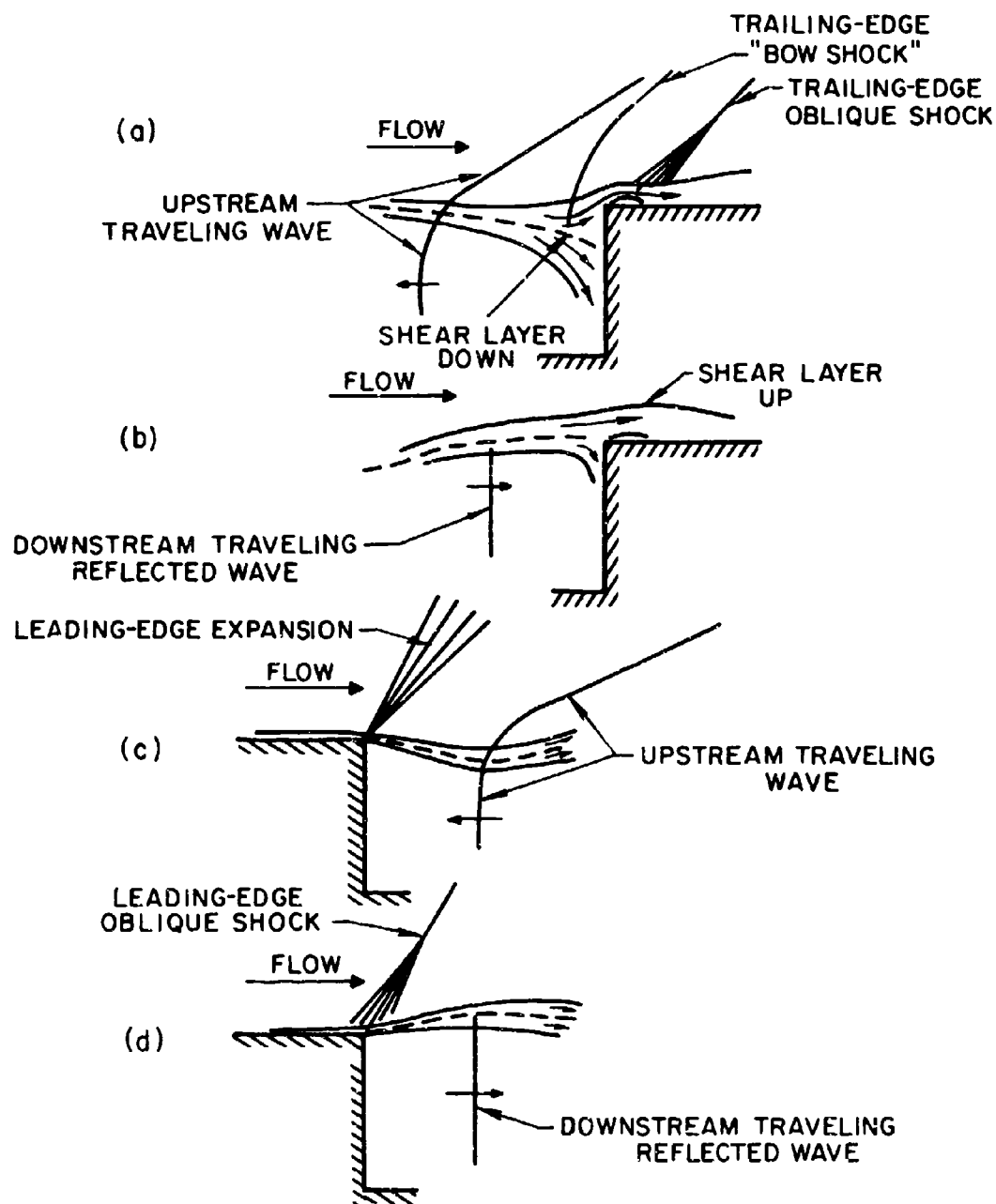


FIG. 5. STAGES OF TRAILING-EDGE FLOW IMPINGEMENT (a and b), AND LEADING-EDGE FLOW SEPARATION (c and d) WITHIN OSCILLATION CYCLE.

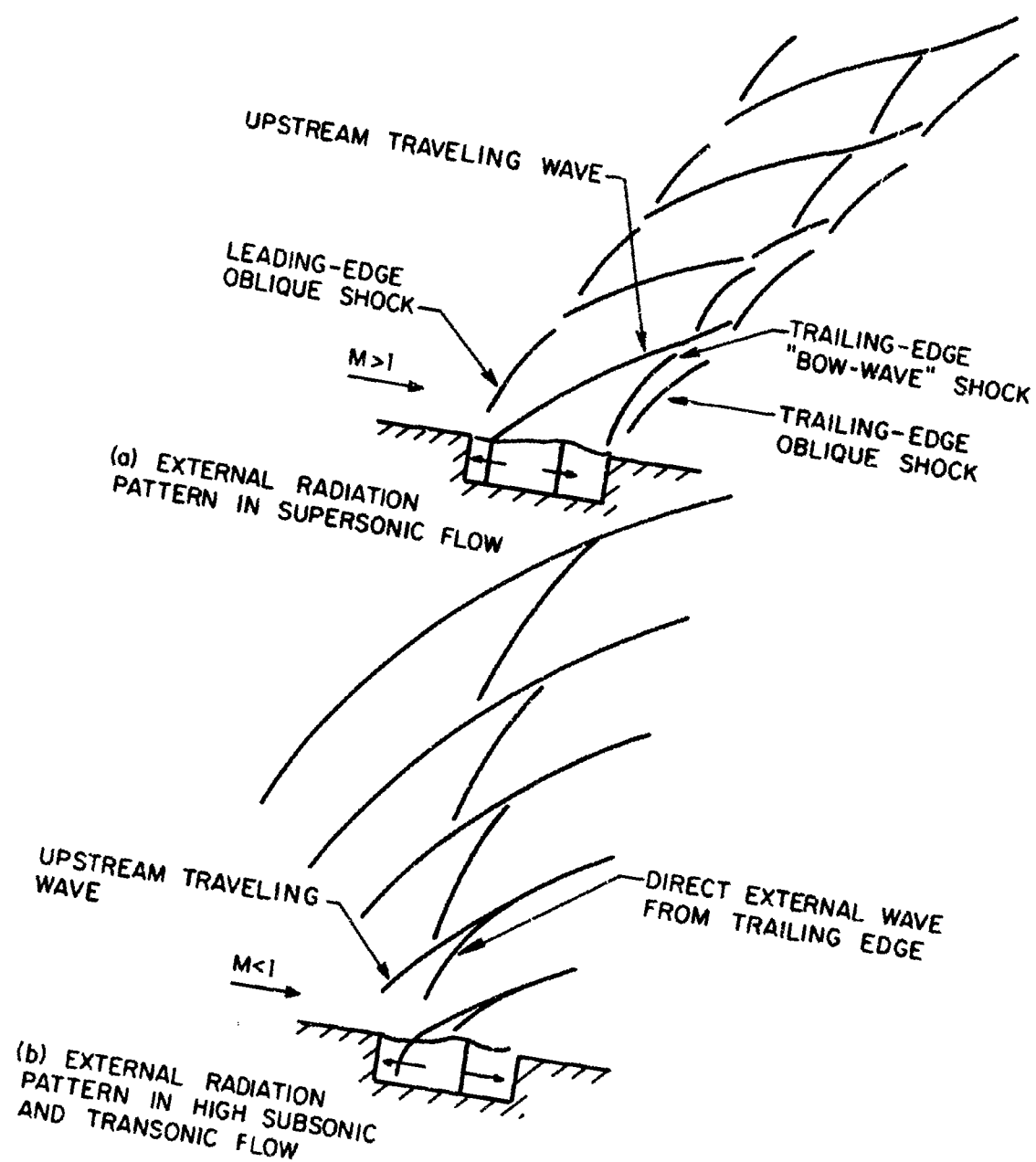


FIG. 6. TYPICAL CAVITY EXTERNAL RADIATION PATTERNS.

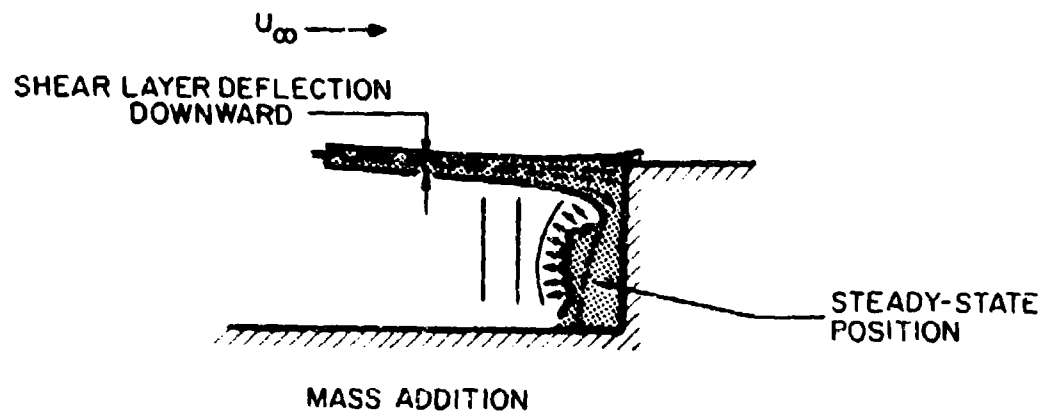
3.4 Physical Model

It is now possible to summarize the physical mechanism of the oscillation process and discuss some additional aspects of the phenomenon. As indicated in the previous sections, the mass addition and removal process at the cavity trailing edge is caused by unsteady motion of the shear layer. This process produces a piston-like effect at the rear bulkhead, which sets up the internal wave structure that forces the shear layer. This shear layer motion is responsible for the trailing-edge mass addition and removal. The wave motion of the shear layer and the wave structure within the cavity are strongly coupled and cannot be considered separately as long as the wave length is comparable to or exceeds the cavity depth. The cavity internal wave structure is composed primarily of upstream and downstream traveling wavetrains. Their combination produces a modal unsteady pressure field in the cavity. Of course, other waves are present to satisfy the detailed boundary conditions imposed by the details of cavity geometry, shear layer shape, and the mass addition process. The upstream waves radiate energy away from the cavity and, therefore, decay as they move upstream. These waves reflect from the front bulkhead to become the downstream traveling wave system. The downstream waves draw energy from the mean flow and amplify as they move downstream. This amplification must provide enough shear layer displacement at the trailing edge to sustain the process, overcoming the many sources of losses in the system. At least for the simplified analytical model of the shear layer dynamics, presented in Sec. 4, the spatial amplification of the downstream wave is considerable and easily exceeds the decay rate of the upstream wave in almost all cases. This fact probably explains the strong tendency of cavities to oscillate in one or more modes over a broad and continuous range of cavity geometries and flow speeds.

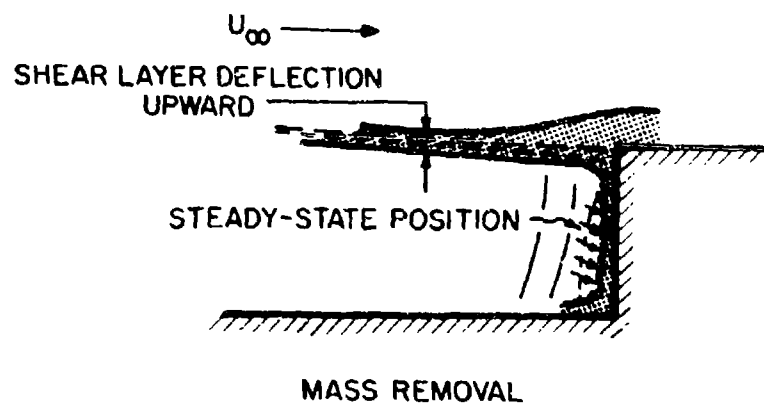
The modal frequencies at which a given cavity oscillates for a given set of flow conditions are determined by the phase and amplitude conditions of the shear layer at the trailing edge as they relate to the mass addition process and the internal wave motion of the rear bulkhead. The trailing-edge mass addition and removal process is essentially a hydrodynamic phenomenon; as such, it is quite complex. In cases where vortex roll up of the shear layer has occurred, this complexity would be further increased.

In flow visualization photographs with subsonic external flow, the shear layer has been observed to roll up into vortices that travel rearward and impinge on the cavity trailing edge. Some investigators have assumed that discrete vortex shedding from the cavity leading edge, which is triggered perhaps by acoustic disturbances in the cavity arising from vortex interaction with the trailing edge, is the basis of the cavity oscillation mechanism. In supersonic flow experiments, discrete vortices are not usually seen, but an amplifying sinuous motion of the shear layer traveling toward the trailing edge is often evident. This motion is also apparent from the water table results. Perturbations to the shear layer indicate a varying vorticity distribution along its length. The apparent traveling wave motion along the shear layer is a result of the dominant amplification of the downstream traveling wave in the cavity. From the analytical results which are documented later, it is apparent that the spatial amplification of the downstream wave is greatest relative to that of the upstream wave when the external flow is subsonic. In this case, it is reasonable that the shear layer, subjected to forcing by the cavity internal wave structure, would roll up into downstream traveling vortices. Thus, the appearance of discrete vortices on the cavity shear layer is completely consistent with the oscillation mechanism previously described. In fact, at subsonic flow speeds, it is likely that the nonlinear process of vortex roll up provides an important amplitude-limiting mechanism. We can conclude that "vortex shedding" is a manifestation of the oscillation process, but it is not essential to the underlying mechanism.

Finally, the trailing-edge mass addition and removal process deserves some detailed examination. Our discussion of steady-flow considerations revealed that a mass flow balance must occur, whereby fluid entrained by the cavity shear layer must be returned to the cavity through a flow stagnation process at the trailing edge. Clearly, when the shear layer is deflected downward relative to its steady-state position, additional mass enters the cavity at the trailing edge. This mass addition is directly in phase with the deflection. The added mass occupies an additional volume at the rear of the cavity, displacing the fluid normally in that region. As mentioned, this displacement has an effect similar to replacing the trailing-edge bulkhead with a piston, which is then displaced by a corresponding amount. In fact, measured pressure-mode shapes in oscillating cavities show that the trailing-edge region does not behave as a hard wall; i.e., pressure modes do not generally exhibit a maximum at the rear bulkhead. Incidentally, the mass entrainment process by the shear layer is not necessarily affected to any great degree by the occurrence of shear layer oscillation. Figure 7a illustrates the mass addition process.



(a)



(b)

FIG. 7. MASS ADDITION AND REMOVAL PROCESS BY SHEAR LAYER DEFLECTION AT THE CAVITY TRAILING EDGE.

The other half of the oscillation process involves the removal of an equal amount of mass again at the trailing edge. The mechanism for this mass removal is not as easily understood as that for mass addition. It is sometimes said that when the shear layer is deflected upward, the fluid near the trailing edge is entrained out of the cavity. This statement is, at least, imprecise; it is difficult to imagine entrainment at the trailing edge being capable of removing as much mass in a time span as was added by a downward deflection in a comparable time span. This is because the mass added during downward deflection occurs at a relatively high velocity due to the velocity gradient in the shear layer; this presumably has a much stronger effect than removal by entrainment. It is possible that waves arriving at the rear bulkhead from the front portion of the cavity help push the mass out at the trailing edge. While this effect is almost certainly present, it does not seem sufficiently strong. Perturbation velocities from these waves are much smaller than the freestream velocity. Furthermore, the types of overpressures produced by waves arriving at the rear bulkhead seem inadequate to achieve the required level of mass removal.

The correct explanation for the mass removal mechanism involves the way an upward shear layer deflection affects the normal steady-state mass addition. Certainly, when the shear layer is moved upward, the normal mass addition process is substantially reduced. Therefore, the "mass removal" process may really be a lack of the steady-state mass addition. Since the average situation in the cavity involves continuous mass addition at the trailing edge to balance the shear layer entrainment, a reduction of this addition acts as a mass removal. Furthermore, this "mass removal" effect can be the same magnitude as the extra mass addition caused by downward shear layer deflection. The mass removal process is illustrated in Fig. 7b.

SECTION 4

ANALYSIS

4.1 Introduction

The physical mechanisms at work in oscillating cavities have been sufficiently described so that an analytical model for the cavity wave structure can now be considered. The first two sections will discuss the formulation of the problem and introduce the ideas that are the basis for the simplified model. The following sections will then develop the analysis in detail and discuss the results. The final section will analyze a semiempirical frequency prediction scheme showing length-to-depth ratio dependence.

4.2 Analytical Model for Cavity Oscillation

4.2.1 General Considerations

From Sec. 3, it is clear that the cavity wave structure can be modeled as follows. The fluid motion within the cavity is governed by the solution of the wave equation in a region bounded by a rigid front bulkhead and floor, with a free shear layer on top, and a rear bulkhead, which oscillates like a piston. This oscillating bulkhead approximates the pseudopiston effect of mass addition and removal at the trailing edge. The external flow, which, to a good approximation, is governed by the convective wave equation, is on the other side of the shear layer, which begins at the leading edge. The internal and external solutions should be joined by applying the proper dynamic and kinematic conditions across the shear layer. If the cavity leading edge is a sharp corner, then the Kutta condition should be applied to the shear layer at this edge, which makes its displacement equal to zero at the leading edge. Although the shear layer motion should not be constrained at the trailing edge, the internal and external regions should remain separated. The effect of the trailing-edge mass addition and removal process is accounted for entirely by the equivalent oscillation of the rear bulkhead. The relationship between the shear layer displacement at the trailing edge and the oscillation of the rear bulkhead is considered in the pseudopiston analysis in Appendix A.

The exact shape of the oscillating rear bulkhead is unknown. We need not assume that it moves as a rigid wall, since it is only an approximation to the actual trailing-edge mass addition and removal process. The most important feature of its motion

is that a net unsteady mass flow is produced. Little can be said about its actual time-dependent shape, i.e., about the moments of mass flow. These details depend on the actual hydrodynamic processes at the trailing edge, and these are complex. However, as long as the cavity depth is less than a wavelength, the net mass addition and removal must be the primary physical effect. The moments of mass flow will alter structural details, but they are not of any great consequence to the basic physical process. In fact, these details probably vary from cycle to cycle, because of the turbulent character of the mass addition and removal process.

4.2.2 Real Flow Effects

In addition to the idealization of the mass addition process, there are other real flow effects that must be considered. One such effect is flow recirculation in the cavity.

As mentioned earlier, the recirculation level depends not only on the external flow Mach number and Reynolds number and the cavity length-to-depth ratio, but also on the cavity width and the thickness and state (laminar or turbulent) of the shear layer. In turn, these shear layer characteristics depend not only on external flow conditions, but also on the thickness and state of the upstream boundary layer. Although the recirculation velocities can be fairly large, it is believed that their effect on the internal wave motion is secondary. Near the cavity floor, the recirculation flow will move forward; while near the shear layer, where entrainment occurs, the recirculation motion will be rearward. The net effect is probably a tilting of the wavefronts. If this effect acts on an upstream wave that then reflects to become a downstream wave, the tilt direction will be reversed in the (mirror image) reflection process. The effect of recirculation flow on the downstream wave will then be to rotate the wavefront to a more upright position. In other words, there is a certain degree of cancellation associated with the effect of flow recirculation. It seems likely that the effect of flow recirculation on wave motion introduces uncertainties that are no greater than those due to the basic lack of information about the detailed shape of the oscillating rear bulkhead (i.e., pseudopiston due to the mass addition process).

Another concern introduced by real flow effects is the proper treatment of the shear layer dynamics. The simplest approach is to treat the shear layer as an infinitely thin vortex sheet, i.e., an idealized velocity discontinuity. In this approach, the freestream velocity is above the shear layer, and there is

no mean flow velocity in the cavity below the shear layer. The fluid in the cavity can be assumed to have approximately the correct thermodynamic properties: namely, freestream static pressure, and a static temperature equal to the freestream stagnation temperature (equal stagnation enthalpy on both sides of the shear layer). This basic approach is taken in the subsequent analysis. Because of the infinitely thin shear layer, this approach tends to overestimate the strength of the interaction between the fluid regions. This overestimation is believed to produce a spatial amplification rate for the downstream traveling waves that is disproportionately large. In fact, this excessive amplification of the downstream wave seems to be responsible for the main shortcoming of the analysis, i.e., its inability to predict more than the first pressure-mode shape over much of the Mach number range.

The free shear layer over a real cavity has a finite thickness that increases toward the rear of the cavity. If the shear layer is turbulent, this increase can be considerable; for a subsonic external flow, the thickness can be as much as 20% of the downstream distance from the leading edge. The thickness behavior is further influenced in a complicated way by the upstream boundary layer. Fortunately, the upstream boundary layer thickness is small compared to the ultimate shear layer thickness in many cavity applications. Even with this simplification, however, the shear layer thickness and profile are not easily predicted. It is believed that the shear layer thickness produces a significant effect on the cavity dynamics by altering the kinematic and dynamic conditions that match the internal and external solutions. This effect would be roughly similar to the inclusion of an effective inertia due to the shear layer thickness. If the spatial variation of shear layer thickness is not too great over the wavelength, then the problem can be managed analytically if the shear layer structure is modeled in a simple manner. The analytical results indicate that the inclusion of shear layer thickness effects (which will reduce shear layer amplification rates) is an important topic, which is worthy of future theoretical investigation.

4.2.3 A Simple Analytical Model

Once the important features of an analytical model are reviewed, it is appropriate to discuss the actual solution of the problem or an acceptable approximate solution. The external and internal regions can both be solved by transform methods with the application of appropriate boundary conditions. The

two solutions must be matched kinematically and dynamically across the shear layer. If the shear layer is treated as an infinitely thin discontinuity, then this matching corresponds to applying the material surface condition and requiring equal static pressures. If shear layer thickness effects are included, then a more complicated matching condition must be applied. The physical solution is then obtained by inverse transforms.

This formal approach is subject to severe mathematical difficulties. Indeed, the effort required may not be justifiable on physical grounds. Because the details of the trailing-edge mass addition process cannot be determined, any effort spent assuring that other cavity boundary conditions are satisfied in detail is wasted. Specifically, a different set of mass flow moments at the rear bulkhead will change the detailed wave structure elsewhere; hence, the strength of waves required to satisfy the boundary conditions will be altered. Therefore, it is proposed to use a simple physically motivated solution that satisfies only the most basic conditions and that does not include the finer details. In fact, this is the only approach that is really justifiable. When the cavity problem is reduced to its essence, only the basic upstream and basic downstream waves are considered. The reflection condition at the front bulkhead will be satisfied only to the extent that the instantaneous net mass flow induced by the waves be zero; moments of mass flow are not required to vanish. This approach is consistent with the rear bulkhead condition, where there is an oscillating net mass flow. The Kutta condition will be applied at the leading edge only in the sense that the spatial envelope of the waves decays exponentially upstream. This approach allows the problem to be reduced to the motion of waves between a shear layer and a boundary. The frequency of these waves is real corresponding to an oscillating phenomenon; therefore, their wave number is complex, corresponding to propagation and spatial amplification or decay. Since only basic waves are considered, and only one condition (front bulkhead reflection) is required to relate the wave strengths, transform techniques are no longer required.

At this point, the oscillation frequency of the rear bulkhead or pseudopiston is still undetermined. Determination of this frequency may come through a set of phase and amplitude-matching conditions, which are arrived at by separate consideration of the trailing-edge mass addition process and then the synthesis of the two analyses. For instance, a simple condition would require the shear layer motion to be in phase with the oscillating rear bulkhead. However, because of the complexity of the processes at the trailing edge, especially in view of real flow effects, it is easy to believe that significant phase shifts between the shear layer and pseudopiston may occur.

Given this latitude, it is possible to suppose, alternatively, that within some limits the phase and/or amplitude of the mass addition process adjusts to a condition most favored by the internal wave dynamics of the cavity. This adjustment might serve, for instance, to accommodate a resonance of the system. Or, as another possibility, the condition might be the frequency that gives the maximum shear layer displacement for a given pseudopiston displacement, thereby maximizing the energy removal from the mean flow for a given level of cavity pressure oscillations. This last condition seems to be the correct one in that, in later sections, it will be shown to give the best agreement between the present theory and the experimental measurements. Such conditions are actually satisfied for a set of frequencies, given the cavity geometry. Each frequency corresponds to a different mode of oscillation. Experiments show that these modes often occur simultaneously. The cavity geometry and the flow Mach number determine which mode level dominates; however, it is frequently the second mode. Presumably, this dominance can be determined theoretically. It may correspond to which mode can extract the most mean flow energy or to which mode produces the lowest impedance of the pseudopiston.

4.3 Wave Motion of a Shear Layer Above a Boundary

In this section, we discuss the wave motion between a shear layer and a boundary. The ultimate goal is to understand the speed and amplification characteristics of the type of waves that are responsible for the cavity oscillation phenomenon. The basic solutions developed here will eventually be superimposed to represent the boundaries of a cavity being forced by a piston at the rear bulkhead. In this manner, the modal structure within the cavity can be established.

Consider a shear layer and a parallel solid boundary separated by a distance, D . Between the shear layer and the boundary is an inviscid, compressible fluid with a sound speed, a_c . On the other side of the shear layer is an inviscid, compressible fluid moving with uniform velocity, U_∞ , and having a sound speed, a_∞ . It is of interest to find the relation that governs the motion of small amplitude waves under the shear layer (see Fig. 8).

The wave motion within the cavity is analyzed using the coordinate system (I) in Fig. 8. The perturbation velocity potential is governed by the simple wave equation in two dimensions:

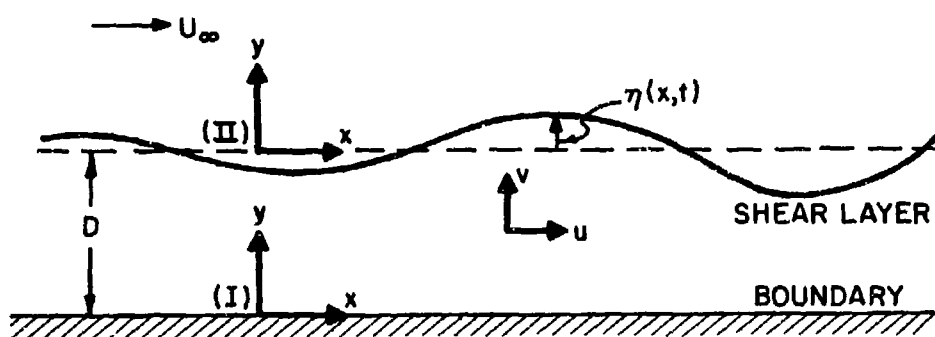


FIG. 8. WAVES ON A SHEAR LAYER ABOVE A BOUNDARY.

$$\phi_{xx} + \phi_{yy} - \frac{1}{a_c^2} \phi_{tt} = 0 \quad . \quad (4.1)$$

Assume solutions of the form,

$$\phi \propto e^{\alpha y} e^{ikx} e^{i\omega t} \quad , \quad (4.2)$$

where

$$\alpha^2 = k^2 - \frac{\omega^2}{a_c^2} \quad . \quad (4.3)$$

A more general solution for fixed frequency can be constructed

$$\phi = e^{i\omega t} \sum_{n=1}^m C_n e^{ik_n x} \cosh \alpha_n y \quad , \quad (4.4)$$

where C_n represent arbitrary constants. Similarly, solutions with different frequencies could be added if desired. Notice that the condition of zero normal velocity at the boundary is satisfied by using the hyperbolic function to re-express the y -dependence.

The perturbation pressure at the shear layer is

$$\frac{p}{\rho_c} = - \phi_t \Big|_{y=D-} = e^{i\omega t} \sum_{n=1}^m -i\omega C_n e^{ik_n x} \sinh \alpha_n D \quad . \quad (4.5)$$

The displacement of the shear layer is

$$\begin{aligned} \eta &= \int v dt \Big|_{y=D-} = \int \phi_y dt \Big|_{y=D-} \\ &= e^{i\omega t} \sum_{n=1}^m - \frac{i\alpha_n}{\omega} C_n e^{ik_n x} \sinh \alpha_n D \quad . \end{aligned} \quad (4.6)$$

The flow phenomena above the shear layer is governed by the convective wave equation:

$$(1-M^2)\phi_{xx} + \phi_{yy} - 2 \frac{M}{a_\infty} \phi_{xt} - \frac{1}{a_\infty^2} \phi_{tt} = 0 \quad (4.7)$$

The coordinate system (II) in Fig. 8 is now used. Assume solutions of the form

$$\phi = e^{i(kx+\beta y)} e^{i\omega t}, \quad (4.8)$$

with

$$\beta^2 = - (1-M^2)k^2 + 2 \frac{M}{a_\infty} \omega k + \frac{\omega^2}{a_\infty^2} \quad (4.9)$$

As before, these solutions can be added to achieve a more general form,

$$\phi = e^{i\omega t} \sum_{n=1}^m A_n e^{i(k_n x + \beta_n y)}, \quad (4.10)$$

where the A_n are arbitrary constants. The perturbation pressure at the shear layer is now given by

$$\begin{aligned} \frac{p}{\rho_\infty} &= \left(-\phi_t - U_\infty \phi_x \right)_{y=0+} \\ &= e^{i\omega t} \sum_{n=1}^m -i(\omega + U_\infty k_n) A_n e^{ik_n x} \end{aligned} \quad (4.11)$$

The normal velocity at the shear layer is

$$v = \phi_y \Big|_{y=0+} = e^{i\omega t} \sum_{n=1}^m i\beta_n e^{ik_n x} \quad (4.12)$$

We can apply the boundary conditions that static pressures match across the shear layer and that the shear layer be a material surface. The pressure-matching condition requires that the two pressures found by considering the regions above and below the shear layer should be equated. The material surface condition is determined by requiring that the vertical velocity in the upper region calculated from shear layer displacement equals that calculated directly:

$$v \left(= \phi_y \Big|_{y=0+} \right) = \eta_t + U_\infty \eta_x . \quad (4.13)$$

The first term on the right-hand side arises from unsteady shear layer motion and the second from tilting the free stream so it is tangent to the displaced shear layer. The completion of the details leads to the following dispersion relation between frequency and wavenumber:

$$i\omega^2 \beta \cosh \alpha D = \frac{\rho_\infty}{\rho_c} (\omega + U_\infty k)^2 \alpha \sinh \alpha D , \quad (4.14)$$

where

$$\alpha^2 = k^2 - \frac{\omega^2}{a_c^2} ,$$

and

$$\beta^2 = \left(Mk + \frac{\omega}{a_\infty} \right)^2 - k^2 .$$

For disturbances that originate in the vicinity of the shear layer and the boundary, only some of the solutions of the dispersion relation will be admissible. A radiation condition will be used to exclude solutions that represent waves traveling inward from infinity and solutions that become singular at infinity. Furthermore, the case of interest will be the determination of wavenumber k for a fixed real frequency, ω . This corresponds to the case of a forced system that is of interest for the future application of these solutions. When the frequency is real, the wavenumber will generally be complex. This corresponds to waves that travel and amplify or decay spatially.

Because of the transcendental nature of the dispersion relation, there are infinitely many solutions for a fixed frequency. Those that are admissible by the radiation condition can be divided according to whether they travel upstream or downstream. The main interest will be in the speed and amplification of waves that correspond most nearly to plane waves traveling between the shear layer and the boundary. It is these waves that seem to dominate in the oscillation phenomenon of shallow cavities.

The dispersion relation will now be re-expressed in a more appropriate form. If we use the equation of state and the definition of the speed of sound, and assume equal static pressures prior to perturbation, we obtain

$$\rho_{\infty} \frac{a_{\infty}^2}{\gamma_{\infty}} = \rho_c \frac{a_c^2}{\gamma_c} . \quad (4.15)$$

If the ratio of specific heats is the same on both sides of the shear layer, then

$$\frac{\rho_{\infty}}{\rho_c} = \left(\frac{a_c}{a_{\infty}} \right)^2 \equiv \tilde{a}^2 . \quad (4.16)$$

If we assume that the static temperature below the shear layer equals the stagnation temperature above (the appropriate assumption for the application of this analysis to cavity oscillations), then

$$\tilde{a} = \frac{a_c}{a_{\infty}} = + \sqrt{1 + \frac{\gamma-1}{2} M^2} , \quad (4.17)$$

where $\gamma = 1.4$ for air.

It is convenient to define the following nondimensional quantities:

$$\begin{aligned}
S &= \frac{\omega D}{a_c} \\
K &= kD \\
T &= \alpha D \text{ and } T^2 = K^2 - S^2 \\
Q &= (MK + \tilde{\alpha}S)^2 \\
B &= \beta D \text{ and } B^2 = Q - K^2
\end{aligned}
\tag{4.18}$$

Using the above, the dispersion relation can be manipulated into the following form,

$$Q^2 T^2 \sinh^2 T + S^4 (Q - K^2) \cosh^2 T = 0 \quad . \tag{4.19}$$

In the process of obtaining this form, the original relation has been squared. Although the order is now doubled, the ambiguity of signs for the square roots is no longer present and the total number of roots is unchanged.

Solutions of the above form of the dispersion relation were obtained using the computer. Analytical techniques that were also developed were either unsuccessful or not sufficiently accurate over a wide enough range of the parameters to justify their further use. The general spatial configuration of roots in the complex K plane is illustrated in Fig. 9. A detailed map of roots, A , B , and C , is presented in Fig. 10. The roots D and E fall on the negative real K axis; their presentation in Fig. 10 would not be informative since everything falls on a single line. The additional roots indicated in Fig. 9 were computed. However, such a computation follows easily, either by numerical methods or by assumption of large $|K|$ in the dispersion relation in order to achieve an analytical approximation. These roots would be useful only if the internal wave structure of the cavity were to be constructed in greater detail than is the present intention. Appendix B presents all of the roots that were computed.

The next step is to choose the waves that satisfy the boundary conditions of the problem, so that they can be superimposed to (approximately) form the cavity geometry. Then, the detailed dynamics of the system can be investigated. Upstream traveling waves have $\text{Re}K > 0$, and downstream waves have $\text{Re}K < 0$. The condition that disturbances do not amplify away from the boundary, namely that amplitudes are finite or zero as $y \rightarrow \infty$, requires $\text{Im}B \geq 0$. It is also necessary that the spatial envelope

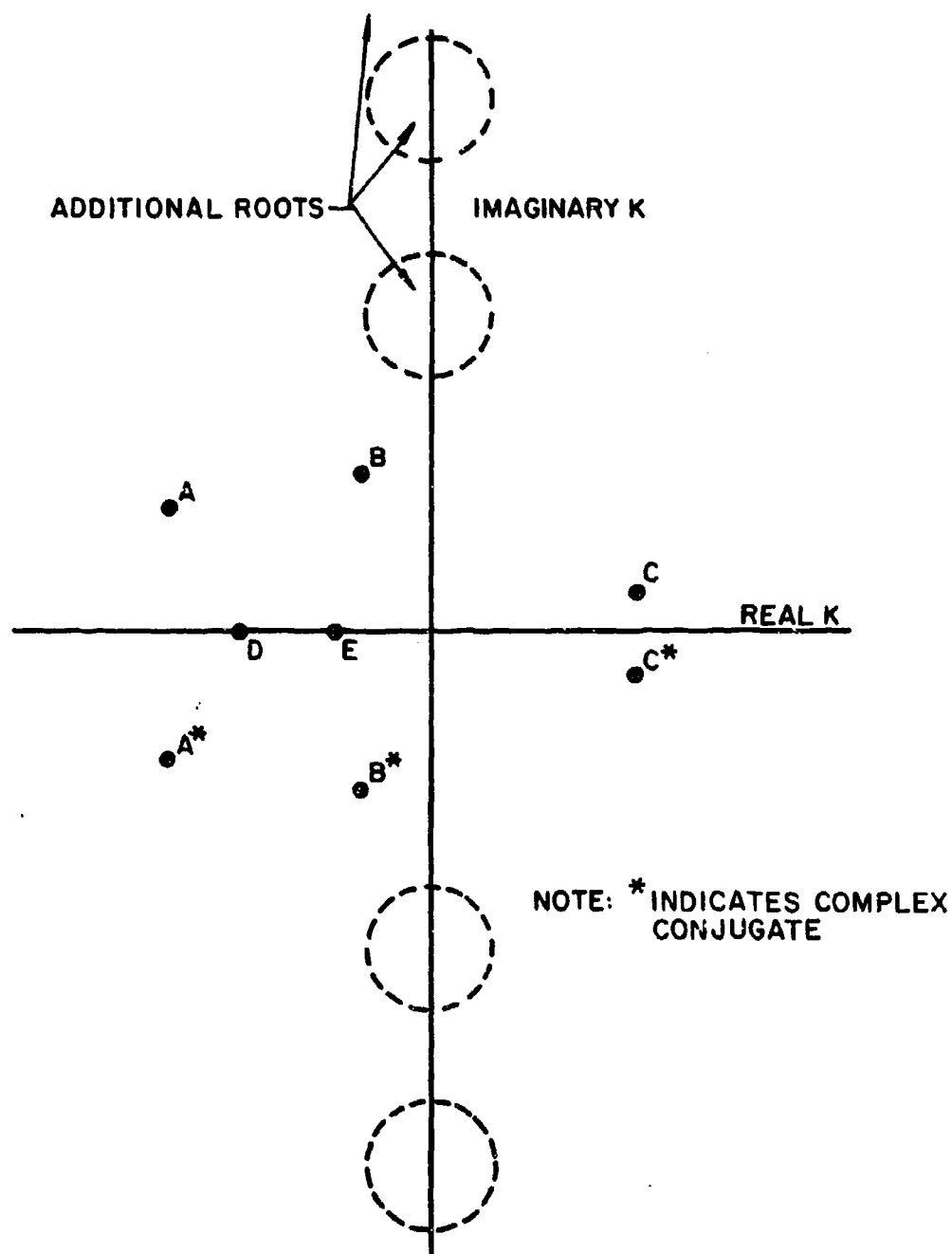


FIG. 9. GENERAL SPATIAL CONFIGURATION OF ROOTS.

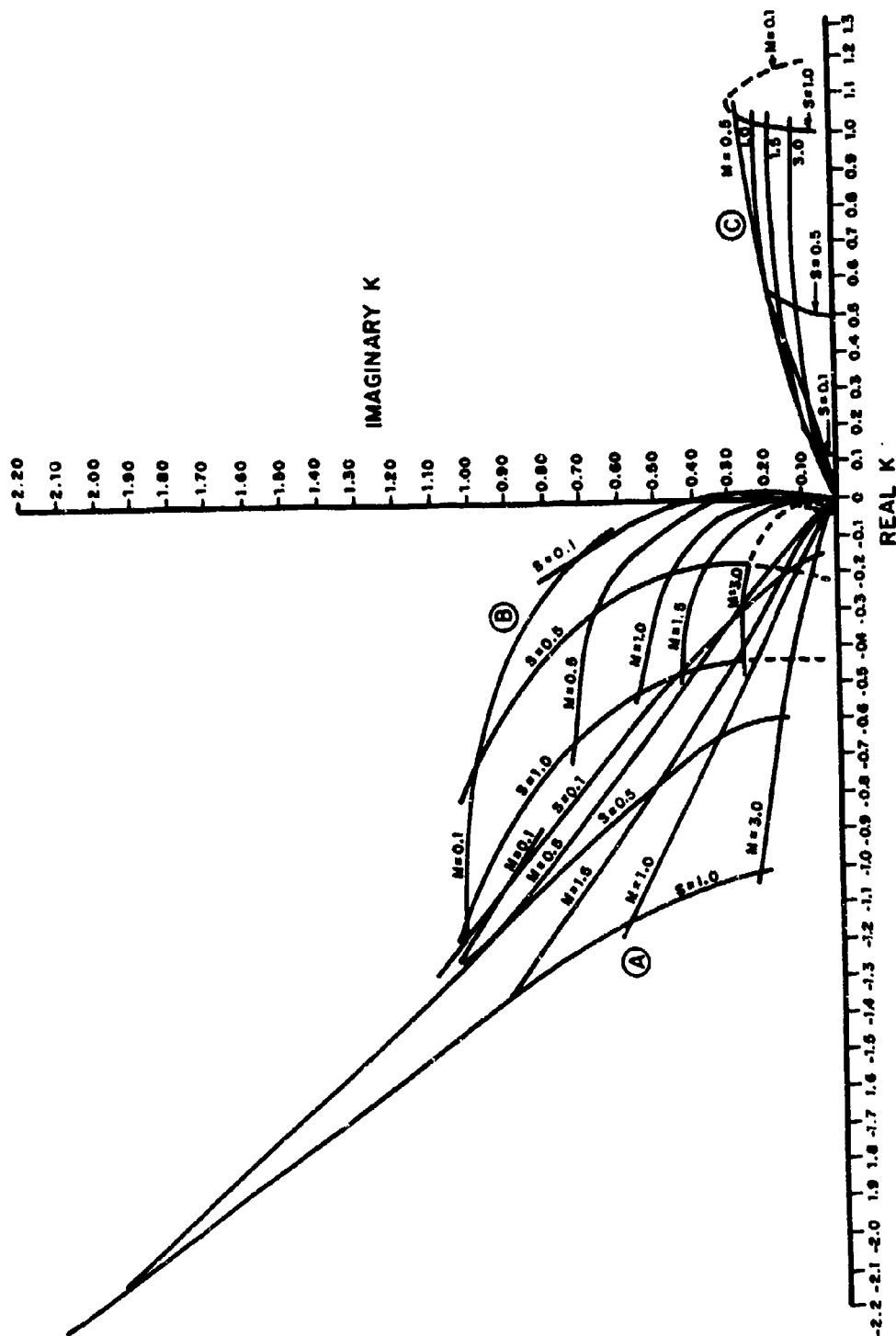


FIG. 10. MAP OF ROOTS A, B, AND C IN THE K-PLANE.

of the waves decays upstream since superfluous upstream influence in this simple cavity model would then be reduced. Furthermore, this requirement is consistent with the idea that the upstream wave radiates energy and decays, whereas the downstream wave draws energy from mean flow and amplifies. To satisfy these conditions, the roots K^* (the complex conjugates) should be used.

The roots A^* , B^* , and C^* are the prime candidates for use in a simple cavity oscillation model. Root C^* is the only upstream traveling wave, so it must be included in the analytical model. Both A^* and B^* are downstream waves, and it must be determined which is the important wave in the cavity oscillation phenomena. If we look at the nondimensional phase speed of these waves at the highest Mach number (see $M=3$ in the table), it is apparent that root A^* behaves as a pressure wave traveling below the shear layer at nearly the speed of sound, while root B^* behaves as a convection wave on the shear layer moving at nearly half the mean flow speed (supersonically relative to the cavity interior when $M=3$). Note that as $M \rightarrow \infty$ the shear layer becomes infinitely stiff, and the pressure waves below the shear layer behave as if in a hard-walled enclosure and travel at the speed of sound. Therefore, it is concluded that C^* is the relevant upstream wave and A^* is the relevant downstream wave.

4.4 Wave Solution Synthesis

Solutions for wave motion between a shear layer and a boundary have been found for the case of real frequency. Two of these waves will be combined to approximate a cavity with a piston at the rear wall, as shown in Fig. 11. The wave solutions must satisfy the following conditions:

1. They must be essential to the phenomenon; i.e., they must represent the basic physical effects and not be needed only to provide higher order structure.
2. Both upstream and downstream waves must be used.
3. They must satisfy the boundary conditions at infinity: i.e., these waves must originate in the region of the shear layer and boundary and not at infinity.
4. They must decay exponentially in the upstream direction. This reduces the upstream influence in this simple model and, in effect, provides an approximate Kutta condition.

In the previous section, it was found that the waves designated as A^* and C^* satisfy these requirements.

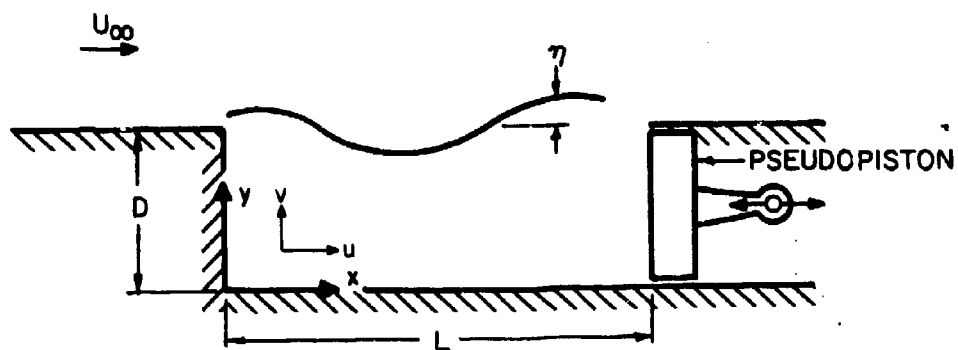


FIG. 11. PSEUDOPISTON ANALOGY.

The upstream wave C^* and the downstream wave A^* can be combined to form an approximation to wave motion in an oscillating cavity. With only two waves, just one boundary condition at the cavity leading edge can be applied. This boundary condition will be that the instantaneous net mass flow through the front bulkhead is always zero. Because these two waves do not have the same phase dependence with respect to depth, their local x-components of velocity cannot cancel over the entire front bulkhead. Thus, the instantaneous moments of mass flow through the bulkhead will generally not vanish. It is felt that these nonzero moments of mass flow only change the details of the cavity wave structure, and they do not produce any alteration of the basic process.

Similarly, the motion of a piston at the cavity trailing edge is defined in terms of the net mass flow at the rear bulkhead position. Again, moments of mass flow will not vanish. This approach is justified because the actual mass addition process does not correspond to a rigid piston shape.

Within the cavity, the velocity potential of this two-wave system is

$$\phi = e^{i\omega t} \left(A e^{ik_A x} \cosh \alpha_A y + C e^{ik_C x} \cosh \alpha_C y \right), \quad (4.20)$$

where A and C are constants. The velocity components are

$$u = \frac{\partial \phi}{\partial x} = e^{i\omega t} \left(ik_A A e^{ik_A x} \cosh \alpha_A y + ik_C C e^{ik_C x} \cosh \alpha_C y \right), \quad (4.21)$$

and

$$v = \frac{\partial \phi}{\partial y} = e^{i\omega t} \left(\alpha_A A e^{ik_A x} \sinh \alpha_A y + \alpha_C C e^{ik_C x} \sinh \alpha_C y \right). \quad (4.22)$$

The shear layer deflection is derived from the vertical velocity component:

$$\eta = \int v dt \Big|_{y=D} = e^{i\omega t} \left(-\frac{i\alpha_A}{\omega} A e^{ik_A x} \sinh \alpha_A D - \frac{i\alpha_C}{\omega} C e^{ik_C x} \sinh \alpha_C D \right). \quad (4.23)$$

The pressure is:

$$\frac{p}{\rho} = -\phi_t = e^{i\omega t} \left(-i\omega A e^{ik_A x} \cosh \alpha_A y - i\omega C e^{ik_C x} \cosh \alpha_C y \right). \quad (4.24)$$

The front bulkhead reflection condition requires that the instantaneous net mass flow vanish, namely

$$\int_0^D u dy \Big|_{x=0} = e^{i\omega t} \left(\frac{ik_A}{\alpha_A} A \sinh \alpha_A y + \frac{ik_C}{\alpha_C} C \sinh \alpha_C y \right) \Big|_0^D. \quad (4.25)$$

Thus, the relationship between the constants is

$$\frac{k_A}{\alpha_A} A \sinh \alpha_A D + \frac{k_C}{\alpha_C} C \sinh \alpha_C D = 0. \quad (4.26)$$

Similarly, the depth average of the lengthwise velocity component is

$$U_m = \frac{1}{D} \int_0^D u dy \Big|_{x=\text{const.}} = e^{i\omega t} \left(\frac{ik_A A}{\alpha_A D} e^{ik_A x} \sinh \alpha_A D + \frac{ik_C C}{\alpha_C D} e^{ik_C x} \sinh \alpha_C D \right). \quad (4.27)$$

The depth average pressure is

$$\frac{p_m}{\rho} = \frac{1}{D} \int_0^D \frac{p}{\rho} dy \Big|_{x=\text{const.}} = e^{i\omega t} \left(-\frac{i\omega A}{\alpha_A D} e^{ik_A x} \sinh \alpha_A D - \frac{i\omega C}{\alpha_C D} e^{ik_C x} \sinh \alpha_C D \right). \quad (4.28)$$

When the depth-averaged velocity and pressure are evaluated at $x = L$, they become the mean velocity and mean pressure on the pseudopiston.

It is convenient to recast these results in nondimensional form. As in Sec. 4.3, let

$$K \equiv kD, \quad S \equiv \frac{\omega D}{\alpha_c}, \quad \text{and} \quad T \equiv \alpha D. \quad (4.29)$$

Recall that the quantities K and T are functions of M_∞ and S . Redefine the constants as

$$\hat{A} = \frac{A}{Da_c} \quad \text{and} \quad \hat{C} = \frac{C}{Da_c}. \quad (4.30)$$

The depth-averaged Mach number of the wave-induced longitudinal velocity perturbation is

$$\hat{M}_m = \frac{U_m}{a_c} \quad (4.31)$$

The nondimensional depth-averaged pressure is

$$\hat{p}_m = \frac{p_m}{\rho a_c^2} \quad (4.32)$$

and the nondimensional shear layer displacement is defined as

$$\hat{\eta} = \frac{\eta}{D} \quad (4.33)$$

If we eliminate one of the constants and nondimensionalize the results, we obtain

$$\hat{M}_m = e^{i\omega t} \frac{1K_A}{T_A} \hat{A} \sinh T_A \left(e^{iK_{AD} \frac{x}{D}} - e^{iK_{CD} \frac{x}{D}} \right) \quad (4.34)$$

$$\hat{p}_m = -e^{i\omega t} iS \frac{K_A}{T_A} \hat{A} \sinh T_A \left(\frac{1}{K_A} e^{iK_{AD} \frac{x}{D}} - \frac{1}{K_C} e^{iK_{CD} \frac{x}{D}} \right) \quad (4.35)$$

and

$$\hat{\eta} = -e^{i\omega t} \frac{1}{S} \frac{K_A}{T_A} \hat{A} \sinh T_A \left(\frac{T_A^2}{K_A} e^{iK_{AD} \frac{x}{D}} - \frac{T_C^2}{K_C} e^{iK_{CD} \frac{x}{D}} \right) \quad (4.36)$$

There are two other quantities of interest. The complex acoustic impedance of the pseudopiston is given by

$$Z = \frac{\hat{p}_m}{\hat{M}_m} = -S \frac{\left(\frac{1}{K_A} e^{iK_{AD} \frac{L}{D}} - \frac{1}{K_C} e^{iK_{CD} \frac{L}{D}} \right)}{\left(e^{iK_{AD} \frac{L}{D}} - e^{iK_{CD} \frac{L}{D}} \right)} \quad (4.37)$$

The complex ratio of $\hat{\eta}/\hat{M}_m$ is also of interest, since its phase indicates the relation between shear layer position at the trailing edge and the pseudopiston motion. The phase angle is zero when the shear layer deflection becomes negative just as the pseudopiston begins to move into the cavity. The magnitude of this quantity is the reciprocal of piston motion per unit shear layer deflection.

$$\frac{\hat{\eta}}{\hat{M}_m} = \frac{-1}{S} \frac{\left(\frac{T_A^2}{K_A} e^{iK_{AD}L} - \frac{T_C^2}{K_C} e^{iK_{CD}L} \right)}{\left(e^{iK_{AD}L} - e^{iK_{CD}L} \right)} \quad (4.38)$$

These formulas can now be used with the results of the previous section to calculate the wave structure in oscillating cavities.

4.5 Discussion of Results

Using the analyses of the previous sections, calculations were carried out to predict pressure-mode shapes and other properties of interest in shallow cavities. For mathematical convenience, the calculations were carried out with nondimensional frequency, S , held constant, while the distance from the leading edge was varied. In this way the mode shapes are immediately obtained. A certain discrete set of distances from the leading edge corresponds to the length-to-depth ratios of cavities that will oscillate freely at frequency S . When the calculation is repeated for a different nondimensional frequency, a different set of length-to-depth ratios will be found. Thus, the dependence of frequency on mode number, length-to-depth ratio, and flow conditions can be generated through this calculation procedure. Other methods, such as fixing length-to-depth ratio and varying frequency, could also be used. It should be noted here that the nondimensional frequency, $S = \omega D/a_c$, is not the same as $S^* = fL/U_\infty$, the Strouhal frequency which is often used to display cavity oscillation results. Of course, they are related:

$$S^* = \frac{\tilde{a}(L/D)}{2\pi M_\infty} S \quad (4.39)$$

$$\text{where } \tilde{a} = \frac{a_c}{a_\infty} = \sqrt{1 + \frac{\gamma - 1}{2} M_\infty^2} \quad .$$

A set of results was computed for the case of $M_\infty = 3.0$ and $S = 1.0$. Although this Mach number is really above the range of greatest interest, the results are instructive for this case; furthermore, a difficulty that occurs at lower Mach numbers is avoided. Figure 12 shows the magnitude of unsteady pressure fluctuations, expressed in dB, as a function of distance from the leading edge. The arrows denote the possible locations of a rear bulkhead. Although no experimental mode shape data are available at $M_\infty = 3.0$, it is encouraging that this computed shape bears a considerable qualitative resemblance to mode shape measurements at lower Mach numbers. Figures 13 and 14 show the magnitude of longitudinal velocity and shear layer displacement, respectively. Since both magnitudes are only determined to within a constant multiple, these curves should be of interest primarily for their shape and relative size.

Figures 15 and 16 show the magnitude and phase of the ratio $\hat{\eta}/M_m$, which is the complex shear layer deflection per pseudopiston velocity. Here, each value of x/D is interpreted as L/D , i.e., as a candidate trailing-edge location. Similarly, Figs. 17 and 18 show the magnitude and phase of the pseudopiston impedance. Finally, Figs. 19 and 20 show the magnitude and phase of the complex ratio $p_m/\hat{\eta}$, which is a type of impedance based on shear layer displacement rather than pseudopiston velocity. These quantities are presented as function of x/D (or L/D) at constant frequency S . (Note that this manner of presentation differs from the more familiar impedance vs *frequency* often seen in acoustics.)

The important question arises as to how the trailing-edge locations (L/D) can be determined from the information presented. Experimental results show that a pressure maximum occurs near, but not exactly at, the trailing edge; very often the pressure maximum occurs just before the trailing edge (see Sec. 6). Of course, the pressure maxima correspond closely to the points of maximum impedance. The vicinity of the pressure maxima seems to bear no special relation to the phase of the shear layer relative to the pseudopiston, $\arg \hat{\eta}/M_m$ (see Fig. 16). It is somewhat surprising that this phase difference is never zero, which would correspond to the intuitive kinematic relation between shear layer position and pseudopiston motion for an oscillating cavity. However, as mentioned earlier, there is reason to expect that significant phase shifts are introduced by the actual mass addition process. The one quantity that behaves in a distinct manner near the qualitatively expected trailing-edge locations is $|\hat{\eta}/M_m|$. This quantity, illustrated in Fig. 15, shows a series of distinct and rather narrow peaks occurring slightly

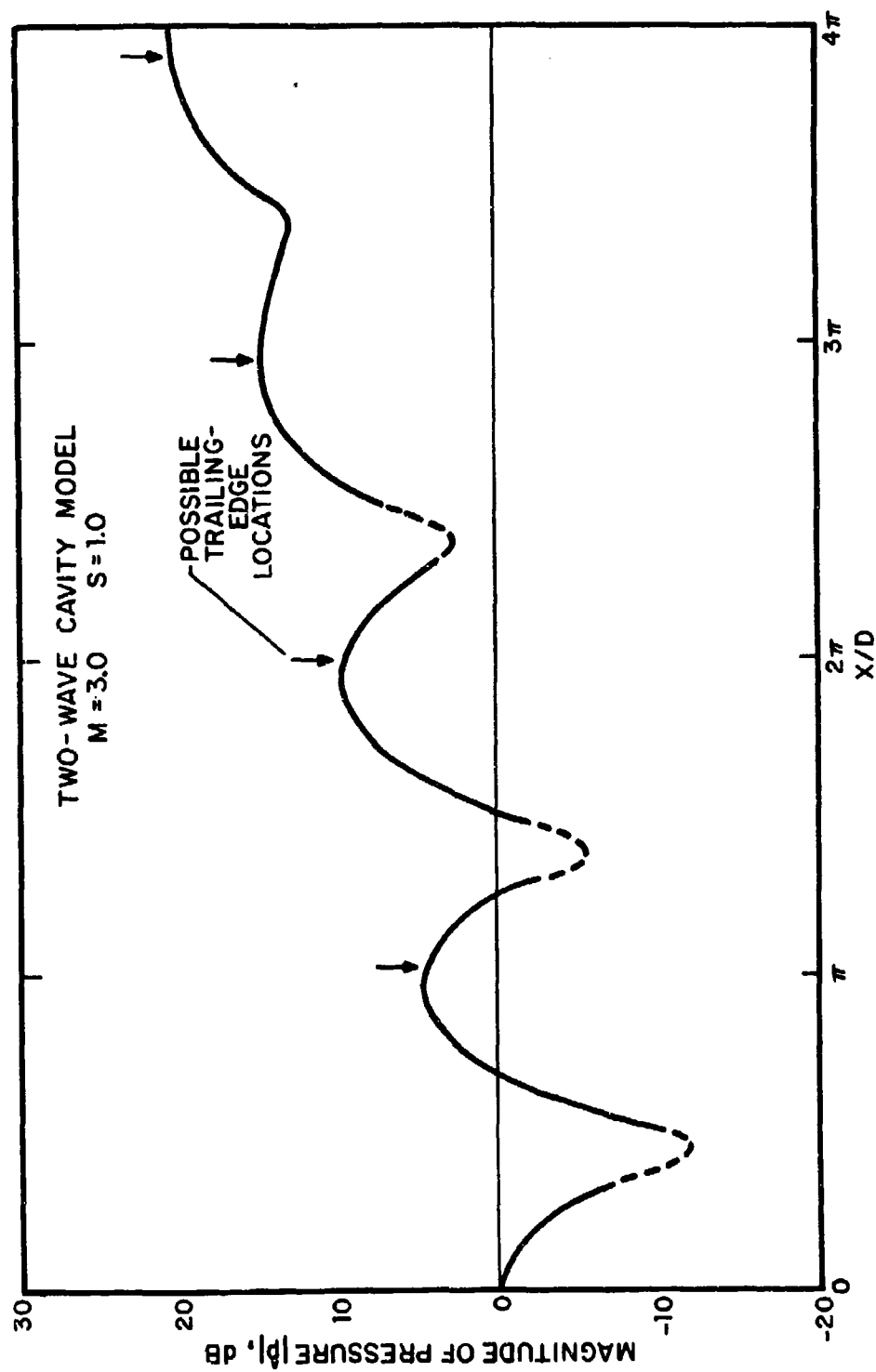


FIG. 12. MAGNITUDE OF UNSTEADY PRESSURE FLUCTUATIONS AS FUNCTION OF DISTANCE FROM THE LEADING EDGE.

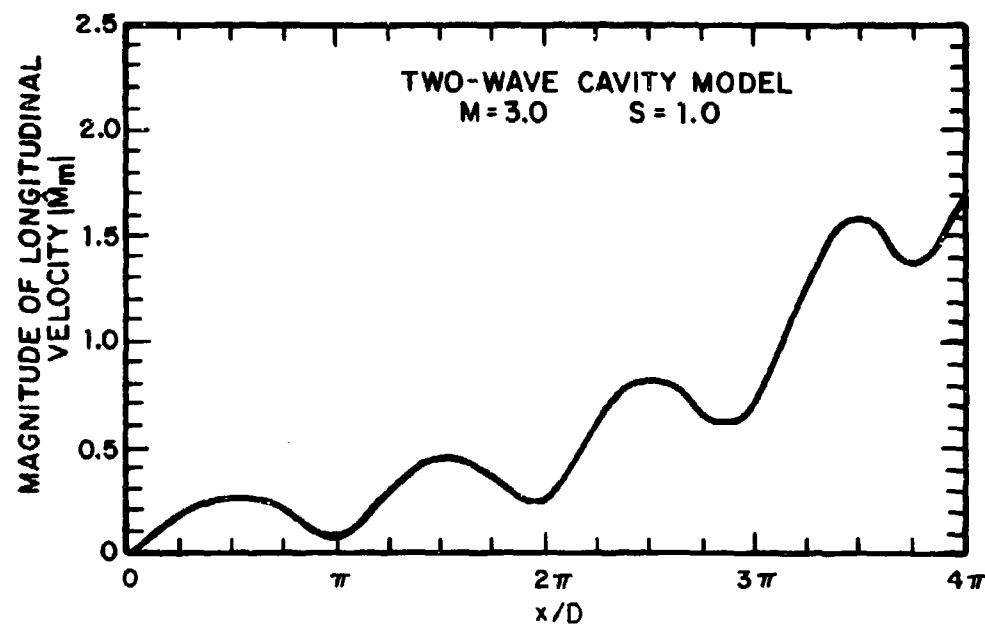


FIG. 13. MAGNITUDE OF LONGITUDINAL VELOCITY FLUCTUATIONS AS FUNCTION OF DISTANCE FROM THE LEADING EDGE.

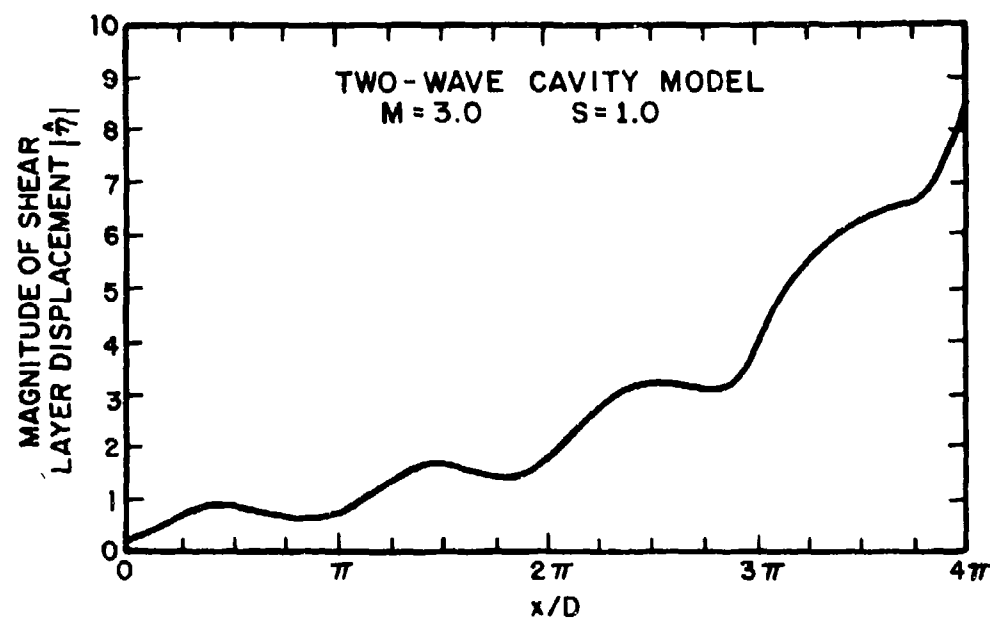


FIG. 14. MAGNITUDE OF UNSTEADY SHEAR LAYER DISPLACEMENT AS FUNCTION OF DISTANCE FROM THE LEADING EDGE.

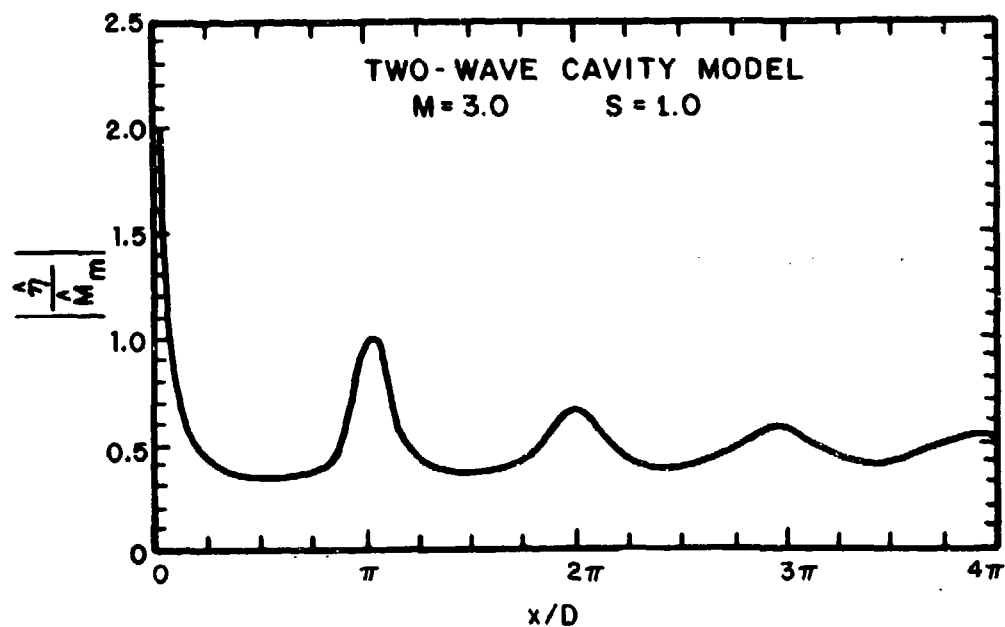


FIG. 15. MAGNITUDE OF THE RATIO OF SHEAR LAYER DEFLECTION AND LONGITUDINAL VELOCITY FLUCTUATION (PSEUDO-PISTON VELOCITY) AS FUNCTION OF DISTANCE FROM THE LEADING EDGE.

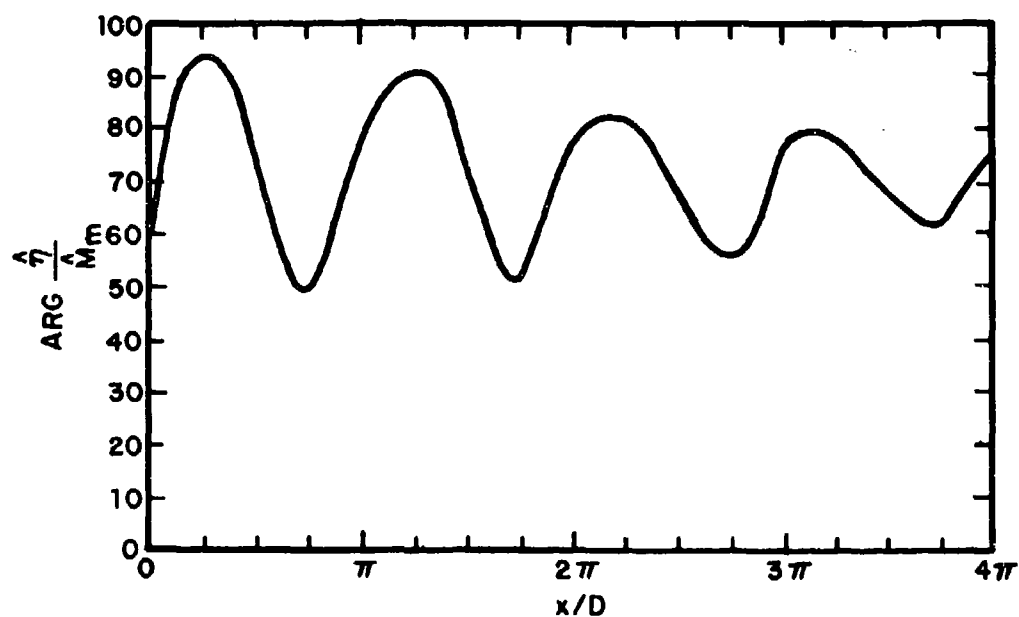


FIG. 16. PHASE OF THE RATIO OF SHEAR LAYER DEFLECTION AND LONGITUDINAL VELOCITY FLUCTUATION.

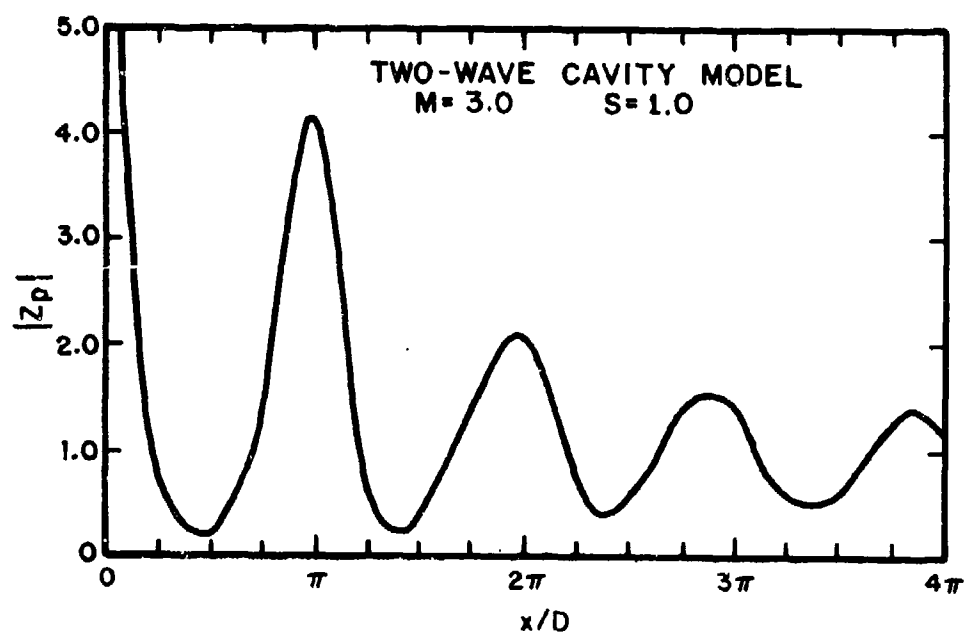


FIG. 17. MAGNITUDE OF THE IMPEDANCE OF A PSEUDOPISTON AS FUNCTION OF ITS DISTANCE FROM THE LEADING EDGE.

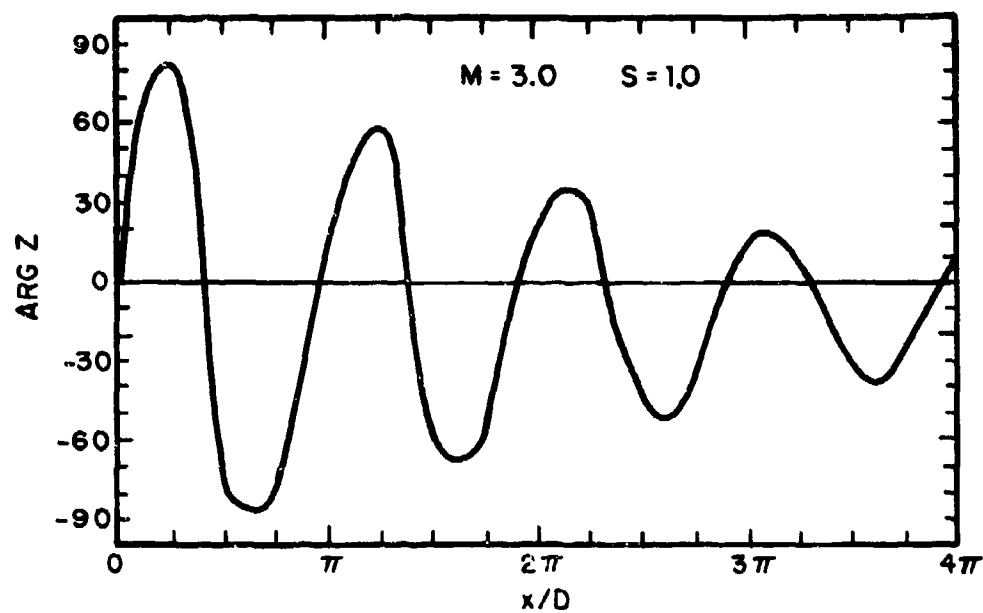


FIG. 18. PHASE OF THE IMPEDANCE SHOWN IN FIG. 17.

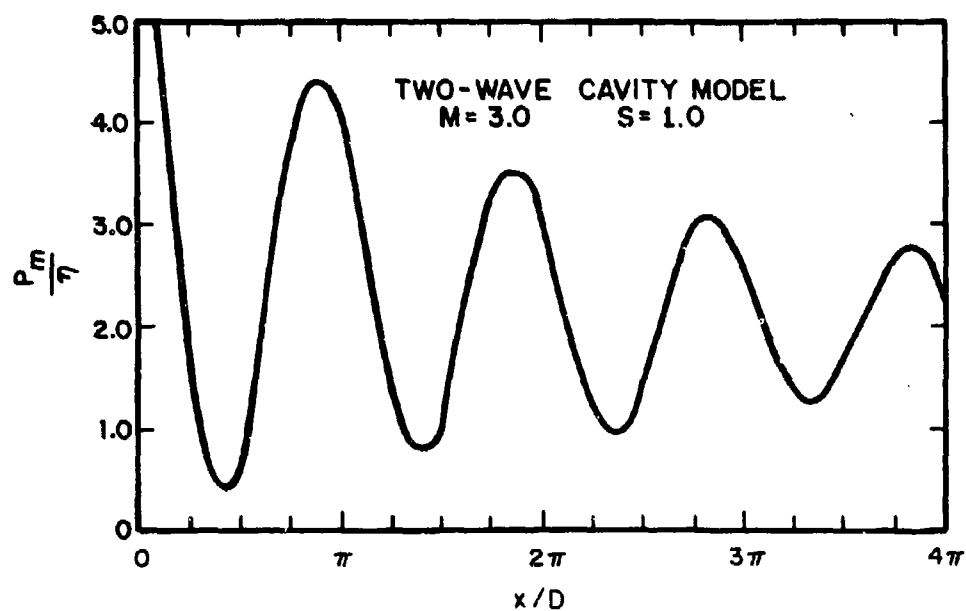


FIG. 19. MAGNITUDE OF AN IMPEDANCE BASED ON SHEAR LAYER DISPLACEMENT AS FUNCTION OF DISTANCE FROM THE LEADING EDGE.

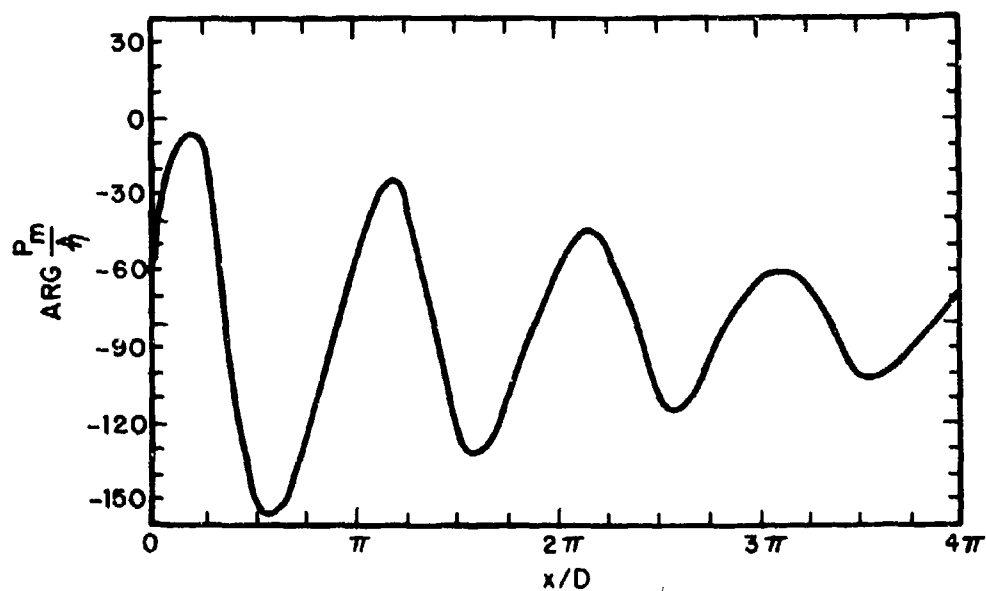


FIG. 20. PHASE OF THE IMPEDANCE SHOWN IN FIG. 19.

behind the pressure maxima. The rest of the curve is relatively flat. It is believed that the maxima of $|\hat{n}/\hat{M}_m|$ may represent the proper trailing-edge locations. The arrows on Fig. 12 were located according to this criteria. The maxima of $|\hat{n}/\hat{M}_m|$ correspond to the most mean flow addition for a given pseudo-piston displacement. Therefore, this condition corresponds to a maximum removal of energy from the mean flow by the trailing-edge mass addition process for a given motion of the pseudo-piston. If the net energy losses from other processes in the cavity are determined essentially by its level of activity (as indicated by the pseudopiston motion), then these criteria provide the most addition of energy to overcome these losses.

A somewhat different viewpoint can bring us to the same conclusion. From Fig. 13, it is apparent that the magnitude of wave-induced longitudinal velocity in the cavity is never zero, except at the leading edge. Therefore, without the trailing-edge mass addition and removal process, the proper boundary condition could never be satisfied at the rear bulkhead. However, it is nearly satisfied in the vicinity of the velocity minima, since in this location the least pseudopiston motion is required to provide the proper boundary condition. Clearly, the trailing-edge mass addition process operates most efficiently when the maximum shear layer deflection is available for a given pseudo-piston motion. Thus, the boundary condition at the trailing edge is most easily satisfied whenever $|\hat{n}/\hat{M}_m|$ is a maximum.

Once the criterion for picking the trailing-edge location is established, the oscillation frequencies for a fixed cavity geometry can be determined. Then, it may be possible to determine the relative strength of these modes of oscillation. It is believed that the determination of the dominant mode is related to a condition such as: which mode gives the lowest impedance of the pseudopiston; or which mode removes the most energy from the mean flow; or for which mode does the mass addition process operate most efficiently. This important area of research should receive more attention in the future, particularly since the answer has an importance which extends beyond the present problem.

The present analysis is less successful when the calculation is made for lower Mach number. This problem is illustrated in Fig. 21, where the Mach number is $M_\infty = 1.0$ and $S = 1/2$. It can be seen that only the first mode appears, and that the magnitude of unsteady pressure increases rapidly with increasing x/D . A similar trend is found when the calculation is repeated for $M_\infty = 1.0$ and $S = 1.0$. Although the first mode is predicted successfully, none of the higher modes is found because the

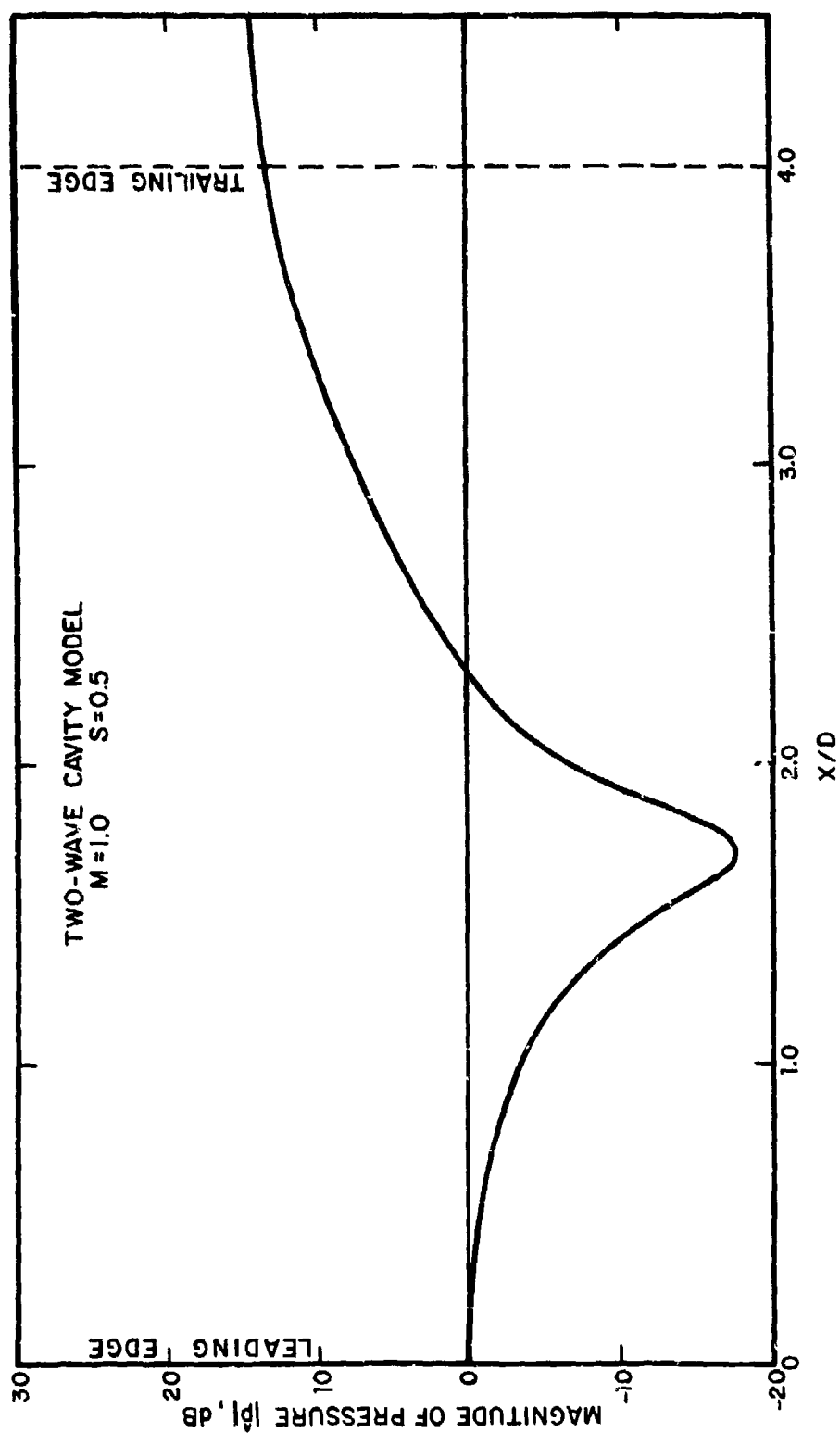


FIG. 21. MAGNITUDE OF UNSTEADY PRESSURE FLUCTUATIONS AS FUNCTION OF DISTANCE FROM THE LEADING EDGE.

magnitude of pressure increases rapidly without additional nodes. This result contradicts the experiments where modes as high as the fourth are detected. In fact, the second mode is often the one with dominant pressure levels. Because this shortcoming is found everywhere below about $M = 2.0$ for all S , an extensive investigation was undertaken to identify the problem. During this investigation, several alternate boundary conditions at both leading and trailing edges were tried. The effect of including the shear layer convection wave B^* was also considered for several different boundary conditions. For instance, when this additional wave is included, the Kutta condition can be applied in addition to the reflection condition at the front bulkhead. Finally, the possible effects of adding some of the other waves, and of doing the problem more formally, were considered. No dramatic improvements over the basic model were made, and some results were much worse. Nor did it seem worthwhile to make the problem more complicated.

Careful investigation shows that the source of the problem is that the spatial amplification rate of the downstream wave greatly exceeds that of the upstream wave over much of the Mach number range. This fact is apparent from the basic wave solutions which show that the imaginary part of K_A^* exceeds that of K_C^* ; the discrepancy increases with decreasing Mach number. Not far behind the leading edge, the exponential amplitude growth of the downstream wave dominates so completely that pressure nodes can no longer be formed; i.e., the energy extracted by the downstream wave from the flow greatly exceeds that radiated by the upstream wave. This fact does add theoretical support to the observation that cavity oscillations are self-sustaining under almost all flow conditions. However, since higher modes are commonly observed experimentally, it must be concluded that either the amplification rate of the shear layer is overestimated or that the ultimate amplification of the downstream wave is limited by some additional process. An example of the second possibility would be the nonlinearity introduced by the shear layer rolling up into discrete vortices, which has been observed at subsonic flow speeds. The present analytical difficulty extends well into the supersonic flow time where roll up is much less likely.

It is believed, therefore, that this simple model, which assumes an infinitely thin shear layer, overestimates the amplification rate of the downstream wave. This difficulty can be resolved by accounting for the finite thickness and different flow velocity of the shear layer. This effect could be included analytically in a future research effort. The

accuracy required for the cavity problem does not involve detailed theoretical flow solutions in the shear layer region. Once the shear layer is properly accounted for, it is expected that much better results could be obtained at lower Mach numbers, using basically the same analytical approach as described. If the present high Mach number results are any indication, this simple analytical approach may eventually lead to a complete and detailed theoretical understanding of the physics of the oscillation phenomenon.

4.6 Frequency Prediction

In this section, the wave solutions found in Sec. 4.2 are used as the basis for a semiempirical frequency prediction scheme. The approach taken is similar to that of Rossiter (1966). This discussion helps to illustrate the relationship between Rossiter's assumptions and the present physical model.

The pressure modes in the cavity are made from the superposition of upstream and downstream waves whose phase speeds are different. Suppose the average distance between pressure maxima is λ_p . Because of the different phase speeds and amplification rates, the actual distances between pressure maxima need not all be the same. Let $L + \delta = n\lambda_p$, where n is an integer and L is the cavity length. The quantity δ is an undetermined value that accounts for the facts that the cavity trailing edge is not actually a reflection plane (pressure maxima), that there are phase shifts in the system, and that λ_p is only an average value.

If T is the oscillation period,

$$\frac{L+\delta}{c_{pAr}} + \frac{L+\delta}{c_{pCr}} = nT, \quad (4.40)$$

where the mode number n equals the number of pressure minima in the cavity, c_{pAr} and c_{pCr} are the real part of the phase speed of the downstream wave and the upstream wave, respectively.

$$c_p = \frac{\omega}{k} = \frac{\omega}{|k|^2} k^* \quad (4.41)$$

Therefore,

$$c_{p_r} = \omega \frac{k_r}{|k|^2} \quad (4.42)$$

Then,

$$\frac{L+\delta}{\omega} \left(\frac{|k_A|^2}{k_{Ar}} + \frac{|k_C|^2}{k_{Cr}} \right) = \frac{2\pi}{\omega} n \quad (4.43)$$

Defining $K = kD$,

$$\left(\frac{|K_A|^2}{K_{Ar}} + \frac{|K_C|^2}{K_{Cr}} \right) = \frac{2\pi n}{\frac{L}{D} \left(\frac{L+\delta}{L} \right)} \quad (4.44)$$

Suppose the factor δ is a fraction (positive or negative) of a wavelength, namely $\delta = \alpha \lambda_p$. Since $1 + \delta = n \lambda_p$, and $L = n \lambda_p - \delta$:

$$\frac{L+\delta}{L} = \frac{n}{n-\alpha} \quad (4.45)$$

Hence,

$$\left(\frac{|K_A|^2}{K_{Ar}} + \frac{|K_C|^2}{K_{Cr}} \right) = \frac{2\pi(n-\alpha)}{L/D} \quad (4.46)$$

where K_A and K_C are functions of M_∞ and S . If M_∞ , n , and L/D are specified, and a value of the empirical constant α is assigned, then the above equation determines S . From this, the cavity Strouhal number, $S^* = fL/U_\infty$, can be determined.

$$S^* = \frac{\tilde{a}(L/D)}{2\pi M_\infty} \quad (4.47)$$

where $\tilde{a} = \sqrt{1 + \frac{\gamma-1}{2} M^2}$.

Figure 22 shows these results plotted for $\alpha = 0.1$ for $n = 1.0$, and $\alpha = 0.25$ for $n = 2, 3$, and 4 . The Rossiter formula is also shown.

The results show the effect of length-to-depth ratio. The predicted Strouhal numbers begin to fall below the measured results when $M < 1.0$. This problem can be traced once again to the excessive amplification rate of the downstream wave, which affects the phase speed. If the calculation is repeated by setting the imaginary part of K equal to zero (no amplification), then the computed frequencies fall above the measured results at low Mach number. This fact suggests that lowering the amplification rate will raise the present results at low Mach number, which then gives better agreement with the experiment. It is noted that there is no guarantee that the empirical constant α is independent of Mach number. However, substantial variations in α must be introduced to account for the discrepancy at low Mach number.

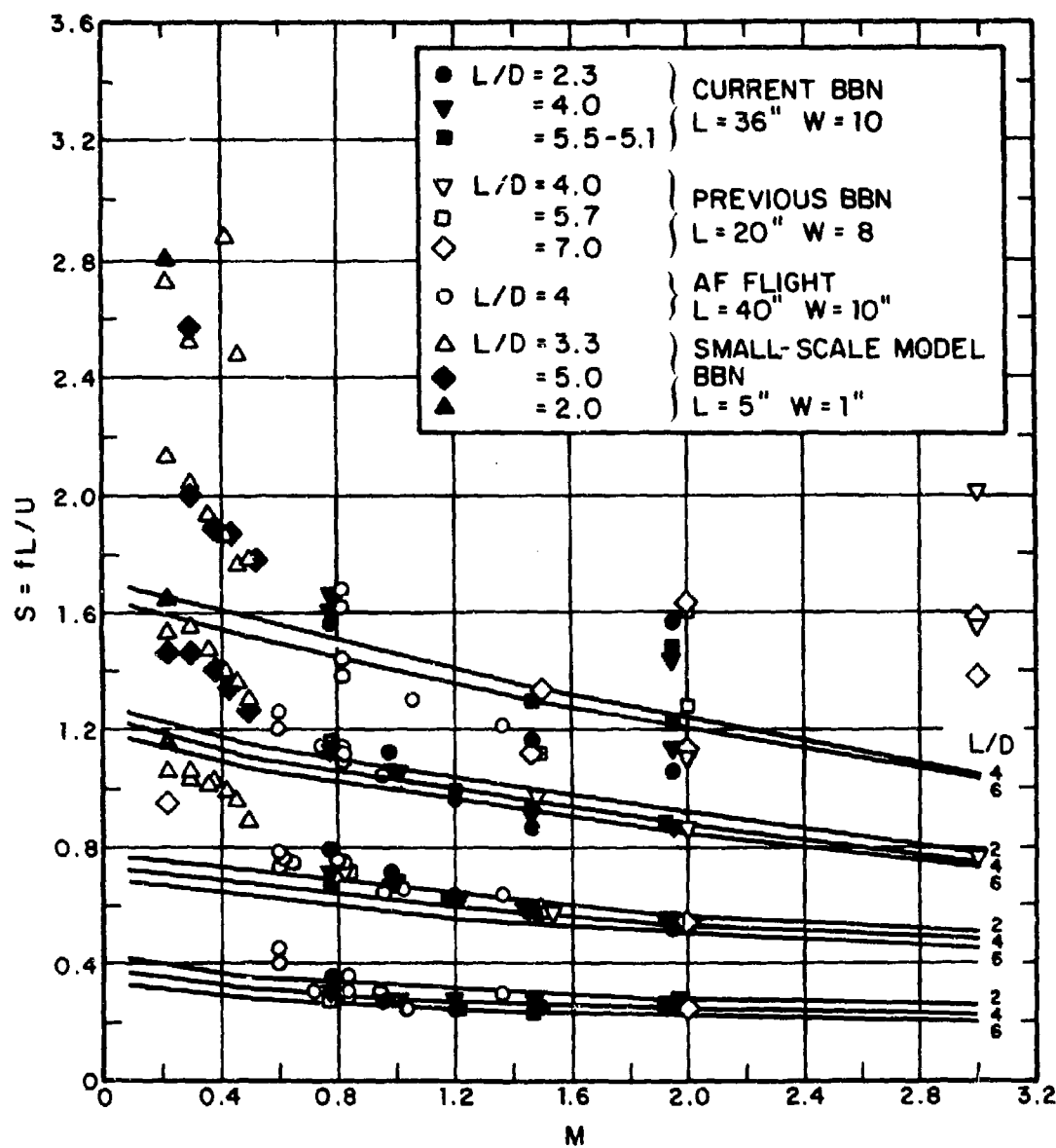


FIG. 12. COMPARISON OF SEMIEMPIRICALLY DERIVED LENGTH-TO-DEPTH RATIO DEPENDENCE OF RESONANT FREQUENCIES WITH EXPERIMENTAL DATA.

SECTION 5

EXPERIMENTAL CONSIDERATIONS

5.1 Scope of Experimental Studies

The analytical considerations, presented in the previous sections, provided insight into the basic physical phenomena that are responsible for the occurrence of flow-induced pressure oscillations in shallow cavities. In particular, it was determined that the onset of pressure fluctuations depends on the balance between energy supplied by the external flow and energy dissipated by viscous losses and acoustic radiation, so that an excess of energy drawn from the external flow results in the onset and sustenance of oscillations and vice versa.

While the oscillation onset is linked to both phase and gain criteria, no particular onset velocity was found to exist for shallow cavities. However, a set of general aerodynamic criteria was established that define a region (in terms of geometry and flow parameters) where the least damping of shear layer wave motion occurs; thus, the oscillation process sustains itself. The analysis had a twofold purpose: (1) to determine the oscillation frequencies, the mode shapes, and mode levels in a resonant cavity; and (2) to establish criteria for stabilizing the flow in order to suppress the oscillation. The analysis was reasonably successful since it provided resonant frequencies as a function of geometric and aerodynamic parameters and, to some extent, the mode shapes; however, because of the extreme complexity of the flow/cavity interaction, no conclusive model could be developed to predict the mode levels accurately. The analysis was successful in establishing criteria for shear layer stabilization (a requirement for the suppression of pressure oscillations).

To evaluate the analytical predictions and to gain practical information, an experimental program was initiated. One important purpose of this program was to verify the resonant frequency predictions and the theoretically derived mode shapes, as well as to provide reliable information on maximum levels and mode-amplitude distribution in the cavity for a variety of cavity length-to-depth ratios and freestream Mach numbers. Another purpose of the experiments was to verify the criteria for shear layer stabilization and to find and optimize geometric changes of the basic rectangular cavity configuration for maximum oscillation suppression.

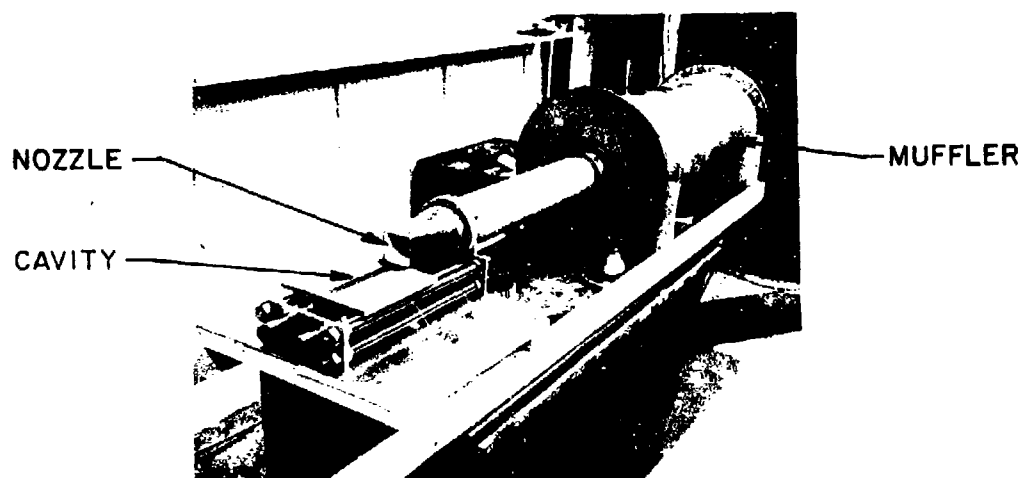
In order to attain these goals, it was necessary to conduct the experiments in a large flow facility primarily to eliminate the uncertainty usually associated with scaling. It was also desirable to conduct the experiments over a large Mach number range, to duplicate typical flight envelopes of modern aircraft. Finally, a test setup was necessary that allowed quick changes in cavity geometry.

The experiments were conducted in the NASA Lewis 8 x 6 ft Transonic Wind Tunnel, which met all the above conditions. In preparation for these large-scale experiments, however, tests were conducted in a small-scale wall-jet flow facility at BBN. This facility allowed a quick survey of a large number of configurations, so that some optimization of geometric changes could be made prior to large-scale testing. These small-scale tests, however, comprised only the subsonic Mach number range. In a supplementary effort, therefore, a water table flow visualization apparatus was constructed that proved to be helpful in visualizing the unsteady phenomena inside and outside the cavity for simulated supersonic external flow. The water table tests also served to check stabilization configurations.

5.2 Experimental Techniques: Small-Scale Studies

5.2.1 Exploratory Studies: Wall-Jet Flow Facility

Subsonic flow experiments were conducted using the test setup shown in Fig. 23. High-pressure air is fed through an absorptive muffler into a converging nozzle with a square opening of 3×3 in². The lower nozzle rim is flush with a plate, which contains a rectangular cavity 1 in. wide by 2.5 in. deep by 8 in. long. When insert blocks are used, the geometry can be readily changed to form cavities of length-to-depth ratios from 0.5 to 20. In all cases, however, the width is constant at 1 in. The flow emanating from the nozzle forms a wall jet, and the flow on the plate surface has the aerodynamic properties of any surface flow with a slow boundary layer growth (see Fig. 24). Along the unconstrained jet boundaries, the shear layer grows in accordance with the free mixing process, surrounding a potential core of low turbulence, which is reminiscent of quiescent air above a surface boundary layer. In all experiments, care was taken that the cavity mouth area was well within this potential core regime, so that the free shear layer of the wall jet would not affect the cavity pressure oscillation process. Since only cavity internal fluctuating pressures were measured, rather than farfield radiated acoustic pressures, there was no danger of shear layer acoustic refraction to affect the measurement data.



(a) TEST SETUP



(b) CLOSE-UP OF DRAG-FORCE LINK

FIG. 23. SMALL-SCALE WALL-JET FACILITY.

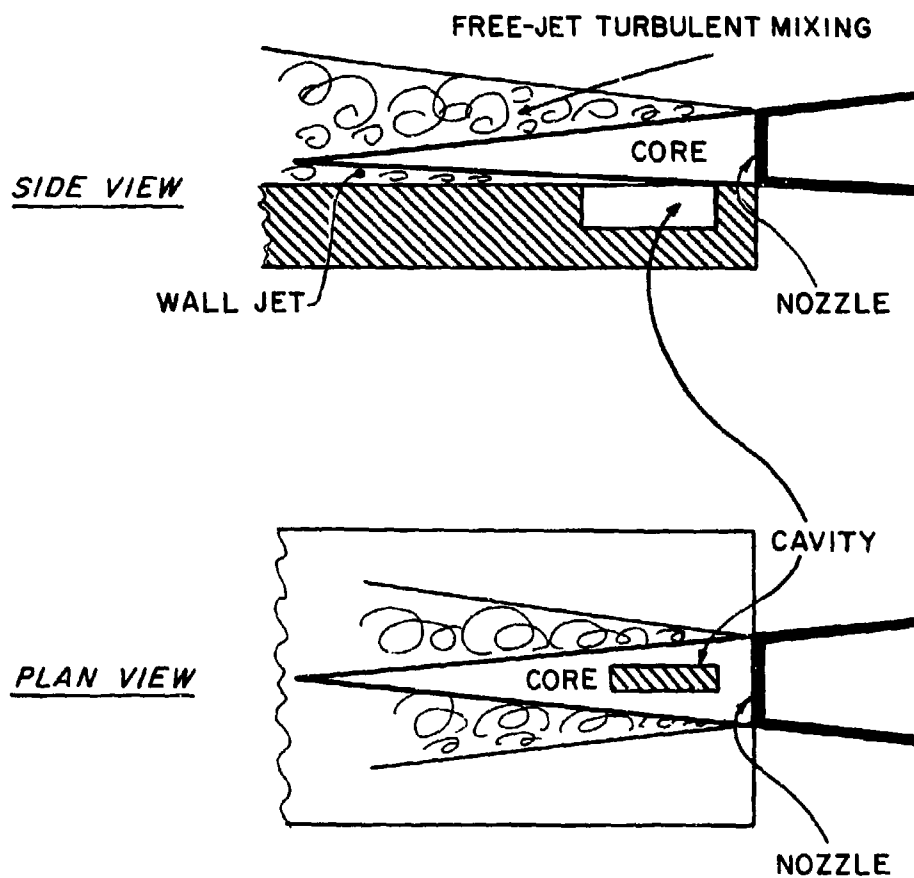


FIG. 24. LOCATION OF EXPERIMENTAL CAVITY UNDER A WALL-JET FLOW.

Prior to exiting from the nozzle, the flow passes through a honeycomb structure to extract any swirl and through several mesh wire grids to minimize the turbulence intensity in the potential core flow. Sandpaper roughness across the exit lip of the nozzle provides turbulent boundary layer flow to interact with the cavity mouth. Since it had been established in flight tests (Smith *et al.*, 1974) that inlet flow in aircraft bays under most flight conditions is turbulent, most of the experiments were conducted with the surface roughness at the nozzle exit. Exit flow speed could be varied from 0 to over 700 ft/sec. Flow speed is monitored through a pitot-static tube in the nozzle exit cross section.

Cavity internal fluctuating pressures were measured with BBN type 376 1/4 in.-diam. piezoelectric pressure sensors located at the leading-edge and the trailing-edge bulkheads. Sensor signals were usually fed into a GR type 1564A 1/10-octave band analyzer, and spectra plotted out on a GR type 1521 Graphic Level Recorder in real time.

One important issue of the study was the evaluation of the steady-state (dc) drag induced by the basic cavity configuration and the change in drag due to geometric cavity modifications through oscillation suppression devices. To measure dc drag, the plate containing the cavity was supported by low friction ball bearings that, in turn, ran on two horizontal steel rods (see Fig. 25). The drag forces (i.e., forces in the mean flow direction) were transferred via a 1/4-in. diameter steel ball to a (BBN-developed) force link, which was attached to a heavy steel frame. A bias force was provided through a spring pressing against the cavity block in the downstream direction with several times the force expected from the cavity drag. Force transfer through a steel ball eliminated the possibility, of any force or moment transfer, other than in the direction of the sensitivity axis of the force link, which, of course, coincides with the direction of flow-induced drag. The system was calibrated by applying a known force in the flow direction and reading the output voltage of the force gauge, after cancelling out the bias force. The force measurement system was perfectly linear in the range of measurements taken.

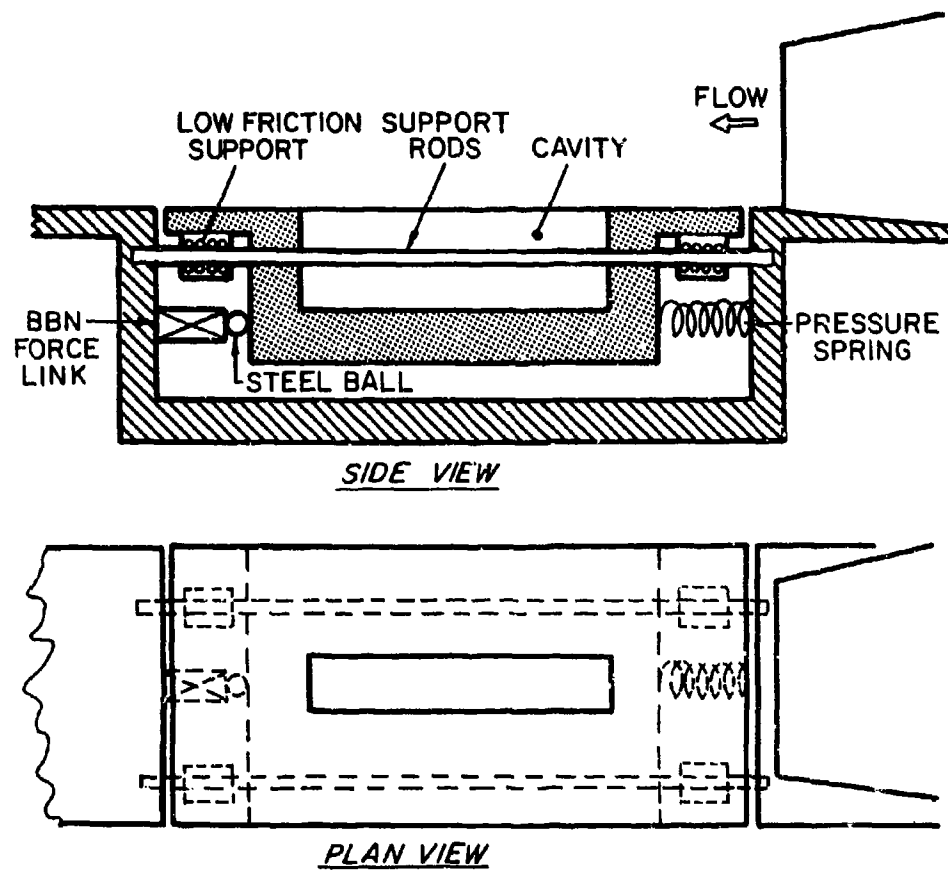


FIG. 25. EXPERIMENTAL SETUP FOR DRAG MEASUREMENTS.

Three-dimensional flow visualization was obtained by feeding smoke into the cavity near the floor and the leading-edge bulk-head. Short-duration flash photographs allowed visualization of the oscillating shear layer in a qualitative manner.

5.2.2 Exploratory Studies: Water Table Facility

Since the small-scale flow facility permitted only subsonic flow experiments, some exploratory studies were conducted in a water table facility which allows supersonic flow simulation.

A simple water table setup permits two-dimensional simulation of the pressure oscillation phenomenon. Since pressure oscillations in shallow and long cavities are basically two-dimensional in character, a high degree of similarity, especially on the unsteady, or periodic, part of the phenomenon can be achieved.

Figure 26 shows a schematic of the setup, which essentially involves a slightly inclined transparent glass plate supporting the water flow. Using the optical system of an overhead projector, a direct projection on a screen is possible; the surface waves and their motion are shown at a high contrast. Optimum simulation of the phenomenon is achieved by using a water depth of about $1/4$ in.; blocks defined a cavity of 2-in. depth (in the plane of the water), and variable lengths (2 in. to 8 in.). Direct observation of the unsteady phenomena is possible; however, a motion film camera with a moderately high speed (e.g., 54 frames per sec) sufficiently slows the phenomenon so that the motion of the shear layer, the external leading-edge and trailing-edge shock wave formation, and the cavity internal pressure wave (Heller *et al.*, 1973) can be followed. The analysis developed in Sec. 4 of this report is essentially based on the water table visualization results.

5.3 Experimental Techniques: Large-Scale Studies

5.3.1 Wind Tunnel Facility

The NASA Lewis 8 by 6 ft Wind Tunnel is a continuous closed-circuit flow facility. A remotely variable nozzle contour allows operation in the Mach number range from about 0.8 to 2.1. Since the facility is an atmospheric tunnel, stagnation and/or dynamic pressure of the free stream is a function of the operational Mach number and cannot be changed independently of Mach number. A plot of stagnation pressure, dynamic pressure, and unit Reynolds number as function of tunnel Mach number appears in Fig. 27. The drop in static pressure for increasing Mach number defines a simulated altitude as shown in Fig. 28.

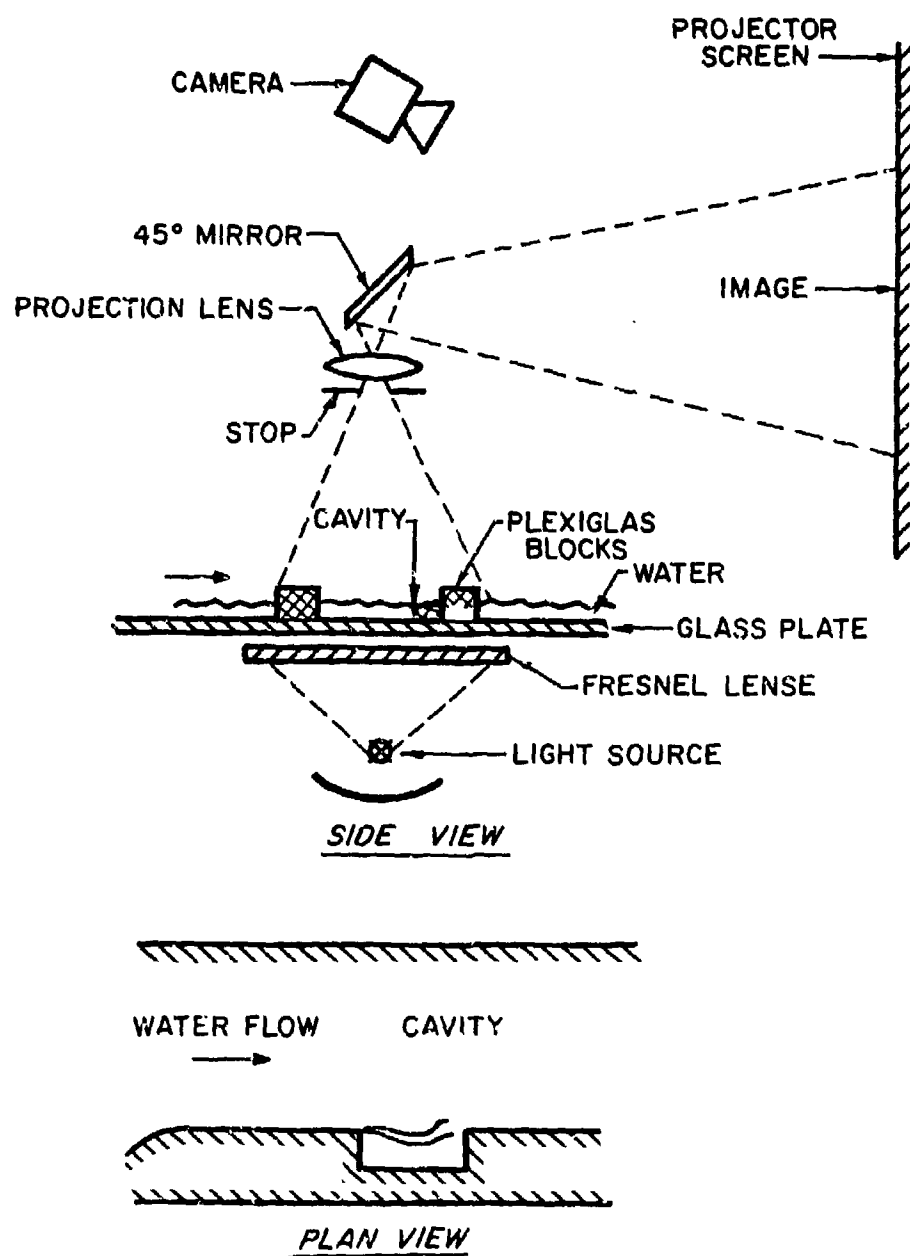


FIG. 26. SETUP FOR WATER TABLE FLOW VISUALIZATION EXPERIMENTS.

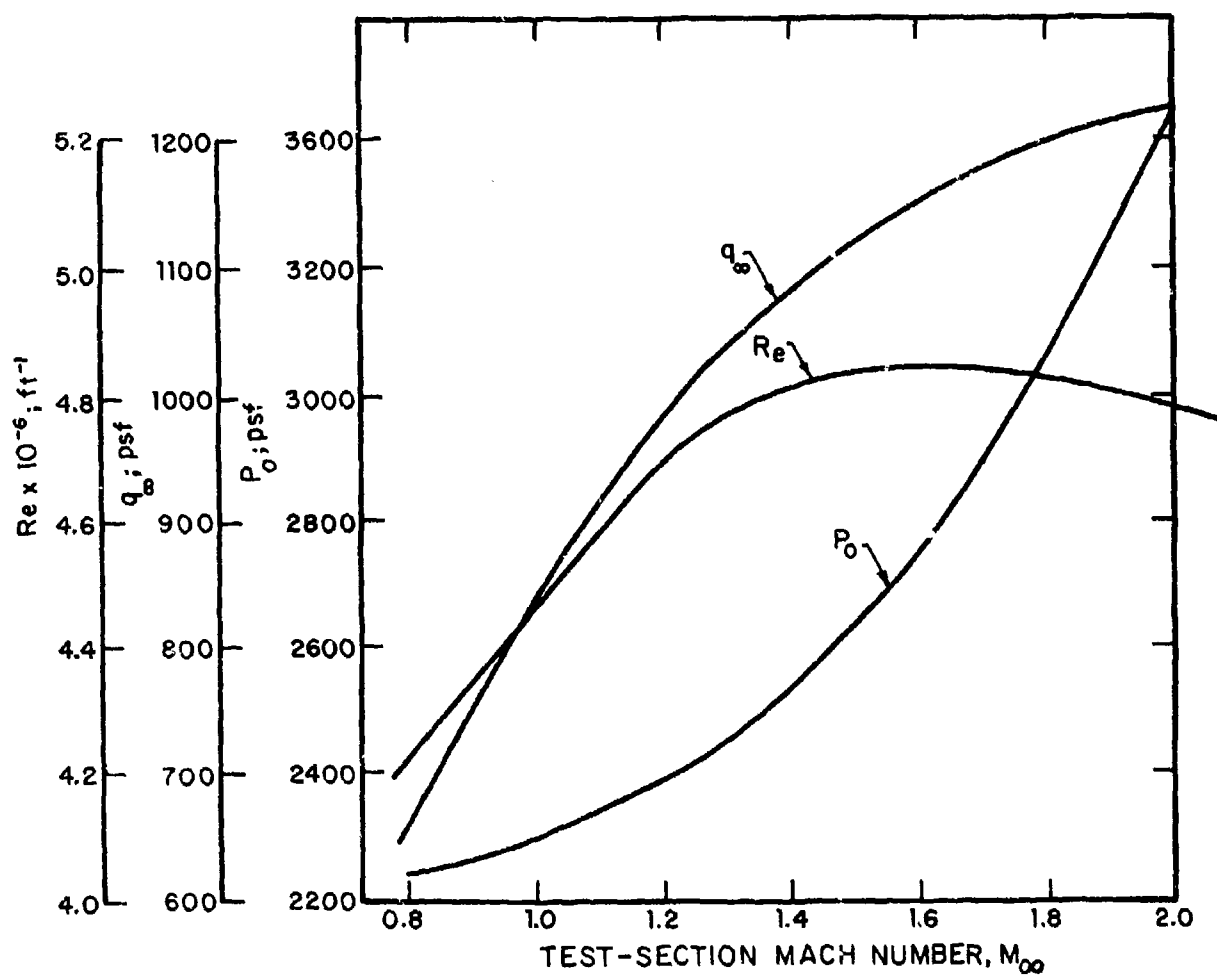


FIG. 27. NASA LEWIS 8 x 6 ft WIND TUNNEL. MACH NUMBER DEPENDENCE OF UNIT REYNOLDS NUMBER, RE PER FOOT, FREESTREAM DYNAMIC PRESSURE q_∞ , AND TOTAL PRESSURE P_0 .

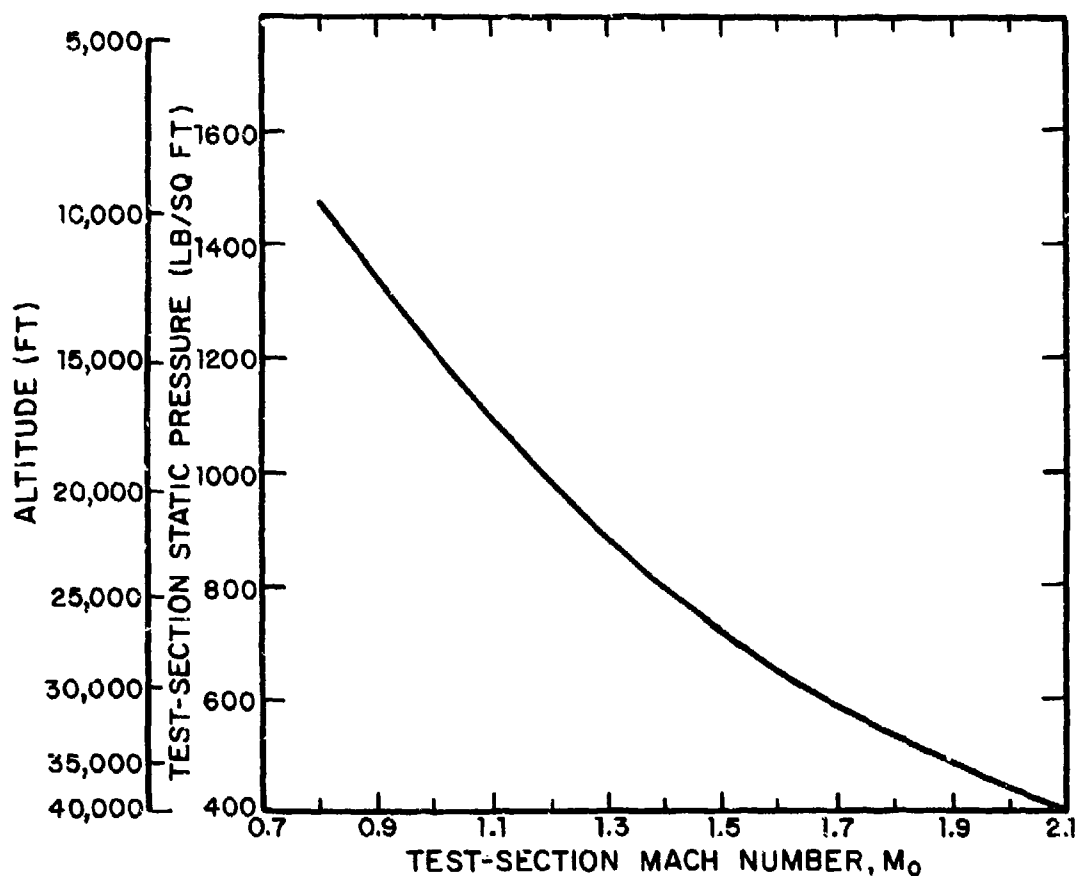


FIG. 28. NASA LEWIS 8 x 6 ft WIND TUNNEL. MACH NUMBER DEPENDENCE OF FREESTREAM STATIC PRESSURE AND CORRESPONDING ALTITUDE SIMULATION.

5.3.2 Cavity Model

The cavity model is shown in Figs. 29 to 31. Cavity width is 9 in., the length is 36 in., and the floor position can be remotely controlled between a depth of 16 in. and 6 in., resulting in length-to-depth ratios of $2.25 < L/D < 6.0$ (Fig. 29). Figure 30 shows the partially disassembled cavity with the driving mechanism for the floor movement. The cavity was made entirely of 1-in. aluminum, with Teflon strips to seal the floor against the cavity walls. Figure 30 also shows the traverse rod, which contains a BBN type 376 sensor, 5 in. below the cavity surface plane. The rod could also be driven remotely to survey the cavity internal pressure field. Figure 31 shows the assembled cavity with two extensions, one at each of the leading- and the trailing-edge bulkheads. These extensions measure 6 in. long by 6 in. deep and 8.5 in. wide, which increases the total cavity length to 48 in. However, they were not used to increase the cavity length but to allow changes in the cavity geometry at leading- and trailing-edge areas, such as slants or roundings, or to accept the drive mechanism for changing the angle of upstream canard spoilers (see Sec. 7.3). Figure 32 also shows two remotely drivable rods near the rear end of the cavity; these rods support leading- or trailing-edge cowls or guide vanes and vary the position of such suppression devices in the vertical direction.

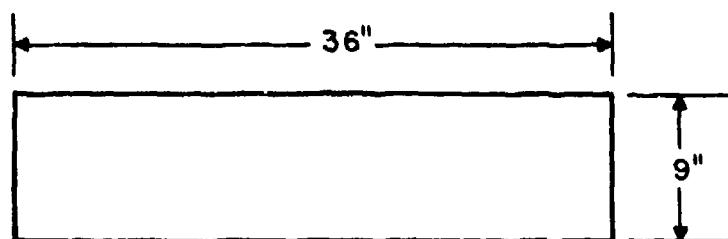
Hence, in any given test, there was the possibility to vary independently the position of the floor, the traverse rod, a leading- or trailing-edge oscillation suppression device, and the canard spoilers. Figure 33 shows the cavity model installed in the tunnel test section. Since the test section walls are perforated, the cavity mouth area is surrounded by a flat smooth plate, providing a surface for natural boundary layer growth. The distance from the plate leading edge to the cavity leading edge is 76 in. A closeup of the installed cavity appears in Fig. 34, which shows the traverse rod and two laterally displaced pitot-static tubes in the floor.

5.3.3 Instrumentation

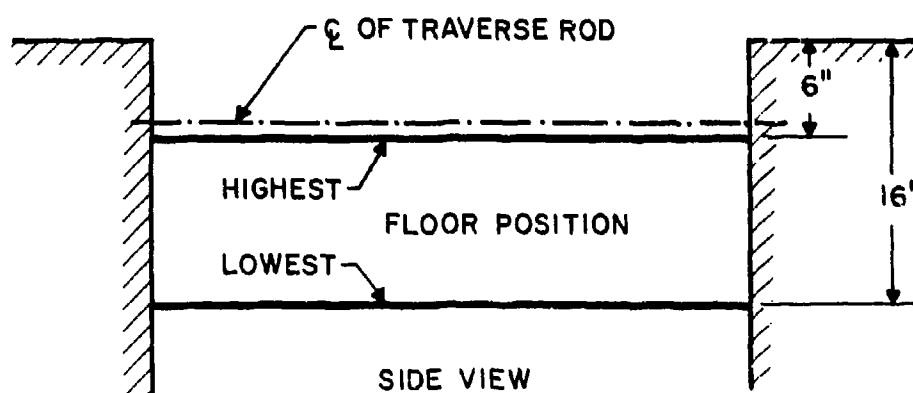
Both mean-flow and unsteady-flow quantities were measured.

Mean-Flow Quantities

Boundary Layer Profile. A boundary layer rake extending 1.5 in. above the surface at the cavity leading edge, but laterally displaced, provides information on steady-state boundary layer characteristics, specifically, velocity-profile, boundary



PLAN VIEW



SIDE VIEW

FIG. 29. LARGE-SCALE CAVITY MODEL DIMENSIONS.



FIG. 30. CAVITY MODEL WITH SIDEPLATE REMOVED.



FIG. 31. CAVITY MODEL WITH LEADING-EDGE AND TRAILING-EDGE EXTENSIONS.

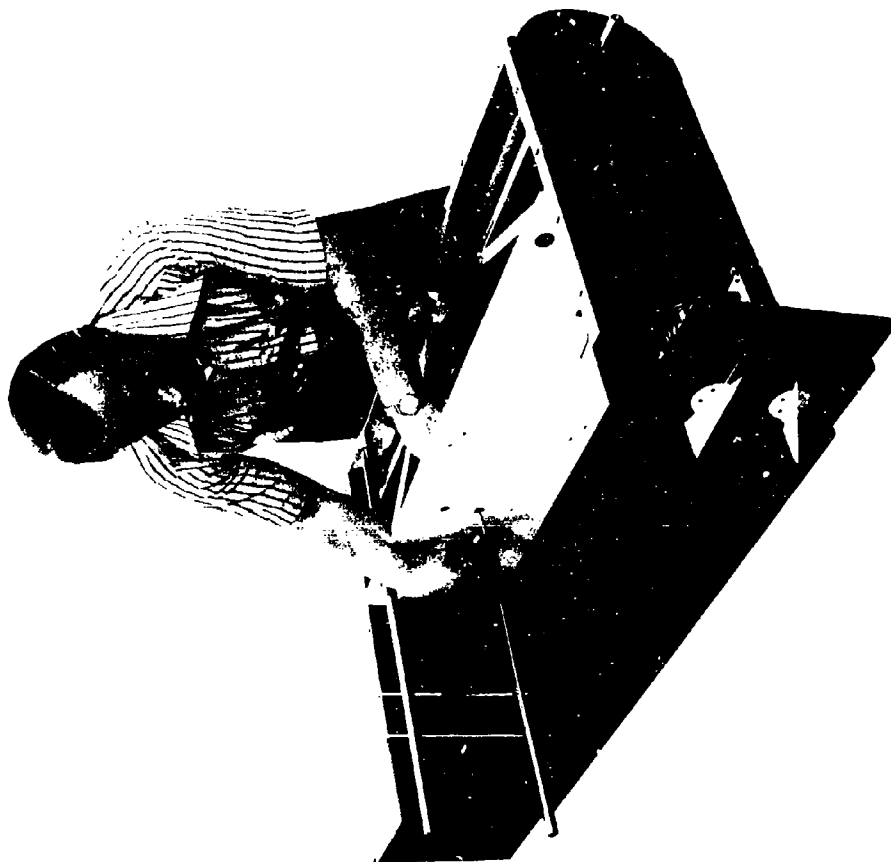


FIG. 32. CAVITY MODEL WITH REMOTE-CONTROL TRAILING-EDGE RODS
AND UPSTREAM DELTA-WING SPOILERS.

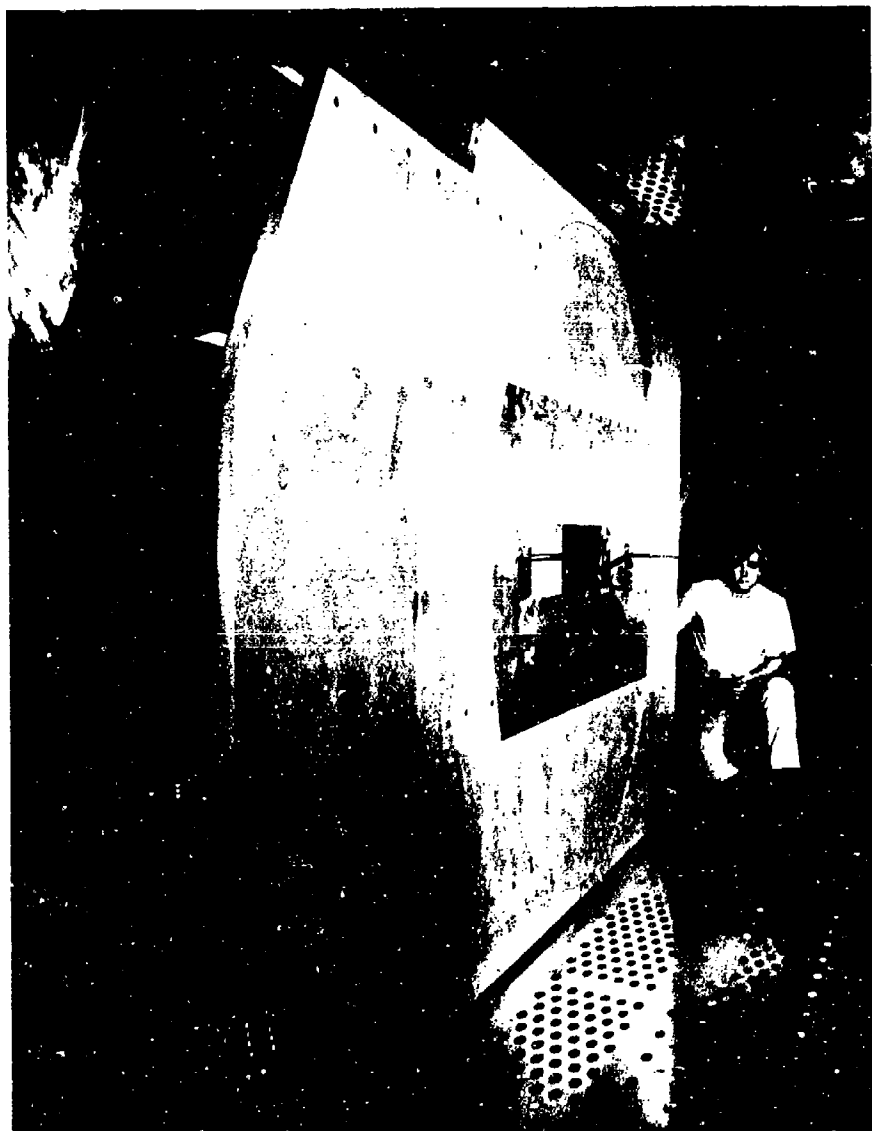


FIG. 33. CAVITY MODEL IN TEST SECTION OF NASA LEWIS 8 x 6 ft WIND TUNNEL.



FIG. 34. CLOSEUP OF INSTALLED CAVITY MODEL.

layer thickness, and displacement thickness. Similar information is obtained from a rake downstream of the cavity located on the cavity centerline. This rake extends 13 in. above the surface plane. Figure 35 provides details on rake location.

Recirculation Velocity. Qualitative information on recirculation velocities is obtained through two pitot-static tubes attached to the cavity floor facing in the downstream direction.

Static Pressures. Several static pressure taps are provided along the cavity floor and the forward and aft bulkhead (see Fig. 35).

Cavity Internal Temperatures. Two thermocouples at the locations indicated in Fig. 35 provide information on cavity internal temperature and, hence, on cavity internal speed of sound.

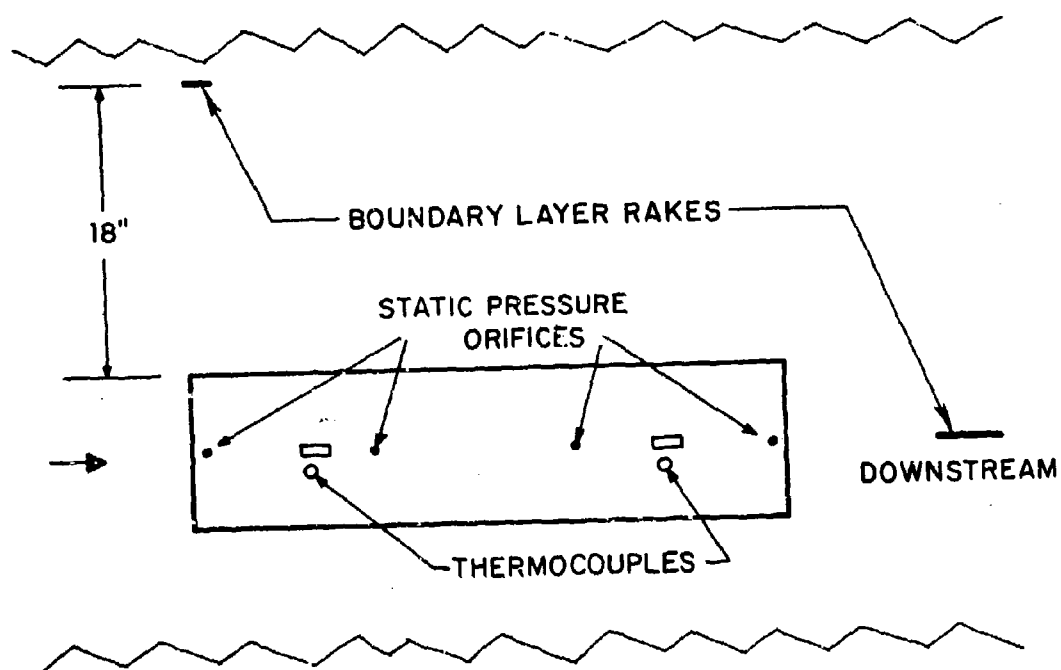
Unsteady Quantities

Fluctuating Pressures. Fluctuating-pressure levels (sound pressure levels) are measured through 9 BBN type 376 1/4-in. diameter piezoelectric pressure sensors. Sensor locations are shown to scale in Fig. 36. There is one sensor each in the surface plane upstream and downstream of the cavity leading and trailing edge on the centerline (Sensors 1 and 8); one each in the forward and aft bulkhead (Sensors 2 and 7); four in the floor, two of these in a corner position (Sensors 3 and 6); and two near the center of the floor but near opposite side walls (Sensors 4 and 5). One sensor is imbedded in the traverse rod (Sensor 9).

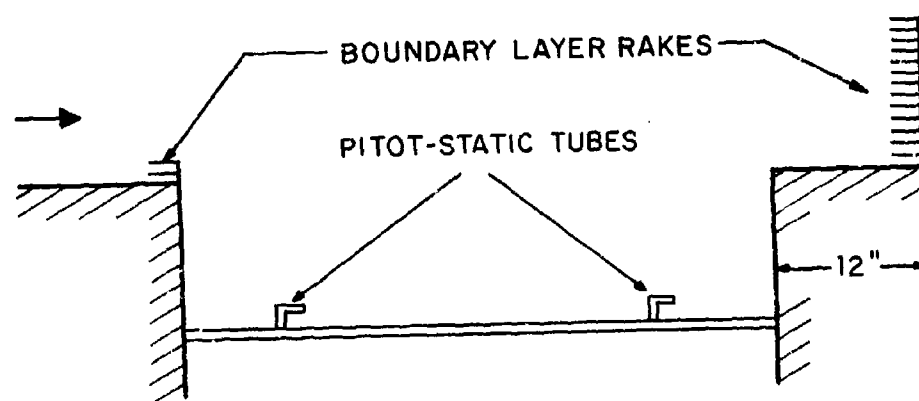
Vibration. One accelerometer is located at a middle location on the floor, outside of the cavity, to monitor vibration for possible interference with fluctuating-pressure measurements.

5.3.4 Data Acquisition and Reduction

Figure 37 shows the data acquisition system, consisting of 9 BBN type 376 pressure transducers, 1 BBN type 501 accelerometer, 10 Preston 8300 XWB Amplifiers with stepwise adjustable 1 to 1000 gain, 10 voltage dividers, and 1 Sangamo 4700 14-channel tape recorder.



PLAN VIEW



SIDE VIEW

FIG. 35. INSTRUMENTATION FOR STEADY-FLOW QUANTITY MEASUREMENTS.

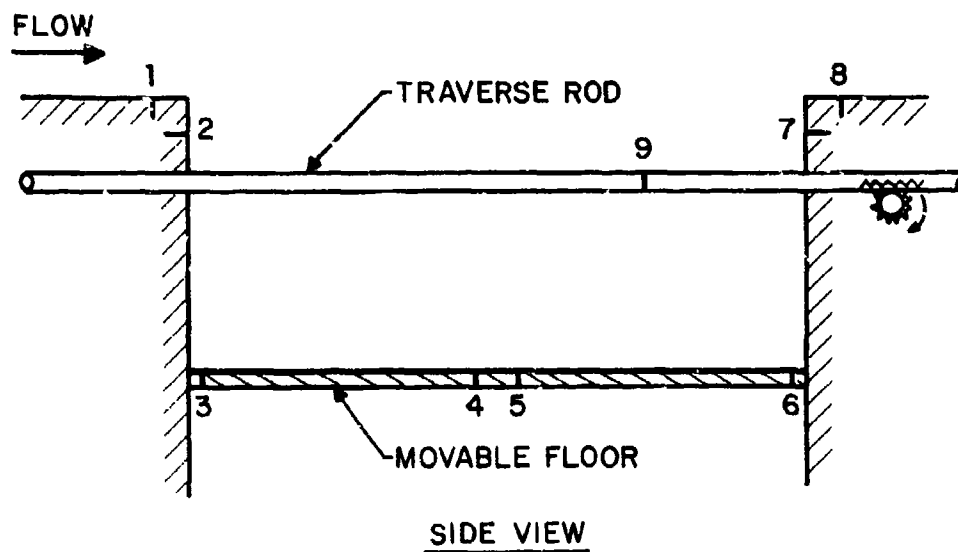
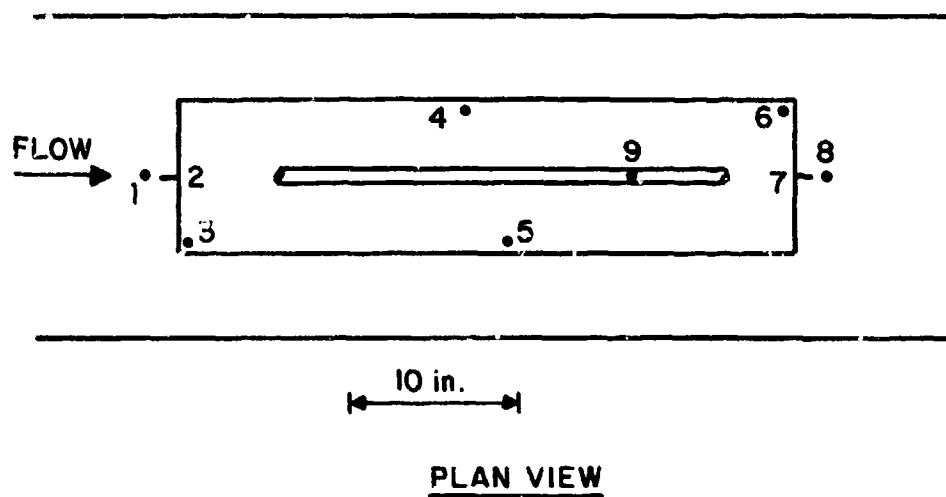


FIG. 36. FLUCTUATING-PRESSURE SENSOR LOCATIONS.

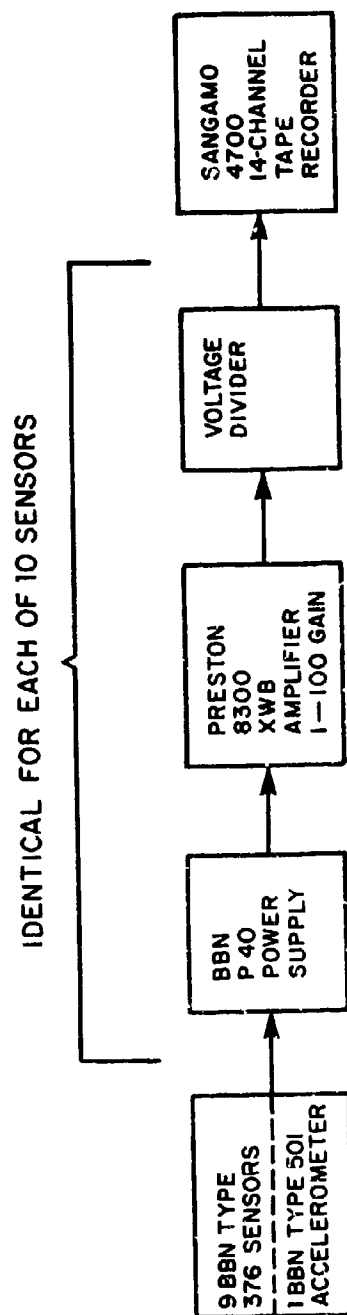


FIG. 37. DATA ACQUISITION SCHEMATIC.

The voltage dividers compensate for the different sensor sensitivities, so that the input voltage to the tape recorder for a given pressure level was the same for each pressure sensor (provided the sensor signal is put through the same amplifier gain). All recordings are made at 30-ips tape speed; the system frequency response ranges from 20 Hz to beyond 40,000 Hz. The data analysis system, which is shown in Fig. 38, consists of one Sangamo 4700 14-channel tape recorder, one switch for channel selection, and one Preston Amplifier Type 12048. The signal can then be analyzed either in: 1/3-octave bands using a General Radio type 1925/1926 Real Time Analyzer and type 1522 Graphic Level Recorder; or in 10-Hz constant bandwidth using a General Radio type 1900-A Wave Analyzer with a type 1521-A Graphic Level Recorder. A Hewlett Packard type 521C frequency counter is used to determine resonant frequencies accurately.

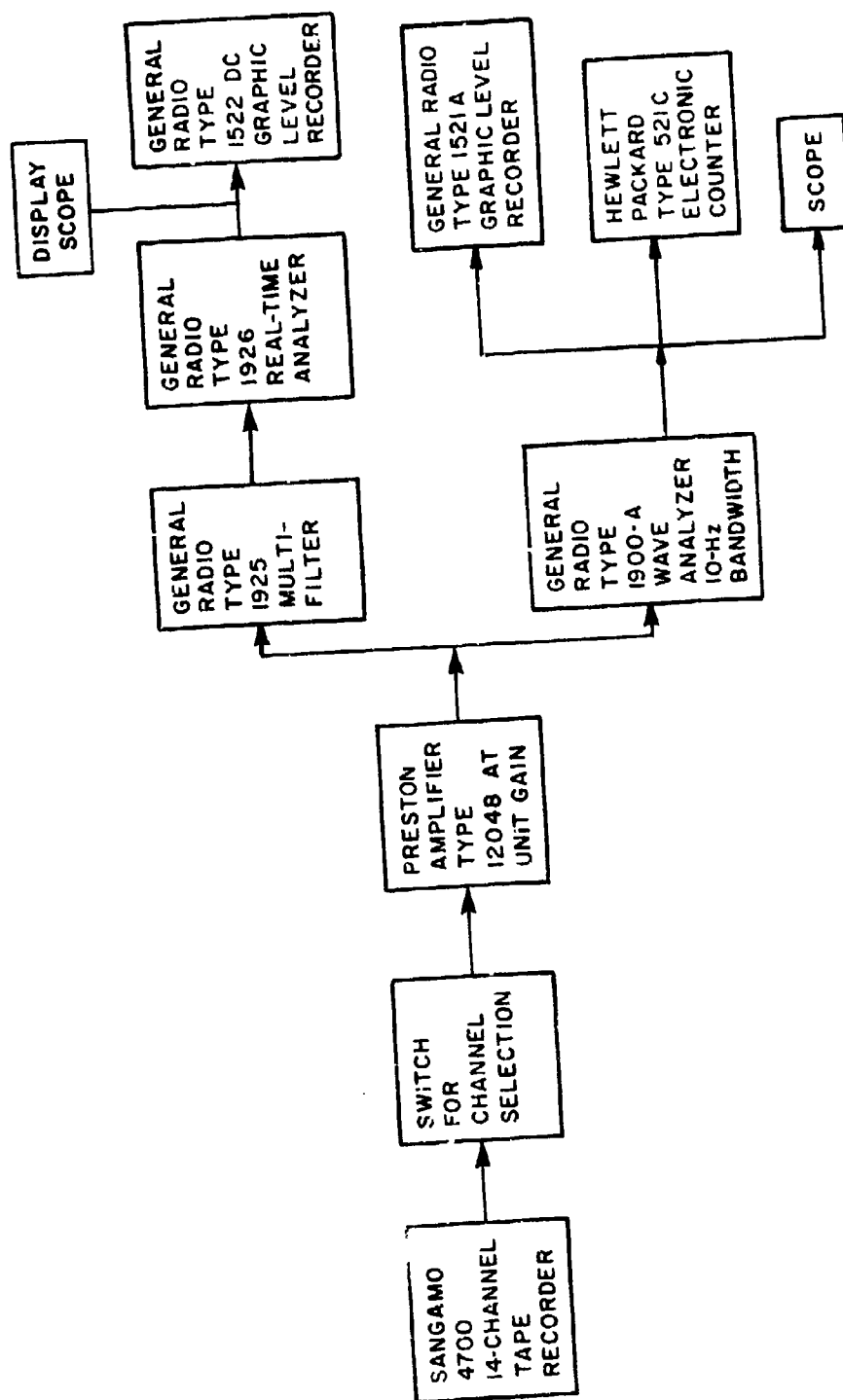


FIG. 38. DATA REDUCTION SCHEMATIC.

SECTION 6

TEST RESULTS: BASIC CAVITY

6.1 Flow Visualization

In this section, both subsonic and supersonic flow visualization results will be discussed. Cavity pressure oscillation mechanisms for external subsonic and supersonic flow are quite similar; hence, the subsonic visualization results can be interpreted on the basis of the supersonic visualization results, for which much more detailed information was obtained.

Figure 39 represents a complete sequence of the water table simulation* for a typical oscillation cycle for external supersonic flow of about $M = 1.5$. The motion pictures were edited to show the mass injection process, which starts with the shedding of a shear layer from the leading edge (frames 1 to 7). The separated shear layer approaches the trailing edge (frames 8 to 12), and flows over the trailing edge (frames 13 to 17). Thereafter, the shear layer "whips" down (frames 18 to 24), thus exposing the trailing edge to the free stream, which causes a "bow wave," i.e., a shock front, to occur at the trailing edge in (frames 24 to 30). Simultaneously, the downward motion of the shear layer causes a pressure wave (frame 24) to appear in the joint region of the trailing-edge bulkhead and the floor; this pressure wave subsequently moves towards the leading edge (frames 24 to 39), straightening out along its path. The pressure wave also causes the shear layer above to bend outward into the free stream. This outward bend causes a shock front to trail along with the pressure wave in the upstream direction (frames 26 to 40). Since this shock front travels against the free stream with the speed of the cavity internal pressure wave (roughly with Mach 1, the speed of sound in the cavity), the effective speed against the free stream is higher than the free-stream speed. Consequently, the trailing shock front is inclined more than would correspond to the freestream Mach angle. Upon arrival at the leading edge (frame 39), the cavity internal pressure wave is reflected and travels downstream in the cavity (frames 40 to 50). Once the external shock wave has arrived at the leading edge, it separates from its originator, i.e., the outward bump in the shear layer, and trails out in the freestream medium. Since the downstream-traveling cavity internal pressure

*In this sequence, flow is from right to left.

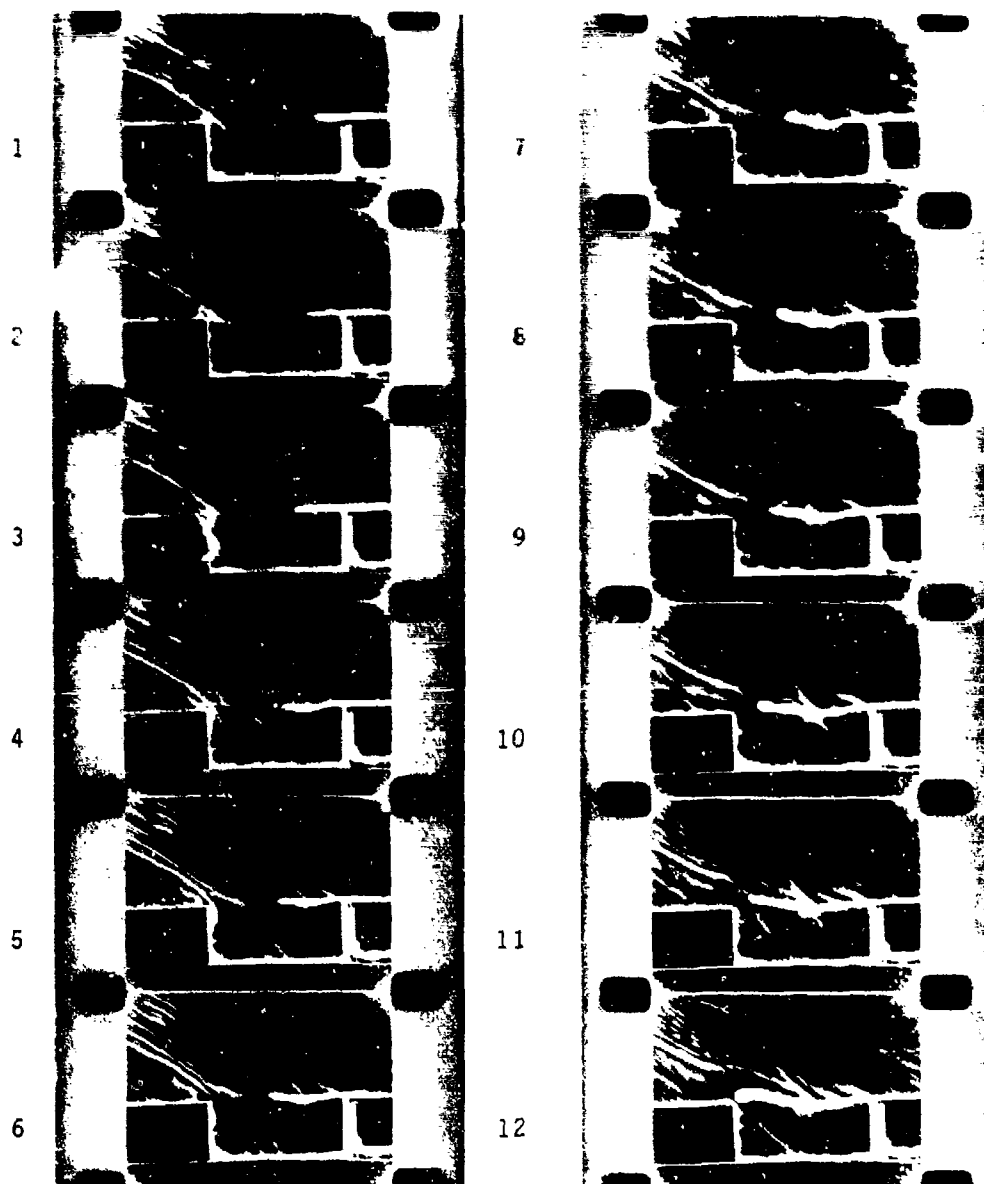


FIG. 39. WATER TABLE VISUALIZATION OF OSCILLATION CYCLE UNDER SIMULATED EXTERNAL SUPERSONIC FLOW $M_{\infty} = 1.5$. FLOW FROM RIGHT TO LEFT.

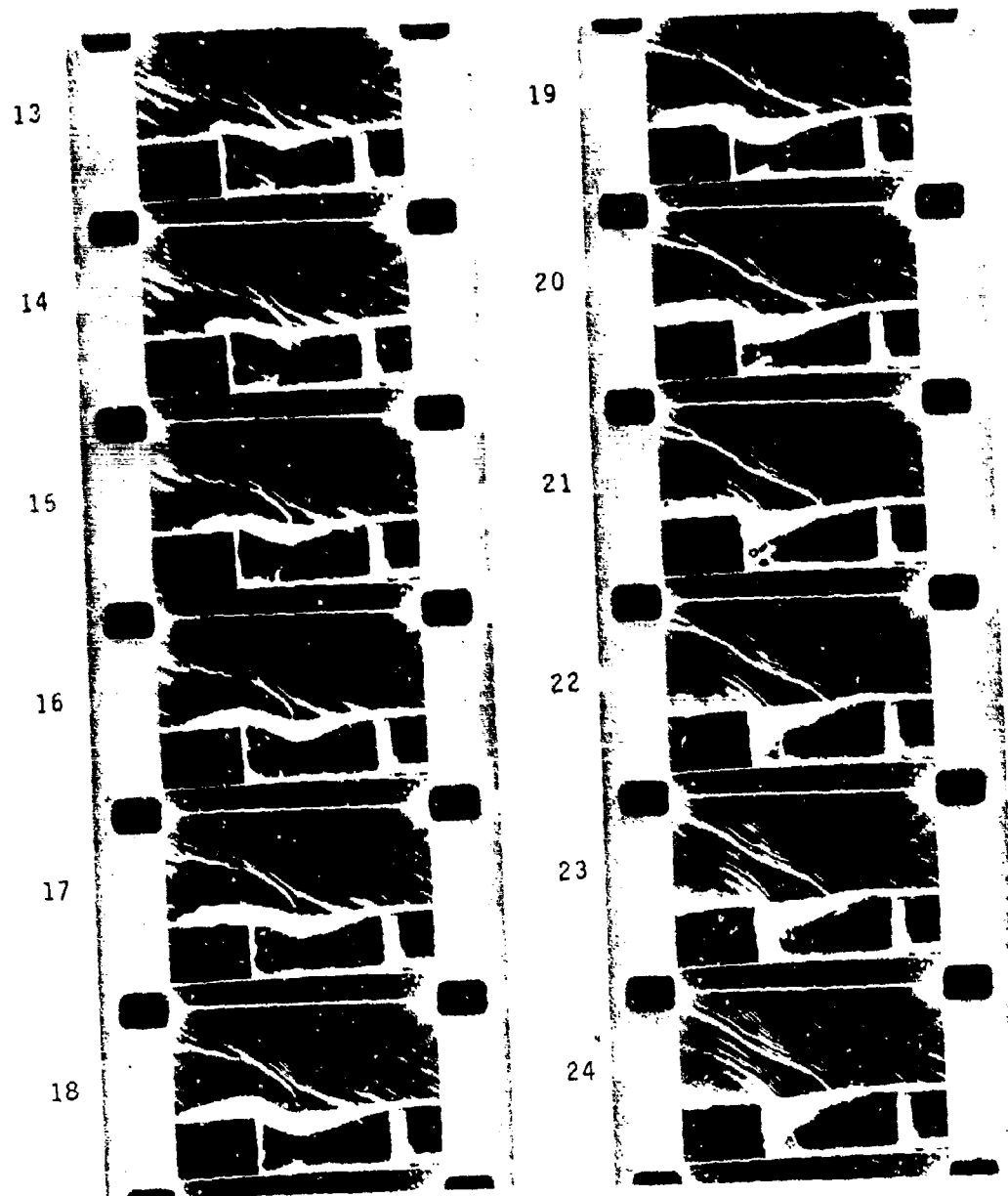


FIG. 39. (CONTINUED)

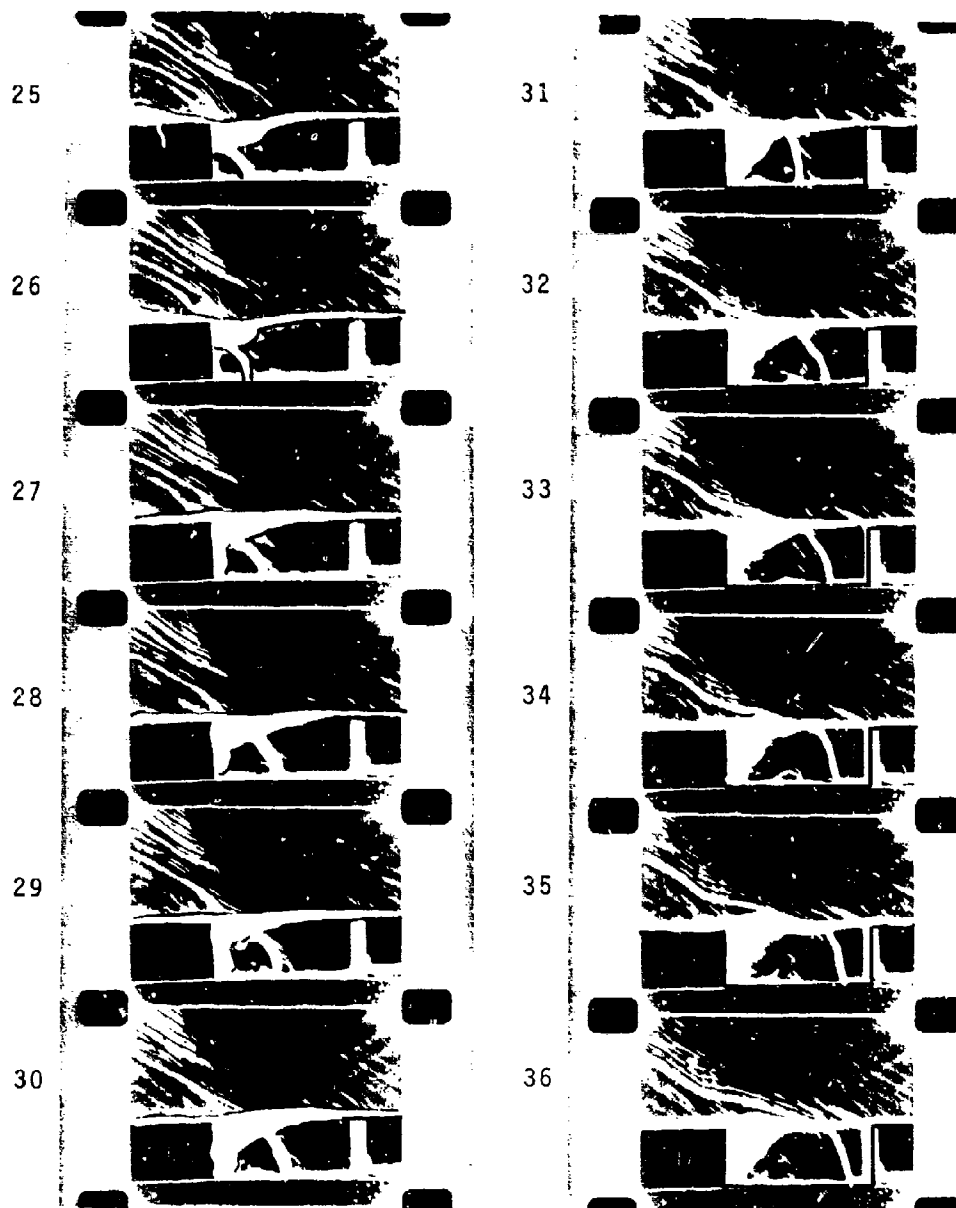


FIG. 39. (CONTINUED)

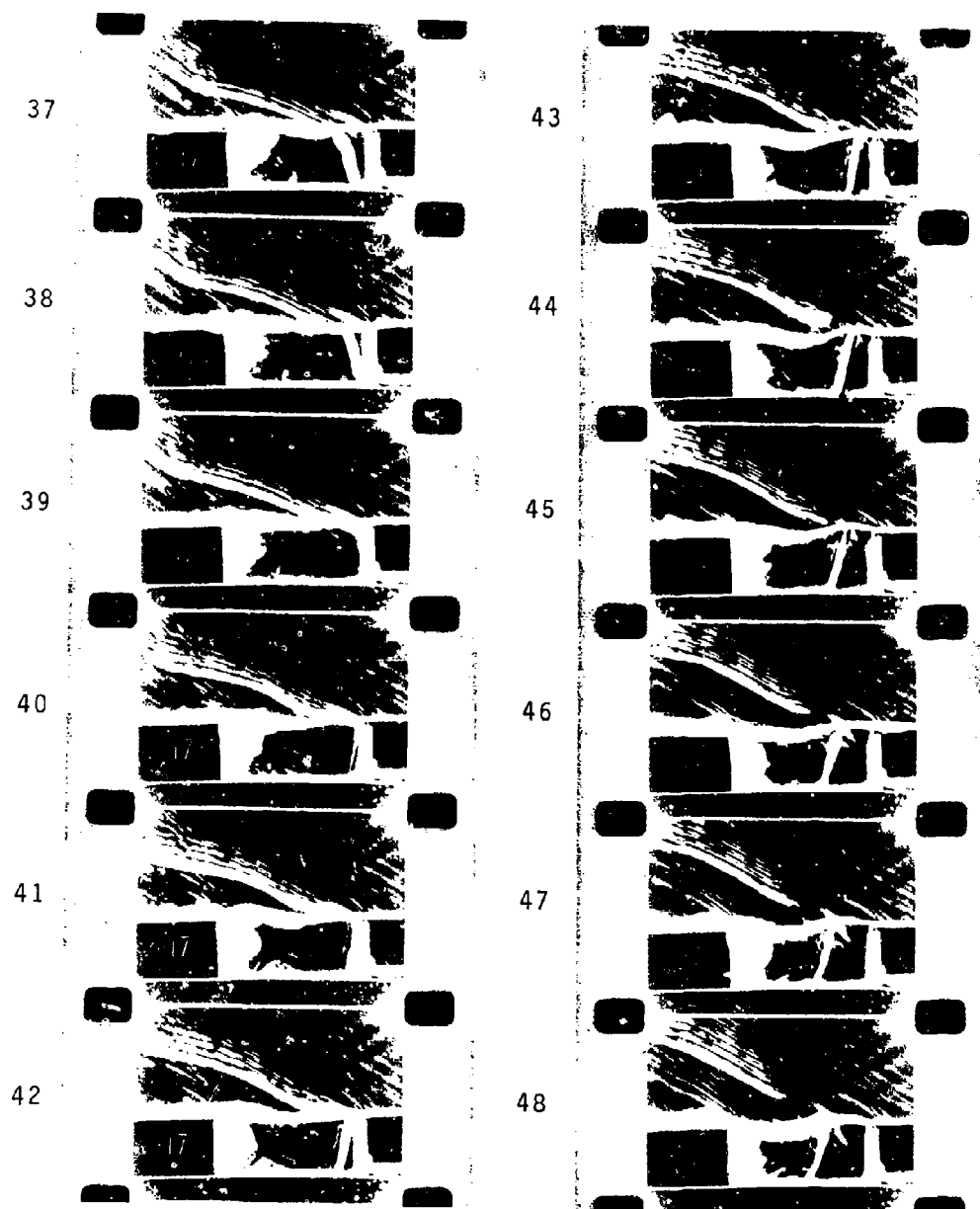


FIG. 39. (CONTINUED)

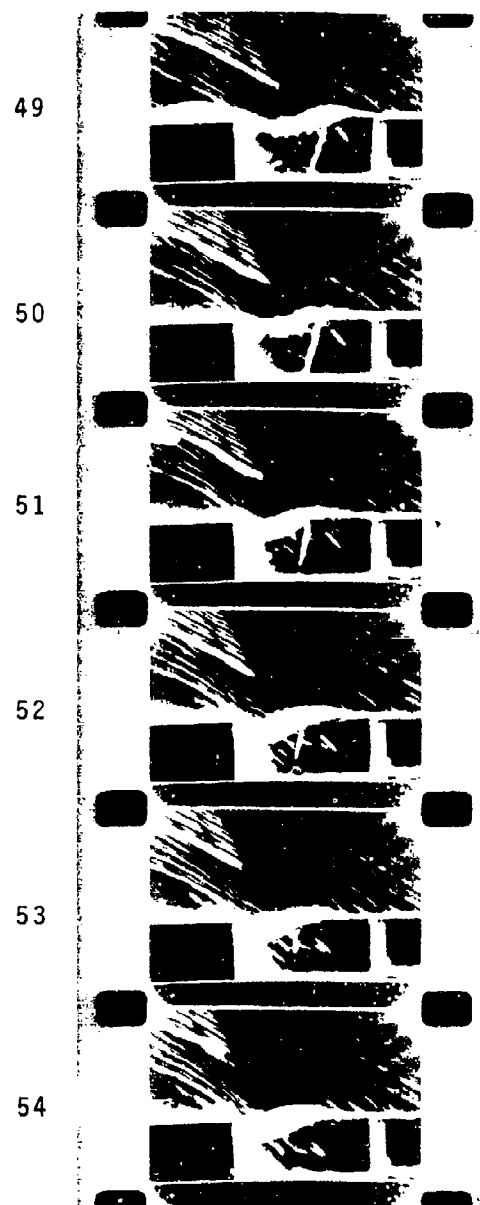


FIG. 39. (CONTINUED)

wave propagates with the cavity internal speed of sound (roughly Mach 1), the pressure wave speed is now subtracted from the external flow speed and the "bump" in the shear layer travels with an effectively subsonic speed, which causes no external shockwave.* The pressure wave travels further downstream and dissipates its energy along its cavity internal path. Meanwhile, probably around frame 50 ± 5 , a new downlash of the shear layer at the trailing edge occurs, which causes a new pressure wave to originate, whereupon the process repeats itself.

The above sequence shows clearly the generating process for a fundamental mode. However, higher order modes can be simulated as shown in Fig. 40 (which, again, is an excerpt from the motion picture). Here, the cavity trailing-edge bulkhead was moved forward and backward in a piston-like manner forcing the cavity at a higher frequency than the naturally† occurring fundamental frequency.

The generation mechanisms for supersonic and subsonic external flow are believed to be quite similar. This belief is substantiated by the experimental data that relate resonant Strouhal numbers to freestream Mach numbers on one hand, and resonant mode levels and freestream Mach numbers on the other hand (see Secs. 6.6 and 6.8). In both sets of data, there is a smooth transition from the subsonic over the transonic to the supersonic flow regime. The main difference lies in the appearance of the external shear layer. In the supersonic case, the external shear layer exhibits a wavy, though continuous, shape, resulting in an up-and-down motion at the trailing edge; as described above, this results from the forcing of the internal pressure wave motion. In the subsonic case, the external shear layer tends to roll up to form individual vortices. In the three-dimensional visualization photograph, shown in Fig. 41, two individual vortices convect and grow in a downstream direction. This instantaneous picture was taken in the small-scale experimental flow facility (see Sec. 5.2.1) for a Mach number of about 0.25. These pictures correspond qualitatively with those obtained by Rossiter (1966), which are reproduced here as Fig. 42.

*The external flow speed in this simulation was about Mach 1.5; hence, the effective speed of the shear layer bump is $1.5 - 1 = 0.5$, i.e., subsonic.

†In the water table visualization setup, only the fundamental mode can sustain itself.

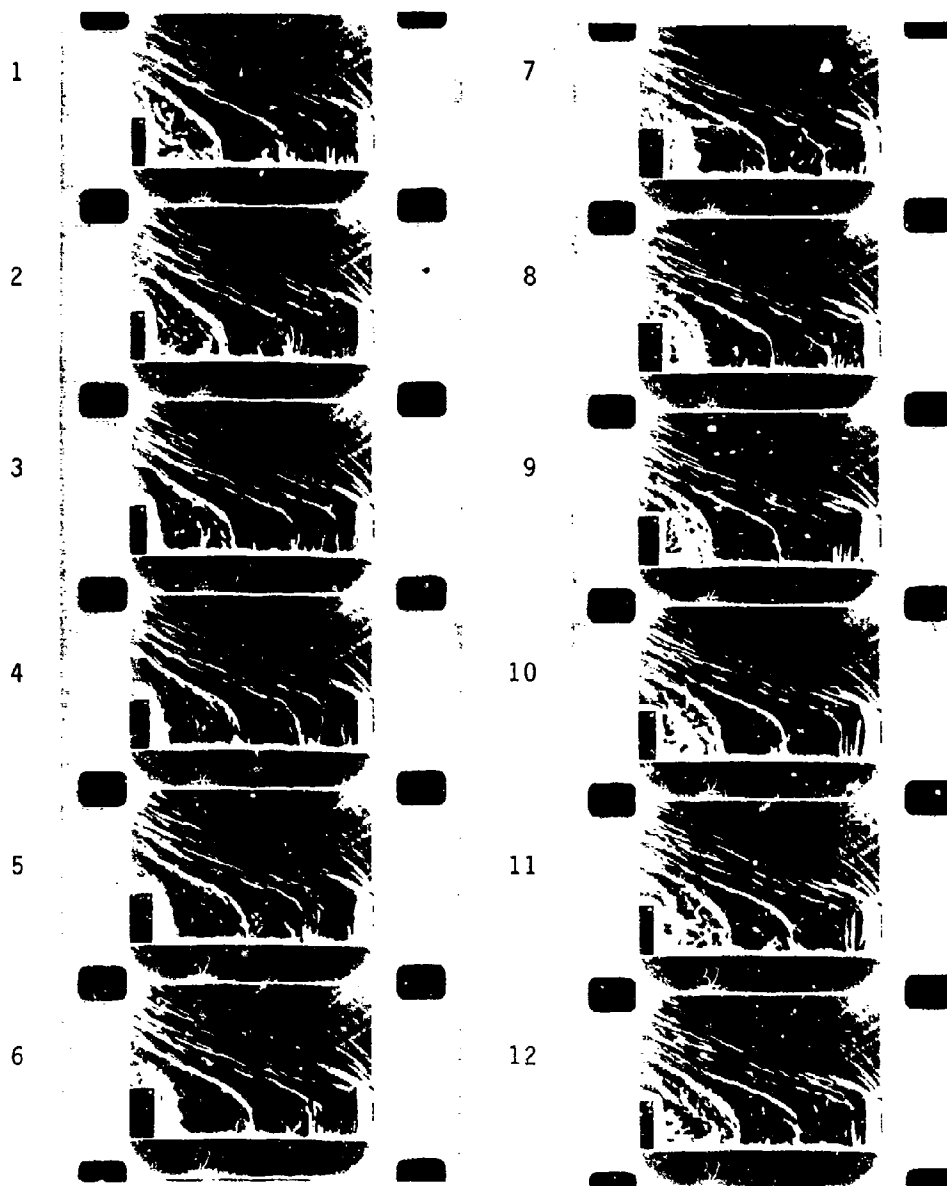


FIG. 40. WATER TABLE VISUALIZATION OF HIGHER ORDER MODES IN CAVITY.



FIG. 41. SMOKE VISUALIZATION OF RESONATING CAVITY UNDER
SUBSONIC EXTERNAL FLOW.

Wind
Direction
→

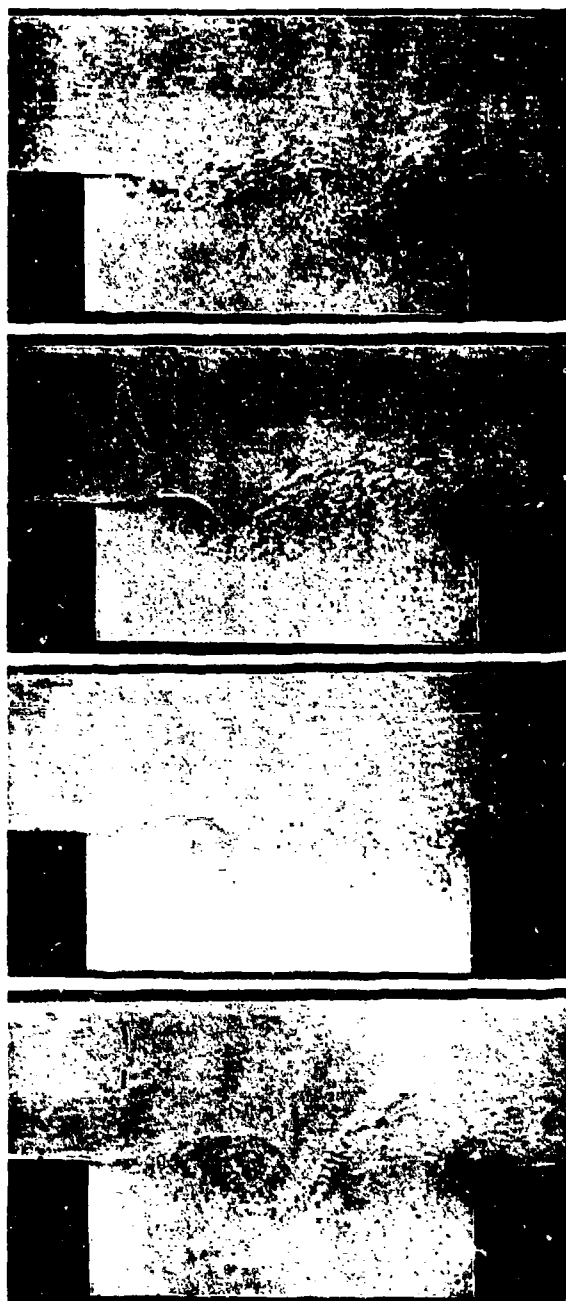


FIG. 42. SHADOWGRAPH VISUALIZATION OF RESONATING CAVITY
AT SUBSONIC FLOW SPEEDS. (After Rossiter, 1966.)

As has been emphasized in Sec. 3, these vortices are not the cause of the oscillation as assumed by Rossiter, but the external manifestation of the oscillation process, which is a result of cavity internal pressure wave motions.

6.2 Boundary Layer Characteristics

As shown in Fig. 27, the unit Reynolds number in the NASA Lewis Research Center 8×6 ft tunnel at Mach numbers above 0.8 is between 4.2 and 4.8×10^6 , which results in Reynolds numbers at the cavity mouth of 26 to 30 million. These Reynolds numbers are high enough to result in fully developed turbulent flow at the cavity mouth.

Boundary layer profiles were measured at the sideline extension of the cavity mouth, and the results are shown in Fig. 43. The profiles in the Mach number range of $0.8 < M_\infty < 1.5$ coincide, showing the shape of a fully developed turbulent boundary layer. The exponent N in the profile equation, $U/U_\infty = (y/\delta)^{1/N}$, corresponds to 7.3. The Mach 2 velocity profile deviates in shape from the lower Mach number profiles, with an exponent N of about 10.5.

The boundary layer displacement thickness is about 0.165 ± 0.006 in. for $0.8 < M_\infty < 1.5$; thus, it is a factor of 35 to 95 times smaller than the cavity depth. Displacement thickness at $M_\infty = 2$ is about 0.14 in. (Fig. 44). Correspondingly, the boundary layer thickness is about 1.0 in. ± 0.13 for $0.8 < M_\infty < 1.5$ and about 0.78 in. for $M_\infty = 2$. Hence, for the shallow cavity experiments ($L/D = 6$), the ratio of cavity depth to boundary layer thickness (D/δ) is 6 to 7; for the deep cavity experiments ($L/D = 2.25$), D/δ is 16 to 20. Thus, the boundary layer dimensions are many times smaller than the cavity depth.

6.3 Mean Pressure

Static pressures in the cavity were measured at six locations, four on the floor, and one each on the forward and the aft bulkhead. Figure 45 presents the static pressure, P_∞ , on the floor at 0.1, 0.33, 0.66, and 0.9 of the cavity length, normalized with the freestream total pressure, P_0 . The information is given for freestream Mach numbers ranging from 0.78 to 2.0, and broken down for three L/D ratios. There is no obvious dependence on the L/D ratio, but the pressure ratio at each Mach number rises towards the trailing edge ($x/L = 1$). Furthermore, the lower the Mach number, the higher is the pressure ratio.

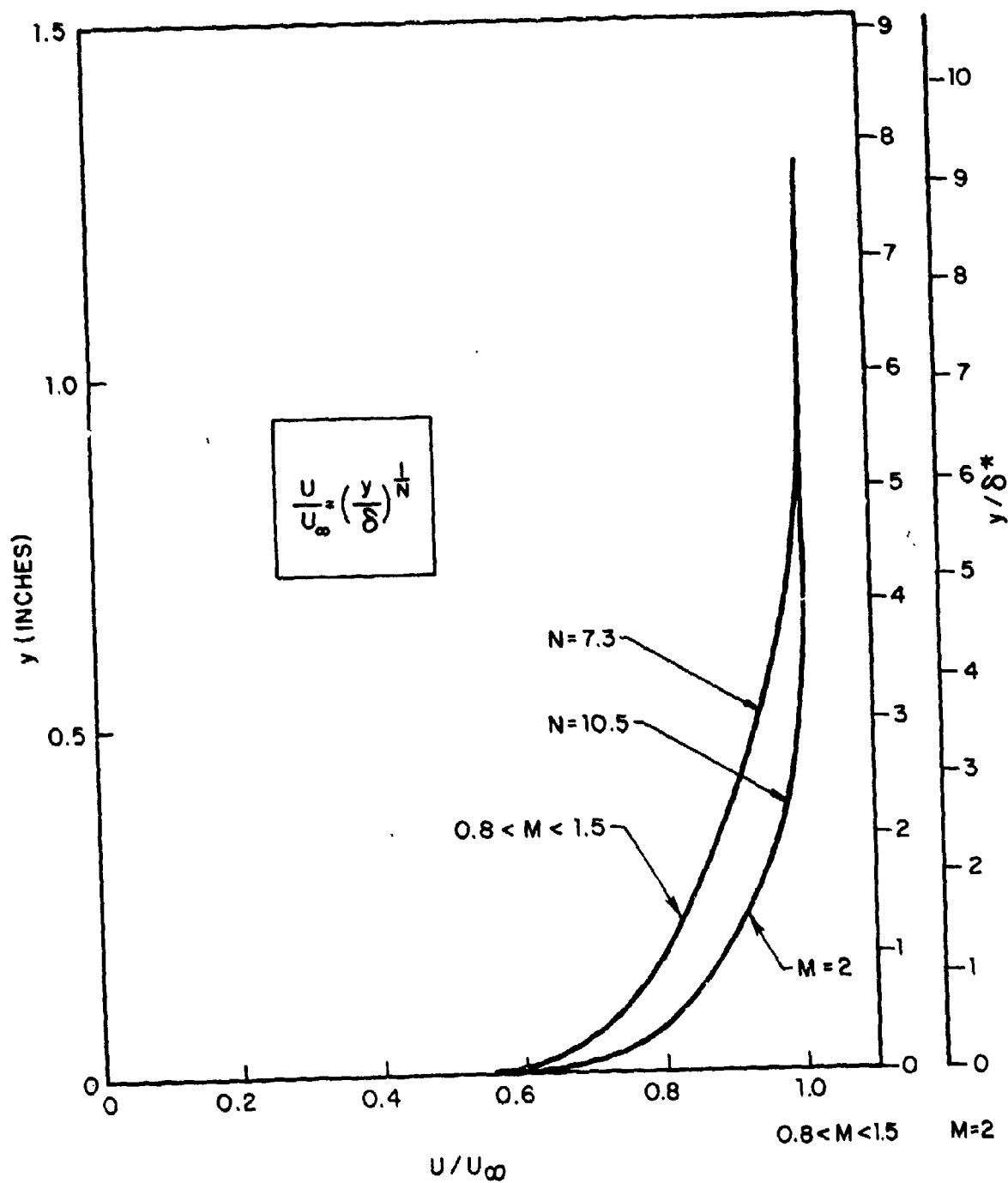


FIG. 43.* VELOCITY PROFILE AT CAVITY LEADING EDGE.

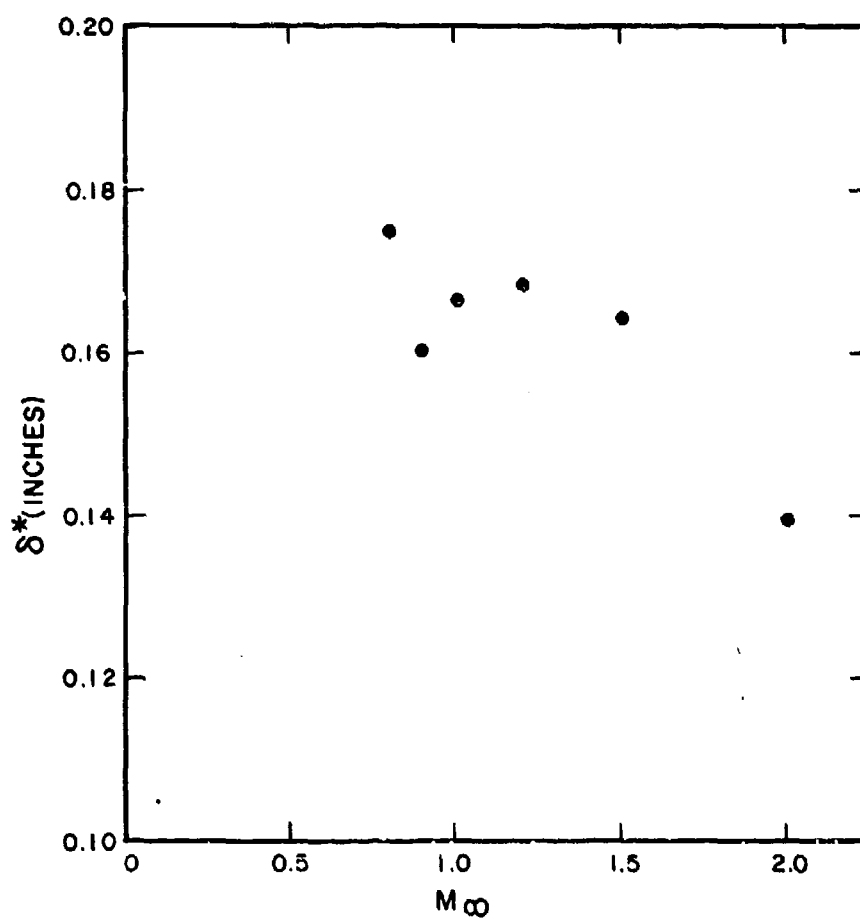


FIG. 44. MACH NUMBER DEPENDENCE OF BOUNDARY LAYER DISPLACEMENT THICKNESS AT CAVITY LEADING EDGE.

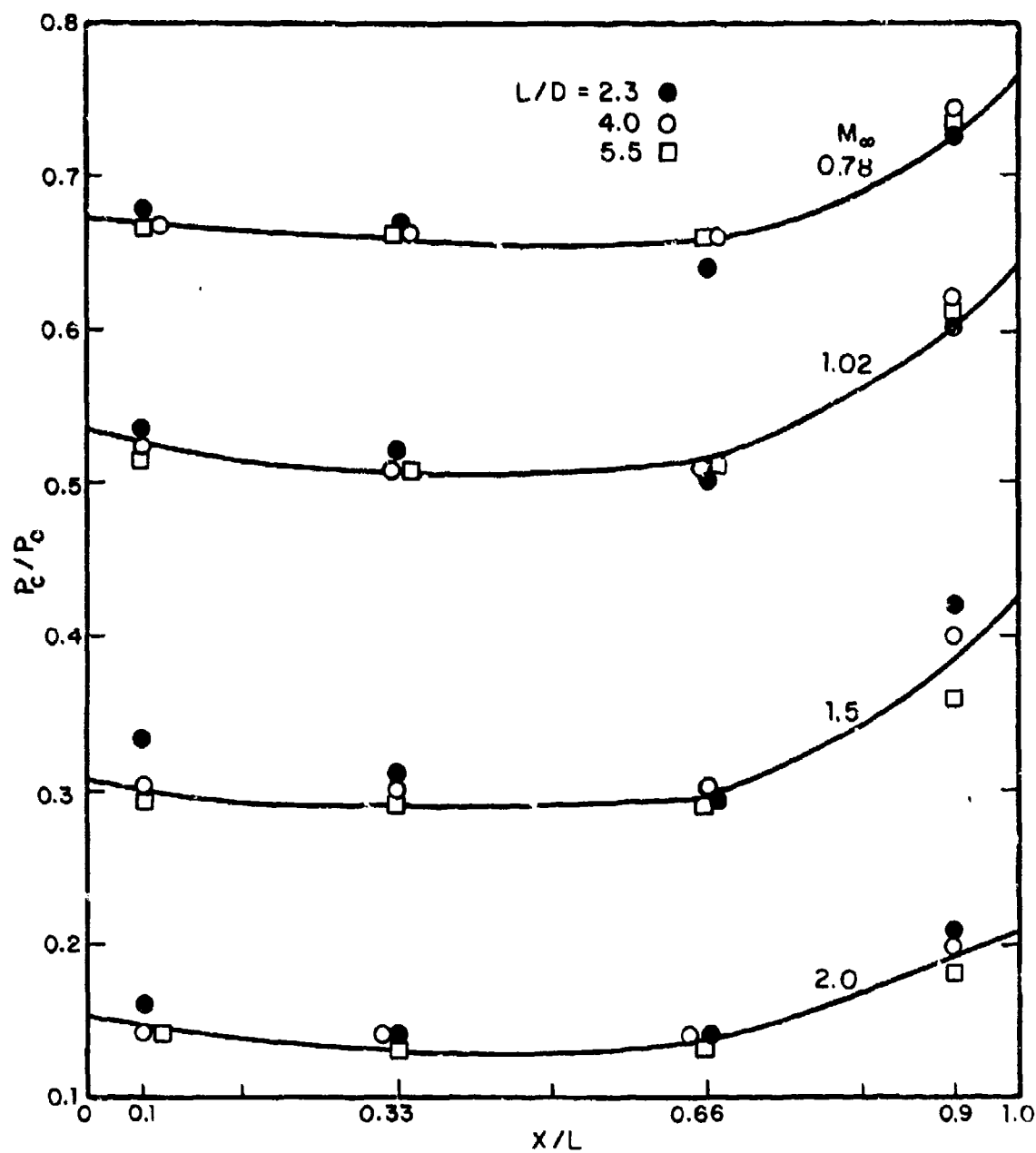


FIG. 45. NORMALIZED STATIC PRESSURE DISTRIBUTION ALONG CAVITY FLOOR.

Figure 46 presents the mean-cavity floor static pressure* reduced by the freestream static pressure, and referenced to the mean-cavity static pressure, as function of Mach number for three L/D ratios. The plot contains data from other investigators. At subsonic Mach numbers, there is no strong L/D dependence. At supersonic Mach numbers, the data fan out, so that higher normalized pressures are observed for lower L/D ratios, and vice versa.

6.4 Cavity Temperature

Temperatures were measured at two locations on the floor. Data are presented as a recovery factor $r \equiv (T_w - T_\infty)/(T_\infty - T_\infty)$ vs freestream Mach numbers in Fig. 47. The recovery factor seems to reach a relative minimum at sonic and slightly supersonic Mach numbers, increasing both toward lower and higher Mach numbers. A systematic dependence on length-to-depth ratio is evident, so that lower L/D ratios result in lower recovery factors. The data, which were obtained in the NASA Lewis Research Center 8 x 6 ft tunnel, however, are systematically lower than those obtained in a previous study (Heller, 1970) in the MIT Naval Supersonic Tunnel.

Heller *et al.* (1970) have argued that the speed of sound in the cavity approaches the stagnation speed of sound in the free stream. This was a key postulate in modifying Rossiter's (1966) equation that relates resonant frequencies in the cavity to freestream Mach numbers. The measured data in Fig. 47 support this earlier conclusion; recovery factors are closer to unity than to zero, as had been assumed by Rossiter.

6.5 Fluctuating-Pressure Data

6.5.1 Spectra

Forty runs were conducted; each run has a different Mach number and length-to-depth ratio of the cavity. Since the cavity contains nine (fluctuating) pressure sensors and one accelerometer, close to 400 individual data points were obtained.

Tests were conducted at the following Mach numbers: 0.8, 0.9, 0.95, 1.0, 1.05, 1.1, 1.2, 1.5, and 2.0. For most of these Mach numbers, data were recorded at three L/D ratios, i.e., 2.3,

*Averaged over the four floor positions.

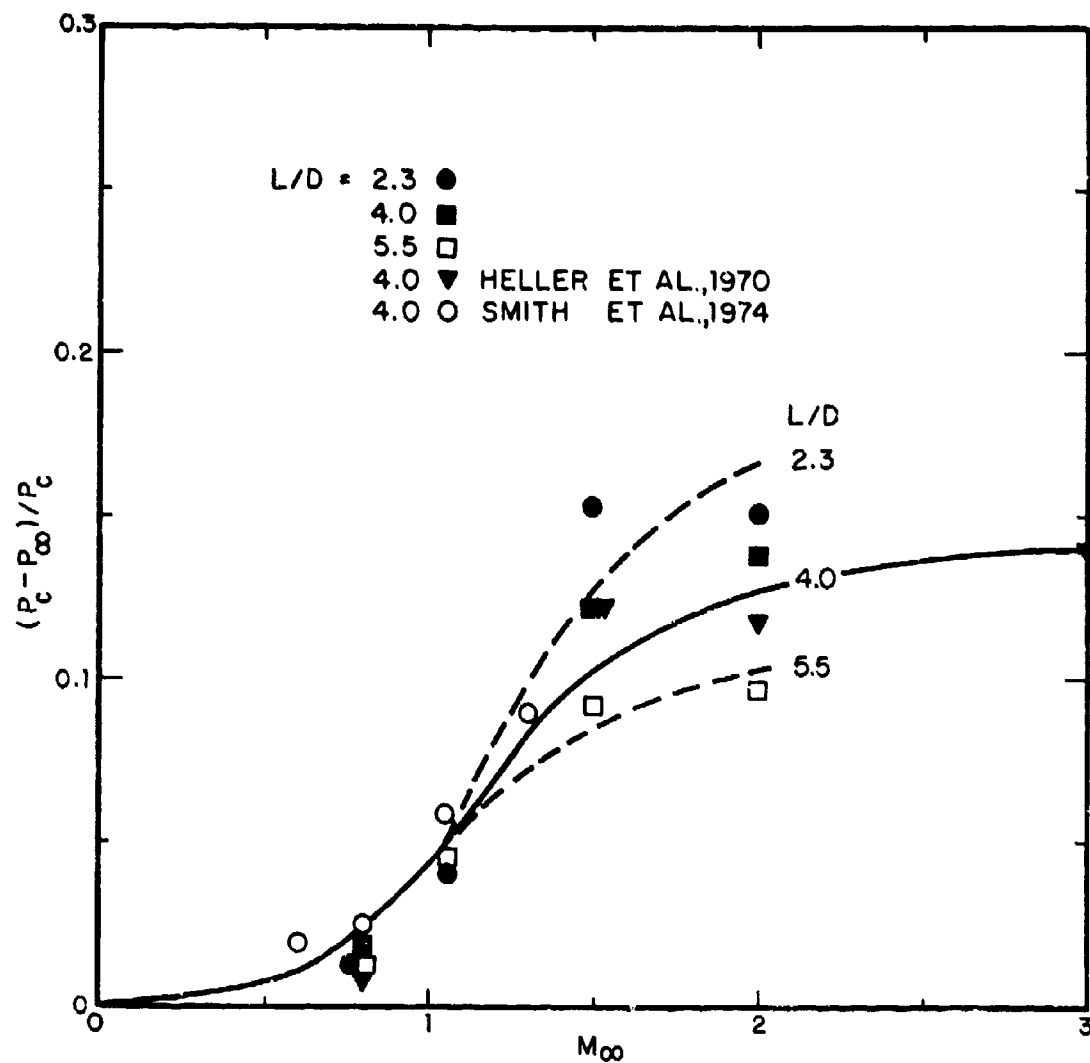


FIG. 46. MACH NUMBER DEPENDENCE OF AVERAGE NORMALIZED STATIC PRESSURE.

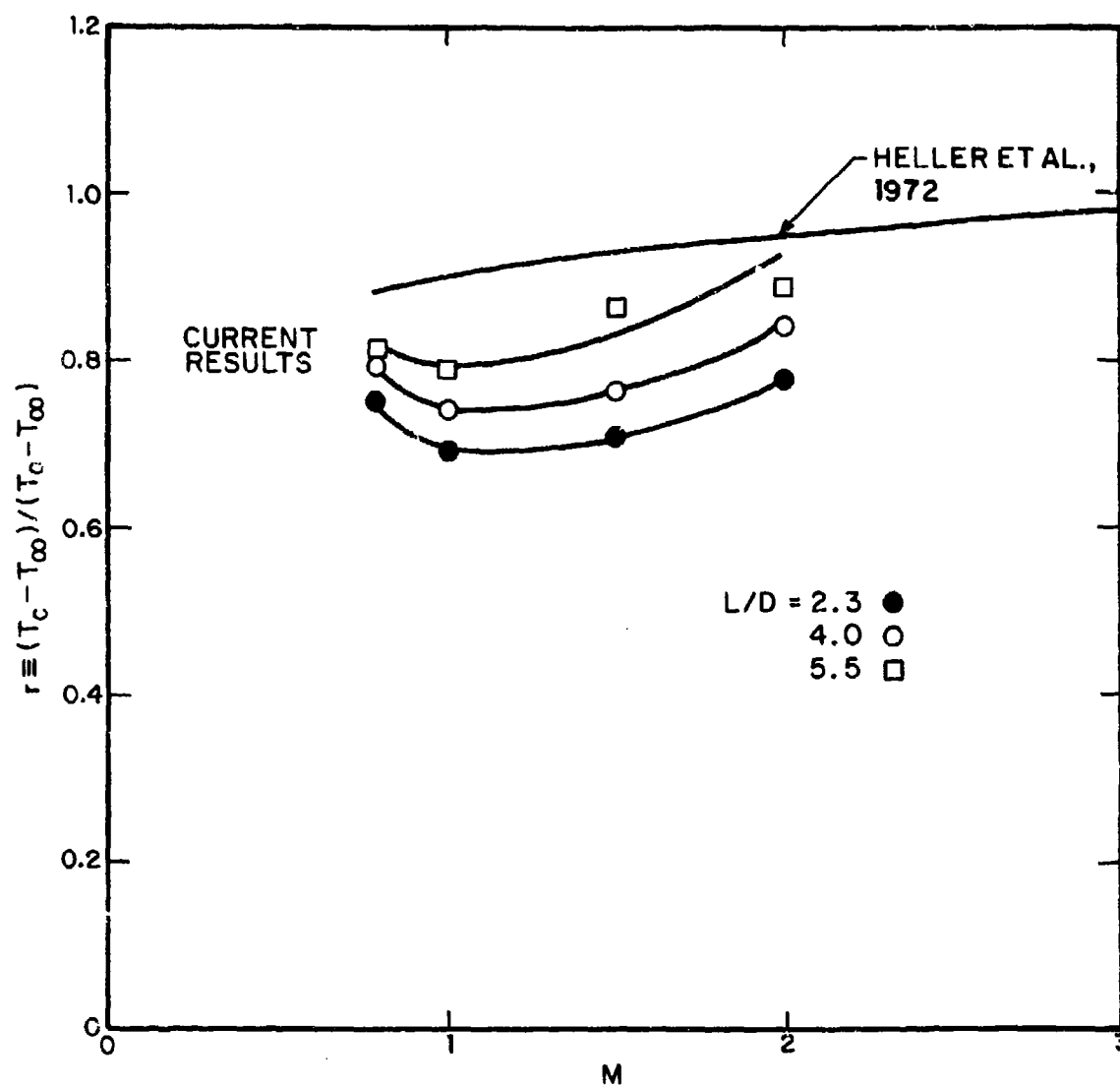


FIG. 47. MACH NUMBER DEPENDENCE OF RECOVERY FACTOR.

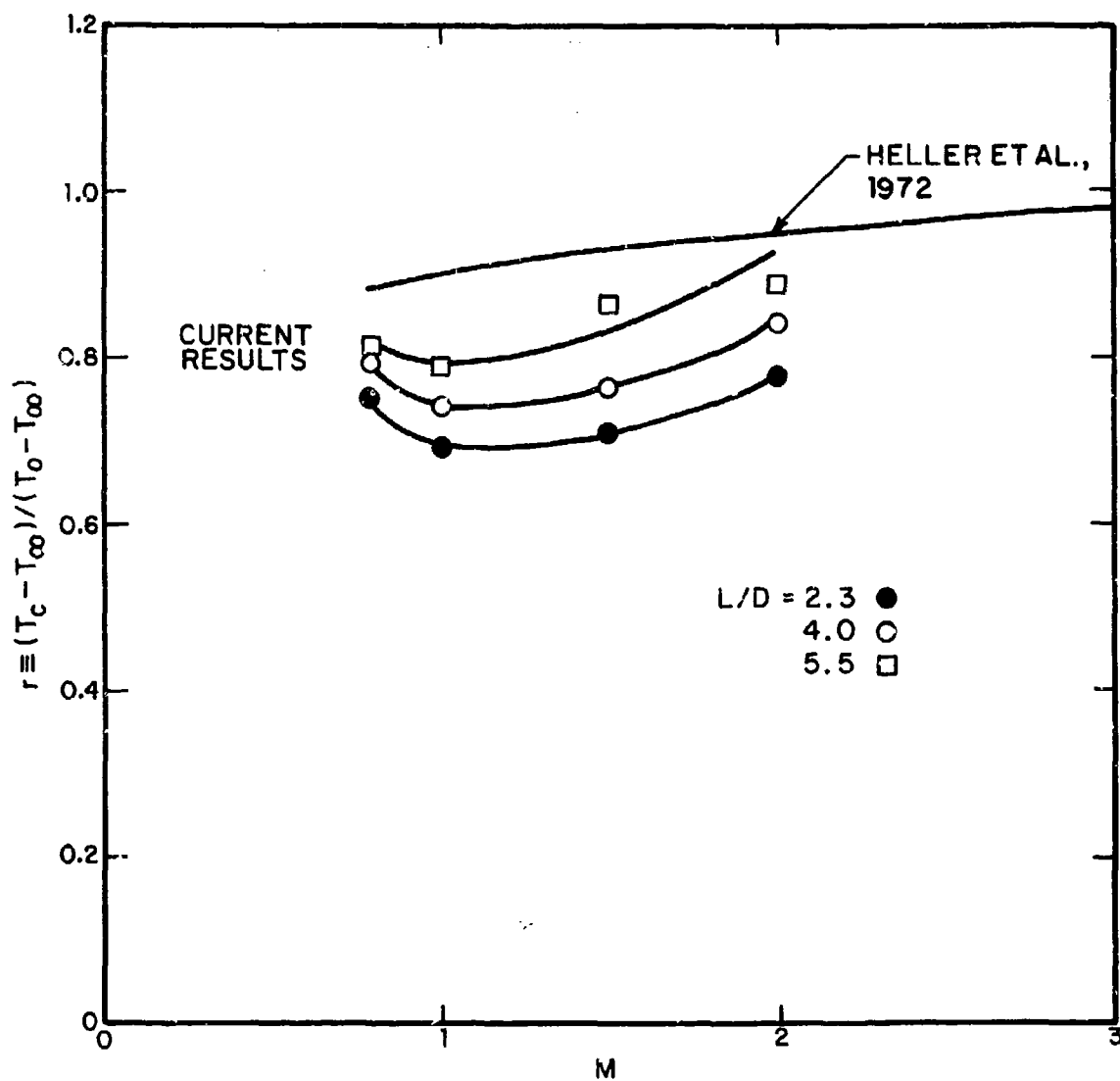


FIG. 47. MACH NUMBER DEPENDENCE OF RECOVERY FACTOR.

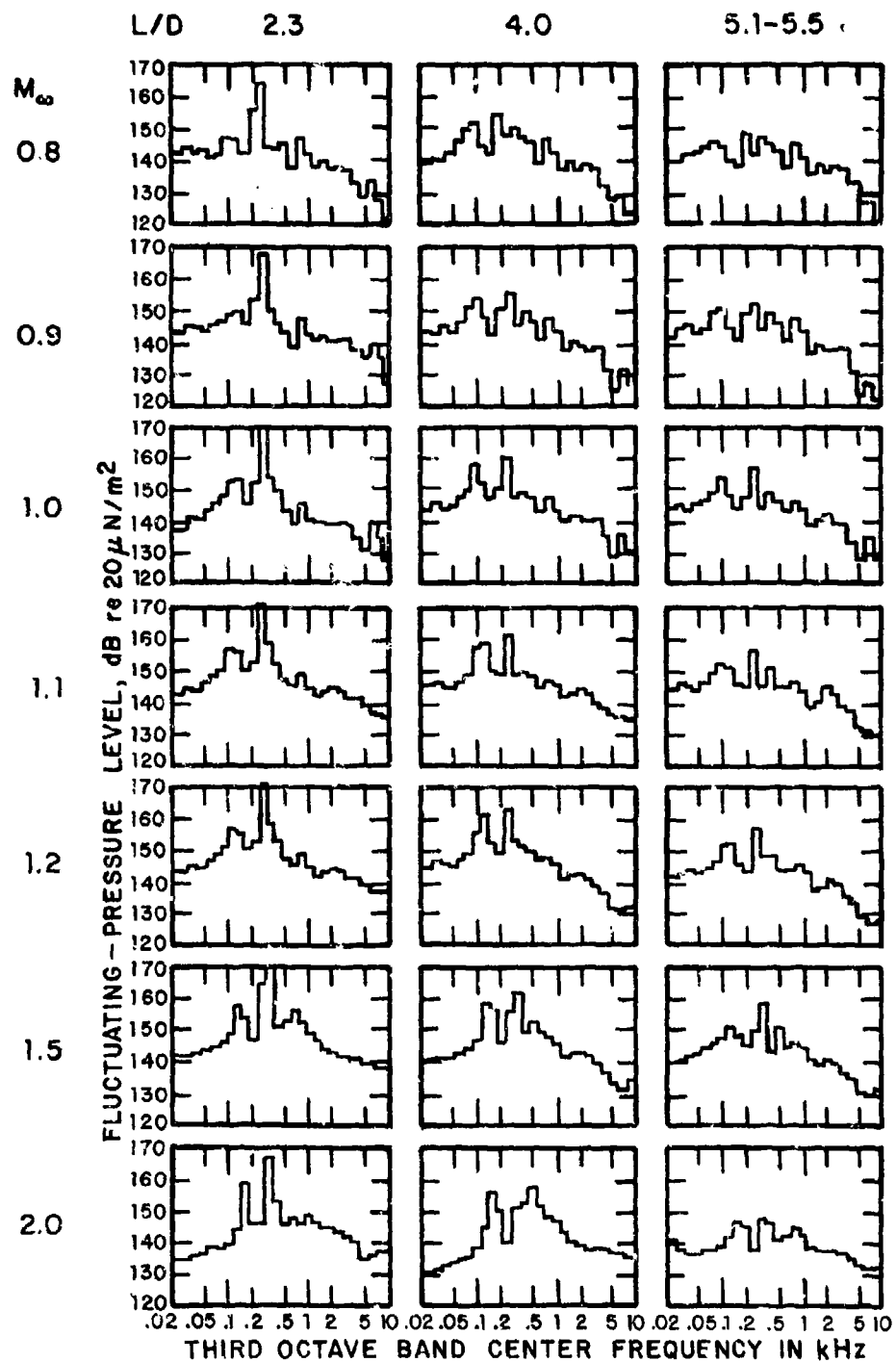


FIG. 48. LEADING-EDGE BULKHEAD SPECTRA, CAVITY LENGTH 3 ft.

TABLE I. CONVERSION FACTORS

M_∞	Ordinate Correction* (dB)	Abcissa Correction†
0.8	184	0.00341
0.9	185	0.00307
1.0	186	0.00281
1.1	187	0.00262
1.2	187.5	0.00239
1.5	188.5	0.00202
2.0	189.5	0.00162

Of course, the frequency scale is only valid for a cavity of 3-ft length. To nondimensionalize the frequency on a Strouhal number basis, we must multiply the frequency abscissas by the appropriate numbers in Table I.

As further illustration of the spectral energy distribution in and near the cavity, Figs. 49 and 50 show 1/3-octave band spectra obtained for an $L/D = 2.3$ cavity at various locations at $M_\infty = 0.8$ and $M_\infty = 1.5$, respectively. Since sensor signals on a cavity leading- or trailing-edge wall, and in corners, are more easily compared than signals from sensors halfway in the cavity, where levels are affected by location, only signals from sensors 1, 2, 3, 6, 7, and 8 (see Fig. 36) are shown.

* To convert ordinate levels in Fig. 49 to read $20 \log (p_{rms}/q_\infty)$, subtract the numbers in the column from the ordinate levels.

† To convert abscissa frequencies in Fig. 49 to Strouhal frequencies, $S \equiv fL/U_\infty$, multiply the frequencies by the numbers in the column.

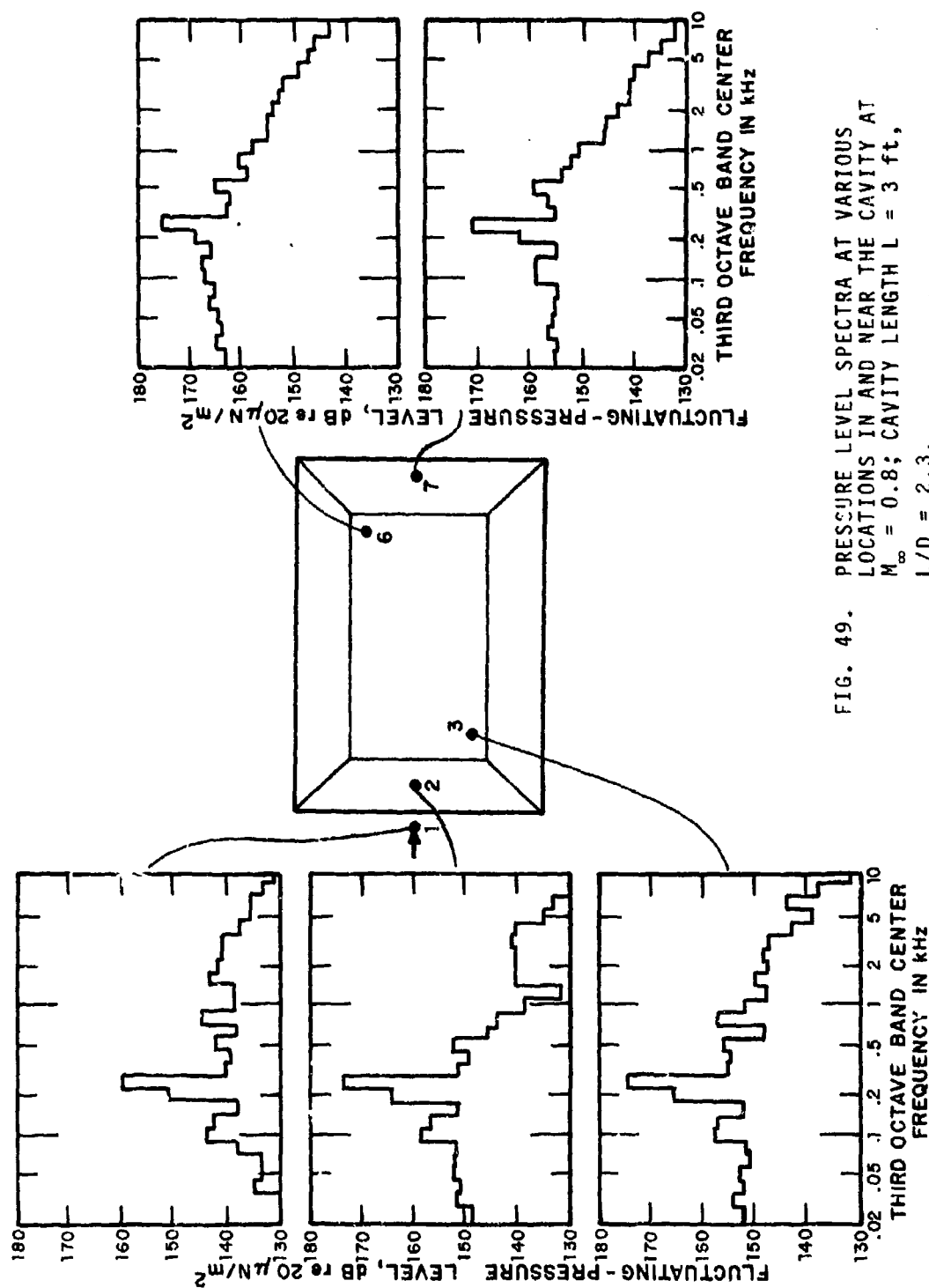


FIG. 49. PRESSURE LEVEL SPECTRA AT VARIOUS LOCATIONS IN AND NEAR THE CAVITY AT $M_\infty = 0.8$; CAVITY LENGTH $L = 3$ ft, $L/D = 2.3$.

Generally, we can conclude that spectral energy distribution and levels are quite uniform inside the cavity near the leading-edge bulkhead. At subsonic speeds, acoustic energy is radiated upstream, so that a generically similar spectrum, although of lower intensity, is observed a short distance upstream of the leading edge. Acoustic characteristics in the trailing-edge region are also quite similar; however, the discrete tone levels are higher than at the leading-edge bulkhead, and broadband noise has increased significantly. Acoustic signatures, a small distance downstream of the cavity trailing edge, correspond to those inside the cavity, but the levels are slightly reduced. The data presented in Figs. 49 and 50 can also be nondimensionalized using Table I.

A more detailed picture about the energy distribution between discrete tones and broadband energy is obtained through narrowband analysis. In Fig. 51, 10-Hz constant bandwidth spectra spanning the 0 to 1000-Hz frequency range are presented for three L/D ratios at the leading- and trailing-edge regions. The Mach number in this test was unity. These spectra show that near the leading edge for deep cavities (L/D = 2.3) almost all energy is in discrete frequency bands; in fact, the broadband energy (in this 10-Hz bandwidth representation) is about 40 dB down from the dominant mode-2. Tone levels near the trailing edge are comparable to, or exceed, those at the leading edge, however, the broadband energy has significantly increased; it is only 25 dB below the mode-2 peak.

For the shallower cavity (L/D = 5.5), the energy is somewhat more evenly distributed between modes; broadband energy at the leading edge is only 25 dB below the mode - 2 peak. At the trailing edge, the mode-2 peak exceeds the broadband energy level by about 18 dB.

6.5.2 Resonant Frequencies

As has been discussed in previous sections, flow-exposed cavities resonate at discrete frequencies, which order themselves along certain modes. In order to determine resonant frequencies accurately, the frequencies were counted by electronic means.

Figure 52 shows nondimensional frequencies, $S_m = f_m L / U_\infty$, as function of freestream Mach number M_∞ . here, f_m is a resonant frequency with $m = 1, 2, 3 \dots$ denoting the mode under consideration, L is the cavity length, and U_∞ is the freestream velocity. Four sets of data are contained: (1) test results for $2.3 < L/D < 5.5$ obtained at the NASA Lewis Research Center

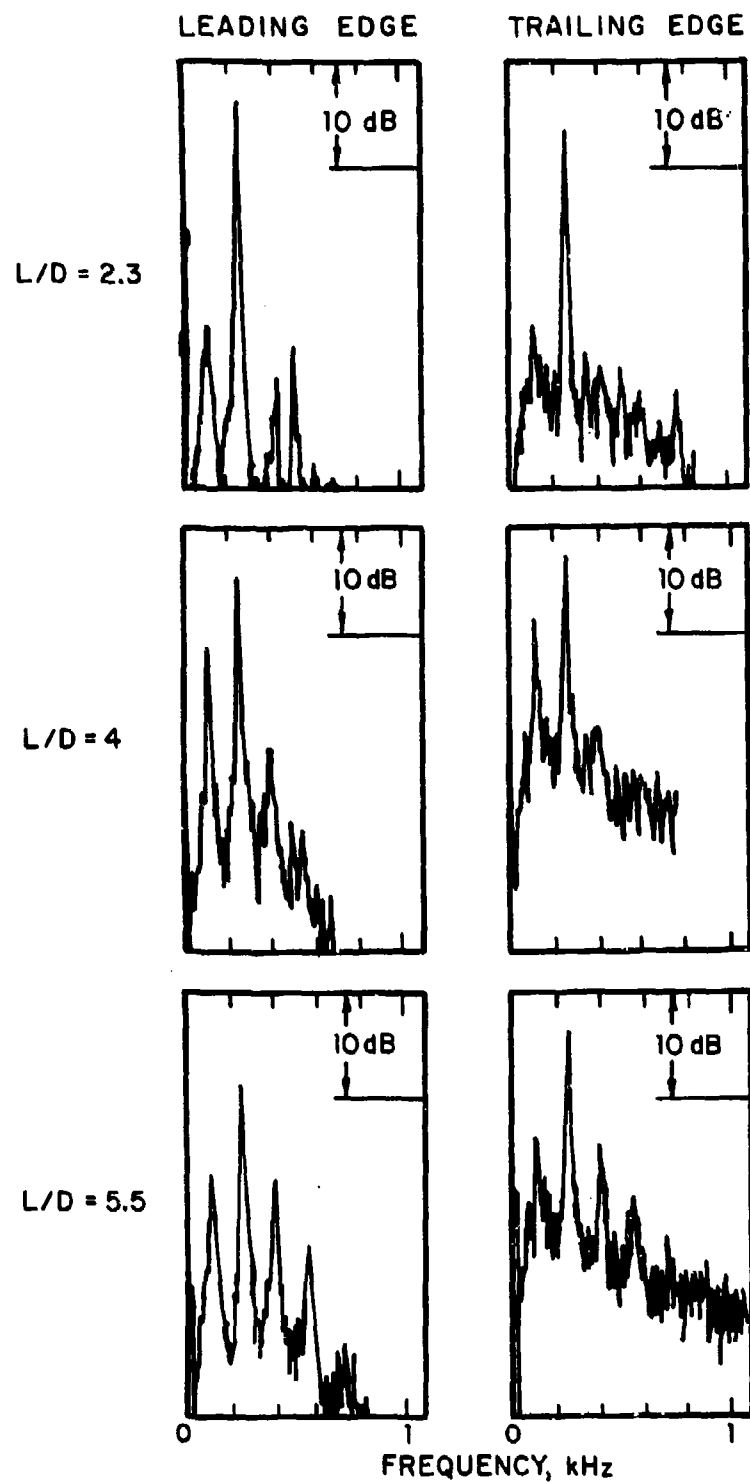


FIG. 51. NARROWBAND ANALYSIS OF LEADING-EDGE AND TRAILING-EDGE BULKHEAD SENSOR SIGNALS.

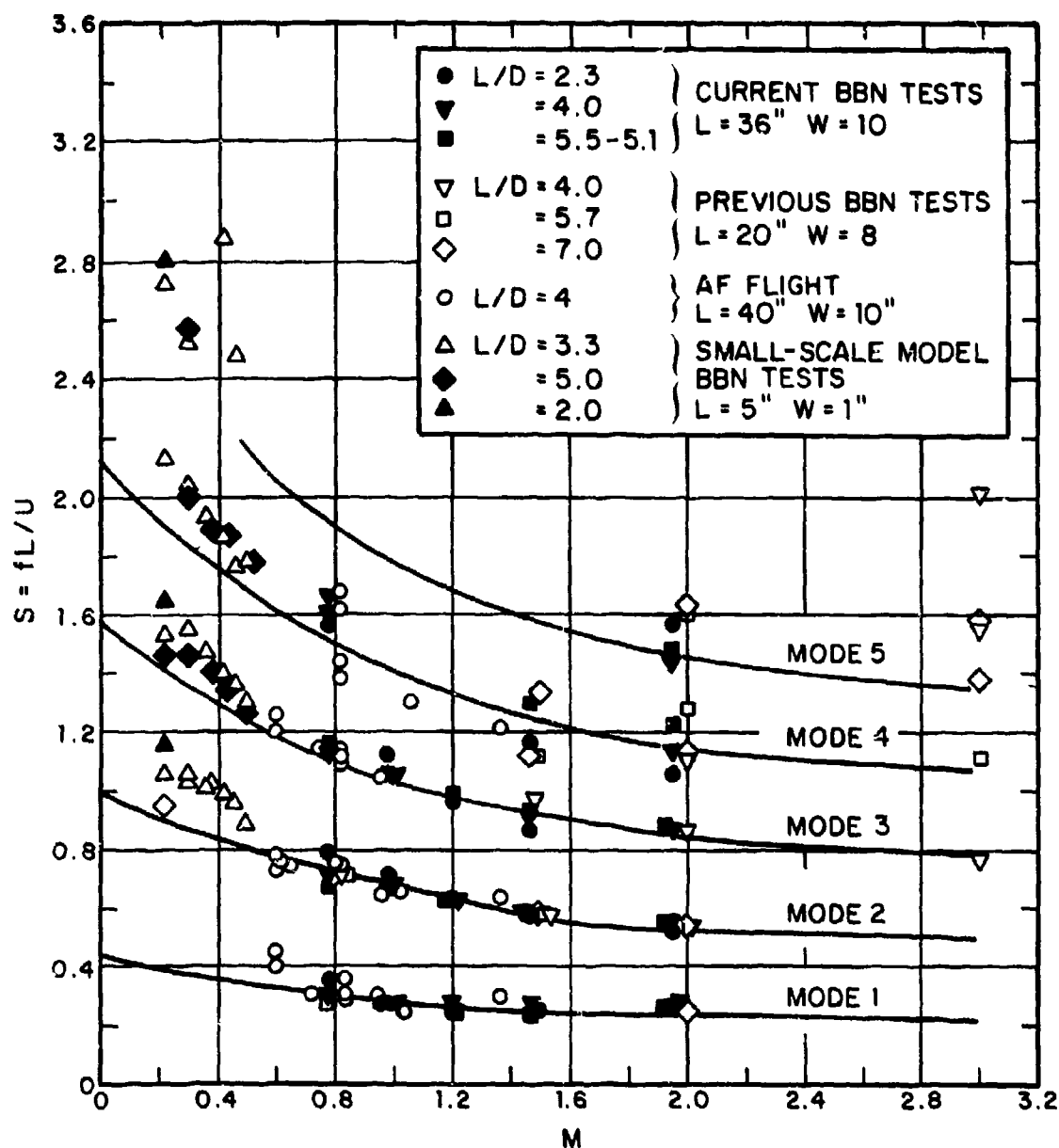


FIG. 52. STROUHAL FREQUENCIES OF CAVITY MODES AS FUNCTION OF MACH NUMBER.

8 x 6 ft wind tunnel; (2) test results from a previous research effort obtained for $4 < L/D < 7$ in the MIT Naval Supersonic Wind Tunnel (Heller *et al.*, 1970); (3) Air Force flight test data for $L/D = 4.0$ (Smith *et al.*, 1974); and (4) small-scale test data obtained in the wall-jet facility for $2.0 < L/D < 5.0$. This plot spans the Mach number range from 0.22 to 3.0.

It is evident that all data points order themselves closely among the various mode curves that were previously (Heller *et al.*, 1970) expressed analytically as

$$S_m \equiv \frac{f_m \cdot L}{U_\infty} = \frac{m - \alpha}{M \left[\left(1 + \frac{\gamma - 1}{2} \cdot M^2 \right)^{1/2} \right] + 1/k_v}, \quad (6.1)$$

where α is an empirical constant, which is close to 0.25 for $L/D = 4$, γ is the ratio of specific heats, and k_v is another empirical constant tied to a disturbance convection speed in the cavity shear layer and found to equal 0.57. No systematic effect of the L/D ratio on nondimensional frequencies is readily discernable in the $2 < L/D < 7$ range, because of experimental scatter. Qualitatively, then, we may state that the lower L/D ratios tend to increase the nondimensional frequency.

At Mach numbers below 0.5, the data points rise faster (towards $M = 0$) than predicted by Eq. 6.1, which restricts the validity of the equation to $M > 0.5$.

Resonant frequencies up to the fifth mode and, possibly, beyond were observed; however, they had dramatically different modal intensities, depending on both Mach number and length-to-depth ratios. Hence, while a resonance can only occur at frequencies determined by Eq. 6.1, this representation of mode frequencies does not determine whether a resonance will, in fact, occur.

6.5.3 Effect of L/D Ratio on Frequencies

Since the general scatter of the large body of experimental data does not allow an accurate evaluation of the mode frequency dependence on the L/D ratio, an experiment on the small-scale wall-jet facility was initiated. In this experiment, the L/D ratio was systematically varied from 0.3 to 6.67, thus encompassing the range from very deep to very shallow cavities. The external

flow speed was kept constant at 245 ft/sec. Figure 53 presents the results in terms of Strouhal numbers vs L/D ratio.

Deep cavity nondimensional mode frequencies increase rapidly with L/D up to $L/D \approx 1$. From dimensional considerations, it is clear that for deep cavities the dependence of S on mode number, Mach number, and L/D must be $S \propto (m/M) \cdot (L/D)$; i.e., for constant m and M, the Strouhal number is directly proportional to L/D. On the other hand, as shown by Heller *et al.* (1970), shallow cavity nondimensional frequencies are nearly independent of L/D.

This behavior is quite clear in Fig. 53. For shallow cavities ($L/D > 2$), the nondimensional resonant frequencies decrease as the cavity becomes shallower. At these relatively low Mach numbers ($M = 0.22$), the increase of the L/D ratio from 2 to 4 results in a 20% decrease in Strouhal number. However, there is reason to believe that at higher external flow speed the effect is less dramatic, and frequency variations for the important first three modes at transonic and supersonic flow speeds are probably less than 5%.

6.5.4 Levels

The question of oscillation onset is best answered by Figs. 54 and 55, where nondimensional resonant levels are presented. These figures pertain to levels that were measured in the leading-edge bulkhead region and the trailing-edge bulkhead region, respectively. Data are presented for modes 1, 2, and 3 and for L/D ratios of 2.3, 4.0, and 5.1. Experimental results from the large-scale NASA Lewis Research Center 8 x 6 ft tunnel tests, the Air Force flight tests, the previous MIT Naval Supersonic Wind Tunnel test, and the small-scale wall-jet tests are included. It should be emphasized that this representation is not a plot of the overall cavity noise level vs Mach number, but a plot of the level of each individual mode vs Mach number. An attempt was made to connect the data points, which, in the leading-edge bulkhead region, order themselves along single curves (see Fig. 54). The uncertainty about modal levels is much greater in the trailing-edge bulkhead data (see Fig. 55). Here, the discrepancy between flight test and wind tunnel test is quite pronounced.

For cavities of $L/D > 2$, it can be concluded that the oscillation onset is gradual, as exemplified in Fig. 56. For the specific case of a mode-2 resonance and an L/D of four, this figure shows the rapid but smooth level increase from $M = 0.2$ to $M = 1$, reaching a relative maximum at $M = 1.2$

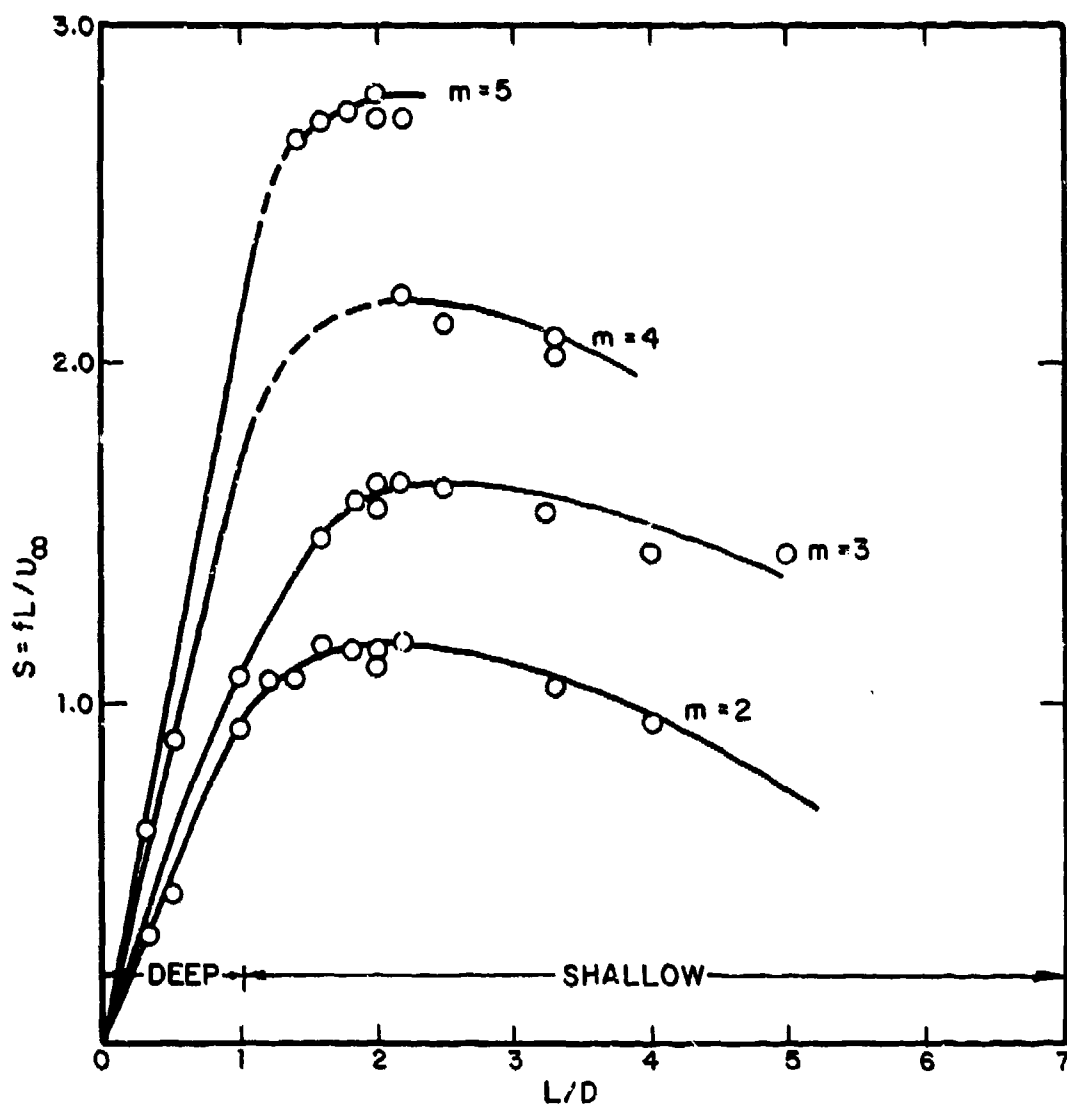


FIG. 53. LENGTH-TO-DEPTH RATIO DEPENDENCE OF NONDIMENSIONAL RESONANT MODE FREQUENCIES FOR $M_\infty = 0.22$.

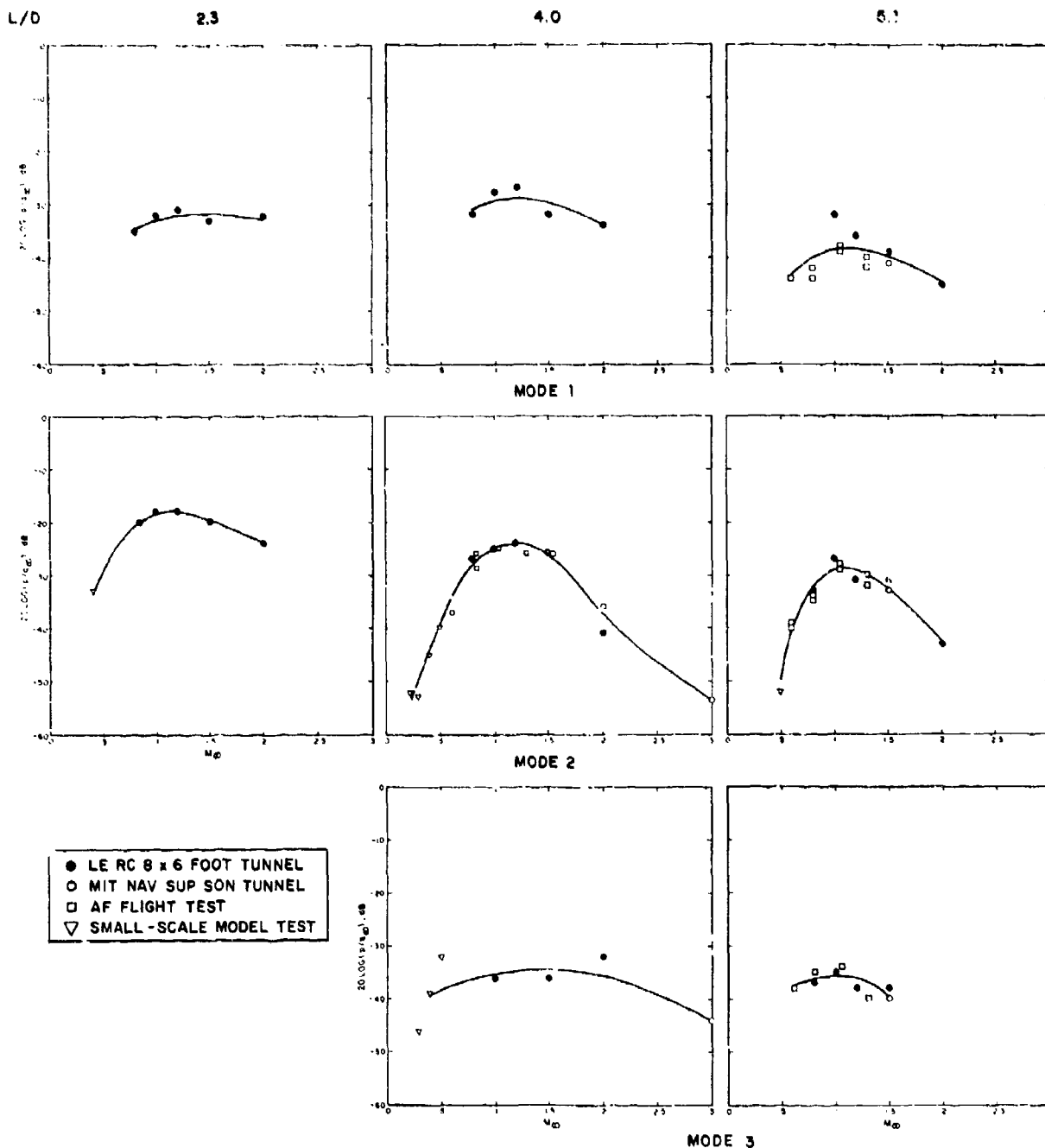


FIG. 54. COMPARISON OF MACH NUMBER DEPENDENCES OF RESONANT MODE LEVELS: LEADING-EDGE AREA.

and decreasing thereafter more gradually. Resonant mode behavior for other conditions, as documented in Fig. 54 is generically quite similar.

In the following series of figures (Fig. 57), the data of Figs. 54 and 55 are presented again to allow direct comparison of mode levels for various L/D ratios.

6.5.5 Mode Shapes

Previous investigations (Smith *et al.*, 1974; Heller *et al.*, 1970) demonstrated that the longitudinal amplitude distribution of resonant frequencies shows great similarity to the resonant behavior of a one-dimensional oscillator resonating in a length-wise direction. However, the resonant frequencies do not directly correspond to ideal "closed-box" longitudinal frequencies, other than at high Mach numbers, where the external flow represents a rather stiff boundary.

The setting up of an ideal standing wave pattern between the fore and the aft bulkhead wall of a resonating cavity requires these walls to be acoustically hard. However, this is not the case, at least as far as the aft bulkhead. The high amplitude oscillatory motion of the shear layer at and near the trailing edge affects the impedance of the cavity aft region. Thus, while standing wave patterns are definitely observed, they do not coincide with a classical closed-space standing wave pattern.

Using the traversing rod, the mode shapes for the first three modes were traced across the cavity span from $0.3 < x/L < 0.9$, where x is the running length coordinate. These traces were obtained only at $M_\infty = 0.8$ and $M_\infty = 1.0$, and for $2.3 < L/D < 5.5$. A typical trace appears in Fig. 58. In all cases, two traces, i.e., one upstream and one downstream, were obtained at each experimental condition. The bandwidth of the trace is 50 Hz. All mode shape traces are shown in Figs. 59 and 60.

In some of the trace presentations, data points from the Air Force flight test (Smith *et al.*, 1974) are included. These data points were obtained at $M_\infty = 0.8$ for altitudes of 3000 and 20,000 ft; thus, they are considered to be comparable to the 10,000-ft altitude simulation in the NASA Lewis facility at $M_\infty = 0.8$. These flight data points were shifted so that they coincide with the mode traces from the wind tunnel tests. The points fall within a ± 4 -dB range of the traces. It should be realized, however, that the mode traces were obtained at a fixed distance from the cavity mouth plane, whereas the flight test data points were

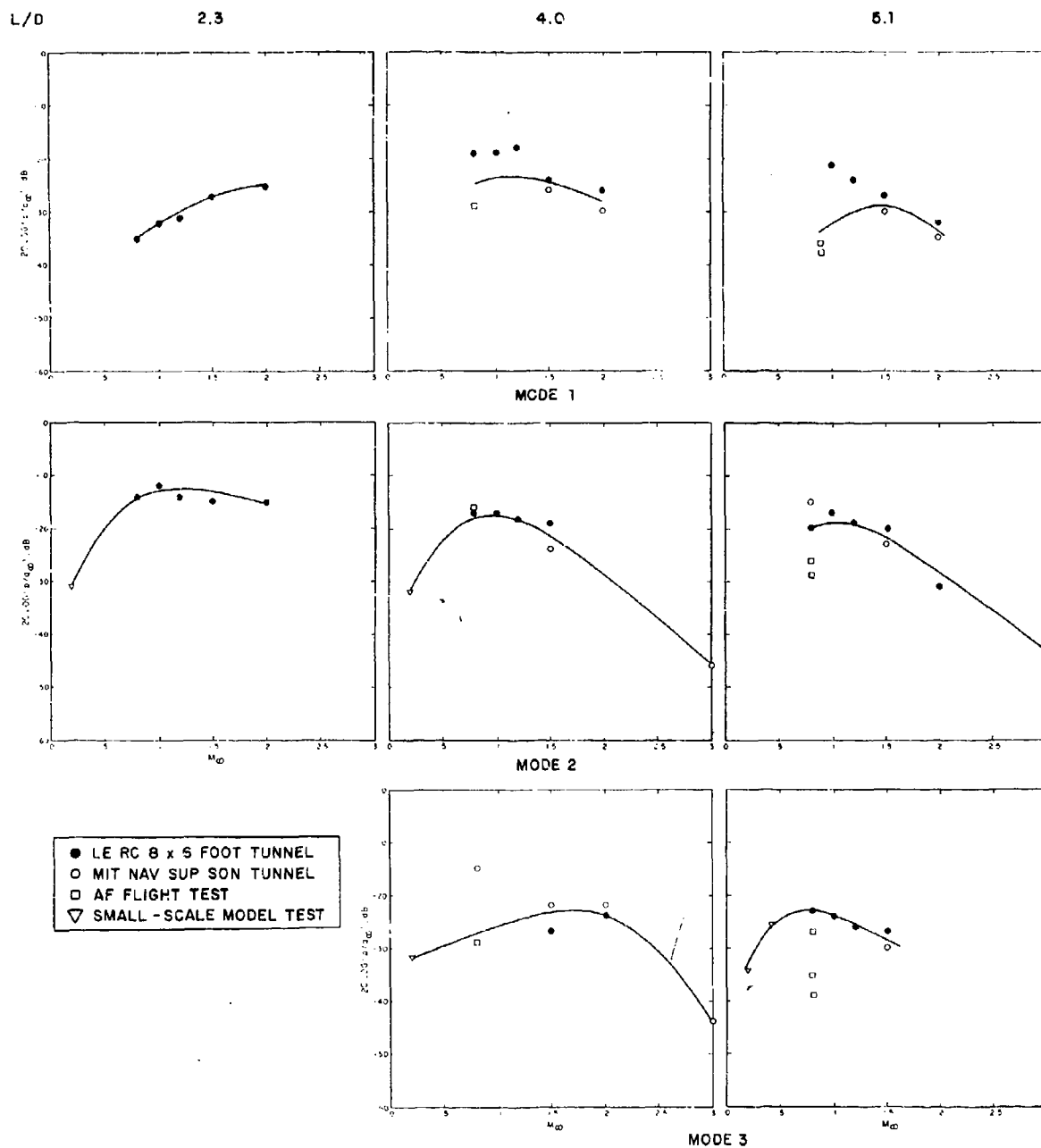


FIG. 55. COMPARISON OF MACH NUMBER DEPENDENCES OF RESONANT MODE LEVELS: TRAILING-EDGE AREA.

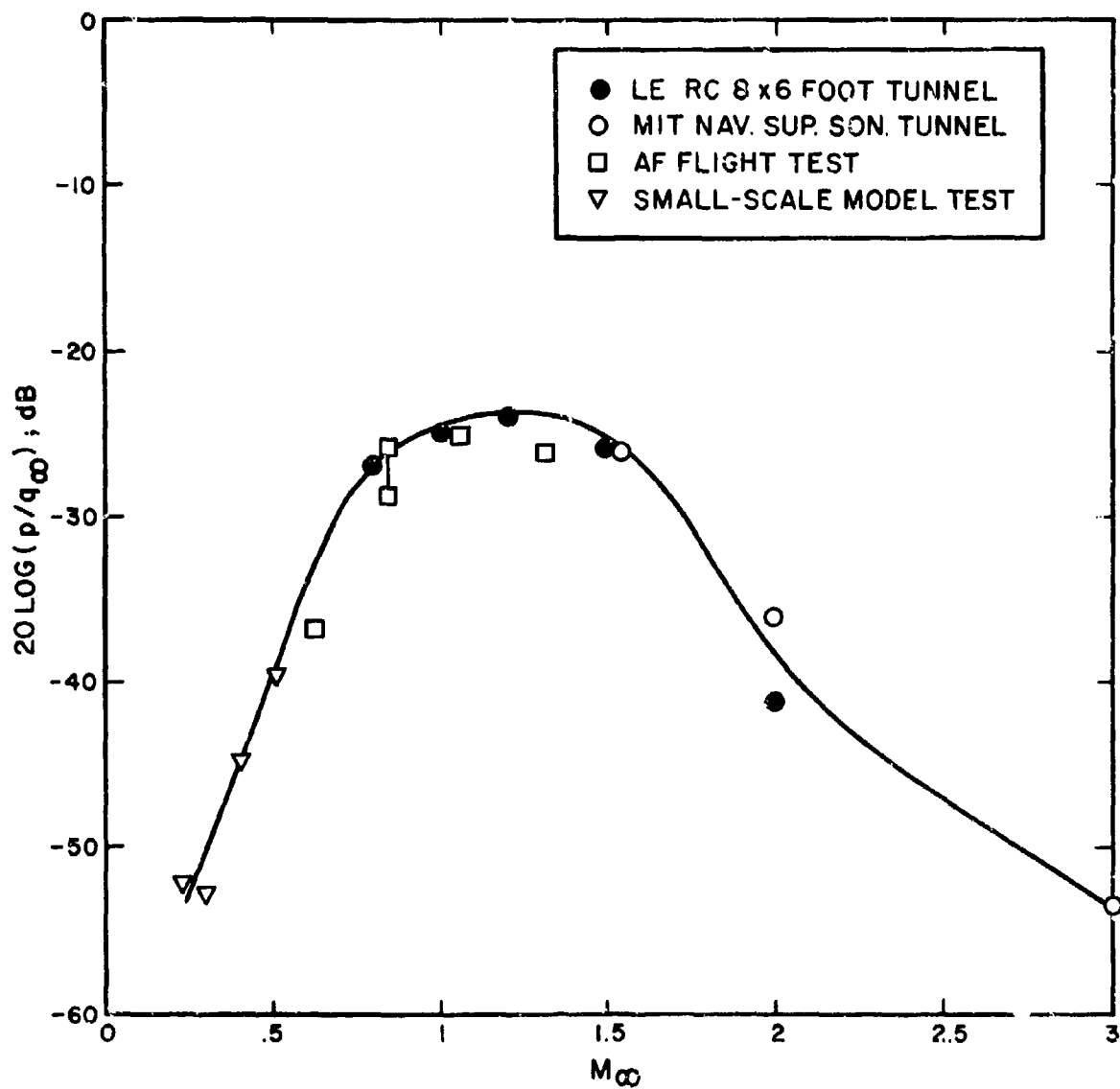


FIG. 56. MACH NUMBER DEPENDENCE OF NORMALIZED MODE-2 LEVELS. CAVITY LEADING-EDGE BULKHEAD REGION: $L/D = 4$.

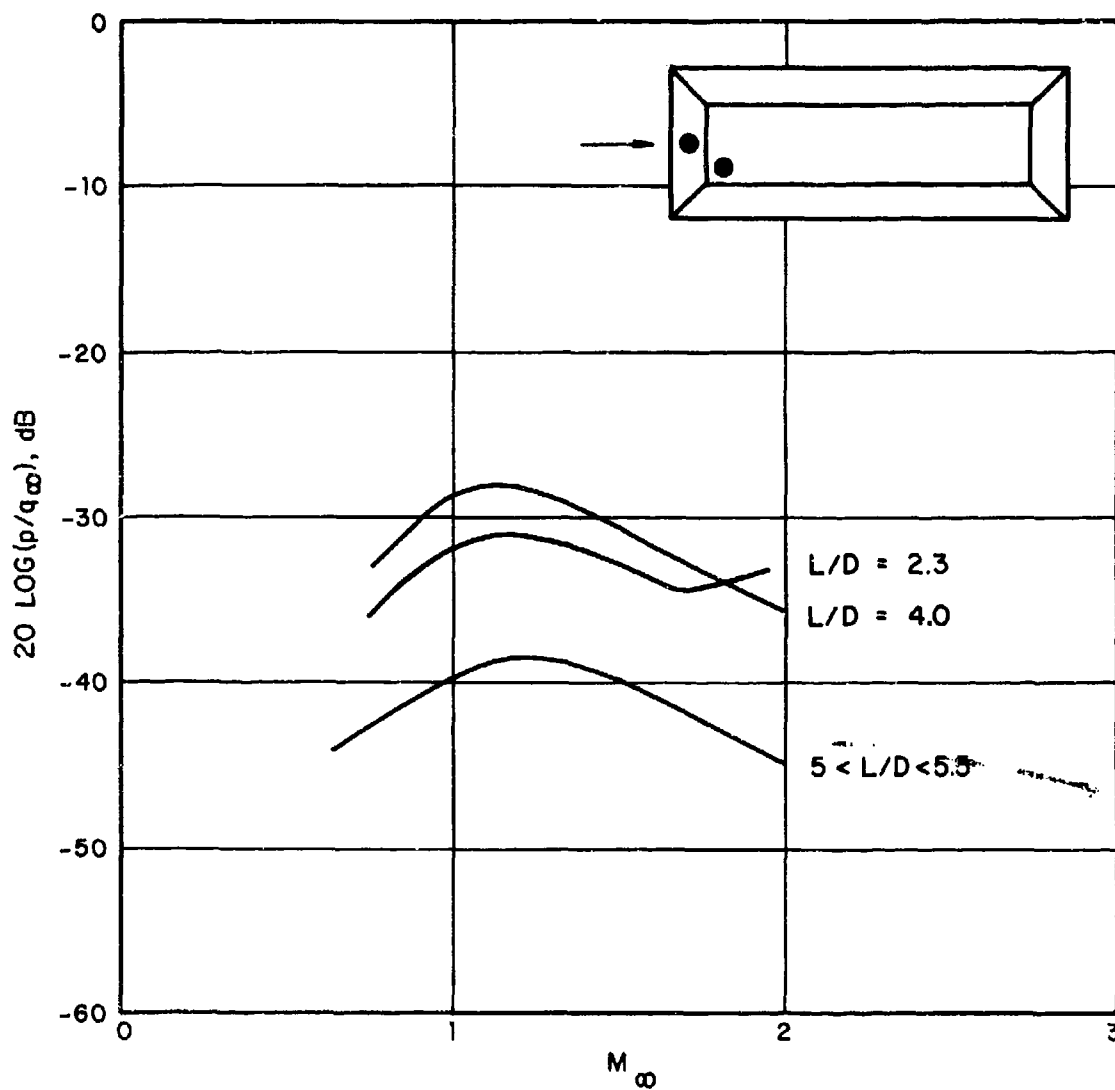


FIG. 57a. MACH NUMBER DEPENDENCE OF NORMALIZED MODE-1 LEVELS AT LEADING-EDGE BULKHEAD FOR VARIOUS L/D RATIOS.

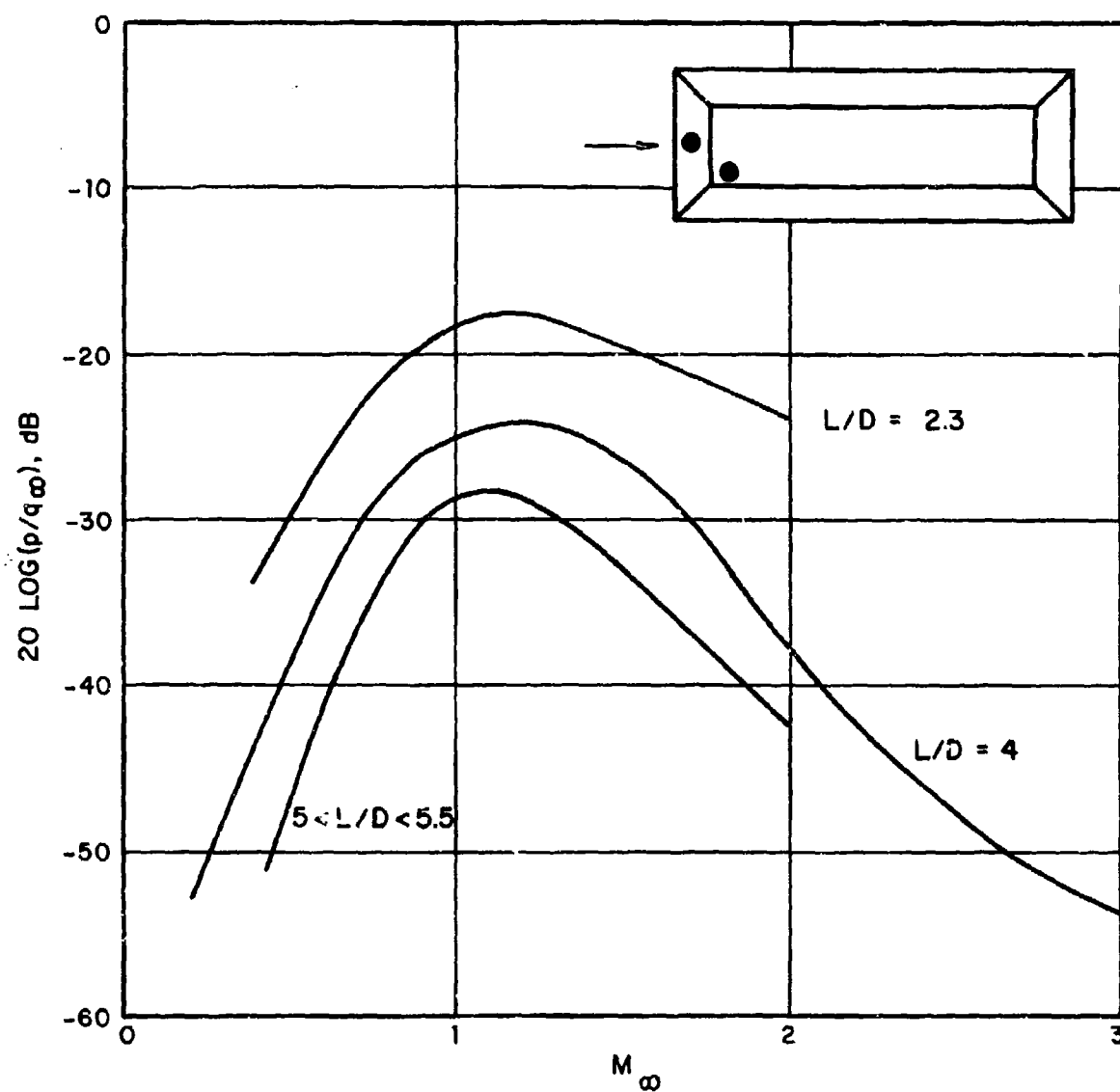


FIG. 57b. MACH NUMBER DEPENDENCE OF NORMALIZED MODE-2 LEVELS AT LEADING-EDGE BULKHEAD FOR VARIOUS L/D RATIOS.

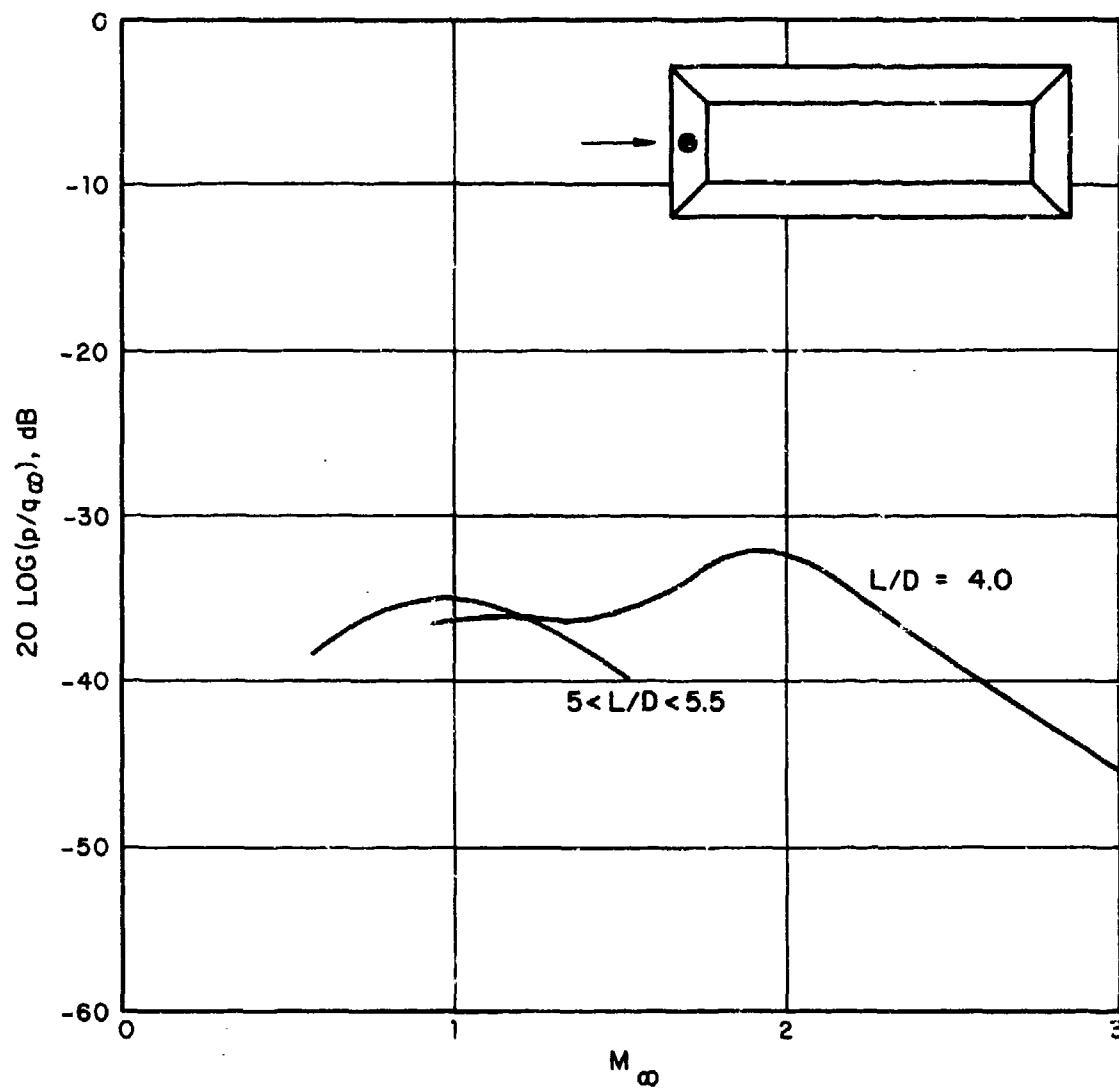


FIG. 57c. MACH NUMBER DEPENDENCE OF NORMALIZED MODE-3 LEVELS AT LEADING-EDGE BULKHEAD FOR VARIOUS L/D RATIOS.

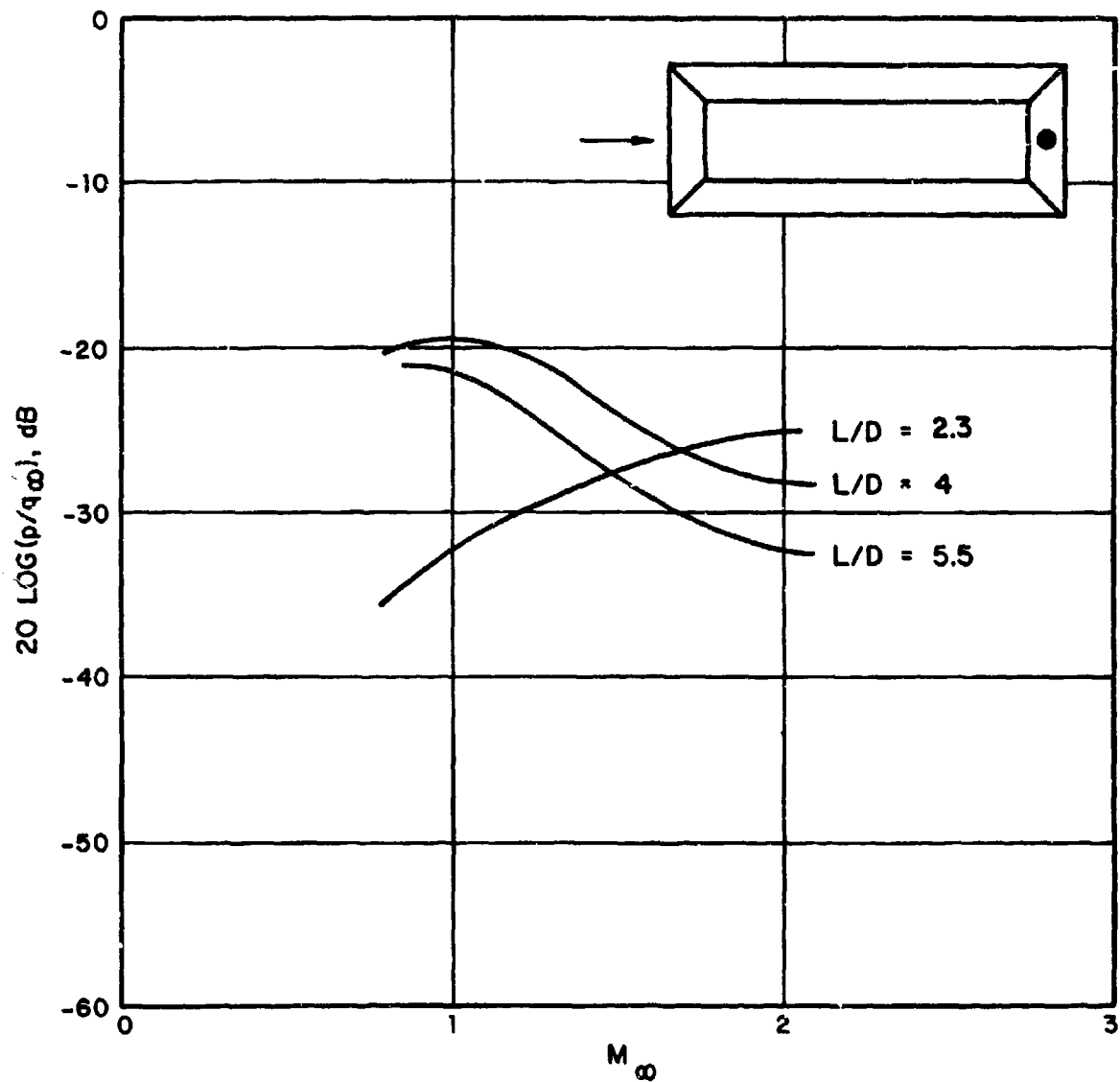


FIG. 57d. MACH NUMBER DEPENDENCE OF NORMALIZED MODE-1 LEVELS AT TRAILING-EDGE BULKHEAD FOR VARIOUS L/D RATIOS.

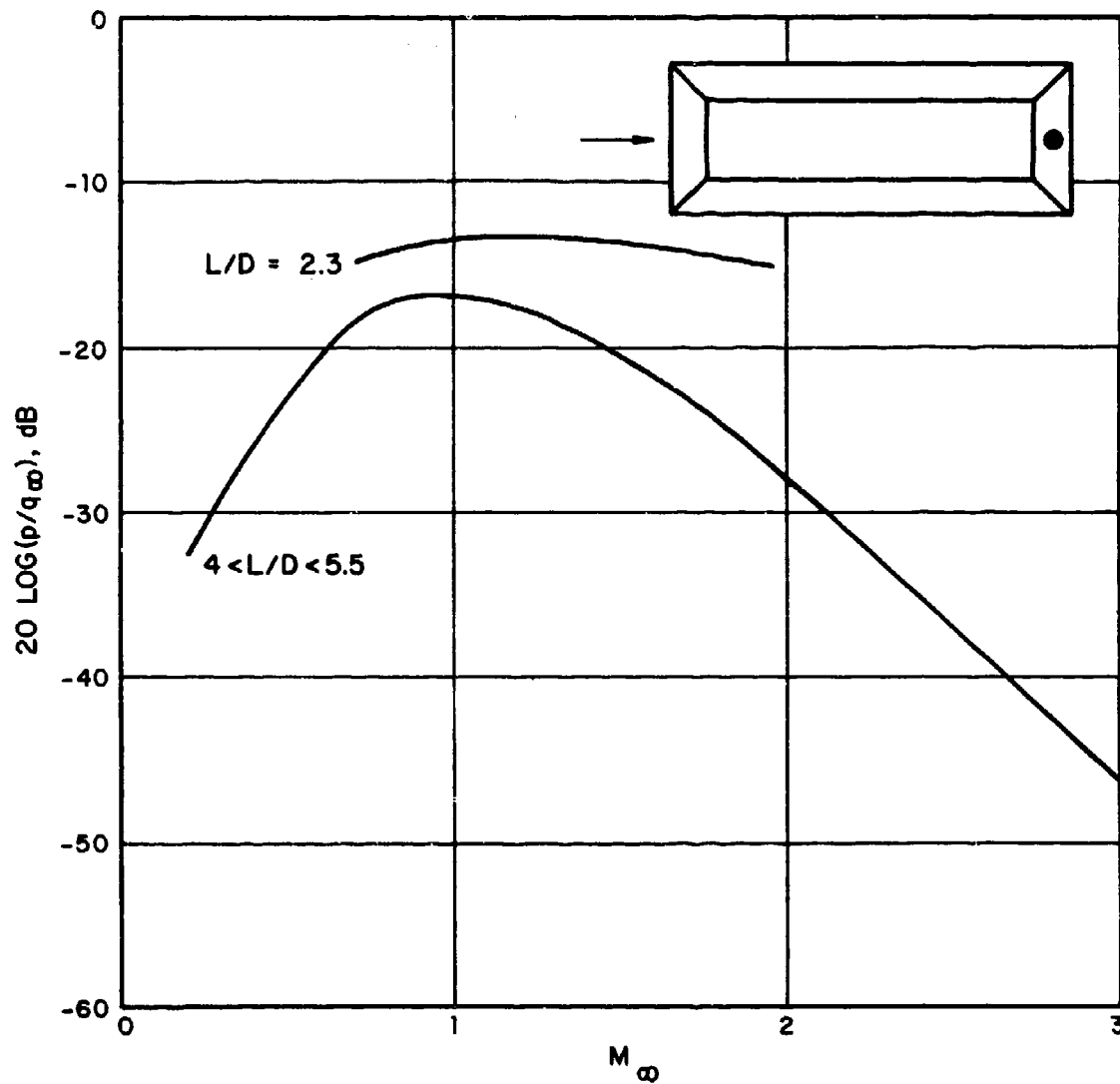


FIG. 57e. MACH NUMBER DEPENDENCE OF NORMALIZED MODE-2 LEVELS AT TRAILING-EDGE BULKHEAD FOR VARIOUS L/D RATIOS.

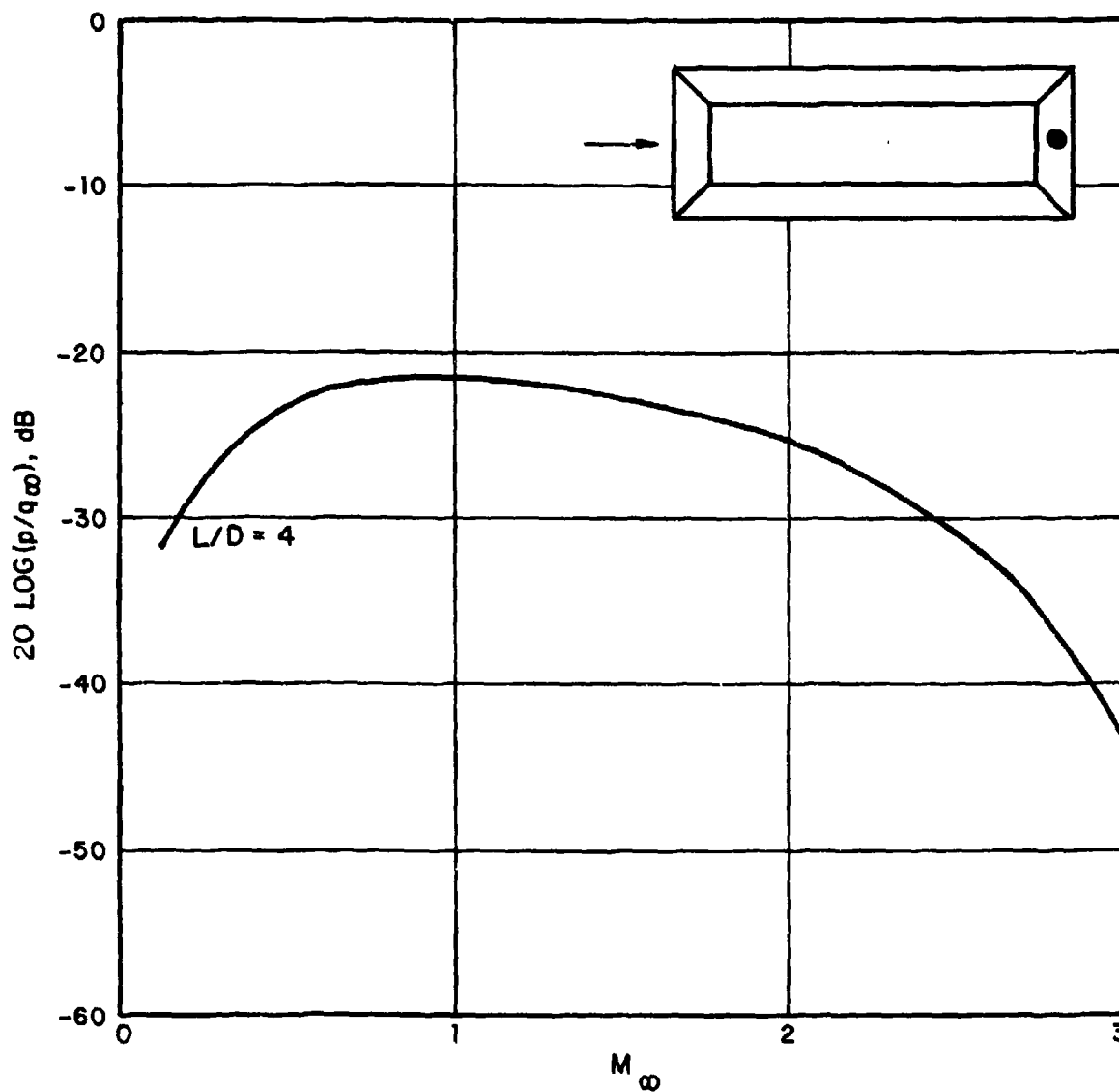


FIG. 57f. MACH NUMBER DEPENDENCE OF NORMALIZED MODE-3 LEVELS AT TRAILING-EDGE BULKHEAD FOR VARIOUS L/D RATIOS.

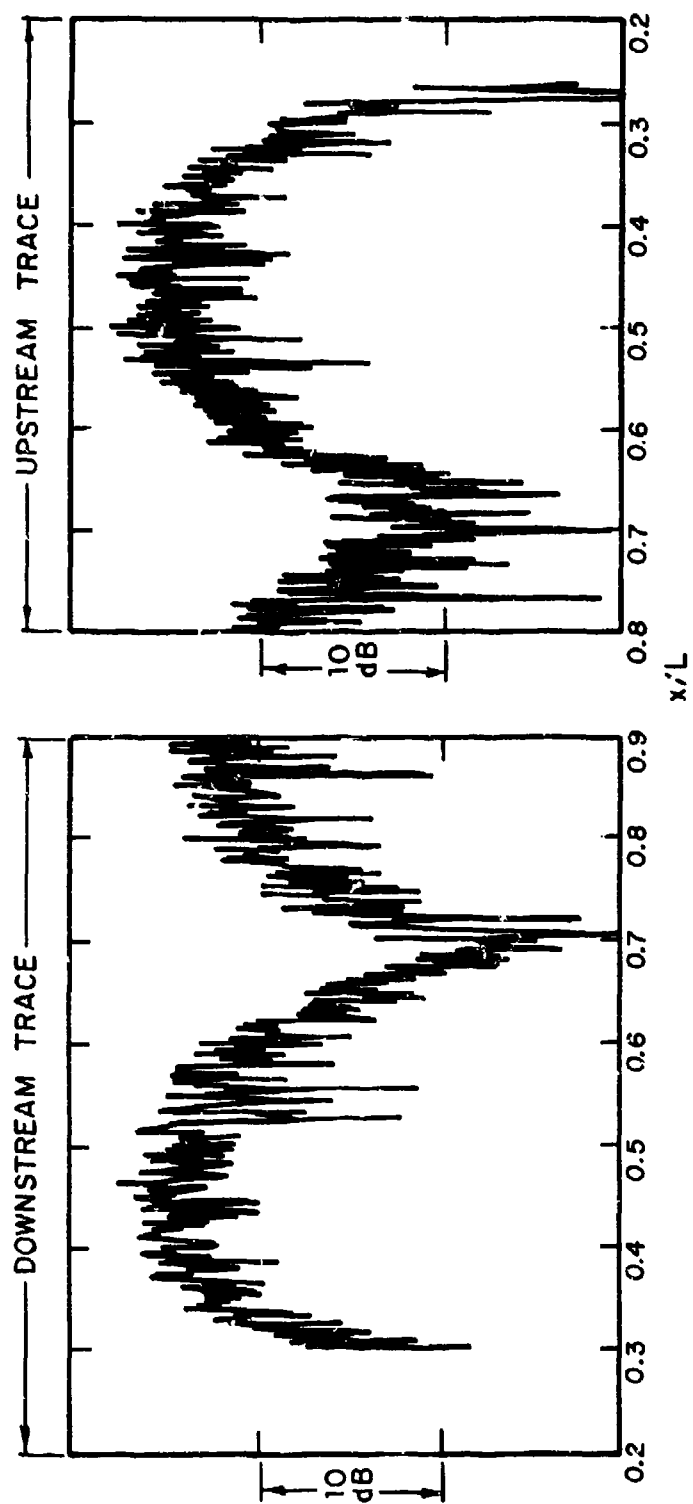


FIG. 58. TYPICAL MODE SHAPE TRACE ACROSS CAVITY SPAN.

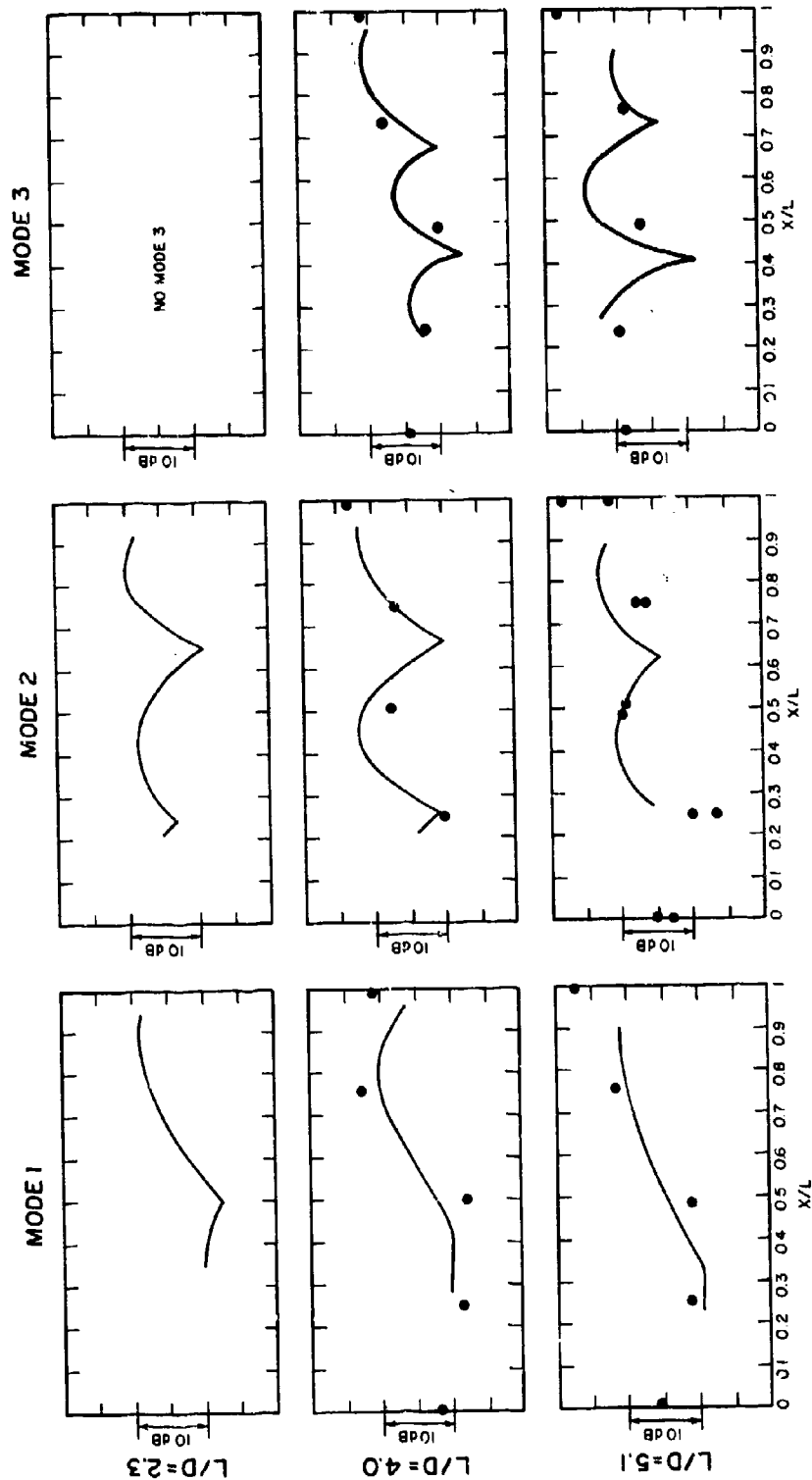


FIG. 59. COMPARISON OF MODE SHAPES FOR CAVITIES WITH VARIOUS LENGTH-TO-DEPTH RATIOS $M_\infty = 0.8$ (contiguous lines - present investigation, data points - Air Force flight test results).

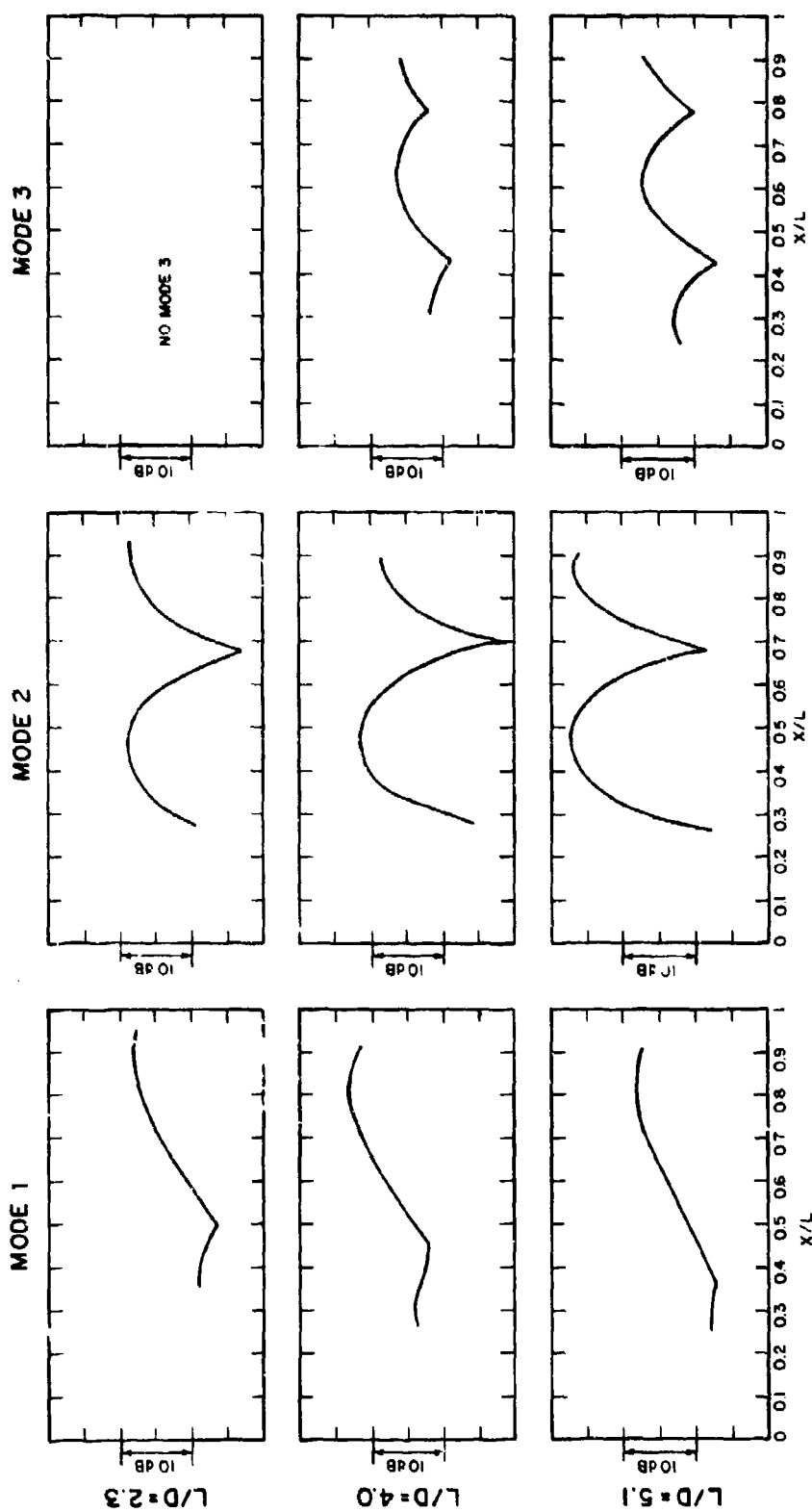


FIG. 60. COMPARISON OF MODE SHAPES FOR CAVITIES WITH VARIOUS LENGTH-TO-DEPTH RATIOS: $M_\infty = 1.0$.

measured on the floor. It is likely that the acoustic field in the cavity changes in a vertical direction, and the data at various vertical positions cannot be compared directly.

Inspection of the mode shape traces for $M_\infty = 1$ allows several general conclusions:

- While all modes exhibit a fairly well-defined pressure minimum, the longitudinal location of the minimum does not correspond to the classical closed-box modal patterns.
- The pressure minimum for mode-1 is displaced from the center of the cavity towards the leading-edge bulkhead for the shallow cavities. Specifically, the minima appear at the following x/L locations.

MODE 1

L/D	x/L
2.3	0.50
4.0	0.45
5.1	0.37

Thus, the shallower a cavity, the more the system deviates from a classical one-dimensional (hard-walled) oscillator. In all cases, the trailing-edge maximum occurs a small distance upstream of the trailing-edge bulkhead. These conclusions are valid at Mach numbers of 0.8 and 1.0.

- The downstream pressure minimum for mode-2 is displaced in the upstream direction, while the upstream pressure minimum appears roughly at the location for a classical one-dimensional oscillator (i.e., at $x/L = 0.25$). However, with increasing Mach number (going from 0.8 to 1.0), the downstream minimum approaches the hard-wall oscillator value of $x/L = 0.75$. Specifically, the minima appear at the following x/L locations:

MODE 2

M	L/D	x/L	
		node 1 ideal 0.25	node 2 ideal 0.75
0.8	2.3	0.25	0.65
	4.0	0.25	0.66
	5.1	0.25	0.63
1.0	2.3	--	0.68
	4.0	--	0.70
	5.1	--	0.69

Furthermore, the downstream maximum does not occur at the trailing-edge bulkhead but is displaced a short distance upstream.

- Pressure minima for mode 3 are equally displaced toward the upstream; the displacement is more at $M_\infty = 0.8$ than at $M_\infty = 1.0$. Again, this indicates that the higher the external flow speed, the more the ideal hard-wall mode shapes are approached.

Specifically, minima appear at the following x/L locations:

MODE 3

M_∞	L/L	x/L		
		node 1 ideal 0.17	node 2 ideal 0.5	node 3 ideal 0.83
0.8	4.0	--	0.43	0.71
	5.1	--	0.38	0.71
1.0	4.0	--	0.43	0.78
	5.1	--	0.43	0.78

Furthermore, the trailing-edge bulkhead pressure maxima are displaced in the downstream direction.

- From the displacements of the pressure maxima and minima, we can derive that the cavity acts acoustically as an effectively shorter cavity. Qualitatively, the lower the Mach number of the external flow, the more the cavity behavior deviates from that of an ideal one-dimensional oscillator.
- From the standing wave patterns, we can define an effective reflection coefficient of the rear wall. This reflection coefficient does not indicate in a physical sense a true absorptive property of the rear bulkhead, but, rather, it is a measure of the relative magnitude of the pressure maximum/minimum ratio within each modal pattern.

The following "Reflection Coefficients" were determined, averaged over all L/D ratios ($2.3 < L/D < 5.1$):

M	Mode 1	Mode 2	Mode 3
0.8	0.40	0.55	0.50
1.0	0.28	0.76	0.40

As the reflection coefficient rises, the trailing-edge walls act harder acoustically. However, the qualitative nature of this conclusion should be emphasized, and no extrapolation of the above numbers is attempted at lower and higher Mach numbers.

6.5.6 Broadband Noise

Previously, it was discussed that flow-induced cavity noise is composed of both discrete and random (i.e., broadband) components. It was noted that broadband noise is substantially higher in the aft cavity region and relatively weak in the leading-edge area. Thus, an attempt was made to separate the broadband from the discrete sound, and to find some commonality for all broadband spectra in the trailing-edge region.

There is some speculation in deriving the broadband portion from a spectrum that contains both components. Figure 61 presents a subsonic ($M = 0.8$) and a supersonic ($M = 1.5$) cavity pressure spectrum, as measured through Sensor 7 (trailing-edge

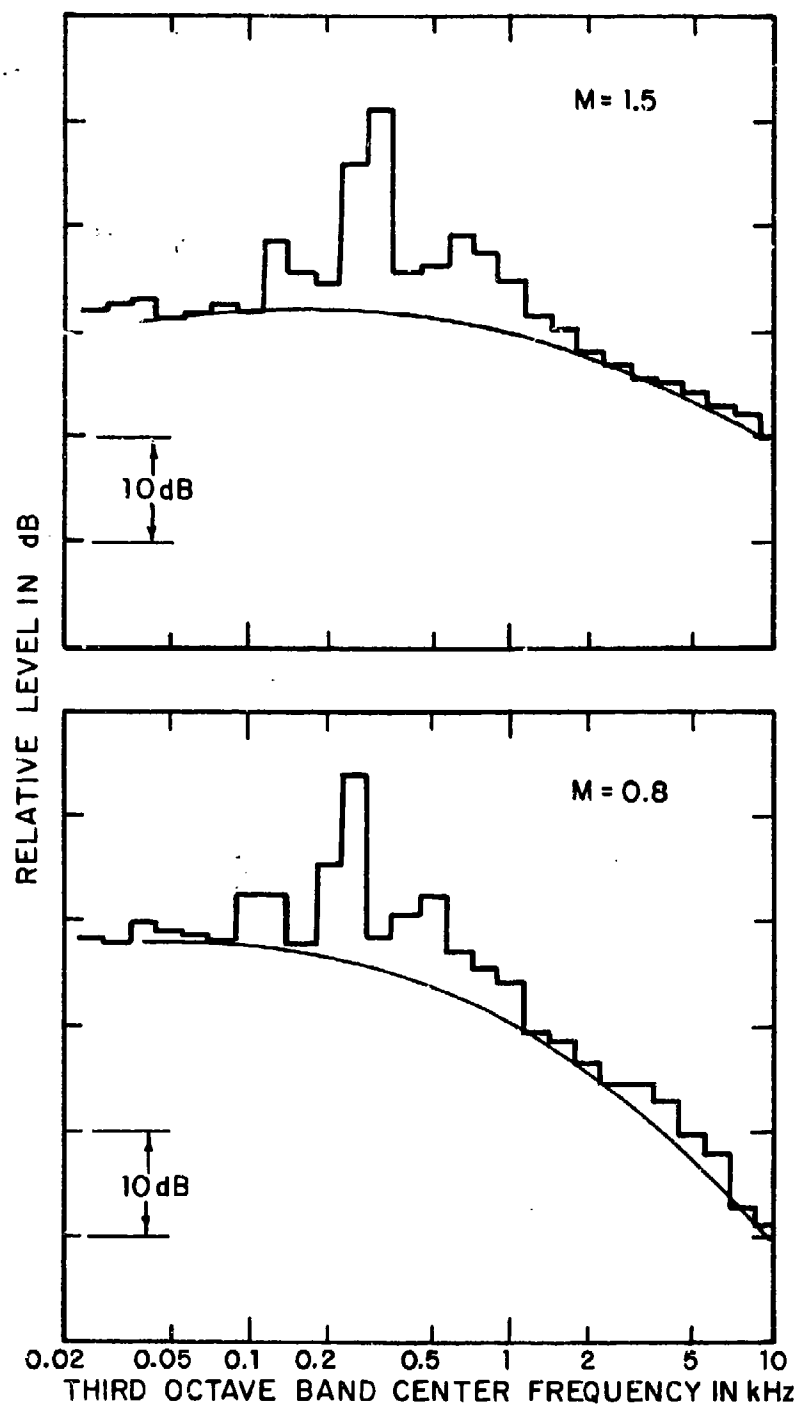


FIG. 61. DERIVATION OF BROADBAND NOISE SPECTRA.

bulkhead). These data pertain to the deep cavity ($L/D = 2.3$), where it was previously determined that only modes 1, 2, and 4 appear strongly. If we disregard those 1/3-octave bands, which contain the appropriate resonance frequencies, we can easily sketch a haystack-shaped "lower bound" spectrum that is attributable to the nondiscrete components. All trailing-edge spectra, encompassing the range $2.3 < L/D < 5.5$ and $0.8 < M < 2.0$, were obtained in this fashion. It was found that all broadband spectra [expressed in terms of $(20 \log p_{rms}/q_\infty)$ vs Strouhal number ($S = fL/U_\infty$)] fall within a range of about ± 2.5 dB, and that there is not any discernible dependence on Mach number in this Mach number range (Fig. 63).

Broadband noise levels in the leading-edge region were found to be at least 10 dB lower than at the trailing edge. A similar result was reported by Smith *et al.* (1974) in their flight test program.

6.5.7 Consecutive Cavities

A series of tests was conducted on two consecutive cavities as shown in Fig. 63. The cavities were formed by inserting a 1-in. thick center plate with the cavity floor in the topmost position, i.e., 6 in. down from the cavity mouth. Hence, two cavities, which were 17.5 in. long, 6 in. deep, and 9 in. wide, were formed. Thus, the L/D ratio of each is 2.9. Sensors 3 and 4 (see Fig. 38) are now located near the leading- and the trailing-edge bulkhead, respectively, of the upstream cavity; Sensors 5 and 6 are at corresponding locations in the downstream cavity.

Experiments were conducted at Mach numbers of 0.8, 0.9, 0.95, 1.0, 1.05, 1.1, 1.2, 1.5, and 2.0. Figure 64 presents an example of 1/3-octave band spectra at two corresponding measurement locations in both cavities for subsonic ($M = 0.8$) and supersonic ($M = 1.5$) Mach numbers. It is evident that spectra at corresponding locations are similar, with the same relative distribution of discrete and broadband energy.

A detailed plot of the change of nondimensional mode level with freestream Mach numbers in the range $0.8 < M_\infty < 2.0$ for the first three modes appears in Fig. 65. This figure shows the similar behavior of the upstream and downstream cavities. Levels in the leading-edge area are 3 to 9 dB lower than at the trailing edge.

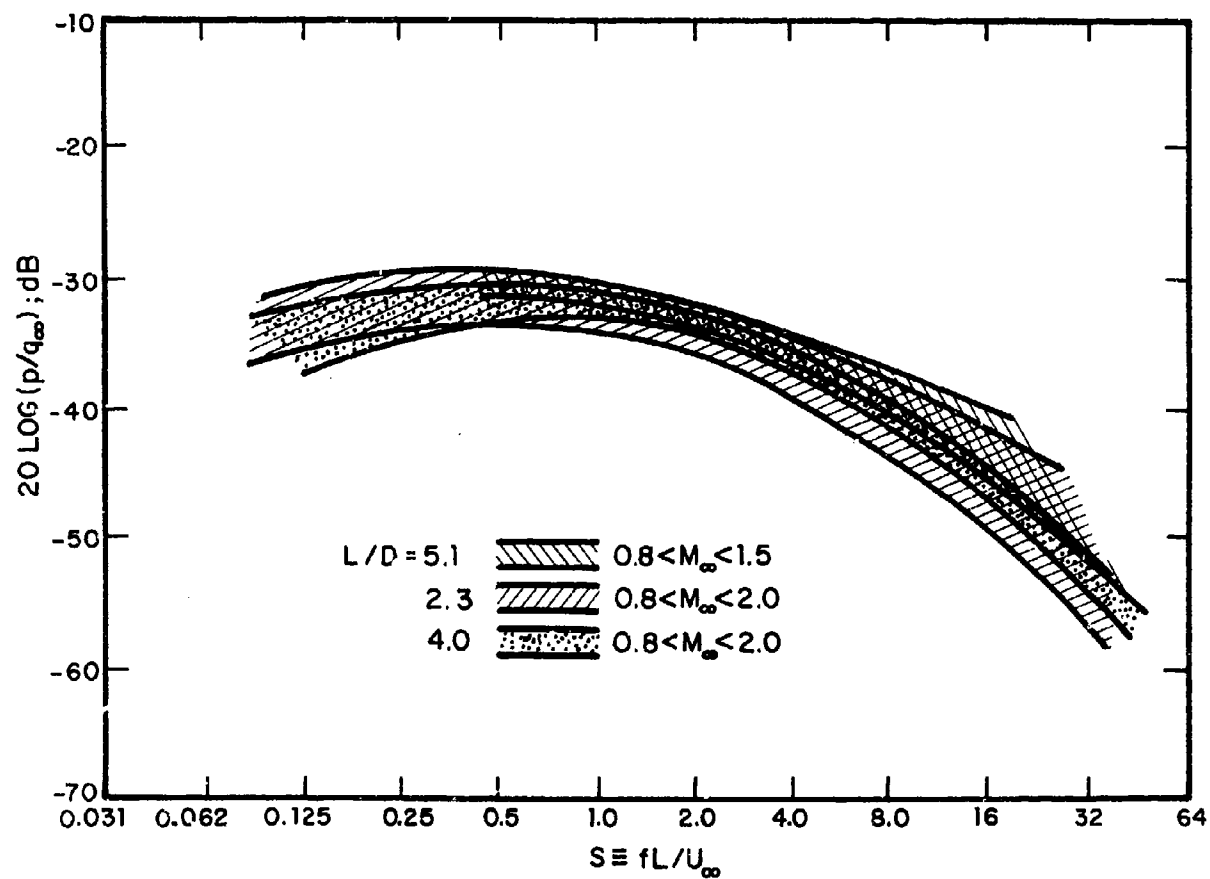


FIG. 62. ENVELOPE OF ALL NONDIMENSIONAL BROADBAND SPECTRA
IN 1/3-OCTAVE BANDS.



FIG. 63. CONSECUTIVE CAVITIES.

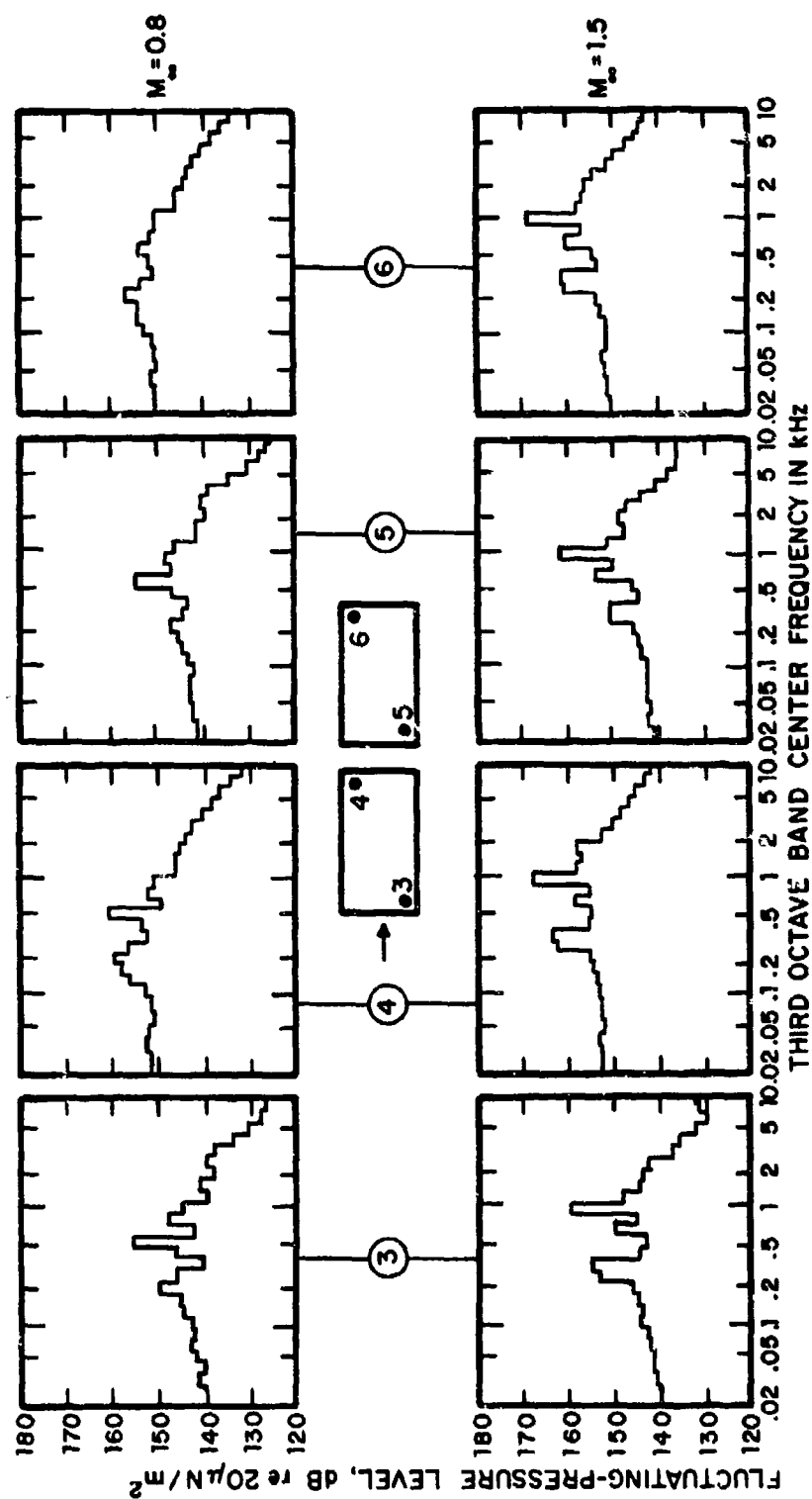


FIG. 64. SPECTRA IN CONSECUTIVE CAVITIES: $L = 17.5$ in., $L/D = 2.9$.

The results shown in Fig. 65 can be compared to Figs. 54 and 55, where the Mach number dependence of mode levels is shown for the single cavity. For the double cavity, the normalized levels seem to be somewhat lower than for the single cavity case. The significant difference between the single and the double cavity experiments is the relative width. For the single cavity, length-to-width ratio was 4; for the double cavity, it was about 1.9. Although the cavity oscillation phenomenon essentially has a two-dimensional nature (as documented in the independence of resonant frequencies from the length-to-width ratio), the levels are apparently affected by the width, since the proximity of the side walls is likely to influence the characteristics of the cavity internal recirculating flow. The water table experiments also indicated that consecutive cavities oscillate strongly in phase, largely independent of the width of the dividing wall. We are uncertain whether this finding pertains also to the conditions in air. However, the phase characteristics of consecutive cavities are important in the suppression of oscillations. Figure 65 presents motion picture frames from the water table experiments for consecutive cavities, indicating the in-phase oscillation process.

6.6 Aerodynamic Mean Drag

Flow-induced cavity drag was measured with the apparatus described in Sec. 5.2. Only data for subsonic flow speeds were obtained because of the limitations of the small-scale flow facility. The reason for these measurements was twofold: First, no reliable data exist for the drag of long and shallow cavities in flow for an approaching thin boundary layer; second, some information on the effect on drag of the oscillation suppression devices was desired to evaluate the drag penalty to be expected under flight conditions.

In a typical test run, the flow speed over the plate containing the cavity was increased from zero to about 600 ft/sec; thereafter, it was reduced back to zero. In each test, a continuous plot of the dc drag force vs the wall-jet total pressure was obtained. A typical plot appears in Fig. 67. Since both the drag force, D , and the total pressure, P_0 , in the flow are roughly proportional to U_∞^2 (up to about 600 ft/sec), a straight-line plot is obtained in a D vs P_0 linear-linear representation, where the slope is a measure of the drag force coefficient, C_D . Any change in slope indicates a change in the value of C_D .

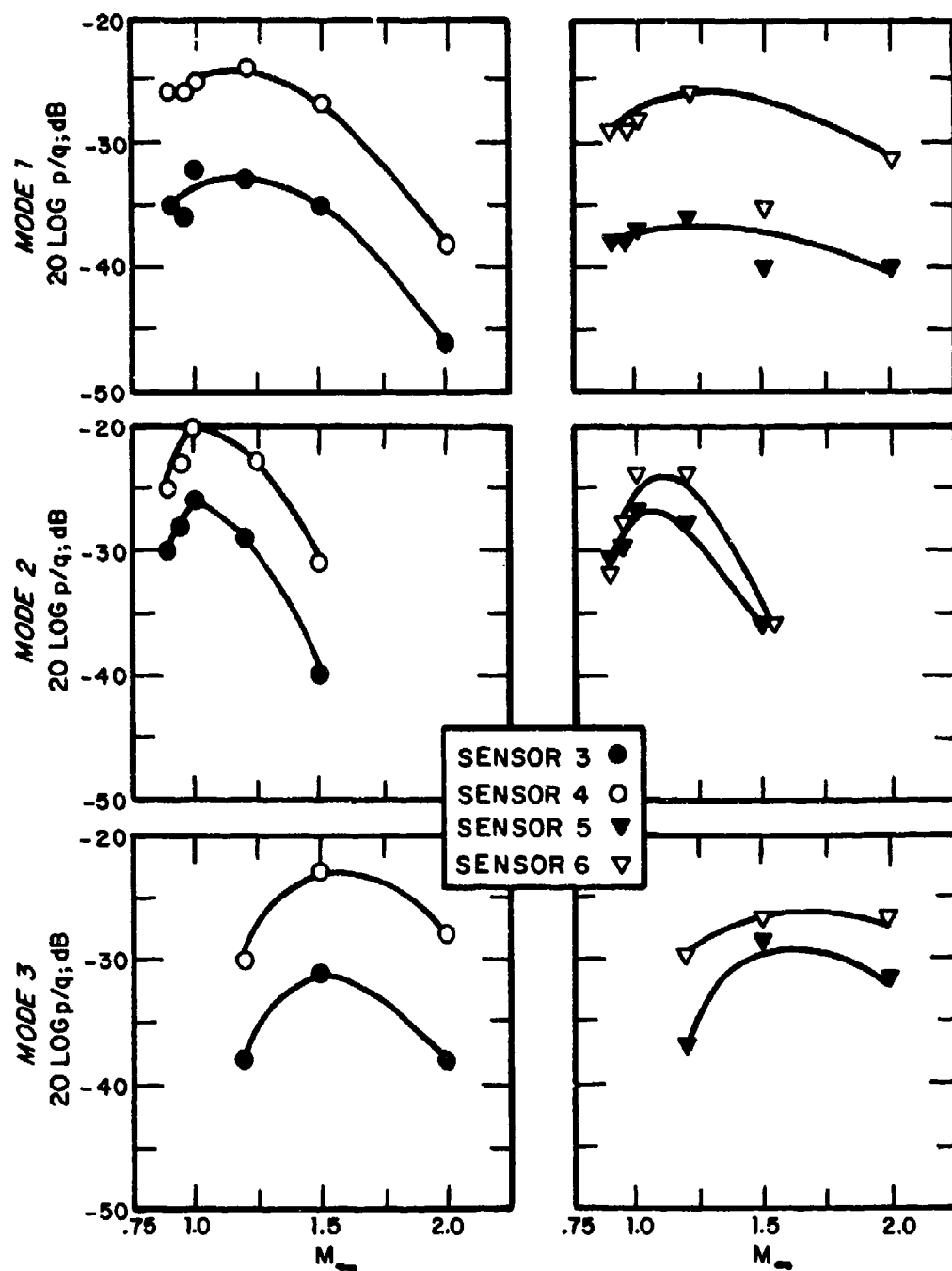


FIG. 65. NORMALIZED MODE LEVELS IN CONSECUTIVE CAVITIES
(for sensor location see Fig. 64).

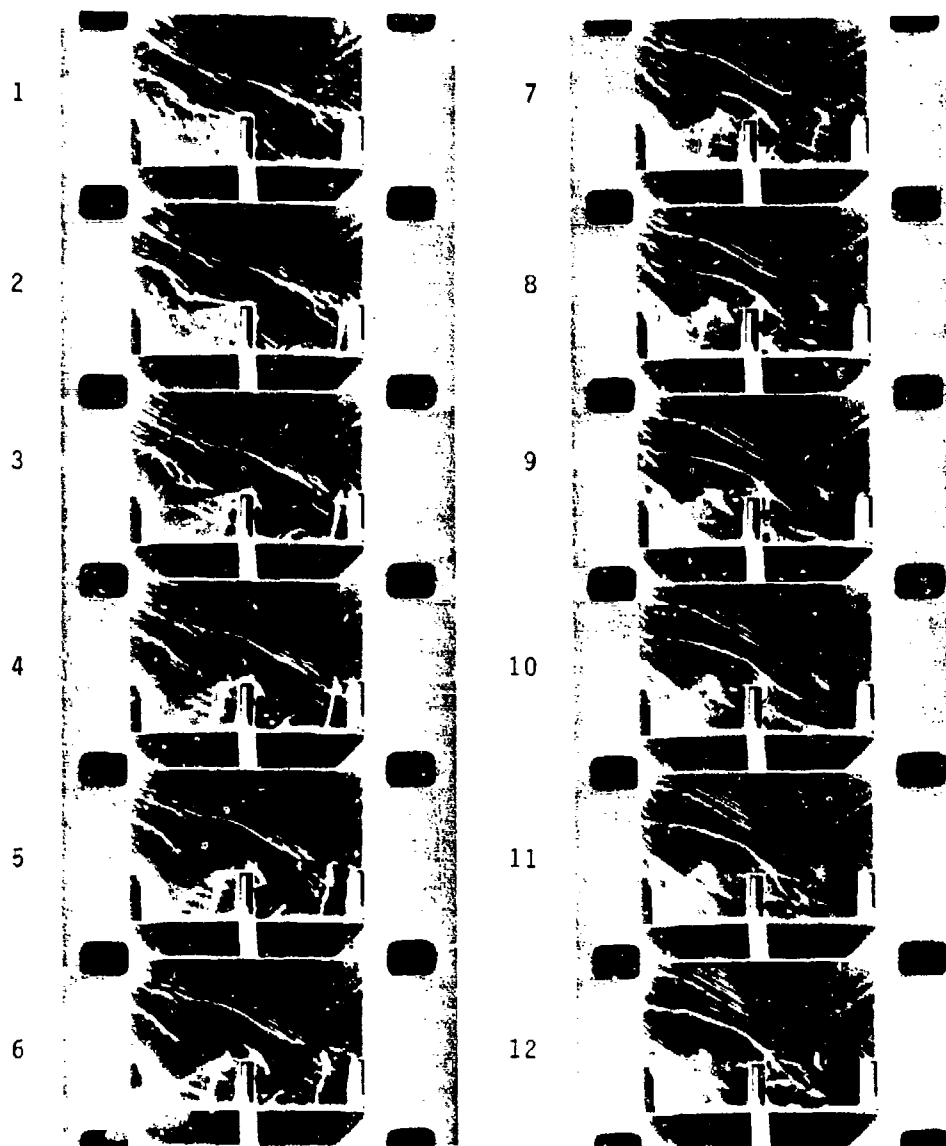


FIG. 66. WATER TABLE VISUALIZATION OF RESONATING CONSECUTIVE CAVITIES UNDER SIMULATED EXTERNAL SUPERSONIC FLOW $M_{\infty} = 1.5$.

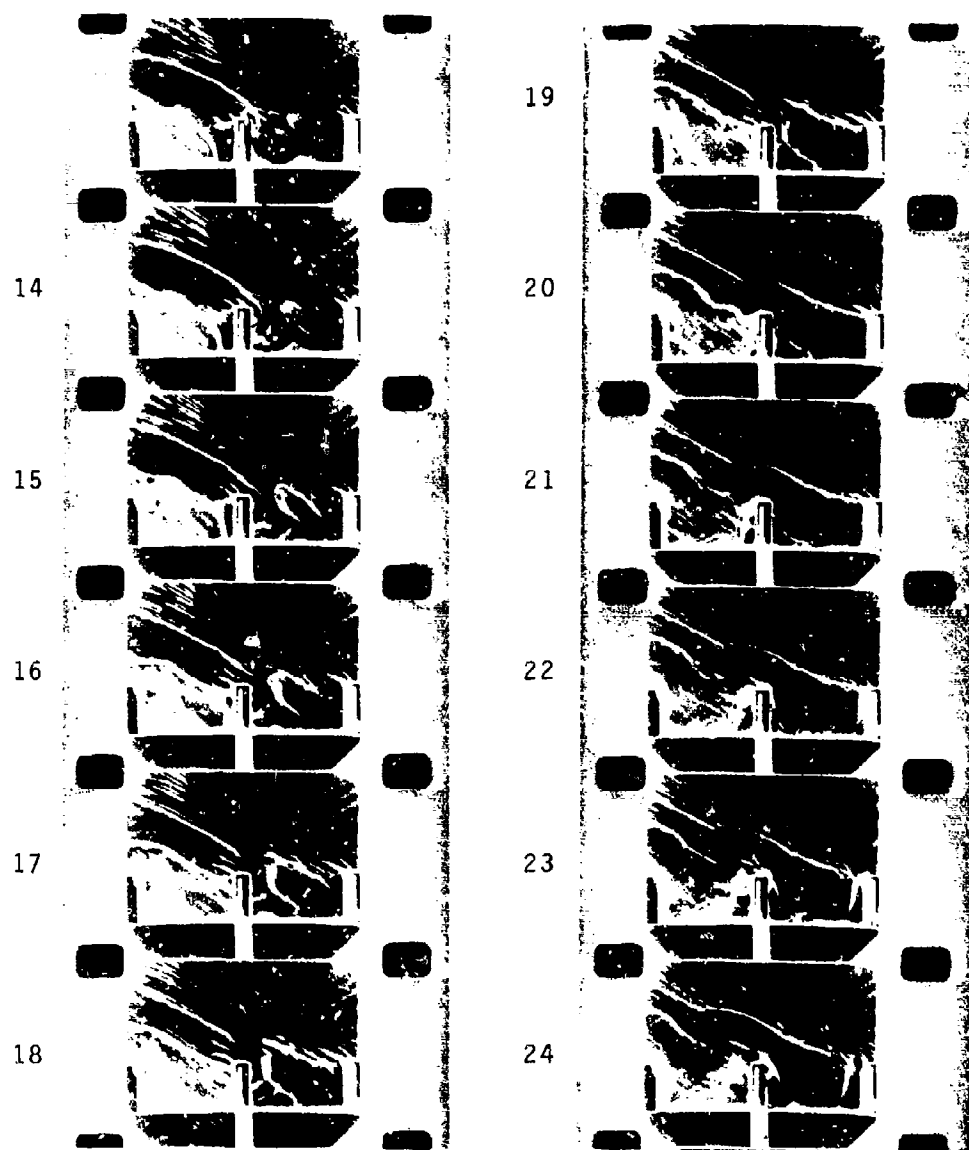


FIG. 66. (CONTINUED)

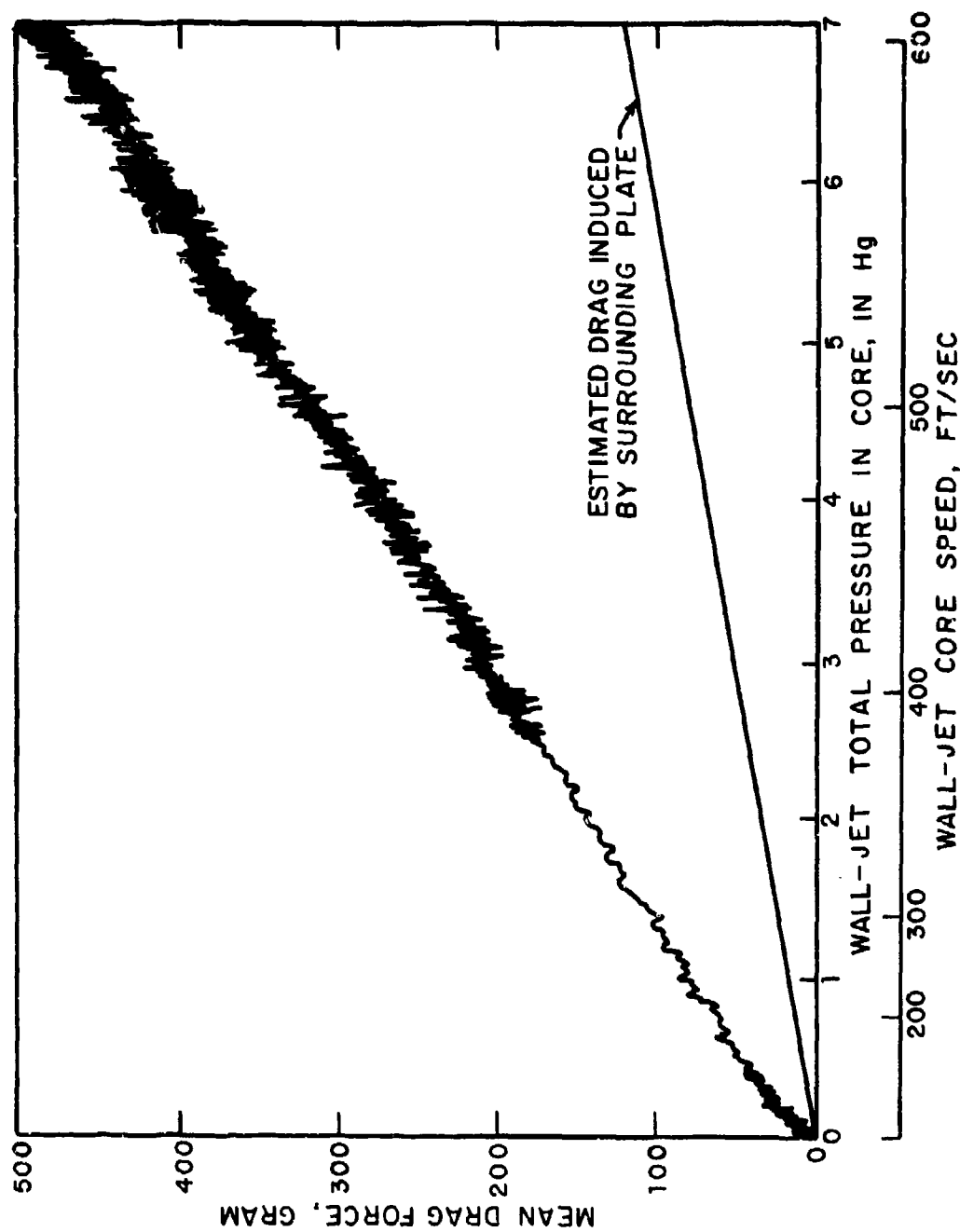


FIG. 67. TYPICAL TRACE OF FLOW-INDUCED CAVITY DRAG $L = 5.5$ in., $L/D = 2.2$. LAMINAR INFLOW.

The measured drag is composed of that which is induced by the cavity, and that which is due to the surrounding surface being under the highly turbulent mixing region of the wall jet. Since the cavity drag force and the plate drag force add to each other, the cavity contribution can be obtained by subtracting the plate contribution.

Cavities of various length-to-depth ratios were tested under laminar inflow conditions. Some test data were obtained for turbulent inflow, which was achieved by tripping the nozzle boundary layer at the nozzle exit.

A plot showing the drag coefficient vs length-to-depth ratio is shown in Fig. 68. The drag coefficient of the cavity is defined as

$$C_D = \frac{D_{\text{total}} - D_{\text{plate}}}{A_{\text{cavity}} \cdot q_{\infty}} \quad (6.2)$$

Here, D_{total} is the measured drag, D_{plate} is that portion of the drag attributable to the surrounding plate, A_{cavity} is the mouth area of the cavity, and $q_{\infty} \equiv 1/2 \rho U_{\infty}^2$ is the freestream dynamic pressure. The data in Fig. 68 are valid in a speed range from $0 < U_{\infty} < 600$ ft/sec. The determining factor for the drag coefficient seems to be the cavity L/D ratio, which causes drag maximum at an L/D value of 10. Fluid dynamic considerations indicate that the free shear layer over short deep cavities span the gap, resulting in a low-energy recirculating flow pattern. On the other hand, long shallow cavities allow the free shear flow to attach to the floor, causing only two weak recirculation regions near the leading-edge and trailing-edge bulkheads. Presumably, cavities with a certain critical length-to-depth ratio (evidently near 10), cause two strong recirculating regions near the leading- and the trailing-edge bulkhead with a relatively brief attachment region in between. This flow pattern causes high drag. Qualitative flow patterns appear in Fig. 68.

Figure 68 is qualitative in nature; the effect of cavity width is neglected, and the ratio of boundary layer to depth has not been considered. Although the cavity mouth area (length

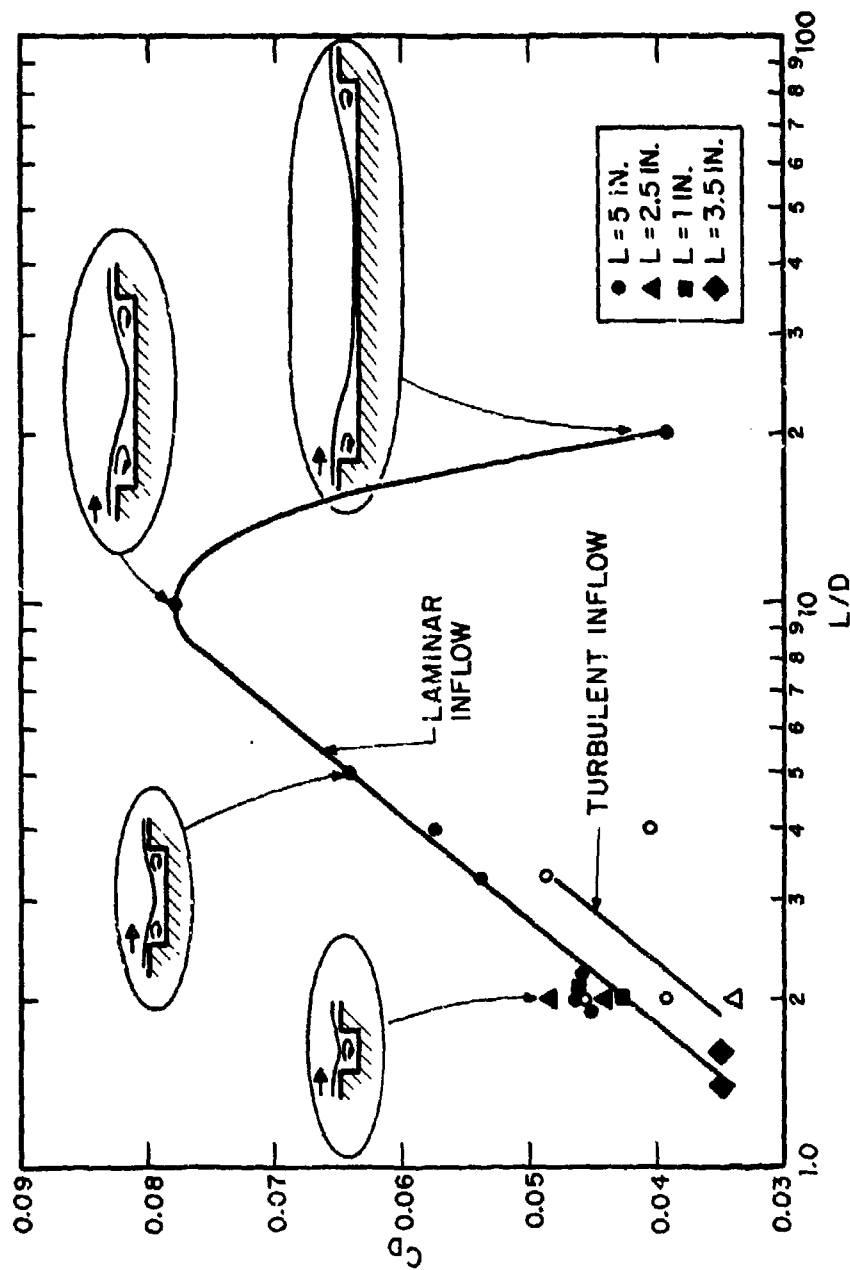


FIG. 68. LENGTH-TO-DEPTH RATIO DEPENDENCE OF CAVITY DRAG COEFFICIENT FOR $M_\infty < 0.6$.

times width) was found to be a good normalizing parameter,* the width-to-length ratio may be just as important as the length-to-depth ratio in determining the actual cavity drag. However, Fig. 68 could be used to obtain rough estimates of the drag of long† shallow cavities at fairly low subsonic speeds for approaching thin laminar boundary layers.

Some data points (open marks) in Fig. 68 pertain to turbulent inflow. They indicate that turbulent inflow causes less cavity drag than laminar inflow.

6.7 Wake Flow Characteristics

The flow downstream of a resonating cavity is highly disturbed. As discussed previously, the shear layer above the cavity oscillates about the cavity trailing edge and periodically ejects fluid mass into the downstream flow field. Thus, there are both mean (or average) and unsteady velocity components in the downstream flow field. The mean-velocity profile, which shows a velocity deficit downstream of the cavity, provides information about the steady-state drag and the wake thickness, i.e., the region above the cavity within which the wake flow represents a disturbance to the mean flow.

Velocity profiles on the cavity centerline were measured with the aft total pressure rake. Figure 69 shows results for $M_\infty = 1$ and $M_\infty = 2$; both profiles contain data on cavities with a length-to-depth ratio of $2.3 < L/D < 5.5$. Qualitatively, the Mach-2 flow profile indicates a much thinner disturbance region for the downstream flow. This is consistent with the smaller dimensions of the approaching boundary layer at Mach 2; it is also consistent with the lower amplitudes of the resonant mode levels at Mach 2, as documented in Figs. 54 through 56. A free shear layer above a cavity is known to become more stable (and stiffer) with increasing supersonic Mach numbers. Hence, we would expect the induced mean drag to decrease with increasing Mach number.

*McGregor, 1969, in his thesis on cavity drag under thick shear layer uses the cavity mouth area successfully as a normalizing parameter into the drag coefficient.

†The term "long" indicates that the length of the cavity is greater than the width, by a factor of 2 to 5.

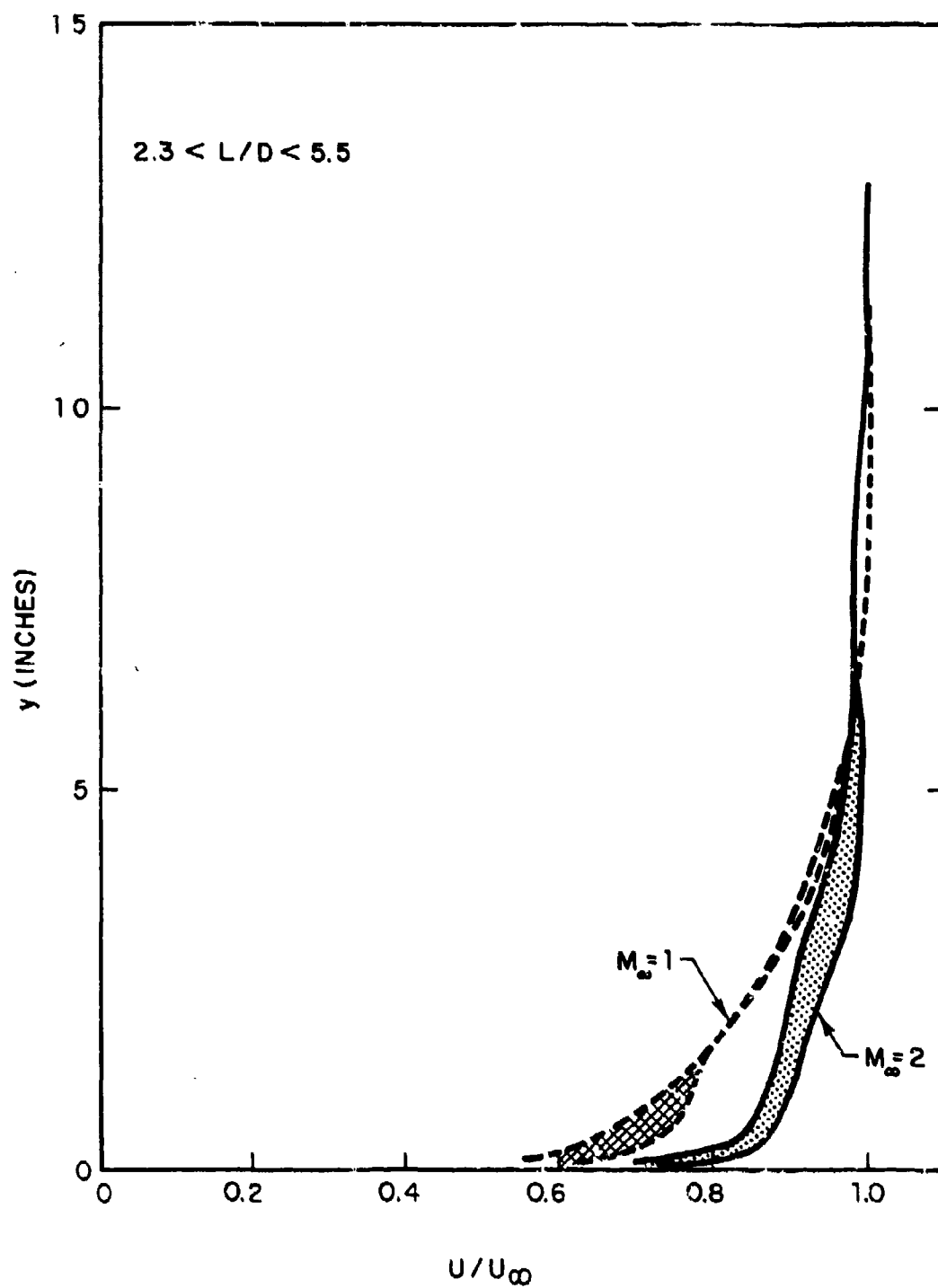


FIG. 69. VELOCITY PROFILES DOWNSTREAM OF CAVITY

Smoothed velocity profiles at the leading edge (forward rake) and downstream of the trailing edge (aft rake) indicate the growth rate of the shear layer above a (resonating) cavity for Mach-1 flow (Fig. 70). The boundary layer thickness increases roughly by a factor of 7 along the cavity length.

By using the momentum thicknesses determined from the upstream and downstream boundary layer rakes, it is possible to make an estimate of that portion of the cavity drag which appears as a momentum deficit in the boundary layer. This can only be an estimate because the downstream rake was located only on the cavity centerline; therefore, no information is available as to the variation of the downstream momentum thickness over the cavity width. Furthermore, the downstream rake was too close to the cavity trailing edge for the pressure in the boundary layer to reach equilibrium; this possibility adds another uncertainty to the calculation. In addition, in order to compute the total drag, the wave drag component would also have to be accounted for, which has not been done.

If D_d is the drag component due to the momentum deficit appearing in the boundary layer, we have

$$D_d = 2\left(\frac{1}{2}\rho U_\infty^2\right) (\delta_{M2} - \delta_{M1}) \cdot W = \frac{1}{2}\rho U_\infty^2 (L-W) C_D, \quad (6.3)$$

where δ_{M1} and δ_{M2} are the upstream and downstream momentum thicknesses, respectively, C_D is a drag coefficient referenced to the cavity mouth area, with L the cavity length, and W its width.

Table II lists the drag coefficients at transonic and supersonic flow speeds for three L/D ratios, as derived from the momentum thickness detriment. The transonic/supersonic drag coefficients are lower than those determined in the small-scale experiments for subsonic speeds. However, it should be noted, that the wave drag component is not included.

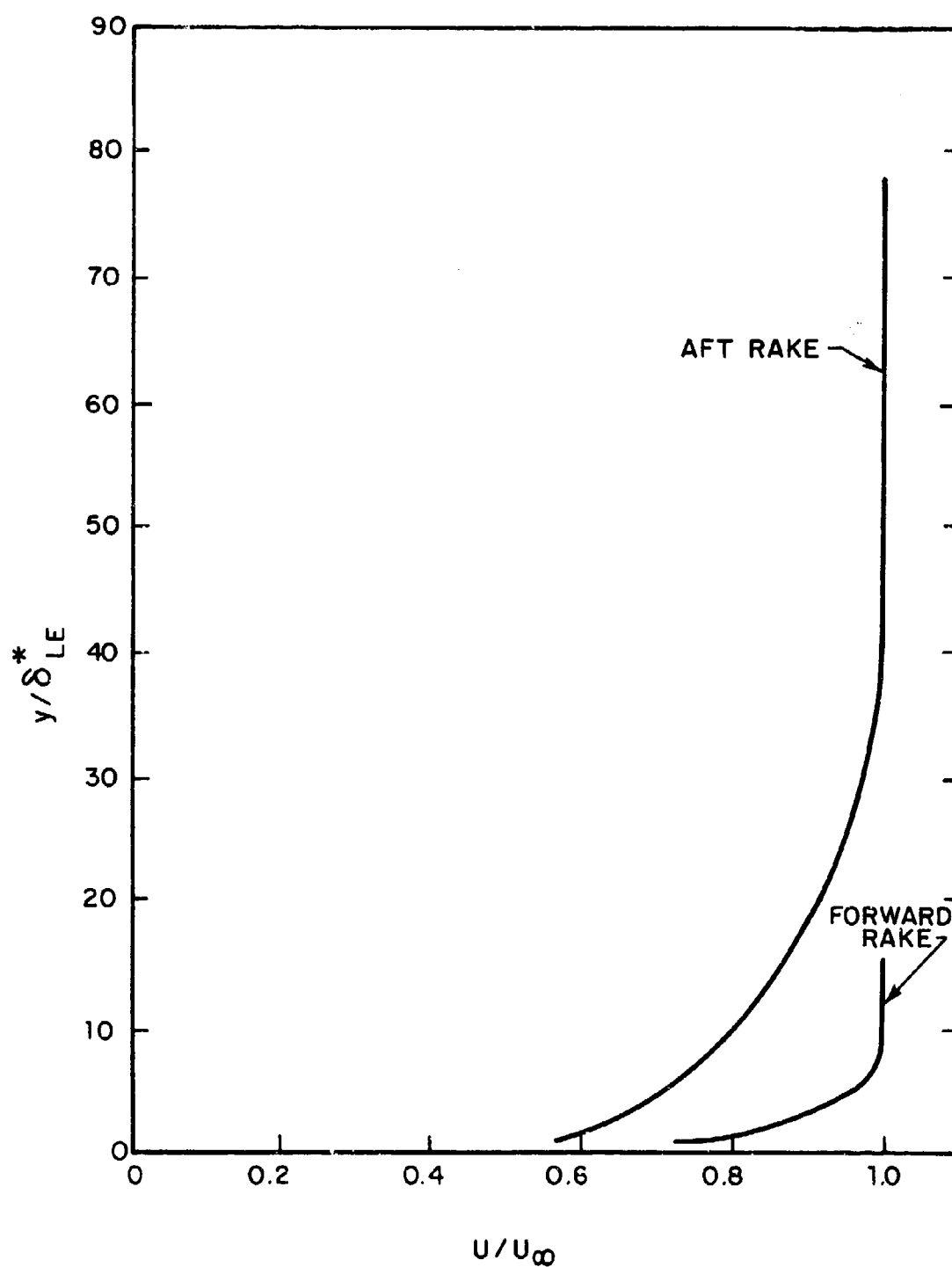


FIG. 70. COMPARISON OF UPSTREAM AND DOWNSTREAM VELOCITY PROFILES AT $M_\infty = 1$.

TABLE II. CAVITY-DRAG COEFFICIENTS AT
TRANSONIC/SUPERSONIC SPEEDS

M_∞	L/D	δ_{M1} (in.)	δ_{M2} (in.)	$C_D = 2 \frac{(\delta_{M2} - \delta_{M1})}{L}$
2.0	2.3	0.032	0.463	0.024
2.0	4.0	0.034	0.449	0.023
2.0	5.5	0.033	0.399	0.020
1.5	5.5	0.062	0.373	0.017
1.5	4.0	0.058	0.501	0.025
1.5	2.3	0.055	0.572	0.029
1.2	2.3	0.066	0.612	0.030
1.2	4.0	0.064	0.576	0.028
1.2	5.5	0.065	0.429	0.020
1.1	5.5	0.078	0.469	0.022
1.1	4.0	0.075	0.605	0.029
1.1	2.3	0.081	0.618	0.030
1.05	2.3	0.072	0.692	0.034
1.05	4.0	0.082	0.665	0.032
1.05	5.5	0.081	0.476	0.022

6.8 Prediction Approaches

The following methods are proposed for the prediction for resonant mode frequencies and amplitudes within the cavity space.

6.8.1 Frequency Prediction

Resonant frequencies can be accurately predicted with the Rossiter equation as modified by Heller *et al.* (1970). The present research data, as well as flight test data reported by Smith *et al.* (1974) and data from another large-scale wind tunnel experiment conducted by Maurer (1974), show conclusively that the modified Rossiter equation is the best available expression to compute resonant frequencies in the Mach number range $0.5 < M < 3.0$.

Figure 52 shows Eq. 6.1 in a graphic form. Although a dependence of mode frequency on length-to-depth ratio exists (see Sec. 6.5.3), it is pointless to enter this complexity in Eq. 6.1, since the variation of mode frequencies for shallow cavities ($L/D > 2$) is quite small.

6.8.2 Level Prediction: Resonant Frequencies

In Fig. 57, the levels of modes 1, 2, and 3 are presented for the leading-edge and the trailing-edge regions, respectively, referenced to the freestream dynamic pressure as a function of freestream Mach number. This detailed information, which also accounts for the length-to-depth ratio, represents a substantial improvement in the accuracy of prediction levels.

6.8.3 Level Prediction: Broadband Noise

Broadband noise within a Mach number range of $0.8 < M_\infty < 2.0$ near the trailing edge can be predicted on the basis of Fig. 62, where a nondimensional $1/3$ -octave band spectrum is presented. Broadband noise was found to be a weak function of the length-to-depth ratio. Furthermore, as a rule of thumb, broadband noise levels decrease by about 10 dB in a linear fashion towards the leading edge.

6.8.4 Mode Shape Prediction

The complexity of mode shape prediction is documented in Figs. 59 and 60. These mode shapes were obtained within the free cavity volume rather than at the cavity floor. Data obtained along the cavity floor by Shaw *et al.* (1974), which used a cavity with a length-to-depth ratio of 4, and data by Heller *et al.* (1970) are presented in Fig. 71. These data points can be described by an empirical equation, which is developed below.

The "standing wave pattern" for each longitudinal mode in the cavity can be described by a cosine relationship. It is assumed that the pressure intensities increase exponentially from the leading to the trailing edge. Furthermore, it is assumed that the physical location of the trailing-edge bulkhead does not correspond to the acoustically effective trailing-edge bulkhead. This assumption follows both from physical considerations and from the pseudopiston analysis advanced in Sec. 4. From the data presented in Fig. 71, it seems that the acoustically effective trailing-edge bulkhead is located some distance upstream of the actual trailing-edge bulkhead.

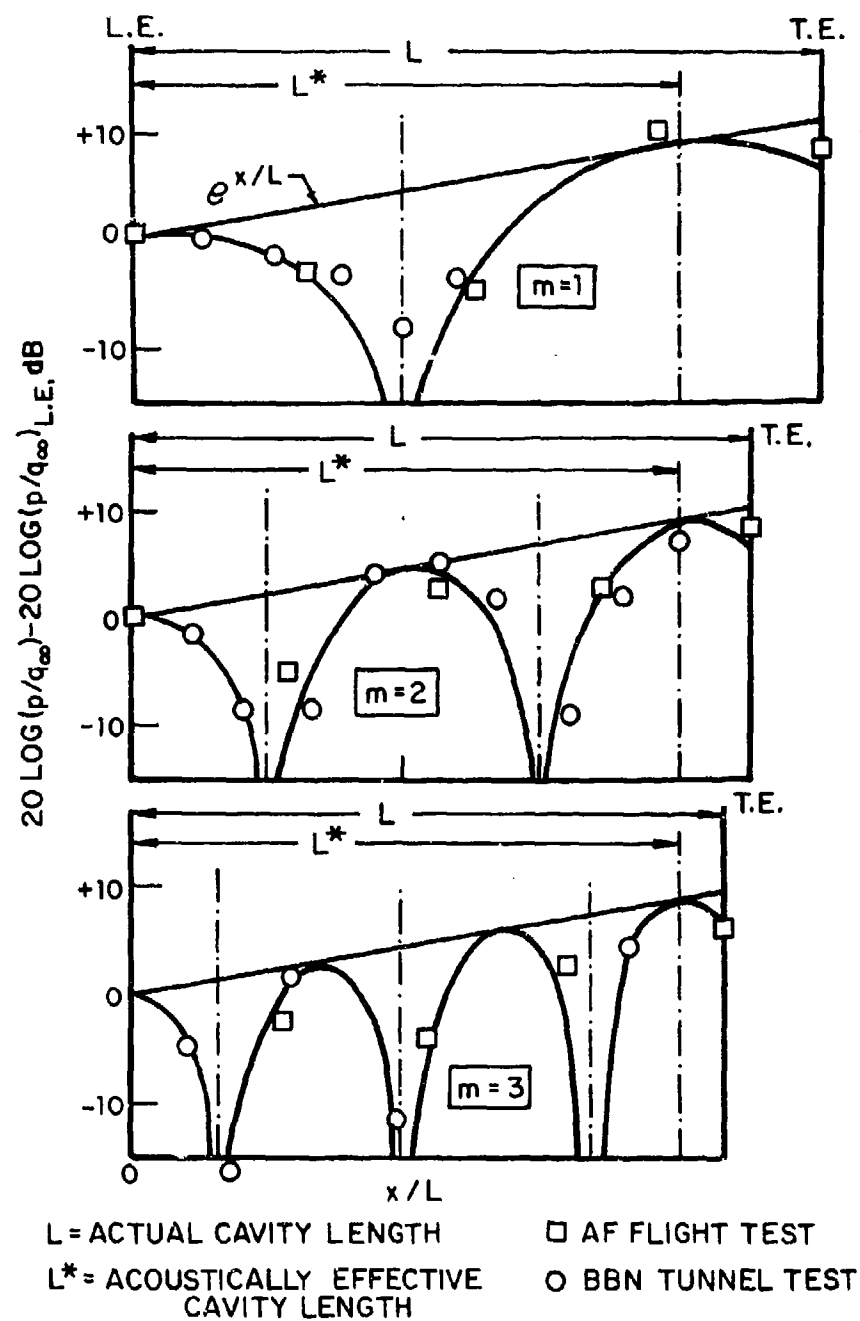


FIG. 71. COMPARISON OF MEASURED AND PREDICTED MODE SHAPES.

Thus, we define $L^* = mL/(m+\alpha)$, where L^* is the acoustically effective cavity length, m is the mode number, and α is the empirical constant in the modified Rossiter equation. The constant is ≈ 0.25 for cavities of $L/D = 4$.

Thus, the mode shape in the cavities should be described in logarithmic form as

$$20 \log(p/q_\infty) - 20 \log(p/q_\infty)_{L.E.} = 20 \log \left[e^{a \frac{x}{L^*}} \left| \cos\left(\frac{x}{L^*} \cdot m \cdot 180\right) \right| \right] \quad (6.4)$$

Here (p/q_∞) is the rms pressure normalized with the freestream dynamic pressure; $(p/q_\infty)_{L.E.}$ is the normalized rms pressure at the leading edge; a determines the exponential growth rate, and x/L^* is the lengthwise position in the cavity, normalized with the acoustically effective cavity length L^* .

The agreement of the proposed analytical experiment with this set of data points is considered rather good, considering the vastly different experimental conditions. In particular, mode-1 mode shapes as measured in the Air Force flight test (Smith *et al.*, 1974) are extremely well described by the proposed formulation. In a logarithmic representation, levels at the nodal points go to $-\infty$. In this representation, a direct exponential growth was assumed, i.e., the exponent a was taken as unity. However, it is possible that the actual growth rate is a function of Mach number and length-to-depth ratio; in mode 3, as depicted in Fig. 71, the growth rate seems to be slower.

It should be possible to obtain agreement of the measured mode shapes as presented in Figs. 59 and 60 by assuming a different growth rate a , and an appropriate value of the length-to-depth ratio dependent quantity α . However, because of the highly empirical nature of the above approach and the general insufficiency of data, no mode shape prediction scheme is offered.

SECTION 7

TEST RESULTS: OSCILLATION SUPPRESSION

7.1 Conceptual Consideration

The analytical considerations presented in the previous sections suggest several potentially successful concepts to minimize the amplitude of cavity pressure oscillation or to eliminate the occurrence of oscillations altogether.

From our understanding of the physical mechanism of pressure oscillations, any of the following methods should affect the oscillation process:

- Introduction of vorticity into the shear layer.
- Suppression of the feedback mechanism.
- Forcing of the approaching shear layer at a frequency that is different from the natural oscillation frequency.
- Change of the phasing of the cavity internal pressure wave propagation.

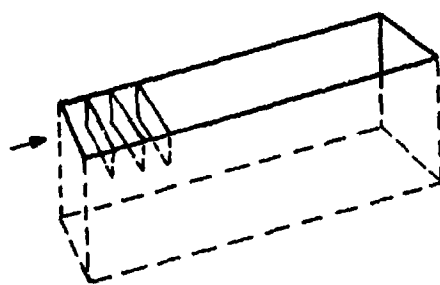
Implementation of these concepts requires geometric changes; to be practical, these changes should not reduce the usable cavity volume. Furthermore, any suppression device should be simple and not result in an excessive weight or drag penalty.

Many configurations were tested in the small-scale wall-jet and the water table facilities before a few selected concepts were evaluated in the large-scale tunnel.

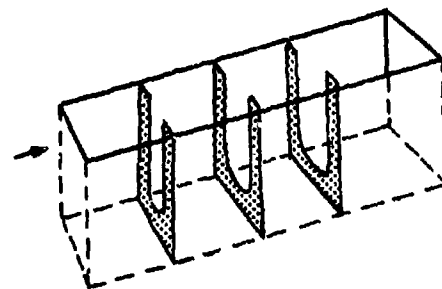
7.2 Unsuccessful Concepts

Figure 72 presents several concepts that did not reduce oscillatory amplitudes, or that sometimes even caused higher levels than observed in the basic cavity. Concepts (a) through (d) were evaluated at subsonic speeds ($M < 0.5$); concepts (e) and (f) were evaluated at subsonic and supersonic speeds ($0.8 < M < 1.5$).

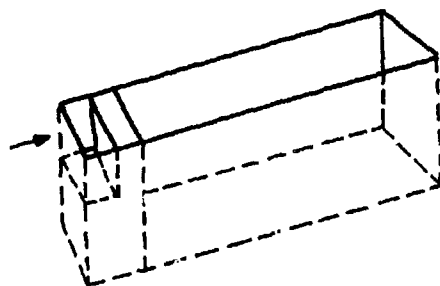
Cavity Internal Transverse Spoilers (Fig. 72a). It was thought that several transverse spoilers would interrupt the process of shear layer oscillation at the leading edge each time that the shear layer dives into the cavity volume. Apparently, however, the layer assumes a new streamline above the spoilers, and the oscillation process is maintained.



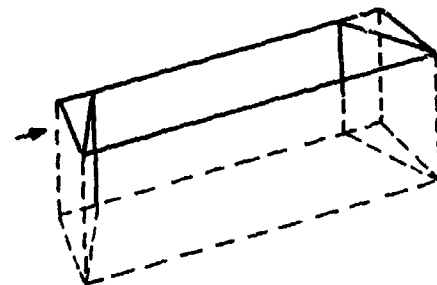
(a)



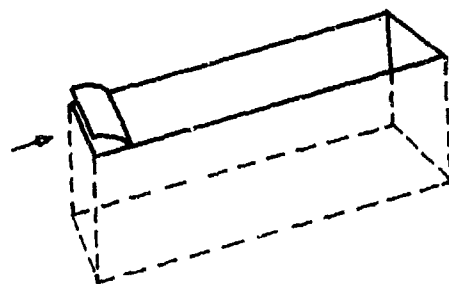
(b)



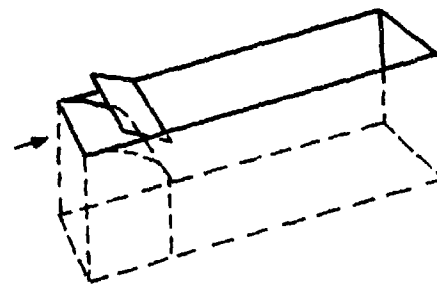
(c)



(d)



(e)



(f)

FIG. 72. PERSPECTIVE REPRESENTATION OF UNSUCCESSFUL SUPPRESSION CONCEPTS.

Internal Baffles (Fig. 72b). Insertion of perforated baffles with an open center portion was thought to interrupt the process of the feedback mechanism. However, the prevention of wave propagation along the cavity rims does not discourage oscillations.

Upstream Spoiler Cavity (Fig. 72c). Although the upstream spoiler cavity was strongly resonating, and, therefore, should cause a highly disturbed wake flow into the main cavity, no reduction in tone level was observed.

Oblique Leading- and Trailing-Edge Bulkheads (Fig. 72d). Oblique leading- and trailing-edge bulkheads were thought to offset the phasing of the internal pressure wave reflection at the leading-edge bulkhead, and/or spread the generation process of the upstream traveling pressure wave near the trailing-edge bulkhead over a certain time period. Thus, the oscillatory process would be randomized, which should result in less pronounced discrete tones. However, no reduction in tone level was observed.

Leading-Edge Air Entrainment (Fig. 72e). Forced fluid entrainment at the leading edge was thought to counteract the motion of the recirculating trapped vortex. However, no favorable effect was observed, probably because only a small region of recirculating flow occurred close to the leading-edge bulkhead. This left the main flow pattern essentially unaffected.

Rounded Leading-Edge Bulkhead in Conjunction with Guidevane (Fig. 72f). It was suspected that the guidevane over a sharp leading-edge corner (Fig. 72e) would not permit enough fluid flow to enter the cavity volume to counteract the recirculating internal flow, which would, thus, discourage oscillation. Therefore, a more favorable flow passage in the forward section was constructed by rounding the leading-edge bulkhead with an essentially flat guidevane above (Fig. 72f). This setup allowed variation of the gap width by moving the vane in a vertical direction, thus varying the amount of fluid entrainment.

With the vane in the lowest position, the oscillation amplitudes were large; in fact, discrete tone levels exceeded those of the basic rectangular cavity. When the vane was moved into the freestream flow, the discrete frequencies disappeared, but the broadband noise level increased substantially; thus, the primary purpose of reducing cavity noise levels was defeated.

7.3 Successful Concepts

The successful reductions of oscillatory amplitudes were based either on the stabilization of the shear layer, the prevention of the periodic mass-exchange process, or on a combination of both. Shear layer stabilization is achieved by two means: either through introduction of vorticity into the shear layer through upstream spoilers, or by provision of an inherently stabilizing trailing-edge shape. Prevention of the mass-exchange process is achieved through a detached trailing-edge cowl.

Figure 73 contains sketches of successful configurations, and Figs. 74 through 76 give the dimensional information. These configurations are: leading-edge spoilers, trailing-edge slant, leading-edge spoilers together with trailing-edge slant, and detached trailing-edge cowl.

These configurations were evaluated in the NASA Lewis 8 x 6 ft tunnel for a variety of freestream Mach numbers and cavity length-to-depth ratios. The setup allowed variation of the spoiler angle of attack over a 360° range. The spoilers were always counter-rotated in order to maintain symmetry of the shed vortex wake structure. The trailing-edge cowl (basically a thick airfoil) could be adjusted in its vertical position. Both the spoilers and the cowl could be adjusted during tunnel operation, so that optimization of their positions was possible. Figures 77 through 83 present the test results.

The data showing the effect of oscillation suppression devices have been presented in 1/3-octave bands. If narrowband analysis had been employed in the data reduction, the difference between peak levels of unmodified cavities and cavities with oscillation suppression devices would have been even more pronounced.

7.3.1 Shear Layer Stabilization

Figure 77 shows the effect of deployed spoilers on the sound signature near the leading edge (Sensor 3, see Fig. 36) at a subsonic Mach number ($M = 0.9$) for length-to-depth ratios of 2.3, 4.0 and 5.1. Optimum reduction of the dominant mode 2 tone at 250 Hz is achieved for the $L/D = 2.3$ cavity, when the spoilers are at 45° . The tone level is reduced by 20 dB. For the shallower cavities, spoiler angles between 45° and 90° have similar effects, and the tones are effectively suppressed. Spoilers deployed at 45° reduce tone levels also at supersonic speeds ($M = 1.5$), as shown in Fig. 78.

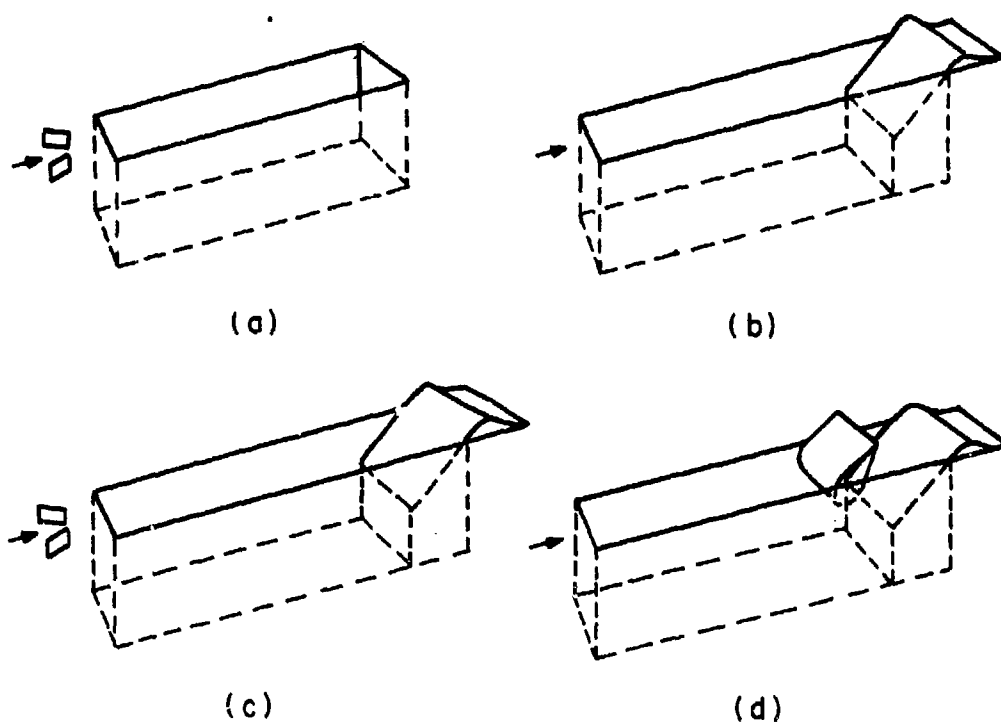
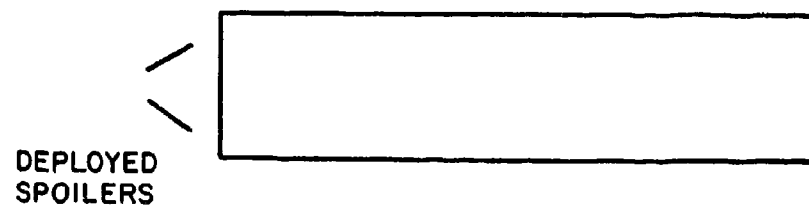
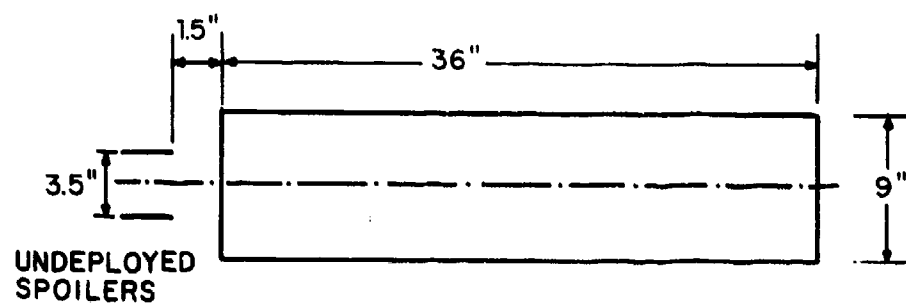
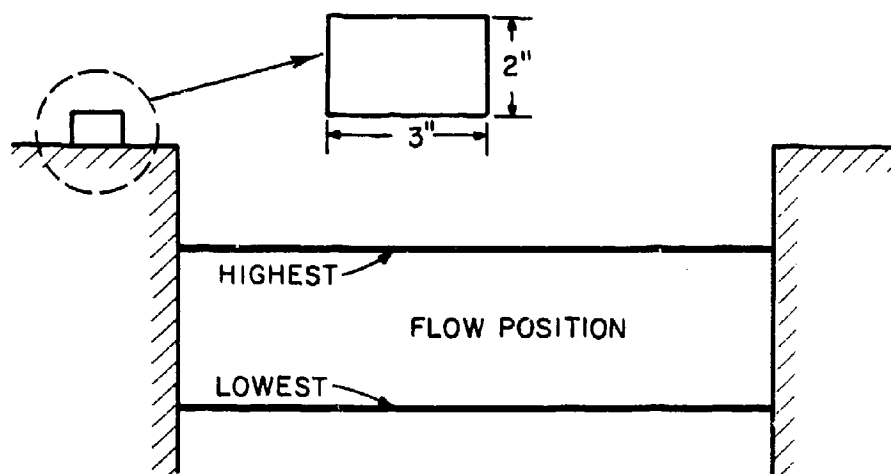


FIG. 73. PERSPECTIVE REPRESENTATION OF SUCCESSFUL SUPPRESSION CONCEPTS.

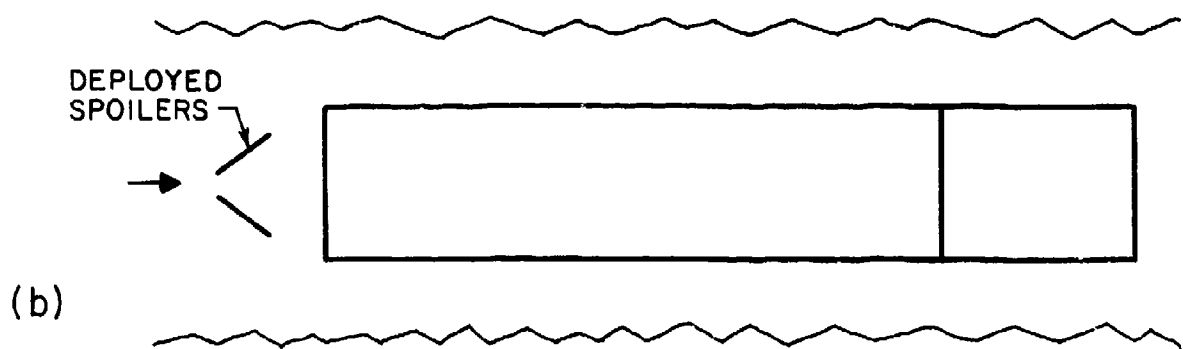
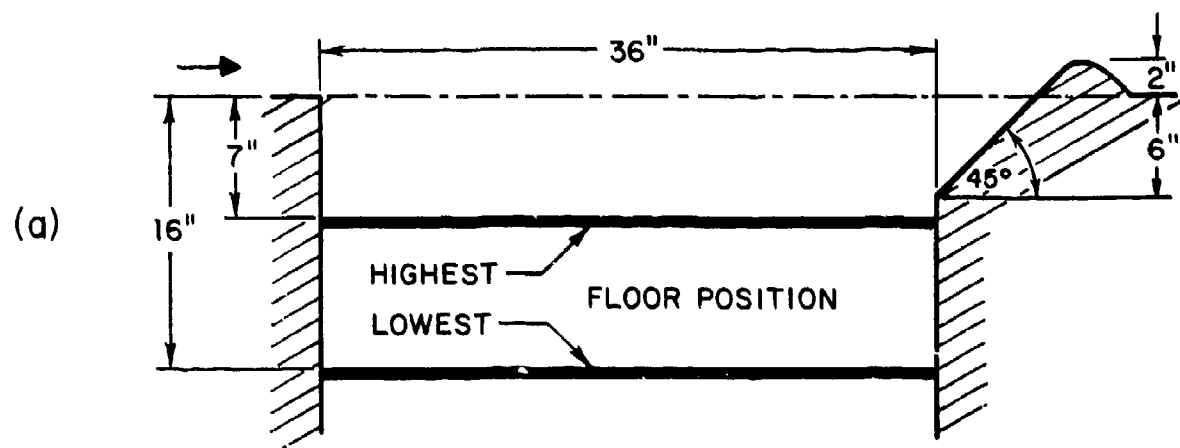


PLAN VIEWS



SIDE VIEW

FIG. 74. BOUNDARY LAYER SPOILERS.



PLAN VIEW



SIDE VIEW

FIG. 75. TRAILING-EDGE SLANT (a) WITHOUT AND (b) WITH UPSTREAM SPOILERS.

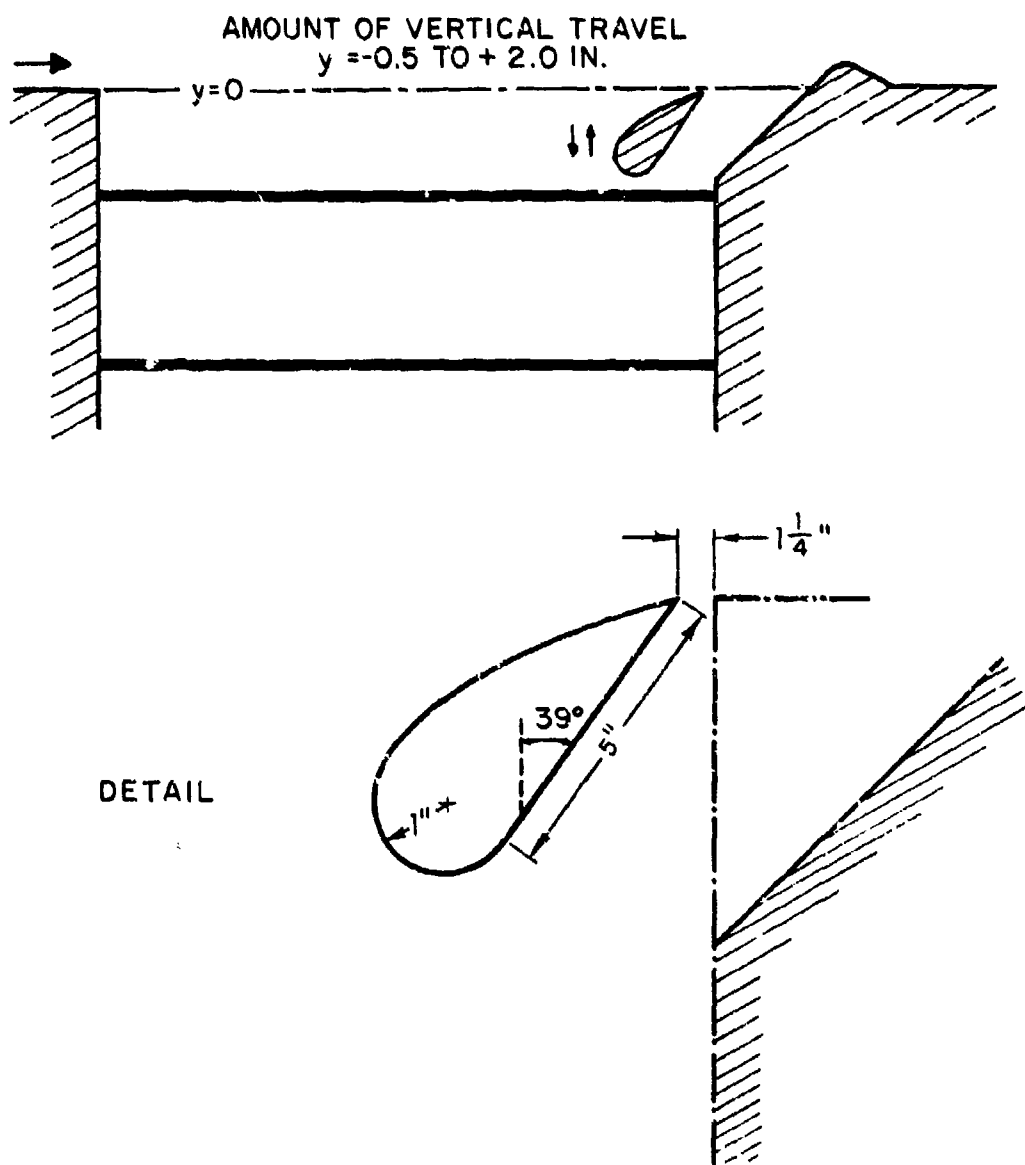


FIG. 76. DETACHED TRAILING-EDGE COWL AND TRAILING-EDGE SLANT.

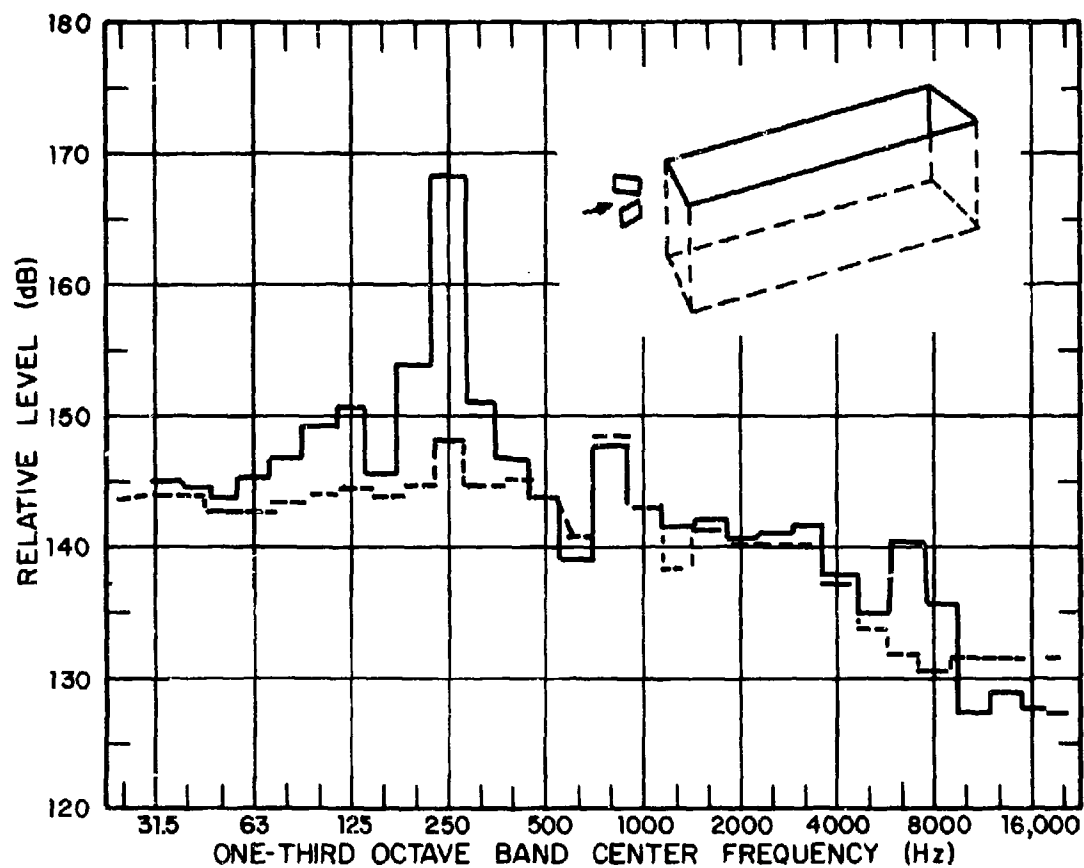


FIG. 77a. EFFECT OF UPSTREAM SPOILERS AT 45° ANGLE OF ATTACK ON LEADING-EDGE BULKHEAD PRESSURE SIGNAL: $M_{\infty} = 0.9$; $L/D = 2.3$ (continuous line refers to unmodified cavity).

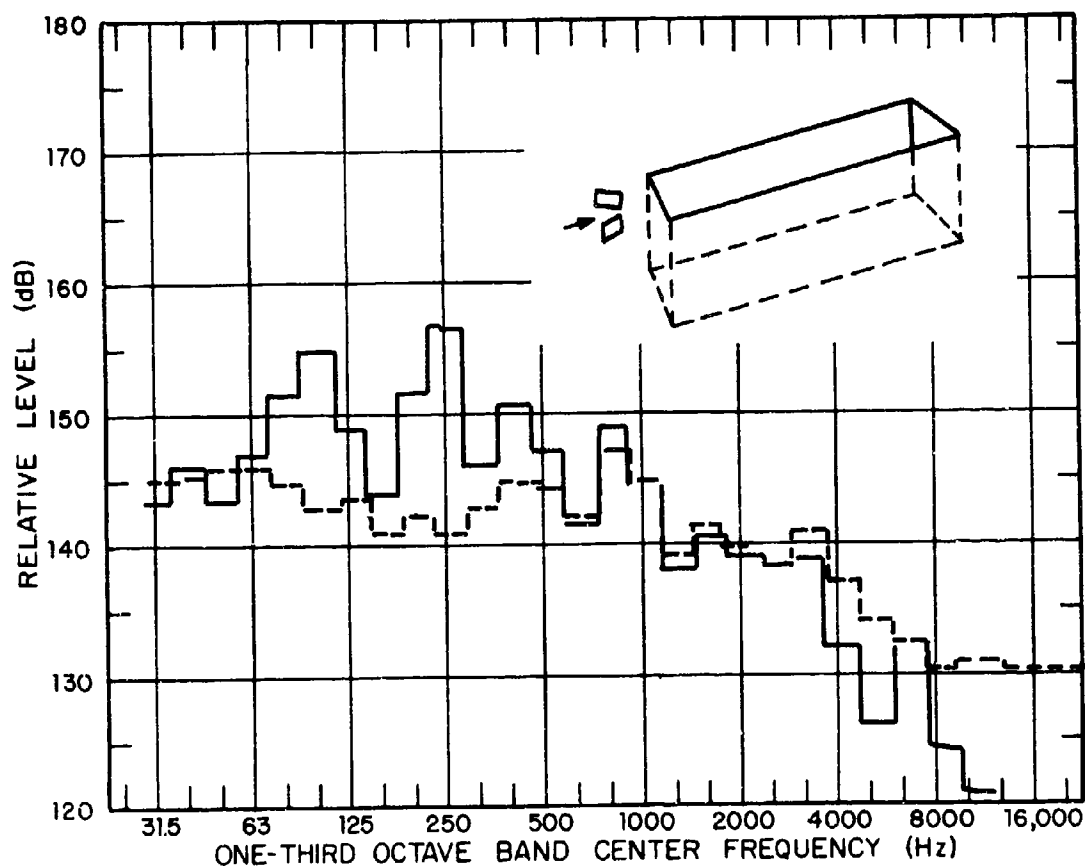


FIG. 77b. EFFECT OF UPSTREAM SPOILERS AT 45° ANGLE OF ATTACK ON LEADING-EDGE BULKHEAD PRESSURE SIGNAL: $M_\infty = 0.9$; $L/D = 4.0$ (continuous line refers to unmodified cavity).

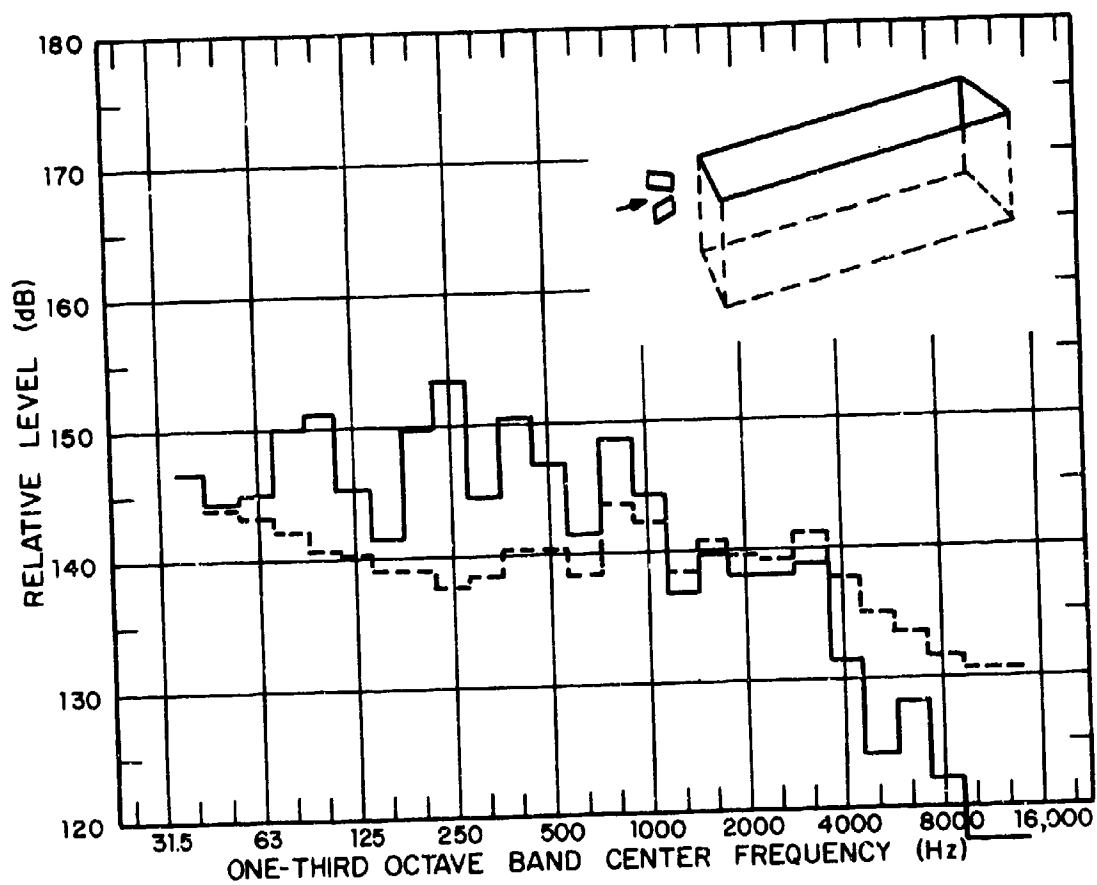


FIG. 77c. EFFECT OF UPSTREAM SPOILERS AT 45° ANGLE OF ATTACK ON LEADING-EDGE BULKHEAD PRESSURE SIGNAL: $M_{\infty} = 0.9$; $L/D = 5.1$ (continuous line refers to unmodified cavity).

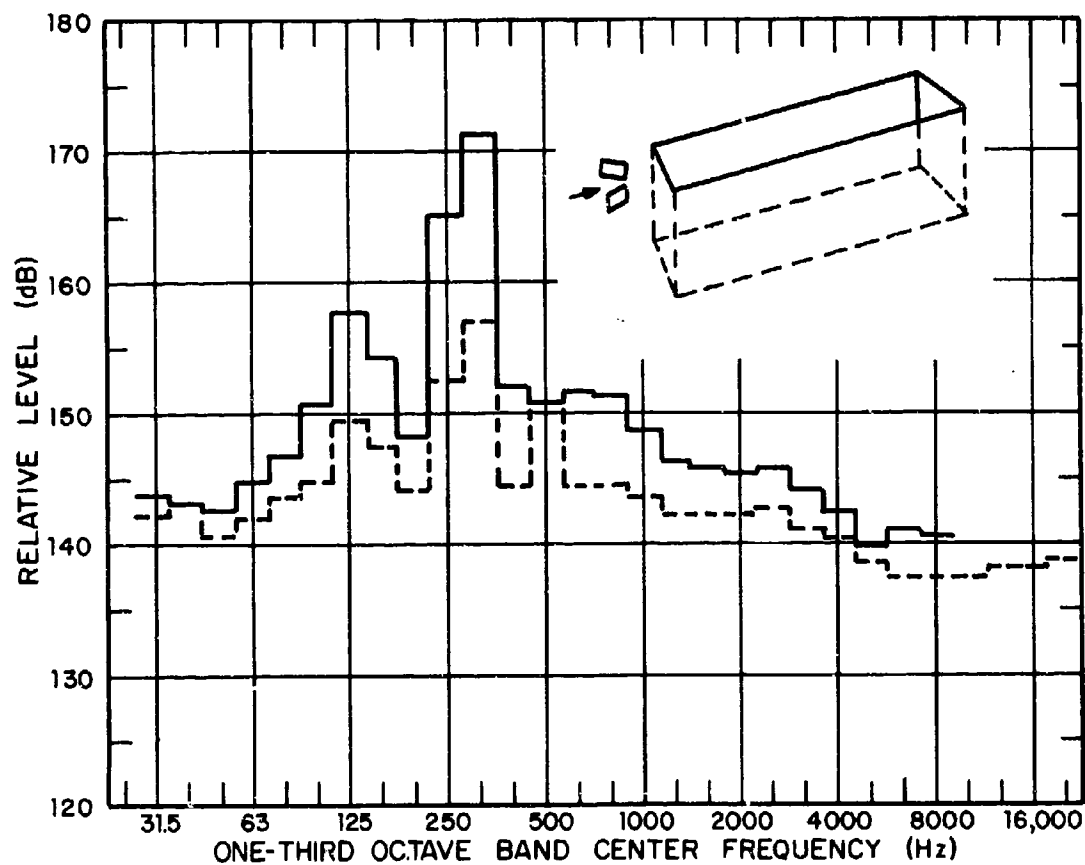


FIG. 78. EFFECT OF UPSTREAM SPOILERS AT 45° ANGLE OF ATTACK ON LEADING-EDGE BULKHEAD PRESSURE SIGNAL: $M_\infty = 1.5$; $L/D = 2.3$ (continuous line refers to unmodified cavity).

Figures 79 through 81 show the effect of a 45° trailing-edge slant as measured with Sensor 3 (see Fig. 36). Substantial tone reductions are achieved at subsonic ($M = 0.8$, Fig. 79), transonic ($M = 1.2$, Fig. 80), and supersonic ($M = 1.5$, Fig. 81) speeds. However, effective tone level reduction for the deepest cavity ($L/D = 2.3$) requires the addition of deployed spoilers; then, mode 2 tone levels are reduced by 5 dB (subsonic Fig. 79a) and by 15 dB (transonic, Fig. 80a, and supersonic, Fig. 81a).

Appendix C presents the physics and theory of flow stabilization through a trailing-edge slant.

7.3.2 Neutralization of Mass-Exchange Process

In the absence of leading-edge spoilers, the performance of the trailing-edge slant is improved by the addition of a detached cowl, as documented in Figs. 82 ($M = 0.8$) and 83 ($M = 1.5$). This configuration has an impressive suppression potential especially for the relatively deep cavity ($L/D = 2.3$), as shown in Fig. 82 and 83. However, the position of the cowl is critical. For example, at $M = 0.8$, the optimum cowl position is 2 in. above the surface plane. In fact, an additional 15 dB were gained by moving the cowl from the zero position to the +2-in. position. At supersonic speed, the optimum cowl position seemed to be about 0.5 in. below the surface plane. The reduction of the mode-2 tone is more than 30 dB. Appendix D discusses the physics of the flow about a detached cowl.

7.4 Consecutive Cavities

On the basis of the successful reduction potential of slanted trailing edges in conjunction with upstream spoilers, a subsonic flow experiment was conducted using the small-scale wall-jet facility. In this experiment, pairs of triangular spoilers were employed upstream of both cavities, and both cavity trailing-edge bulkheads were slanted.

Figure 84 presents results, which compare 1/10-octave band spectra on the forward cavity leading-edge bulkhead for the basic double cavity and the modified double cavity for an external flow speed of 730 ft/sec. The dominant tone amplitude is reduced by more than 30 dB. However, the inflow into the cavity configuration was laminar; therefore, part of the attenuation must be attributed to tripping the boundary layer, thus making the inflow turbulent, which is an inherently quieter condition.

Information was not obtained within the aft cavity, but pronounced tones were not observed in these experiments, which implies the effectiveness of the suppression concept.

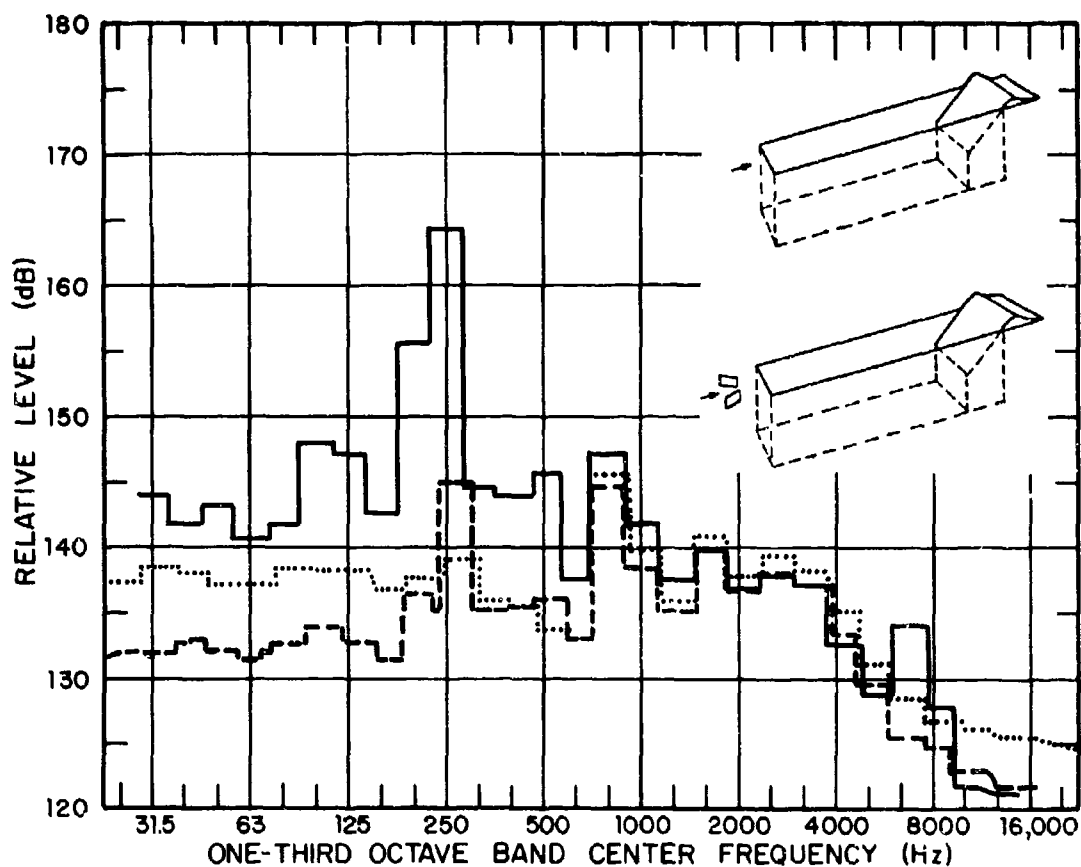


FIG. 79a. EFFECT OF TRAILING-EDGE SLANT WITH AND WITHOUT UPSTREAM SPOILERS ON LEADING-EDGE BULKHEAD PRESSURE SIGNAL: $M_\infty = 0.8$; $L/D = 2.3$ (continuous line refers to unmodified cavity; dashed line refers to trailing-edge slant only; dotted line refers to combination of trailing-edge slant and upstream spoilers).

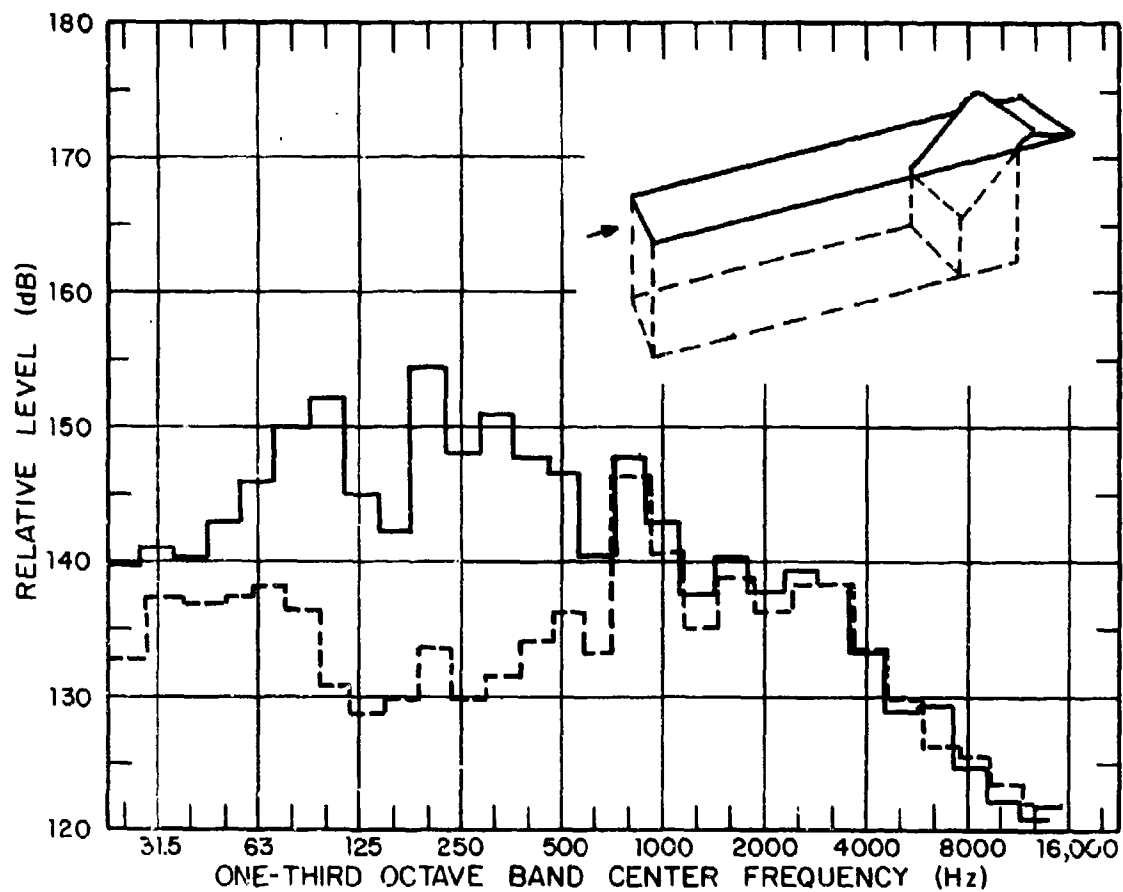


FIG. 79b. EFFECT OF TRAILING-EDGE SLANT ON LEADING-EDGE BULKHEAD PRESSURE SIGNAL: $M_{\infty} = 0.8$; $L/D = 4.0$ (continuous line refers to unmodified cavity).

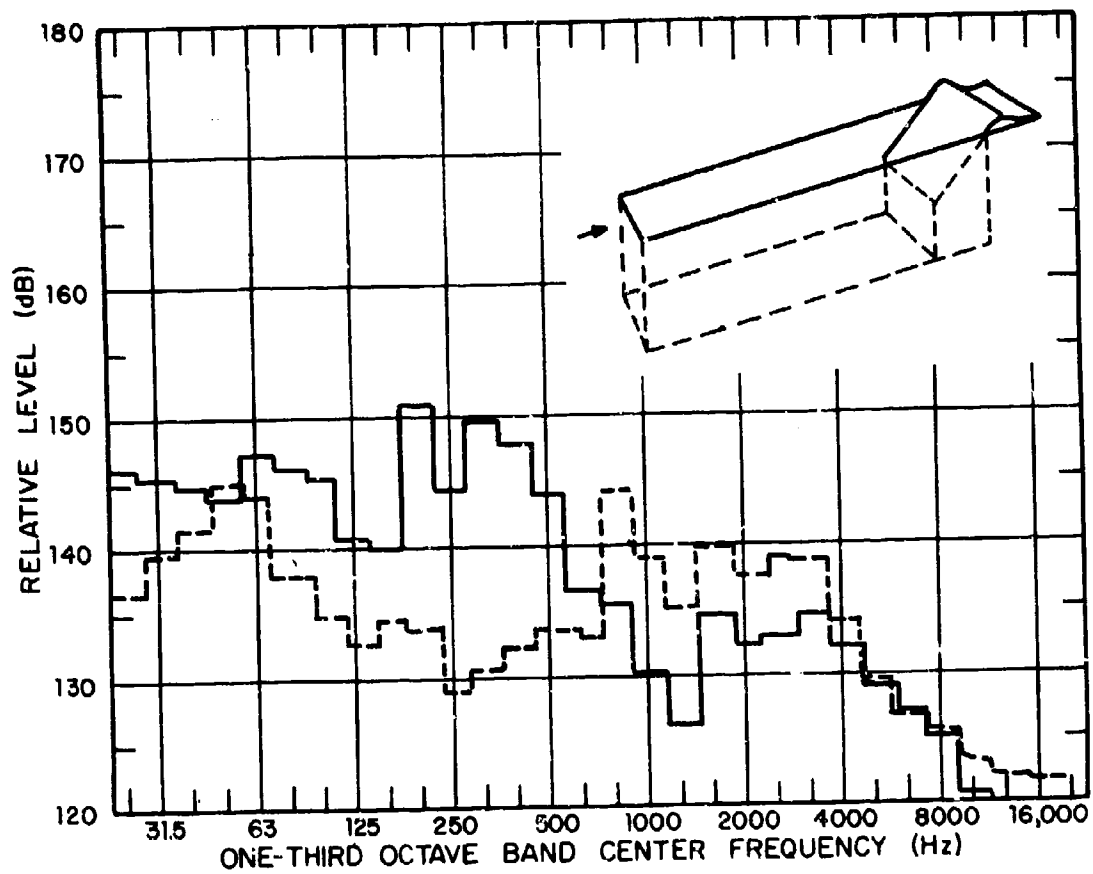


FIG. 79c. EFFECT OF TRAILING-EDGE SLANT ON LEADING-EDGE BULKHEAD PRESSURE SIGNAL: $M_\infty = 0.8$; $L/D = 5.1$ (continuous line refers to unmodified cavity).

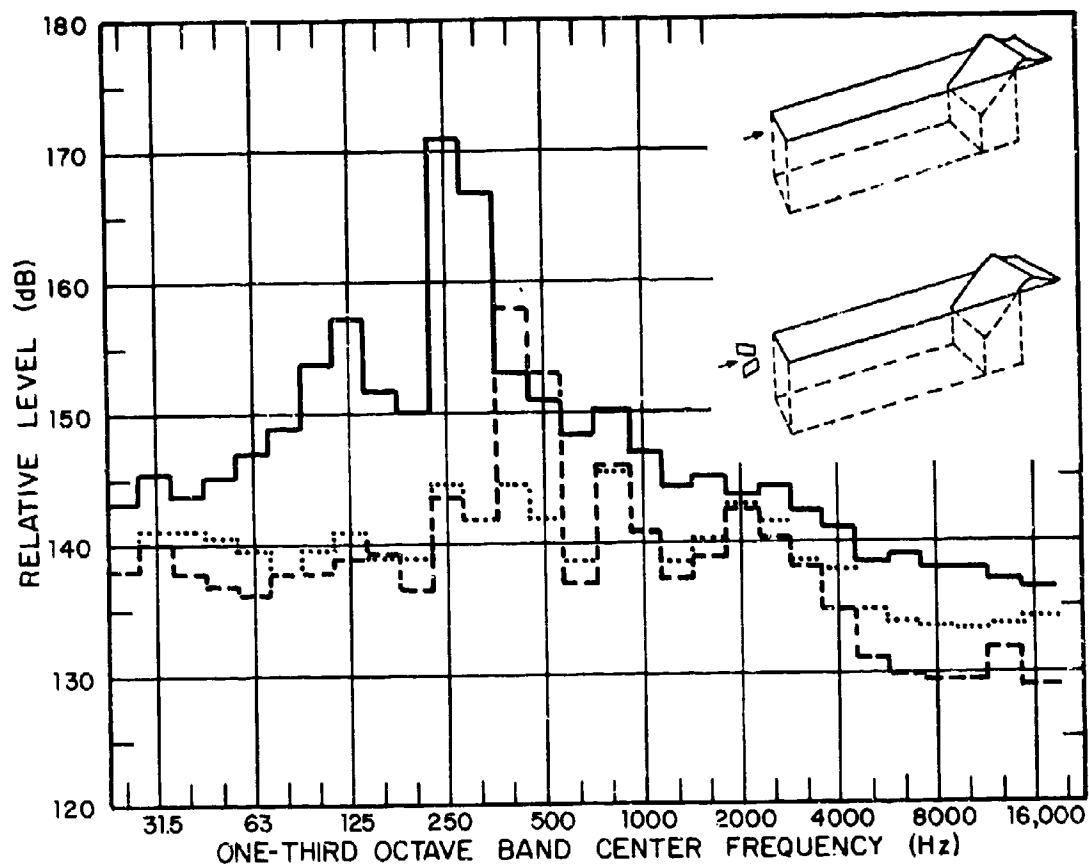


FIG. 80a. EFFECT OF TRAILING-EDGE SLANT WITH AND WITHOUT UPSTREAM SPOILERS ON LEADING-EDGE BULKHEAD PRESSURE SIGNAL: $M_\infty = 1.2$; $L/D = 2.3$ (continuous line refers to unmodified cavity; dashed line refers to trailing-edge slant only; dotted line refers to combination of trailing-edge slant and upstream spoilers).

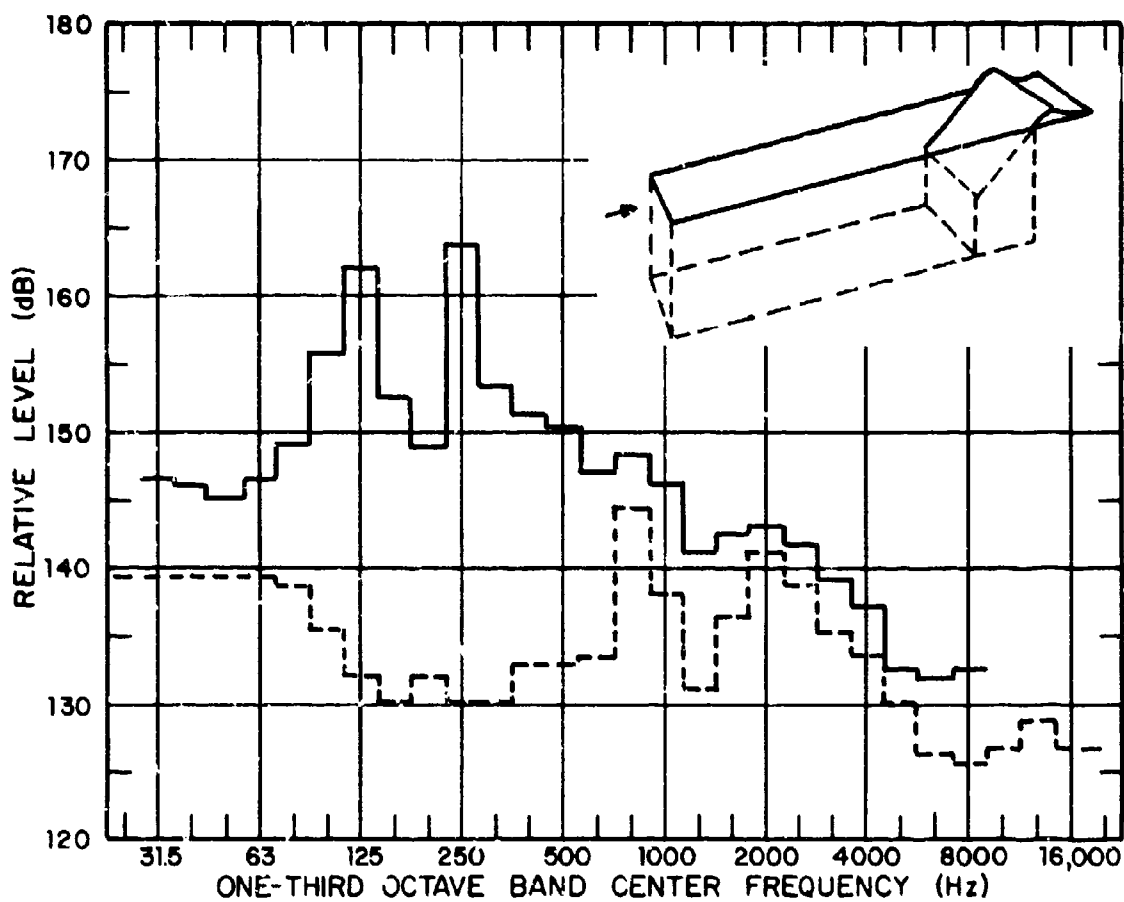


FIG. 80b. EFFECT OF TRAILING-EDGE SLANT ON LEADING-EDGE BULKHEAD PRESSURE SIGNAL: $M_\infty = 1.2$; $L/D = 4.0$ (continuous line refers to unmodified cavity).

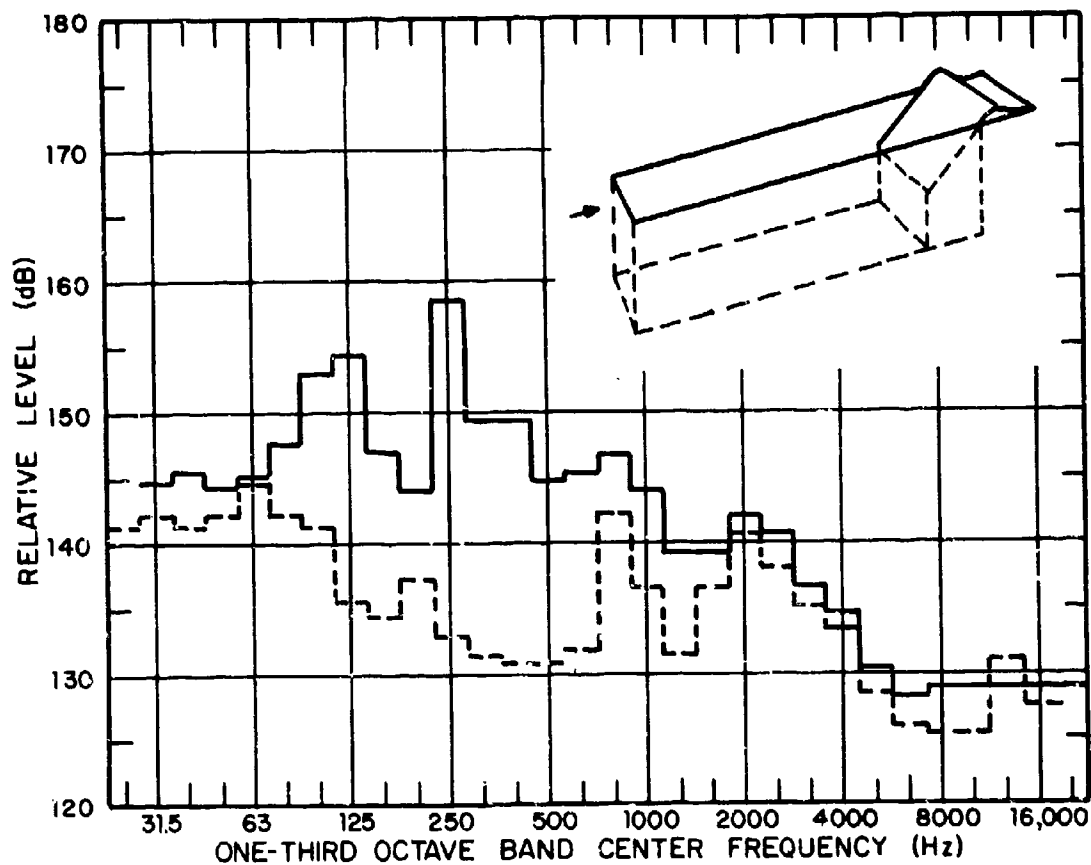


FIG. 80c. EFFECT OF TRAILING-EDGE SLANT ON LEADING-EDGE BULKHEAD PRESSURE SIGNAL: $M_\infty = 1.2$; $L/D = 5.1$ (continuous line refers to unmodified cavity).

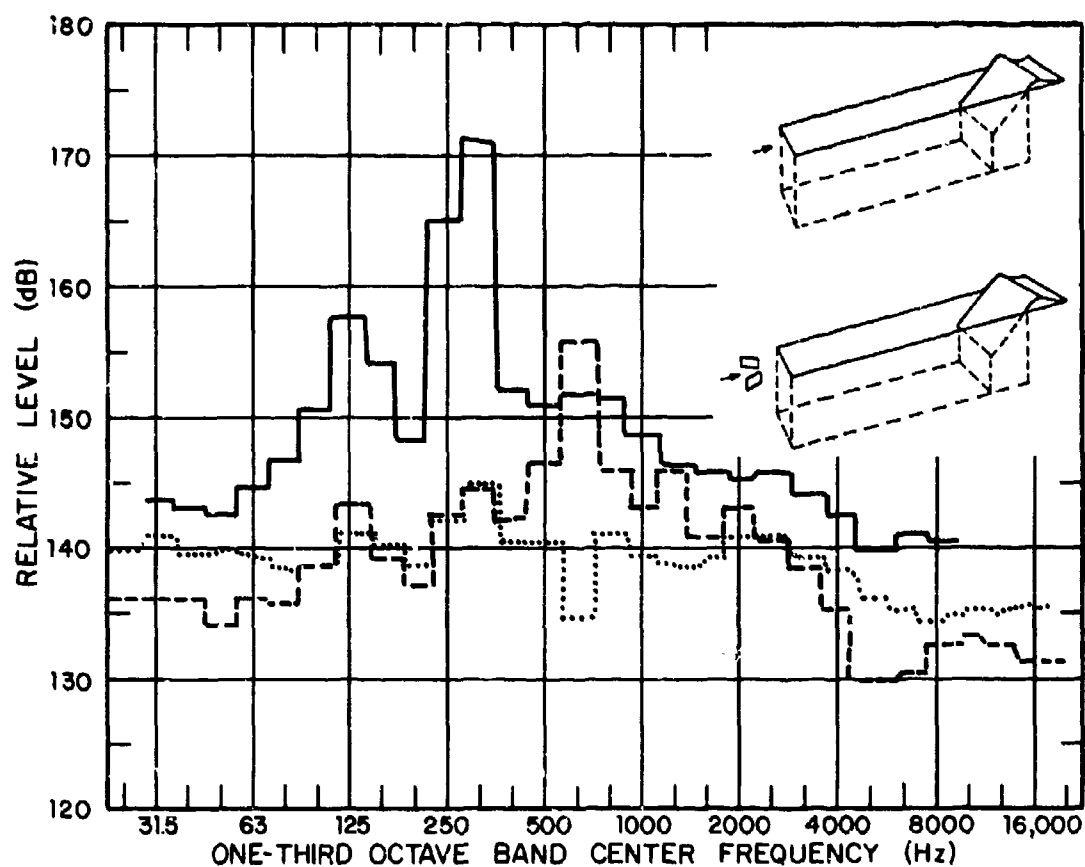


FIG. 81a. EFFECT OF TRAILING-EDGE SLANT WITH AND WITHOUT UPSTREAM SPOILERS ON LEADING-EDGE BULKHEAD PRESSURE SIGNAL: $M_\infty = 1.5$; $L/D = 2.3$ (continuous line refers to unmodified cavity; dashed line refers to trailing-edge slant only; dotted line refers to combination of trailing-edge slant and upstream spoilers).

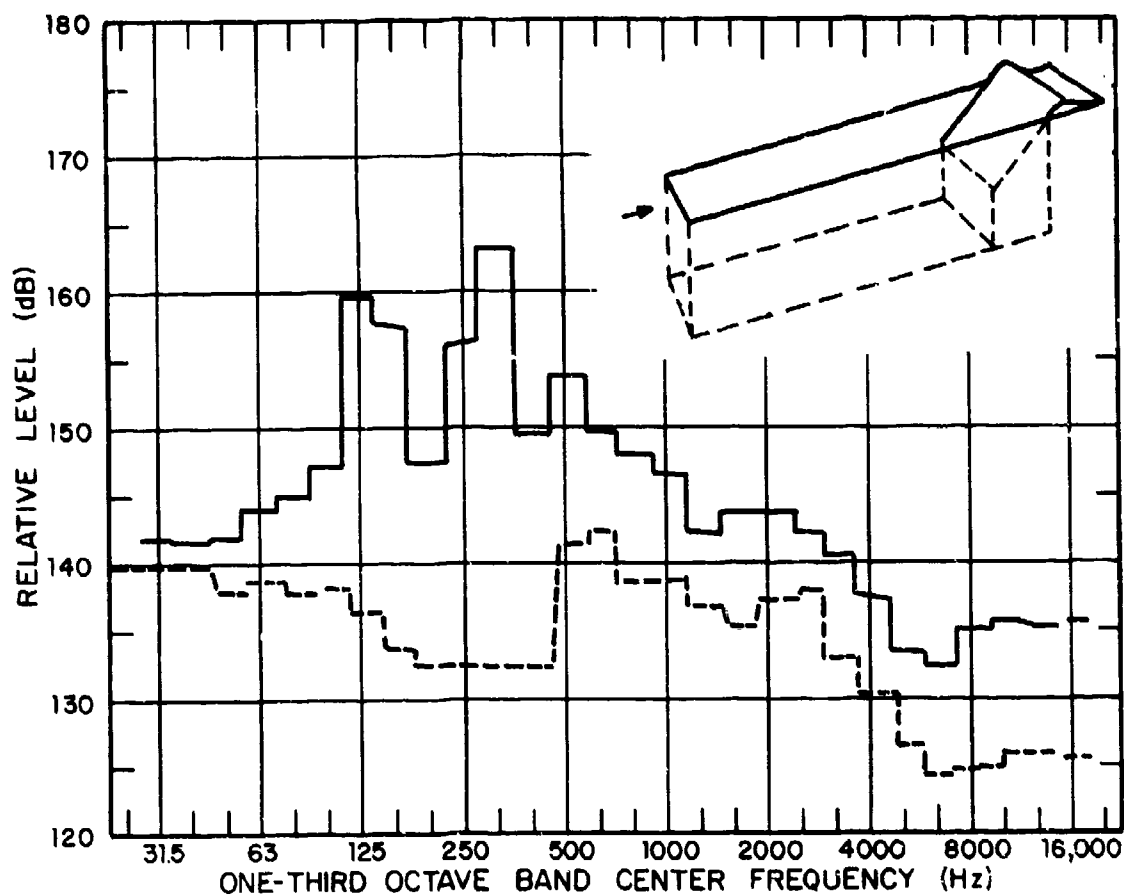


FIG. 81b.

EFFECT OF TRAILING-EDGE SLANT ON LEADING-EDGE
BULKHEAD PRESSURE SIGNAL: $M_\infty = 1.5$; $L/D = 4.0$
(continuous line refers to unmodified cavity).

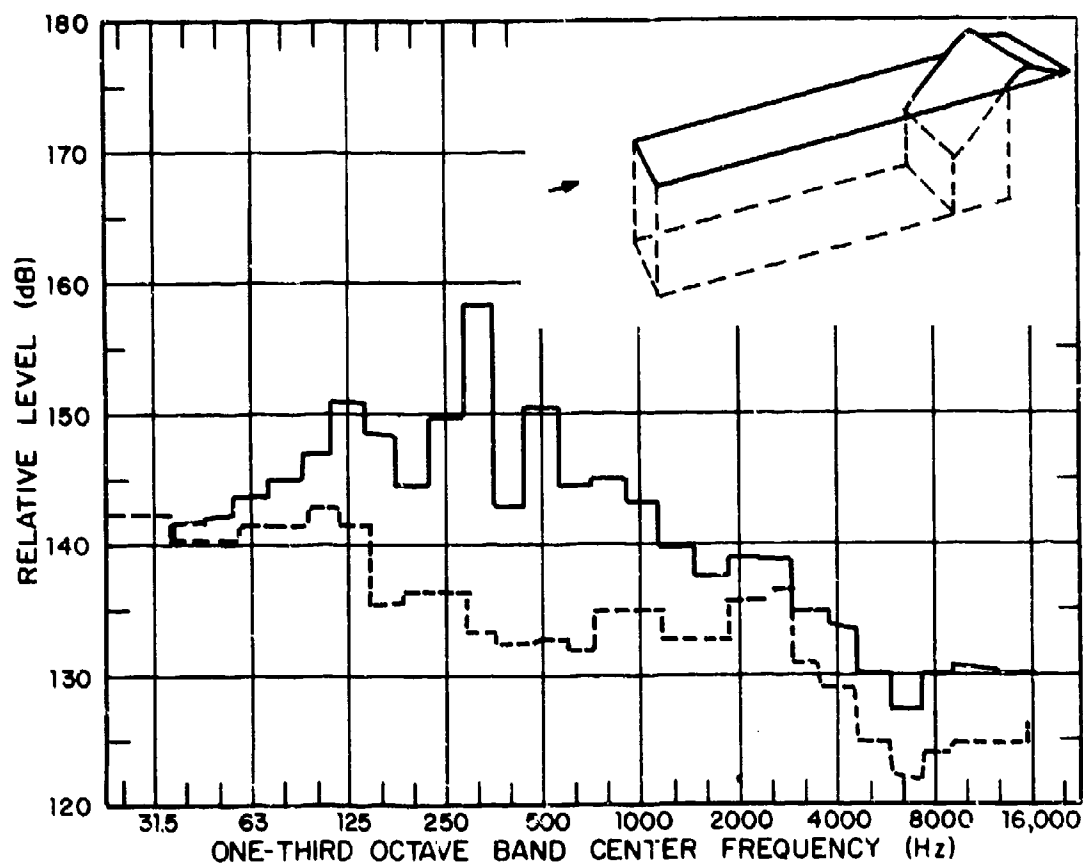


FIG. 81c. EFFECT OF TRAILING-EDGE SLANT ON LEADING-EDGE BULKHEAD PRESSURE SIGNAL: $M_{\infty} = 1.5$; $L/D = 5.1$ (continuous line refers to unmodified cavity).

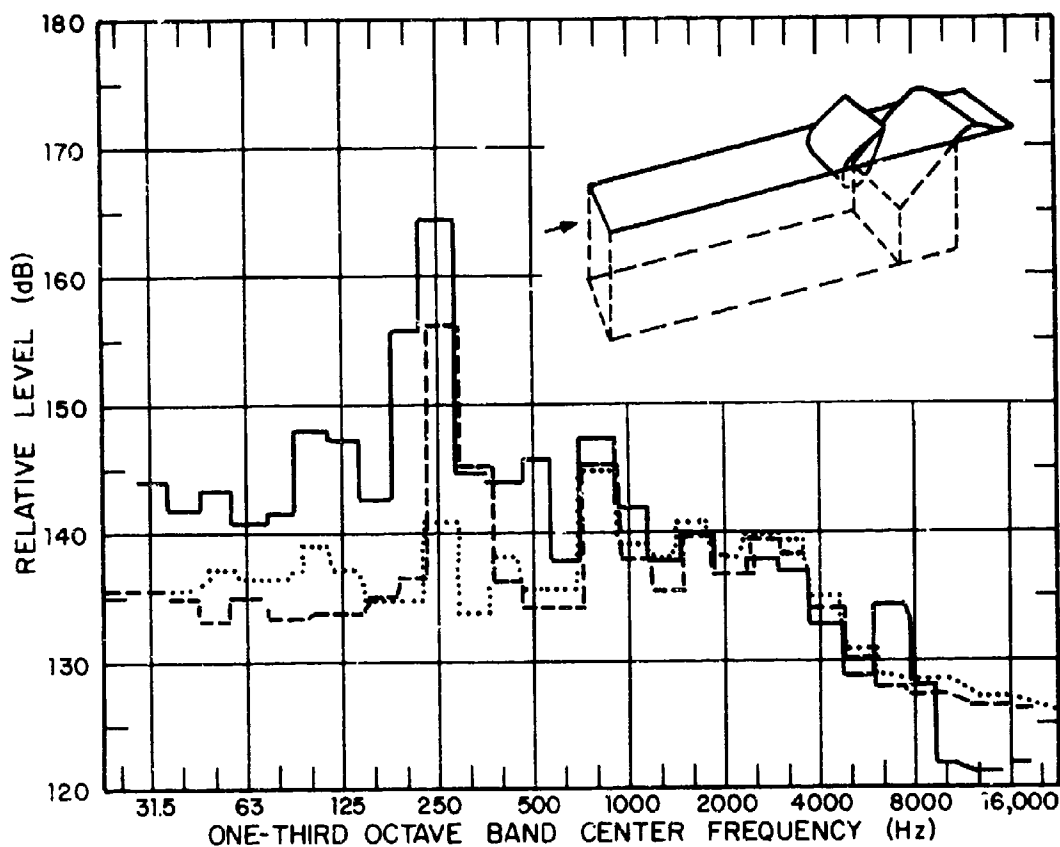


FIG. 82a. EFFECT OF TRAILING-EDGE SLANT IN COMBINATION WITH A DETACHED COWL ON LEADING-EDGE BULKHEAD PRESSURE SIGNAL: $M_\infty = 0.8$; $L/D = 2.3$ (continuous line refers to unmodified cavity; dashed line refers to cowl trailing edge located at cavity mouth level; dotted line refers to cowl trailing edge located 2 in. above cavity mouth level).

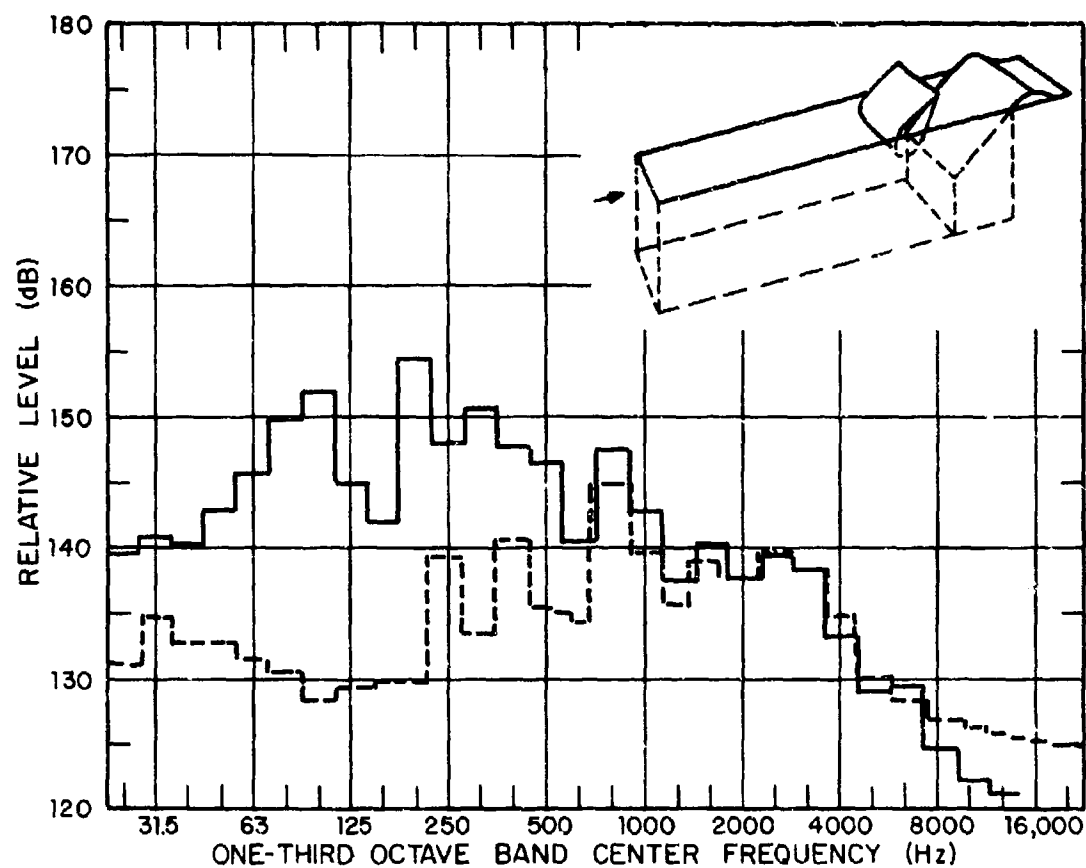


FIG. 82b. EFFECT OF TRAILING-EDGE SLANT IN DETACHED COWL ON LEADING-EDGE BU, $M_{\infty} = 0.8$; $L/D = 4.0$ (continuous ; unmodified cavity). ATION WITH A PRESSURE SIGNAL: refers to

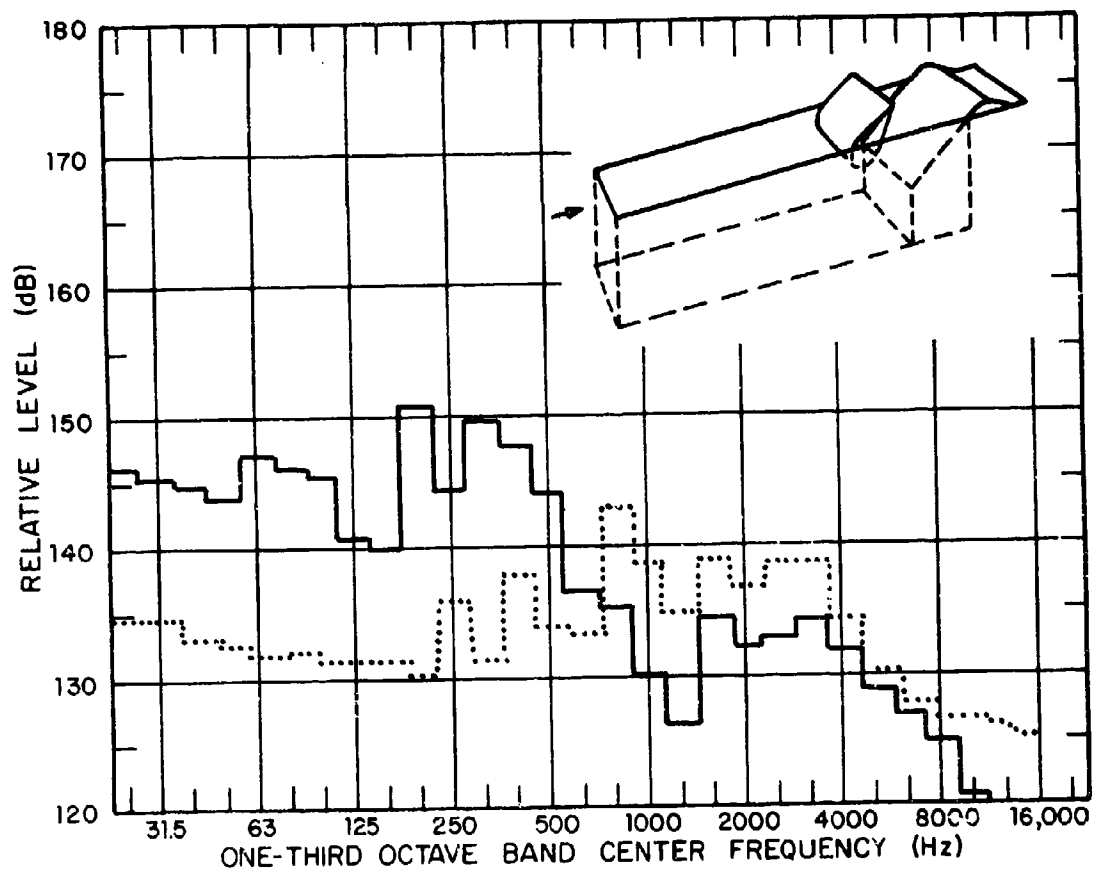


FIG. 82c. EFFECT OF TRAILING-EDGE SLANT IN COMBINATION WITH A DETACHED COWL ON LEADING-EDGE BULKHEAD PRESSURE SIGNAL: $M_{\infty} = 0.8$; $L/D = 5.1$ (continuous line refers to unmodified cavity).

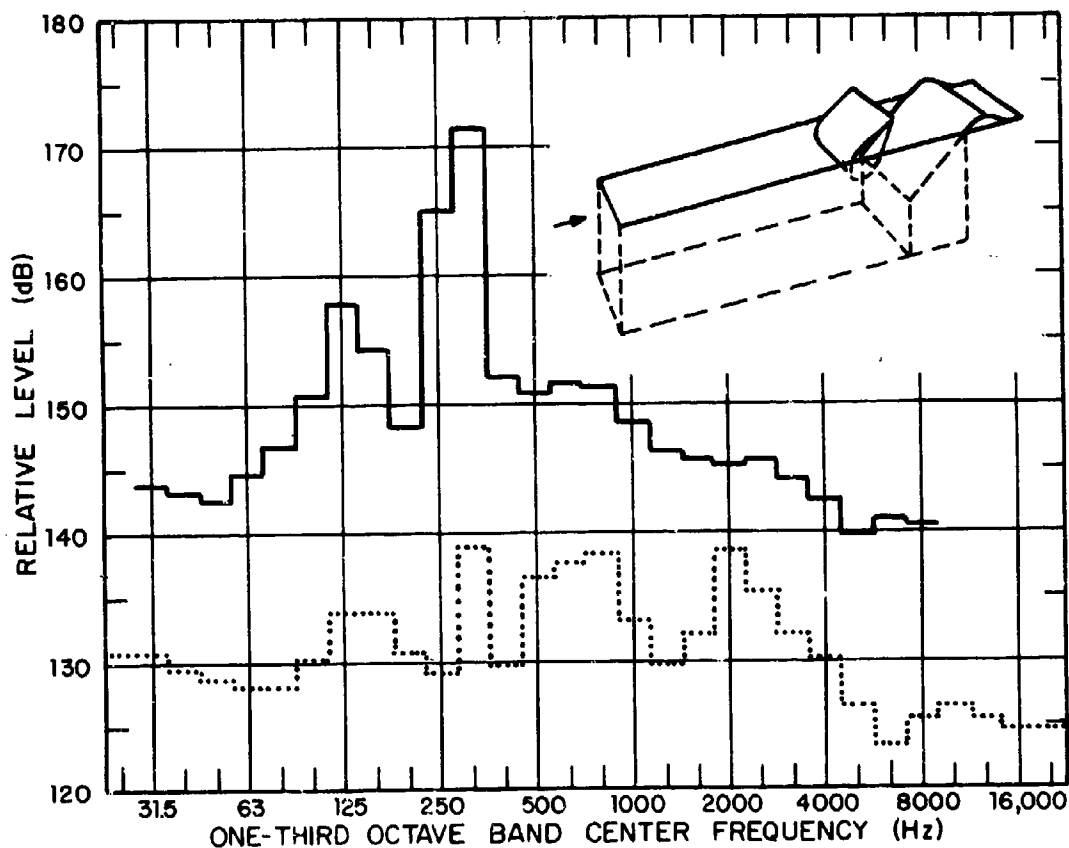


FIG. 83a. EFFECT OF TRAILING-EDGE SLANT IN COMBINATION WITH A DETACHED COWL ON LEADING-EDGE BULKHEAD PRESSURE SIGNAL: $M_{\infty} = 1.5$; $L/D = 2.3$ (continuous line refers to unmodified cavity).

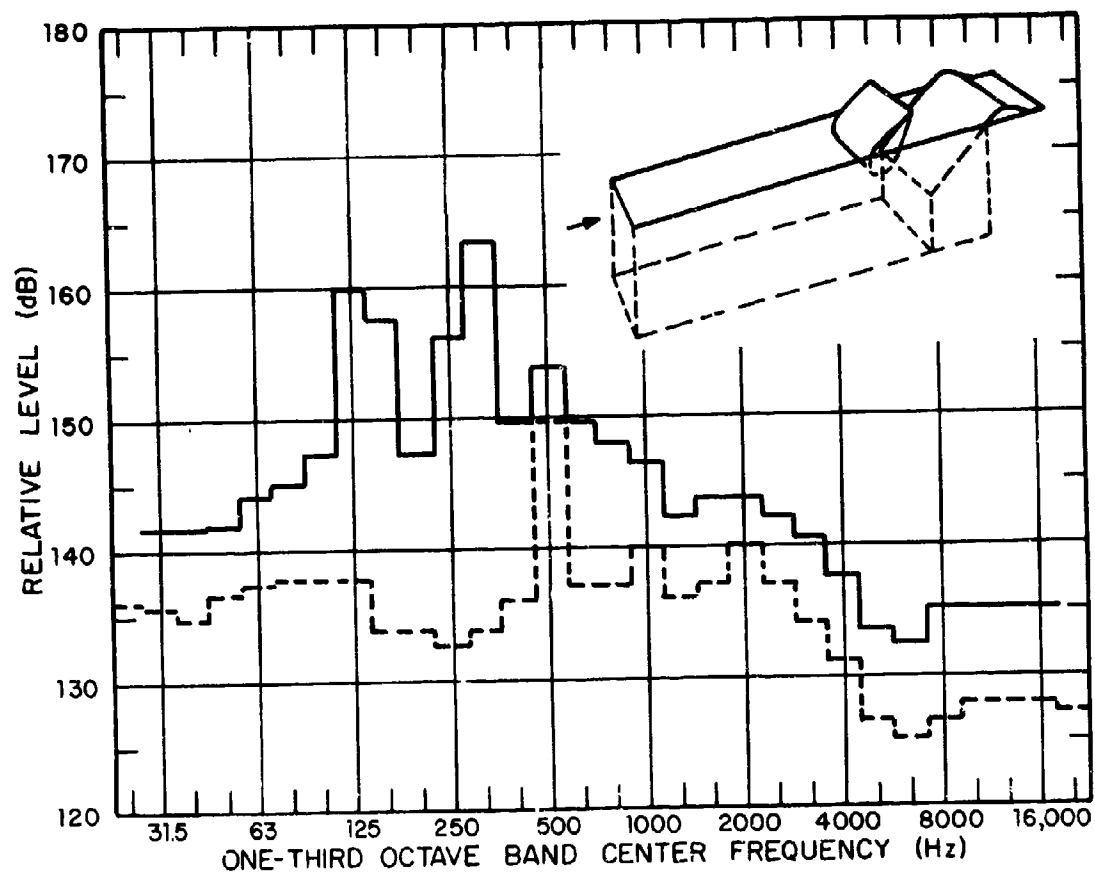


FIG. 83b. EFFECT OF TRAILING-EDGE SLANT IN COMBINATION WITH A DETACHED COWL ON LEADING-EDGE BULKHEAD PRESSURE SIGNAL: $M_{\infty} = 1.5$; $L/D = 4.0$ (continuous line refers to unmodified cavity).

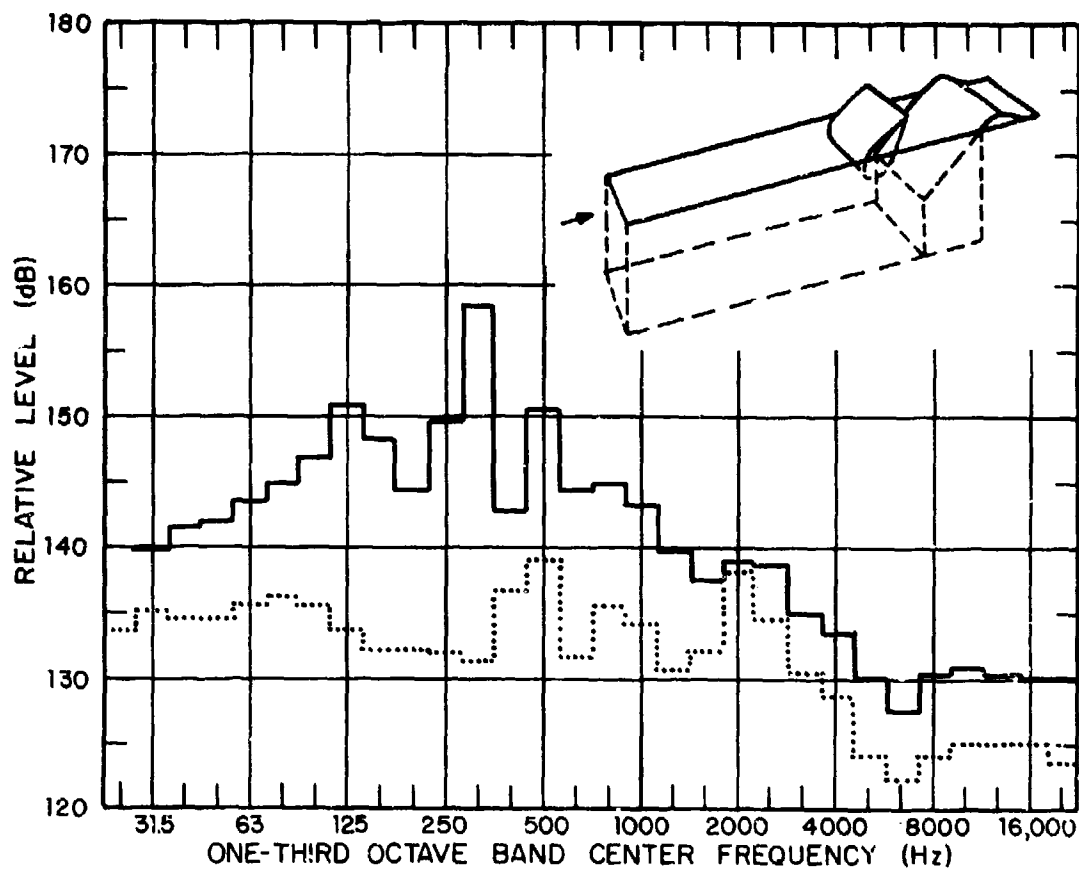


FIG. 83c. EFFECT OF TRAILING-EDGE SLANT IN COMBINATION WITH A DETACHED COWL ON LEADING-EDGE BULKHEAD PRESSURE SIGNAL: $M_{\infty} = 1.5$; $L/D = 5.1$ (continuous line refers to unmodified cavity).

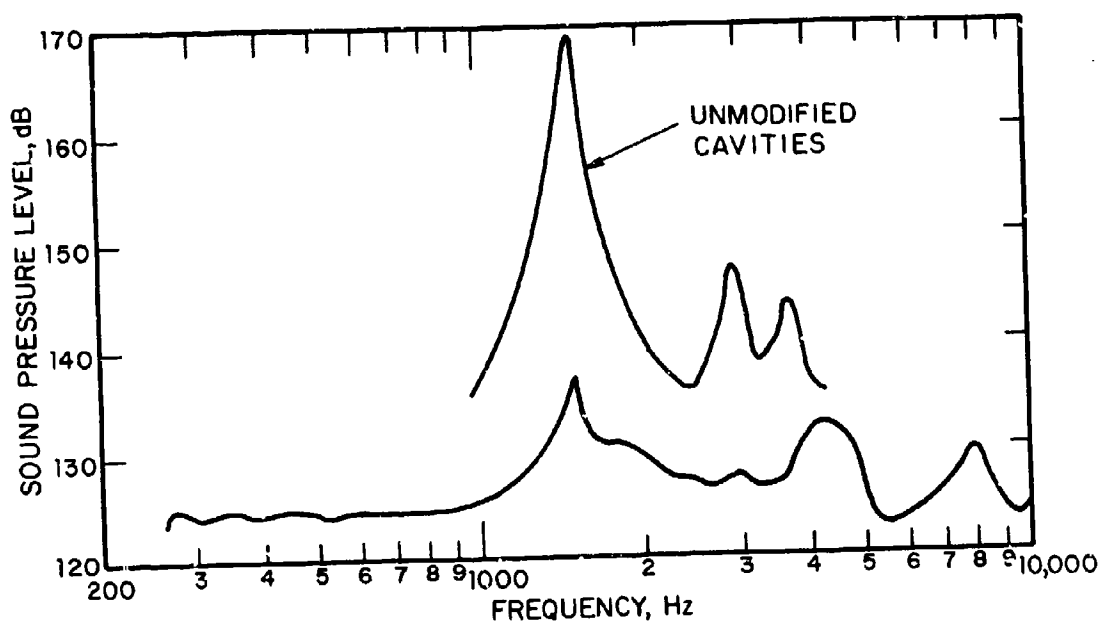
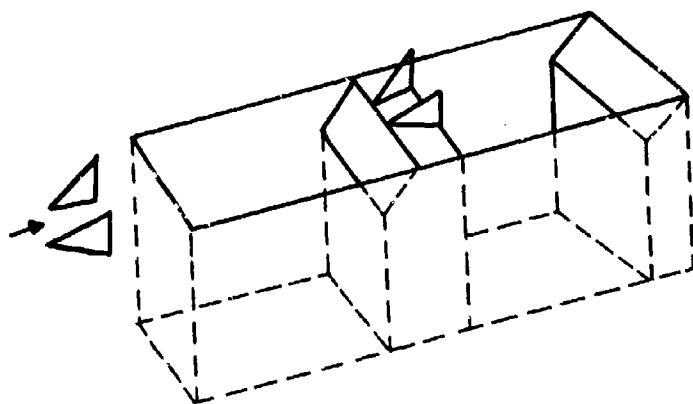


FIG. 84. EFFECT OF TRIANGULAR SPOILERS AND TRAILING-EDGE SLANTS ON PRESSURE LEVELS AT THE LEADING EDGE OF THE UPSTREAM CAVITY OF A DOUBLE CAVITY SYSTEM.

7.5 Drag Induced by Suppression Devices

Using the small-scale wall-jet facility, a rectangular (basic) cavity with length-to-depth ratio of 2 was measured for drag due to (1) a trailing-edge slant, (2) two inclined triangular spoilers at angle of attack of 35° , and (3) a combination of these two measures. Figure 85 shows the drag as a function of flow speed for the four configurations under consideration. These data, which pertain to a specific configuration, indicate that the trailing-edge slant scarcely increases the drag. However, spoilers which have particular dimensions and are deployed at a particular angle of attack raise the drag by about 40%; the combination of trailing-edge slant and spoilers raise it by about 60% above that of the basic cavity.

7.6 Evaluation of Suppression Devices

The value of an oscillation amplitude reduction device is measured in terms of its effectiveness over a broad range of flight regimes, its ease and simplicity of implementation into an existing or new aircraft design, and its possible adverse effects on aircraft performance.

7.6.1 Acoustic Effectiveness

Obviously, deeper cavities ($L/D \leq 2$) require some drastic measures to reduce the oscillation amplitude, while shallower cavities ($L/D > 2$) can be "quieted" in a fairly simple and straightforward manner. The following conclusions can be drawn from the experimental results, which are valid for long ($L/W \approx 4$) and shallow ($2.3 < L/D < 5.1$) cavities.

- At subsonic speeds, two slightly separated flat-plate rectangular spoilers, which are twice the height of the local boundary layer thickness and $1/10$ as long as the cavity length at a 45° angle with respect to the freestream flow direction, effectively reduce the dominant discrete-tone levels to the broadband noise level (in $1/3$ -octave bands) for cavities with length-to-depth ratios of $2.3 < L/D < \infty$. The trailing edge of the spoiler should be close to the cavity leading edge. The two spoilers should be separated laterally by about one third of the cavity width and placed symmetrically with respect to the cavity centerline. (For reference, see Fig. 77.)
- At supersonic speeds, the same spoilers still show a significant, although lesser, degree of level reduction. (For reference, see Fig. 78.)

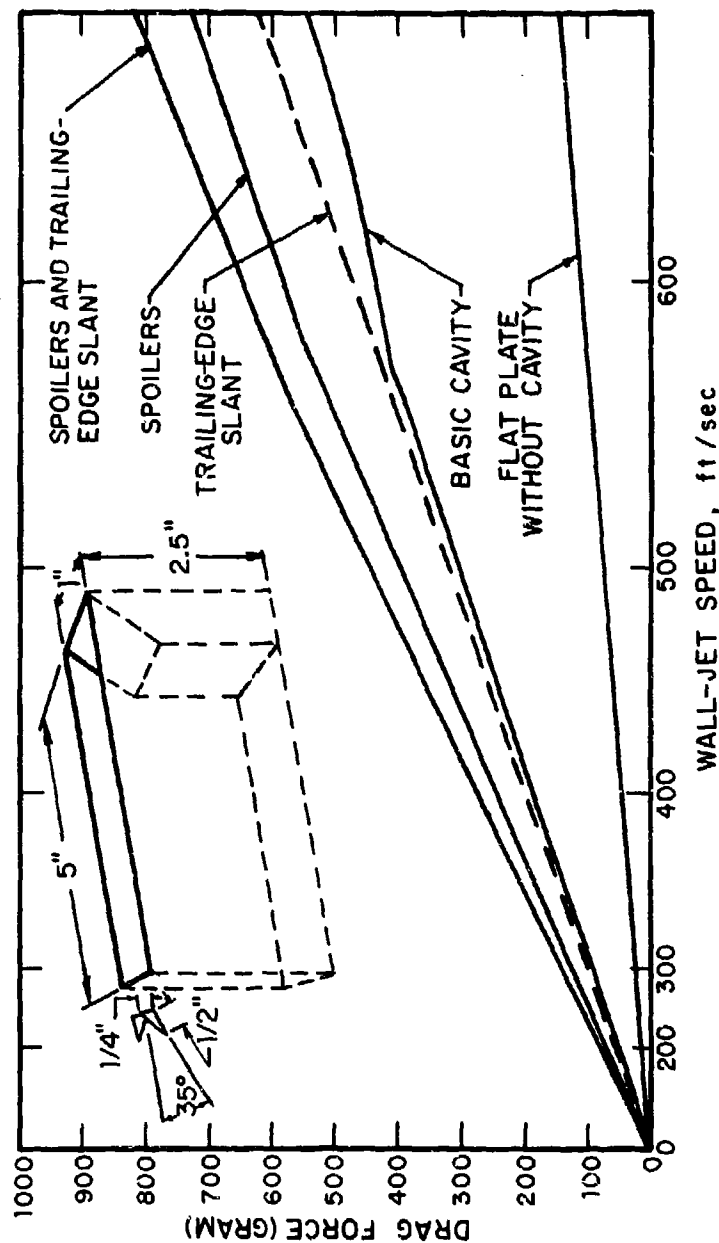


FIG. 85. FLOW-INDUCED CAVITY DRAG WHEN SUPPRESSION DEVICES ARE EMPLOYED.

- Dramatic level decreases are achieved by a 45° slanted trailing edge, whose projected vertical dimension should be at least twice the vertical dimension of the naturally grown shear layer at the location of the trailing edge. The trailing-edge slant can protrude above the cavity surface plane one fourth to one third of the slant length. Although not specifically explored, this protrusion may be superior to a level termination at the surface plane.
- The trailing-edge slant is effective at subsonic ($M_\infty = 0.8$), transonic ($M_\infty = 1.2$), and supersonic ($M_\infty = 1.5$) speeds since it not only reduces the discrete-tone levels but also large portions of the broadband noise. (For reference, see Figs. 79, 80, and 81.)
- For the relatively deeper cavities ($L/D \approx 2.3$), employment of the spoilers at a deployment angle between 30° and 45° brings further reduction in noise levels. In fact, spoilers, in conjunction with a slanted trailing edge, represent the best configuration explored within this investigation; thus they are recommended for implementation in aircraft design.
- In the absence of upstream spoilers, the performance of the slant can be improved by a thick inclined airfoil (also referred to as cowl) some distance upstream of the slanted trailing edge, so that a channel is formed between the surface of the slant and the lower (flat) surface of the airfoil. For best results, the airfoil maximum thickness at the quarter chord should be about 25 to 30% of the length. The length itself should be of the same dimensions as the slant length. This arrangement achieves dramatic reductions, but the critical position of the airfoil depends in an as yet not fully understood manner on the Mach number. (For reference, see Figs. 82 and 83.)
- The combination of spoilers and slanted trailing edge also seems to be effective when employed with two consecutive cavities. (For reference, see Fig. 84.)

7.6.2 Implementation into Aircraft Design

The least space-consuming reduction device is the double spoiler upstream of the cavity leading edge. The spoiler could be retracted for cruising at the deployment angle of 30° or 45° , and only deployed when needed. Alternatively, the spoilers can continuously protrude above the aircraft surface at a 0° angle; this angle can then be changed to 30° or 45° when needed.

The slanted trailing-edge configuration takes more space. However, by letting the slant extend above the surface, the space penalty can be minimized. A substantial amount of near trailing-edge volume would be consumed by the slant and detached-cowl configuration.

7.6.3 Effects on Aircraft Performance

The effect on aircraft performance of any of the proposed suppression devices would be minimal, since the open cavity already represents a major generator of steady and unsteady drag.

Although a resonant cavity does not generate more drag than a quiescent cavity,* a stabilized flow would represent aerodynamically a cleaner flight condition, even if there was some small increase in drag.

From this viewpoint, the slanted trailing edge represents an optimum configuration, since it causes no real increase in cavity drag (see Fig. 85). Even in conjunction with the deployed spoilers, the drag increase is less, than if only the spoilers were deployed.

*This is in contrast to McGregor's (1969) findings. However, in McGregor's experiments, the boundary layer thickness was about the same dimension as the cavity depth and, furthermore, reflecting tunnel walls were used to enhance the sound.

SECTION 6

CONCLUSIONS

8.1 Principal Results

The two principal results of this research program were:

1. An improvement of the understanding of the generation mechanism of flow-induced pressure oscillations in cavities.
2. Based on this improved understanding, the development and experimental evaluation of acoustic devices that substantially decrease the amplitude of the cavity internal discrete pressure oscillations.

8.2 Oscillation Phenomenon

Extensive water table flow visualization experiments were conducted to study in detail the unsteady interaction of the free shear layer above the cavity and the fluid medium inside the cavity. The mechanism for the oscillations is summarized as follows. When the shear layer goes below the trailing edge, the external free stream impinges on the rear bulkhead of the cavity. This impingement causes mass addition at the rear of the cavity. A strong, essentially plane pressure wave is produced by this process and propagates forward within the cavity. Since this wave is supersonic relative to the external flow, a forward traveling, oblique external wave is also produced. The internal wave reflects off the front bulkhead and returns to the rear of the cavity. The motion of the shear layer is controlled by the forcing imposed by these traveling pressure waves over the length of the cavity mouth. The phase of the shear layer is such that as one pressure wave reaches the forward bulkhead and reflects, another is simultaneously generated at the rear. In this manner, the process sustains itself.

This explanation of the oscillation mechanism is somewhat different from that proposed by previous investigators. The process is generally viewed as a feedback mechanism. Shear layer interaction with the trailing edge produces a wave that reaches the leading edge and triggers a disturbance in the shear layer. This disturbance then convects downstream and amplifies. It may take the form of sinuous instability, vortex shedding, or some combination. The disturbance interacts with the trailing edge to generate another upstream wave, which, again, triggers the shear layer, and so on. Particularly severe oscillations

are believed to occur when the frequency of this process matches the natural frequency of standing wave modes in the cavity, thus causing a resonance to occur.

The viewpoint derived from the water table tests differs in the following way. The upstream wave, which was generated by the trailing-edge/shear layer interaction, and the corresponding downstream reflected wave directly control the shear layer phase by pressure forcing over the length of the cavity, not just by triggering disturbances at the leading edge. The shear layer dynamics are not primarily the result of a free instability, or of an instability triggered solely at the leading edge, but they are a consequence of the forcing from both upstream and downstream traveling pressure waves within the cavity. The superposition of these upstream and downstream waves forms the experimentally observed pressure-mode patterns in the cavity. Special shear layer phenomena, such as vortex shedding, are viewed as a manifestation of this pressure wave forcing, rather than as an essential part of the oscillation mechanism.

8.3 Analytical Work

On the basis of the water table flow visualization experiments, analytical models were developed for the wave motion in the cavity and for the trailing-edge mass addition process.

The water table results have shown that an essential feature of the phenomena is the periodic addition and removal of mass at the rear of the cavity. This is caused by the interaction of the shear layer with the trailing edge. This mass addition and removal produces an effect very similar to replacing the rear bulkhead of the cavity with an oscillating piston. This "pseudopiston" effect explains why pressure modes on the cavity do not behave as if the rear bulkhead were a hard wall. An analytical model was developed to describe the pseudopiston behavior in terms of cavity geometry and flow parameters.

A separate analysis was developed for the wave motions in the cavity. The cavity was modeled as having an oscillating piston at the rear bulkhead to account for the pseudopiston effect. This approach also treats the interaction of the wave modes with the shear layer as an integral part of the oscillation process. Solutions for upstream and downstream waves traveling between a shear layer and a solid boundary are superimposed to approximate an oscillating cavity configuration. At high Mach numbers, this analysis predicts pressure-mode

shapes similar to those observed experimentally; in fact, all the qualitative features are in agreement. At lower Mach numbers, the theory predicts only the lowest pressure-mode shape and fails to predict the higher modes, which the experimental work shows are present. This inadequacy is believed to be caused by the omission of the effect of shear layer thickness in the analytical model. It is recommended that this refinement be the subject of a future research program, so that analytical results, which are valid over the entire Mach number range, will be available.

8.4 Experimental Results

8.4.1 Basic Cavity

Small-scale and large-scale wind tunnel experiments yielded detailed information on the aeroacoustic behavior of shallow rectangular cavities over a length-to-depth ratio range of $2.3 < L/D < 5.1$ and the Mach number range of 0.2 to 2.0. The previously derived law of the Mach number dependence of the resonant mode frequencies was substantiated over the Mach number range, except at low subsonic Mach numbers; in this range, resonant frequencies were observed to be higher than predicted. Additional research is necessary in this area to resolve this discrepancy.

Cavity internal temperatures were measured. Recovery factors were found to be closer to unity than to zero, whereby shallow cavities exhibited higher recovery factors than deep cavities.

A weak dependence of the resonant frequencies on the length-to-depth ratio was found for cavities in the range $1.5 < L/D < 5$ at subsonic flow speeds. Conclusive data at supersonic speeds could not be obtained. More research in this area is necessary to incorporate the length-to-depth ratio effect into the present prediction schemes. Detailed information on the Mach number dependence of resonant mode levels for modes 1, 2, and 3 was obtained. Levels were observed to peak at transonic speeds. Levels were also found to increase generally from the leading- to the trailing-edge region.

Cavity internal pressure-mode shapes were determined for the first three modes and for the range of $2.3 < L/D < 5.1$. In all cases, definite amplitude minima were observed; however, they

were qualitatively displaced in the upstream direction. In all cases, a pressure maximum appeared at the leading-edge bulkhead indicating that this surface acts as a "hard-reflecting wall." In contrast, pressure amplitude maxima were observed a small distance upstream of the trailing-edge bulkhead; this indicates that acoustically the trailing-edge bulkhead is undefined because of the violent flow patterns. In this study, mode shapes were obtained that differ from those observed in Air Force flight tests, however, in the latter experiment, mode shapes were determined on the cavity floor, while in the former experiments, mode shapes were determined within the cavity volume. Thus, dependence of mode shape on the vertical position in the cavity seems to exist; this issue needs clarification.

A nondimensional broadband spectrum was derived from the experimental data. All spectra fall within a ± 4 -dB range for cavities with a range of $2.3 < L/D < 5.1$ and in a Mach number range of $0.8 < M_\infty < 2.0$. However, the nondimensional peak frequency seems to be a function of the thickness of the approaching boundary layer.

Experiments on consecutive geometrically identical cavities reveal that they are strongly coupled and resonate in phase. The Mach number dependence of mode levels for consecutive cavities was found to differ from that of single cavities. However, this may be because of the differing length-to-width ratio of the single and the double cavity system. While resonant frequencies are essentially determined by the cavity length, mode levels seem to be affected by the relative cavity width. This problem has not been studied and requires further research.

8.4.2 Oscillation Suppression

Of the various ways to affect the oscillation process, introduction of vorticity into the shear layer and the provision of a slanted trailing-edge bulkhead were found to have a stabilizing effect on the external free shear layer. Oscillation amplitudes can be minimized solely by a slanted trailing-edge bulkhead, over a Mach number range of at least 0.8 to 2.0, for cavities with length-to-depth ratios above 4. Cavities with a length-to-depth ratio below 4 require the addition of upstream vortex generators (spoilers), which further reduce resonant amplitudes.

A physical explanation of the stabilizing effect of a trailing-edge slant is available. It would be desirable to investigate this concept further through extensive experimental exploration.

Steady-state drag increase with a slanted trailing edge is minimal. The effective drag of the spoilers depends on their size and angle of attack. Drag increases up to 50% above that of the basic rectangular cavity have been observed.

Oscillation amplitudes could not be reduced by the forced entrainment of boundary layer fluid into the cavity at the leading edge, by tilting the leading- and/or trailing-edge bulkheads, by implementation of an upstream "spoiler cavity," or by cavity internal transverse spoilers and baffles.

APPENDIX A

PSEUDOPISTON ANALYSIS

A.1 Overview

It is believed that the cavity oscillation phenomenon is driven by the periodic injection and removal of mass at the trailing edge. This process has an effect that is similar to placing a fictitious piston at the rear bulkhead. The oscillation of this pseudopiston sets up an essentially one-dimensional wave pattern in the cavity that, in turn, forces the shear layer. The deflection of the shear layer at the trailing edge is responsible for the periodic injection of flow from the shear layer and the free stream, and for the periodic removal of mass from the cavity. Under proper conditions of phase and amplitude, the behavior of the pseudopiston and the dynamics of the cavity are related so that a self-sustaining feedback mechanism occurs. Of course, the details depend on freestream conditions and cavity geometry.

The pseudopiston analysis relates the strength and phase of the fictitious piston to the phase and amplitude of the shear layer at the trailing edge, and to the freestream flow conditions and the cavity geometry.

A.2 Analytical Model for the Pseudopiston Process

The actual process of mass introduction and removal at the trailing edge is complicated and messy. Section 3.2.3 gives a general explanation of this process; thus, it is sufficient to state here that a given mass flow is introduced or extracted at the trailing edge. The relation between this mass-flow rate and the shear layer structure and deflection will be discussed later. Our present concern is the piston-like behavior of this mass flow.

The pseudopiston can be modeled in several ways: e.g., as a simple mass flow model, or as a thermodynamic mass addition model.

A.2.1 Simple Mass Flow Model

In this kinematic approach, the motion of the fictitious piston is related directly to the mass flow rate. Once introduced into the cavity, the fluid is assumed to have the same thermodynamic properties as the fluid already in the cavity: namely, freestream static pressure and stagnation temperature (approximately). Hence, the fluid density is determined by $\rho_c = p_\infty / RT_c$.

Then, if mass flows are equated, we obtain

$$\dot{m}(t) = \rho_c DV_p(t), \quad (A.1)$$

or

$$V_p(t) = \frac{\dot{m}(t)}{\rho_c D}. \quad (A.2)$$

The piston displacement is determined directly from the specified mass addition or removal. Steady flow assumptions are used. However, no allowance is made for the effect of the unsteady expansion that the added flow must undergo to achieve the thermodynamic conditions in the cavity. Furthermore, there is no pressure-matching condition across the interface between the cavity fluid and the newly added fluid, since these pressures were assumed to be approximately equal. This model is illustrated in Fig. 86.

A.2.2 Thermodynamic Mass Addition Model

This more refined model accounts for the important thermodynamic and dynamic effects of the mass addition process as it relates to the behavior of a fictitious piston, or pseudopiston. This process is illustrated in Fig. 87a.

Another model, which is really equivalent, is shown in Fig. 87b. This model is based on the idea that there is a steady-state mass addition, \dot{m}_s , into the cavity, and that mass addition and removal are perturbations around this steady-state value. The effective mass addition or removal is given by $\dot{m}_e = \dot{m}_r - \dot{m}_s$, where $\dot{m}_r(t)$ is the actual mass addition at the trailing edge; it is related to the instantaneous shear layer position in an unprescribed manner. For present purposes, \dot{m}_e can be considered a given function of time. Likewise, the piston displacement can be considered as a specified function. These parameters could be interrelated by matching pressure and displacement across the piston and by specifying the relation between the mass flow and shear layer displacement.

The reservoir enthalpy is given and assumed independent of time. Its value may represent some average value found in the shear layer. With this analysis, we can assume that the enthalpy of fluid injected into the cavity is the free-stream enthalpy, because use of a recovery factor makes a difference of only a few percent. This assumption was confirmed by temperature measurements (see Sec. 6.4).

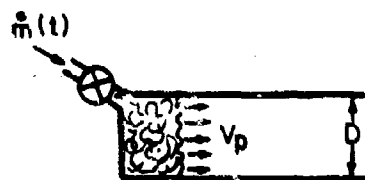


FIG. 86. SIMPLE MASS FLOW MODEL.

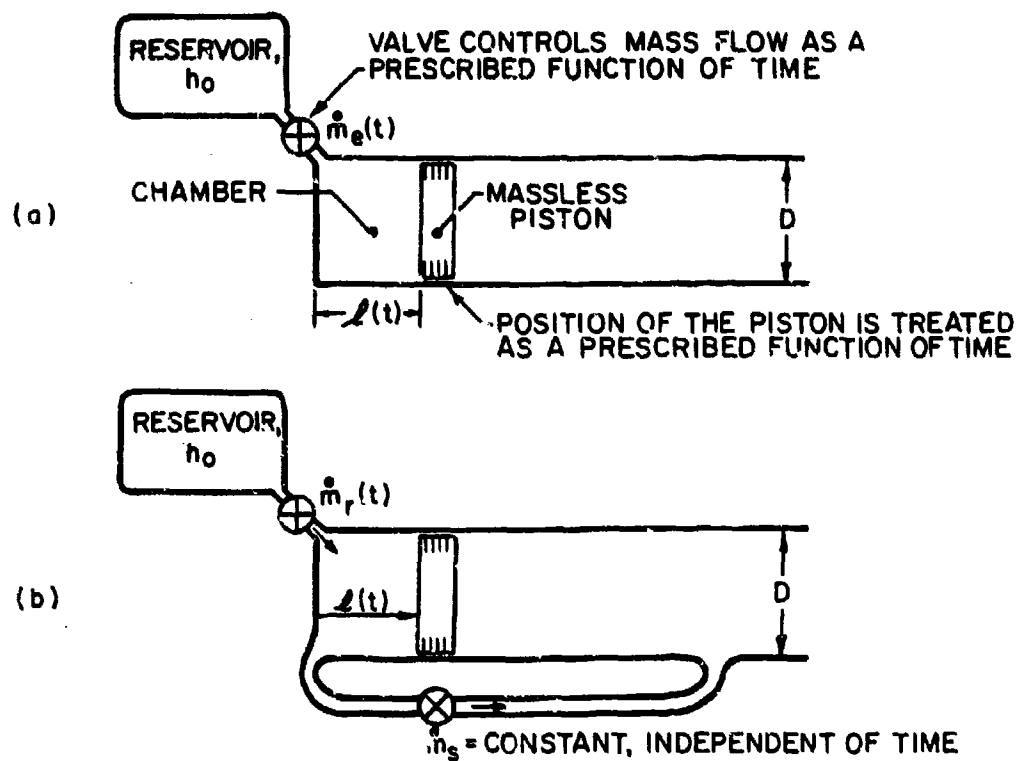


FIG. 87. TWO EQUIVALENT REPRESENTATIONS OF THE THERMODYNAMIC MASS ADDITION MODEL.

The size of the mass addition region, l , is small compared to the length of the cavity, L , which means that the time scale for the oscillation, L/a_0 , is long compared to the time scale for adjustment of conditions within the mass addition region, l/a_0 . In comparison to the time scale of oscillation, the mass addition region has considerable time to adjust to changes in pressure, mass flow, etc., which are produced by the oscillation cycle. Therefore, we can assume that significant departures from thermodynamic equilibrium do not occur in the mass addition region. This justifies the quasi-steady treatment of the mass addition region and the assumption of uniform properties throughout the mass addition chamber. Furthermore, the pressure and energy changes resulting from flow velocity in this region are neglected, since the velocity is presumably small enough to make these effects insignificant.

The mass in the imaginary chamber is

$$\rho(t)Dl(t) = \rho_0 D l_0 + \int_{t_0}^t \dot{m}_e(t) dt, \quad (A.3)$$

where $\dot{m}_e(t_0)$ is equal to zero. For steady flow, l_0 is not necessarily the steady-state value of $l(t)$. The reference value, ρ_0 , is a constant density in the cavity corresponding to conditions at time, t_0 .

At this time $\dot{m}_e(t)$ and $l(t)$ can be considered as given functions of time. Therefore, the density in the chamber is

$$\rho(t) = \rho_0 \frac{l_0}{l(t)} + \frac{\int_{t_0}^t \dot{m}_e(t) dt}{l(t)D}. \quad (A.4)$$

This equation determines the density in terms of quantities assumed given. The equation of state then relates pressure and temperature:

$$p(t) = \rho(t)RT(t), \quad (A.5a)$$

$$p_0 = \rho_0 RT_0, \quad (A.5b)$$

and

$$p_\infty = \rho_c RT_0. \quad (A.5c)$$

for steady-flow conditions.

If we neglect the effect of flow velocity in the chamber, the energy equation is

$$\Delta E = Q + W + E_{MA} \quad , \quad (A.6)$$

where ΔE is the change in internal energy, Q is the heat addition (e.g., heat transfer to or from system), W is the work done on the fluid volume in the chamber (e.g., by the piston), and E_{MA} is the energy addition due to mass addition.

Assuming that significant heat transfer does not occur in the chamber during an oscillation cycle, let $Q = 0$.

The energy equation expressed in detail is:

$$E(t) - E_0 = - \int_{t_0}^t p D \dot{l}(t) dt + \int_{t_0}^t \dot{m}_e(t) h_0 dt \quad . \quad (A.7)$$

Note that $E_0 - E(t_0)$ and $l_0 = l(t_0)$ are reference values determined at $t = t_0$; they are not necessarily the corresponding steady-state values. Nor does the formulation given thus far require that they be steady-state values. The time, t_0 , is chosen so that $\dot{m}(t_0) = 0$.

The specific internal energy is $e(t)$. The temperature is $T(t)$, and

$$E(t) = \rho(t) l(t) D e(t) = \rho l D (c_v T + K) \quad , \quad (A.8)$$

where K is a constant.

Thus,

$$E(t) - E_0 = \rho l D c_v T(t) - \rho_0 D l_0 c_v T(t_0) + DK(\rho l - \rho_0 l_0) \quad . \quad (A.9)$$

Substituting into the energy equation,

$$\begin{aligned} \rho l D c_v T &= \rho_o l_o D c_v T(t_o) + K D (\rho l - \rho_o l_o) \\ &= - \int_{t_o}^t p D \dot{l} dt + \int_{t_o}^t \dot{m}_e(t) h_o dt \end{aligned} \quad (A.10)$$

Differentiating

$$(\rho \dot{l} D)(c_v T + K) + (\rho l D) c_v \dot{T} = -p D \dot{l} + \dot{m}_e h_o \quad (A.11)$$

Using the density relation, (Eq. A.3), we obtain

$$(\rho \dot{l} D) = \dot{m}_e \quad (A.12)$$

Thus,

$$\dot{m}_e (c_v T + K) + \left[(\rho_o D l_o) + \int_{t_o}^t \dot{m}_e dt \right] c_v \dot{T} + p D \dot{l} = \dot{m}_e h_o \quad (A.13)$$

and

$$c_v \left[(\rho_o D l_o) + \int_{t_o}^t \dot{m}_e dt \right] \dot{T} + \dot{m}_e c_v T + p D \dot{l} = \dot{m}_e (h_o - K) = \dot{m}_e c_p T_o \quad (A.14)$$

where T_o is the freestream stagnation temperature.

Next,

$$p = \rho R T = R T \left(\rho_o \frac{l_o}{l} + \frac{\int_{t_o}^t \dot{m}_e dt}{l D} \right) \quad (A.15)$$

and, therefore,

$$pD\dot{l} = RT \left[(\rho_o l_o D) \frac{\dot{l}}{l} + \frac{\dot{l}}{l} \int_{t_o}^t \dot{m}_e dt \right] . \quad (A.16)$$

Substituting into Eq. A.14 gives

$$c_v \left[(\rho_o D l_o) + \int_{t_o}^t \dot{m}_e dt \right] \dot{T} + \left[\dot{m}_e c_v + R(\rho_o l_o D) \frac{\dot{l}}{l} + R \frac{\dot{l}}{l} \int_{t_o}^t \dot{m}_e dt \right] T = \dot{m}_e c_p T_o , \quad (A.17)$$

from which

$$\dot{T} + \left[\frac{\dot{m}_e}{(\rho_o D l_o + \int_{t_o}^t \dot{m}_e dt)} + (\gamma - 1) \frac{\dot{l}}{l} \right] T = \frac{\dot{m}_e \gamma T_o}{\rho_o D l_o + \int_{t_o}^t \dot{m}_e dt} , \quad (A.18)$$

where $R = c_p - c_v$, and $\gamma = \frac{c_p}{c_v}$; therefore, $\frac{R}{c_v} = \gamma - 1$.

The above is a first-order ordinary differential equation for temperature, T . The solution is

$$T = \frac{1}{l^{\gamma-1} (\rho_o D l_o + \int_{t_o}^t \dot{m}_e dt)} \left(\dot{m}_e \gamma T_o l^{\gamma-1} dt + C \right) , \quad (A.19)$$

where C is an arbitrary constant. Using Eq. A.15, the pressure is, therefore,

$$p = \frac{R}{D} \gamma T_o l^{-\gamma} \int l^{\gamma-1} \dot{m}_e dt + C \frac{R}{D} l^{-\gamma} . \quad (A.20)$$

The above expression gives the pressure in terms of $l(t)$ and $\dot{m}_e(t)$. The second term, containing the arbitrary constant, corresponds to an adiabatic compression without mass addition or removal. The constant is determined by the volume and energy of the gas being compressed.

Note that if the arbitrary constant is set equal to zero, and if it is further assumed that \dot{m}_e is directly proportional to l , the result is

$$p = \frac{R}{D} C_s T_0, \quad (A.21)$$

where \dot{m}_e is $C_s l$.

Mass conservation suggests

$$\dot{m}_e = \rho_c D \dot{l} \Rightarrow C_s = \rho_c D. \quad (A.22)$$

Thus, for this special case, we have constant pressure $p = \rho_c R T_0 = p_c (= p_\infty)$. The flow into the cavity is treated as being quasi-steady. Therefore, with this mass conservation assumption, we have the same result that would be obtained using the simple mass flow model for the pseudopiston. Thus, the second model developed in this section is consistent with the first when we make the same assumptions.

A.3 Discussion of Mass Flow, Shear Layer Deflection, and Pseudopiston Motion

The analytical model for mass addition at the rear of the cavity relates the pressure of a fictitious piston to the piston displacement and the mass flow rate behind the piston. The time-dependent mass flow rate depends on the shear layer deflection process at the trailing edge. The shear layer deflection is itself dependent on the piston displacement. This dependence is determined by solving the problem of shear layer forcing by waves in the cavity which are generated by the piston. This solution involves the dynamics of the cavity as a whole, and it is discussed in Sec. 4.

From this analysis, a prescribed piston displacement, $l(t)$, will determine the pressure, $p(t)$, on the front face of the piston and the shear layer amplitude near the trailing edge, $\eta_{T.E.}(t)$. If the mass flow relation, $\dot{m}_e[l(t)]$, were also known, it would be possible to match displacements and pressures with the analytical model for the pseudopiston and determine the oscillatory behavior in this manner. The actual process of mass addition at the trailing edge is extremely complex, and perhaps it cannot be modeled analytically to the required accuracy.

Nevertheless, the present analysis is sufficient to indicate the general dependence of the mass addition process on geometry and flow parameters.

In relating $\dot{m}_e(t)$ to $\eta_{T,E}(t)$ and $l(t)$, there are essentially two problems: the phase relation, and the functional dependence with time. It seems reasonable to believe that $\dot{m}_e(t)$ and $\eta_{T,E}(t)$ could be directly in phase with a negative deflection producing a positive mass flow. Furthermore, from a pseudopiston viewpoint, the mass flow causes the displacement so that we might expect \dot{m}_e to be in phase with l . Figure 88 illustrates this graphically.

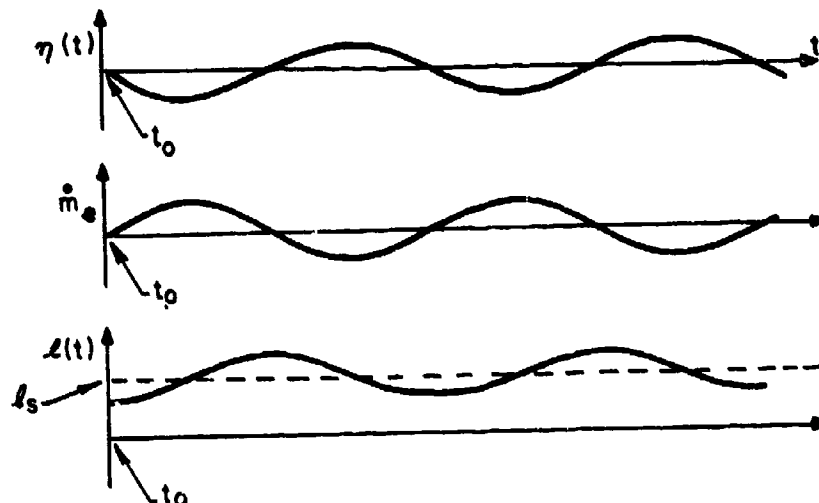


FIG. 88. COMPARISON OF THE TIME BEHAVIOR OF THE SHEAR LAYER DISPLACEMENT, THE MASS FLOW RATE, AND THE PSEUDO-PISTON MOTION.

Although the mass addition process is complex and involves the dynamics of a stagnation point within an unsteady shear layer, the assumption of an in-phase relation between \dot{m}_e and $\eta_{T,E}$ seems reasonable. The relation between $\eta_{T,E}$ and $l(t)$ depends on the dynamics of the whole cavity, and it is not necessary that $\eta_{T,E}$ and $l(t)$ be exactly in phase. There could be a phase shift because of the pressure-matching relation across the pseudopiston. When waves are forced by a piston in a rectangular enclosure, the pressure and displacement at the piston are in phase and the pressure and velocity are out of phase, so that no net work is done. In the cavity problem, energy is radiated from and added

to the system. Presumably, this is manifested as a phase shift between pressure and velocity that is imposed by the effects of shear layer motion.

The greatest source of uncertainty, however, involves the functional relation between \dot{m}_e and $\eta_{T.E.}$. If shear layer deflection is small compared to shear layer thickness, then a linear relation between mass flow and displacement is likely. If displacements of the order of the shear layer thickness are expected, then the functional dependence is more uncertain and is probably complicated.

The expression for pressure, determined from the previous section, is

$$p = \frac{R}{D} \gamma T_0 l^{-\gamma} \int l^{\gamma-1} \dot{m}_e dt + C \frac{R}{D} l^{-\gamma} \quad (A.23)$$

This expression is nonlinear in $l(t)$. If displacements of the chamber are small compared to its steady-state size, i.e., $[l(t) - l_s] / [l(t)] \ll 1$, then the expression can be linearized. This condition corresponds to shear layer displacements that are small compared to shear layer thickness. If, on the other hand, shear layer displacements are of the order of its thickness, the expression for p cannot be linearized with respect to l . In this case, an alternative for analytical purposes is to assume a mass flow dependence on displacement, $\dot{m}_e[l(t)]$, which gives a tractable functional form for the pressure in terms of displacement. Such an approach is somewhat arbitrary because it contains the assumption that an extremely complex process will adjust its behavior to some simple form. However, it receives support because the rest of the cavity would like to behave in a simple modal way. An example of this approach was previously illustrated by the assumption $\dot{m}_e \propto l$, for the quasi-steady flow model. Similarly, more refined forms can be assumed to give the pressure in a desired functional form.

Now let us return to the possibility of linearizing the pressure expression when shear layer displacements are small. Let $\eta_{T.E.}$ be small and $(l - l_s)/l \ll 1$. Write $l = l_s(1 + \epsilon l_1)$ and $\eta_{T.E.} = \epsilon \eta_1$, where ϵ is the maximum of the small amplitude. Let $\dot{m}_e = \rho_{sl} U_{sl} \epsilon \eta_1$, where the $\rho_{sl} U_{sl}$ is the product of density in the shear layer and a characteristic shear layer velocity. Then,

$$p = \gamma \frac{R}{D} T_o \ell^{-\gamma} \int \ell^{\gamma-1} \dot{m}_e dt + C \frac{R}{D} \ell^{-\gamma} . \quad (A.24)$$

Substituting,

$$p = \epsilon \frac{R\gamma T_o}{D\ell_s} \rho_{s\ell} U_{s\ell} \int \eta_1 dt + C \frac{R}{D} \ell_s^{-\gamma} (1 + \epsilon \ell_1)^{-\gamma} + O[\epsilon^2] . \quad (A.25)$$

Now

$$(1 + \epsilon \ell_1)^\gamma = e^\gamma \ln(1 + \epsilon \ell_1) e^{\gamma\{\epsilon \ell_1 + O[\epsilon^2]\}} = 1 + \gamma \epsilon \ell_1 + O[\epsilon^2] ,$$

and

$$p = C \frac{R}{D} \ell_s^{-\gamma} + \epsilon \left(\frac{R\gamma T_o}{D\ell_s} \rho_{s\ell} U_{s\ell} \int \eta_1 dt + C \frac{R}{D} \ell_s^{-\gamma} \gamma \ell_1 \right) + O[\epsilon^2] . \quad (A.26)$$

Choose the arbitrary constant C so that

$$C \frac{R}{D} \ell_s^{-\gamma} = P_c = P_\infty \Rightarrow C = P_c \frac{D}{R} \ell_s^\gamma . \quad (A.27)$$

Therefore,

$$p = p_c + \epsilon \left(\frac{R\gamma T_o}{D\ell_s} \rho_{s\ell} U_{s\ell} \int \eta_1 dt + p_c \gamma \ell_1 \right) + O[\epsilon^2] . \quad (A.28)$$

Note that to order ϵ the pressure changes from mass addition and piston displacement are uncoupled and simply added. Cross terms will appear at $O[\epsilon^2]$. As mentioned before, the relation between η_1 and ℓ_1 results from determining the dynamics of the whole cavity forced by a piston, which is an essentially separate problem.

In practice, there is really no way to determine theoretically ℓ_s , which is the spanwise size of the mass injection and mixing region at the rear bulkhead. The product, $\ell_s D$, is the volume of this region. Roughly, $\ell_s = \beta D$, where β is some constant $< O[1]$.

For shallow cavities, it is possible that δ may be relatively independent of overall cavity geometry and external flow conditions.

Since $p_c = \rho_c RT_o$, let us write

$$\frac{p}{p_c} = 1 + \epsilon \left[\frac{\gamma}{\beta D^2} \left(\frac{\rho_{sl}}{\rho_c} \right) U_{sl} \int \eta_1 dt + \gamma \ell_1 \right] . \quad (A.30)$$

Assume the velocity in the shear layer is $\frac{1}{2}\alpha U_\infty$, where $\alpha \sim O[1]$. This should be the velocity on the dividing streamline of the shear layer near the trailing edge, i.e., the streamline dividing mass entrained from above and the mass entrained from below. If the stagnation enthalpy is unchanged through the shear layer, then

$$h_o = c_p T_o = h + \frac{1}{2}V^2 = c_p T + \frac{1}{2}V^2 , \quad (A.31)$$

$$\frac{T}{T_o} = 1 - \frac{V^2}{2c_p T_o} , \quad (A.32)$$

$$\rho_{sl} = \frac{p_{sl}}{RT_{sl}} = \frac{p_\infty}{RT_o (1 - V^2/2c_p T_o)} , \quad (A.33)$$

and

$$\rho_c = \frac{p_\infty}{RT_o} .$$

Therefore,

$$\frac{\rho_{sl}}{\rho_c} = \frac{1}{1 - V^2/2c_p T_o} = \frac{1}{1 - \alpha^2 U_\infty^2/8c_p T_o} . \quad (A.34)$$

Since $a_\infty = \sqrt{\gamma RT_0}$, $R = c_p - c_v$, and $\gamma = c_p/c_v$, this becomes:

$$\frac{\rho_{sl}}{\rho_c} = \frac{1 + \frac{\gamma-1}{2} M_\infty^2}{1 + \left(1 - \frac{\alpha^2}{4}\right) \frac{\gamma-1}{2} M_\infty^2} \quad (A.35)$$

Finally,

$$U_\infty = M_\infty a_\infty = M_\infty \sqrt{\gamma RT_\infty} = \frac{M_\infty \sqrt{\gamma RT_0}}{\sqrt{1 + \frac{\gamma-1}{2} M_\infty^2}} \quad (A.36)$$

Thus,

$$\epsilon p_1 = \frac{p - p_c}{p_c} = \frac{\gamma^{3/2} (RT_0)^{1/2}}{D^2} \frac{\sqrt{1 + \frac{\gamma-1}{2} M_\infty^2}}{\left[1 + \left(1 - \frac{\alpha^2}{4}\right) \frac{\gamma-1}{2} M_\infty^2\right]} M_\infty \left(\frac{\alpha}{\beta}\right) \int \epsilon \eta_1 dt + \gamma \epsilon l_1 \quad (A.37)$$

This result gives the perturbation pressure of the pseudopiston in terms of effective piston displacement and shear layer displacement based on a linearization of the pressure relation derived earlier. The linearized model implies a specific set of assumptions about the working of the pseudopiston mechanism.

APPENDIX B
TABLES OF ROOTS

Root A
(to obtain A* replace i with -i everywhere)

M		S = 1.0	S = 0.5	S = 0.1
0.1	K	-10.035 + i 110.000	-5.017 + i 15.000	-1.103 + i 10.958
	±T	-10.010 + i 110.025	-5.005 + i 15.012	-1.100 + i 10.960
	±B	9.975 + i 110.060	4.987 + i 15.029	0.956 + i 11.105
	C _p	- 0.050 - i 0.050	-0.050 - i 0.050	-0.052 - i 0.045
0.5	K	- 2.134 + i 1.984	-1.170 + i 10.948	-0.319 + i 10.281
	±T	- 2.012 + i 2.105	-1.107 + i 11.002	-0.310 + i 10.289
	±B	1.862 + i 2.251	0.886 + i 11.214	0.254 + i 10.322
	C _p	- 0.251 - i 0.234	-0.258 - i 0.209	-0.177 - i 0.156
1.0	K	- 1.348 + i 0.919	-0.768 + i 10.504	-0.202 + i 10.159
	±T	- 1.107 + i 1.119	-0.658 + i 10.589	-0.187 + i 10.172
	±B	0.677 + i 1.487	0.341 + i 10.811	0.087 + i 10.200
	C _p	- 0.506 - i 0.345	-0.455 - i 0.299	-0.306 - i 0.241
1.5	K	- 1.142 + i 0.587	-0.642 + i 10.338	-0.172 + i 10.103
	±T	- 0.807 + i 0.831	-0.493 + i 10.441	-0.151 + i 10.117
	±B	0.181 + i 1.228	0.052 + i 10.654	-0.023 + i 10.156
	C _p	- 0.693 - i 0.356	-0.610 - i 0.321	-0.428 - i 0.256
3.0	K	- 1.060 + i 0.234	-0.587 + i 10.166	-0.161 + i 10.066
	±T	- 0.534 + i 0.465	-0.370 + i 10.264	-0.134 + i 10.079
	±B	- 1.113 + i 0.728	-0.732 + i 10.496	-0.274 + i 10.190
	C _p	- 0.900 - i 0.199	-0.789 - i 0.223	-0.532 - i 0.218

NOTES: $T = \alpha D$ and $T^2 = K^2 - S^2$, where $K = kD$ and $S = \frac{\omega D}{a_c}$ and $\tilde{a} = \frac{a_c}{a_\infty}$.

$B = \beta D$ and $B^2 = Q - K^2$, where $Q = (MK + \tilde{a}S)^2$.

$C_p = \frac{C}{a_c}$, where $C_p = \frac{\omega}{K}$ is the phase speed. Thus $C_p = \frac{S}{K}$.

Dispersion Relation: $Q^2 T^2 \sinh^2 T + S^4 (Q - K^2) \cosh^2 T = 0$.

Root B
(to obtain B* replace i with -i everywhere)

M		S = 1.0	S = 0.5	S = 0.1
0.1	K	-1.151 + 11.028	-0.735 + 11.000	-0.131 + 10.677
	±T	-0.934 + 11.267	-0.679 + 11.082	-0.130 + 10.684
	±B	1.246 + 11.023	1.075 + 10.724	0.681 + 10.139
	C _p	-0.483 - 10.432	-0.239 - 10.325	-0.028 - 10.142
0.5	K	-0.653 + 10.728	-0.262 + 10.640	0.011 + 10.275
	±T	-0.420 + 11.131	-0.210 + 10.797	0.010 + 10.293
	±B	0.997 + 10.732	0.735 + 10.394	0.265 + 10.045
	C _p	-0.683 - 10.761	-0.274 - 10.669	0.015 - 10.363
1.0	K	-0.516 + 10.542	-0.189 + 10.455	-0.009 + 10.187
	±T	-0.267 + 11.048	-0.130 + 10.662	-0.008 + 10.212
	±B	0.793 + 10.746	0.548 + 10.455	0.161 + 10.127
	C _p	-0.921 - 10.968	-0.389 - 10.937	-0.026 - 10.534
1.5	K	-0.469 + 10.431	-0.175 + 10.365	-0.019 + 10.159
	±T	-0.202 + 11.003	-0.106 + 10.603	-0.061 + 10.188
	±B	0.660 + 10.798	0.461 + 10.542	0.126 + 10.198
	C _p	-1.156 - 11.062	-0.534 - 11.114	-0.074 - 10.620
3.0	K	-0.438 + 10.268	-0.176 + 10.246	-0.022 + 10.123
	±T	-0.124 + 10.947	-0.081 + 10.535	-0.017 + 10.157
	±B	0.445 + 10.914	0.365 + 10.744	0.114 + 10.352
	C _p	-1.661 - 11.016	-0.969 - 11.344	-0.141 - 10.788

Root C
(to obtain C* replace i with -i everywhere)

M		S = 1.0	S = 0.5	S = 0.1
0.1	K	1.183 + 10.102	0.921	0.484
	±T	0.650 + 10.185	0.774	0.474
	±B	-0.246 + 10.444	10.705	10.461
	C _p	0.839 - 10.072	0.543	0.207
0.5	K	1.038 + 10.240	0.586 + 10.187	0.182 + 10.057
	±T	0.509 + 10.489	0.378 + 10.290	0.156 + 10.067
	±B	-1.163 + 10.055	-0.579 + 10.059	-0.096 + 10.050
	C _p	0.915 - 10.211	0.774 - 10.247	0.500 - 10.157
1.0	K	1.019 + 10.205	0.556 + 10.174	0.164 + 10.079
	±T	0.455 + 10.459	0.335 + 10.289	0.139 + 10.093
	±B	1.857 + 10.121	0.959 + 10.099	0.222 + 10.039
	C _p	0.943 - 10.190	0.819 - 10.256	0.459 - 10.238
1.5	K	1.013 + 10.169	0.541 + 10.149	0.154 + 10.075
	±T	0.412 + 10.415	0.303 + 10.267	0.128 + 10.090
	±B	2.530 + 10.205	1.308 + 10.180	0.317 + 10.088
	C _p	0.960 - 10.160	0.859 - 10.237	0.525 - 10.256
3.0	K	1.005 + 10.104	0.518 + 10.098	0.135 + 10.058
	±T	0.323 + 10.324	0.235 + 10.216	0.103 + 10.076
	±B	4.580 + 10.297	2.334 + 10.280	0.556 + 10.165
	C _p	0.985 - 10.102	0.932 - 10.176	0.625 - 10.269

Root D

M		S = 1.0	S = 0.5	S = 0.1
0.1	K	-20.010	-10.005	-2.019
	±T	19.980	9.992	2.017
	±B	119.980	19.992	12.016
	C _p	- 0.050	- 0.050	-0.050
0.5	K	- 4.050	- 2.043	-0.498
	±T	3.925	1.981	0.488
	±B	13.925	11.979	10.476
	C _p	- 0.247	- 0.245	-0.201
1.0	K	- 2.117	- 1.112	-0.288
	±T	1.866	0.993	0.270
	±B	11.854	10.958	10.226
	C _p	- 0.472	- 0.450	-0.347
1.5	K	- 1.519	- 0.808	-0.198
	±T	1.143	0.635	0.171
	±B	11.074	10.530	10.090
	C _p	- 0.658	- 0.619	-0.505
3.0	K	- 0.820	- 0.417	-0.084
	±T	10.572	10.276	10.054
	±B	10.231	10.047	0.011
	C _p	- 1.220	- 1.199	-1.190

Root E

M		S = 1.0	S = 0.5	S = 0.1
0.1	K	-0.919	-0.456	-0.091
	±T	10.394	10.205	10.041
	±B	10.135	10.032	10.000
	C _p	-1.088	-1.096	-1.099
0.5	K	-0.716	-0.345	-0.068
	±T	10.698	10.362	10.073
	±B	10.261	10.059	0.008
	C _p	-1.397	-1.449	-1.471
1.0	K	-0.574	-0.277	-0.055
	±T	10.819	10.416	10.084
	±B	10.240	10.059	10.007
	C _p	-1.742	-1.805	-1.818
1.5	K	-0.500	-0.243	-0.048
	±T	10.866	10.437	10.088
	±B	10.209	10.051	0.006
	C _p	-2.000	-2.058	-2.083
3.0	K	-0.428	-0.210	-0.042
	±T	10.904	10.454	10.091
	±B	10.178	10.037	10.007
	C _p	-2.336	-2.381	-2.381

APPENDIX C

AERODYNAMIC FLOW STABILIZATION THROUGH A SLANTED TRAILING EDGE

This section will present the physical and theoretical basis for slanting the upper portion of the cavity trailing-edge bulkhead as a means of reducing pressure oscillations in the cavity. Although this is a simple modification, a considerable reduction of levels has been observed experimentally. Slanting the edge seems to be more effective than other modifications of roughly the same size, such as rounding the trailing edge. By studying the reasons for the success of this modification, we can reach a deeper understanding of the shear layer impingement process at the trailing edge.

First, it is appropriate to recall the discussion in Sec. 3.2 entitled Steady-Flow Considerations. It was argued that the shear layer must have a stagnation point at the trailing edge, and that part of the shear layer flow must be returned to the cavity (to replenish entrained fluid) and the rest must go downstream with the mean flow. This view of the steady-flow configuration was then used to explain the mass addition and removal processes at the trailing edge, when the shear layer behaves in an unsteady manner.

The trailing-edge stagnation point must lie within the shear layer itself, and it is expected that the stagnation streamline will be near the center of the shear layer, where the vorticity is greatest. Therefore, it is of interest to examine in some detail the stagnation flow when the flow has vorticity. The physics of this process is examined below in a simplified form. The effects that have been neglected can be expected to alter the flow details, but they will not affect the conclusion.

Consider the nature of the local region around the stagnation point, i.e., a region of dimensions less than the shear layer thickness. It is appropriate to assume a two-dimensional incompressible flow in this region. Shear layer solutions, either laminar or turbulent, show that the shear is nearly constant (constant vorticity) in the middle region of the layer. Therefore, an irrotational stagnation-point flow and a simple shear flow will be combined to find the actual streamline pattern near the stagnation point. For the present case, the stream functions can be simply added together. Generally, stream functions for rotational and irrotational flows cannot be simply combined, because the equations of motion are nonlinear

due to the presence of the convection terms when the flow has vorticity. However, this simple addition can be done when certain conditions are satisfied. The flow must be two-dimensional, the vorticity must be constant everywhere, and the rotational and irrotation parts must independently satisfy the same boundary geometry. In the present case, these conditions are satisfied as long as the region of validity is restricted to the immediate neighborhood of the stagnation point and the orientation of the simple shear flow is correctly chosen.

The stream function of a stagnation point in a constant vorticity flow is

$$\psi = axy + \frac{1}{2} by^2, \quad (C.1)$$

where the first term is the stagnation point, and the second is the shear flow. The corresponding velocity components are

$$u = \frac{\partial \psi}{\partial y} = ax + by, \quad (C.2)$$

and

$$v = -\frac{\partial \psi}{\partial x} = -ay. \quad (C.3)$$

The constant a is related to the strength of the stagnation-point flow, while the constant b is related to the strength of the shear. The vorticity is

$$\zeta = -\frac{\partial u}{\partial y} = -b. \quad (C.4)$$

The streamline pattern is shown in Fig. 89, where the values of the constants have been absorbed into the coordinates. Nevertheless, Fig. 89 gives a realistic picture of the actual flow pattern. The important conclusion is that the effect of shear is to change the direction of the stagnation streamline (and, presumably, the centerline of the shear layer), so that the flow must impinge on the wall (cavity rear bulkhead) at an oblique angle. It cannot impinge normal to the wall, as in the case of no shear.

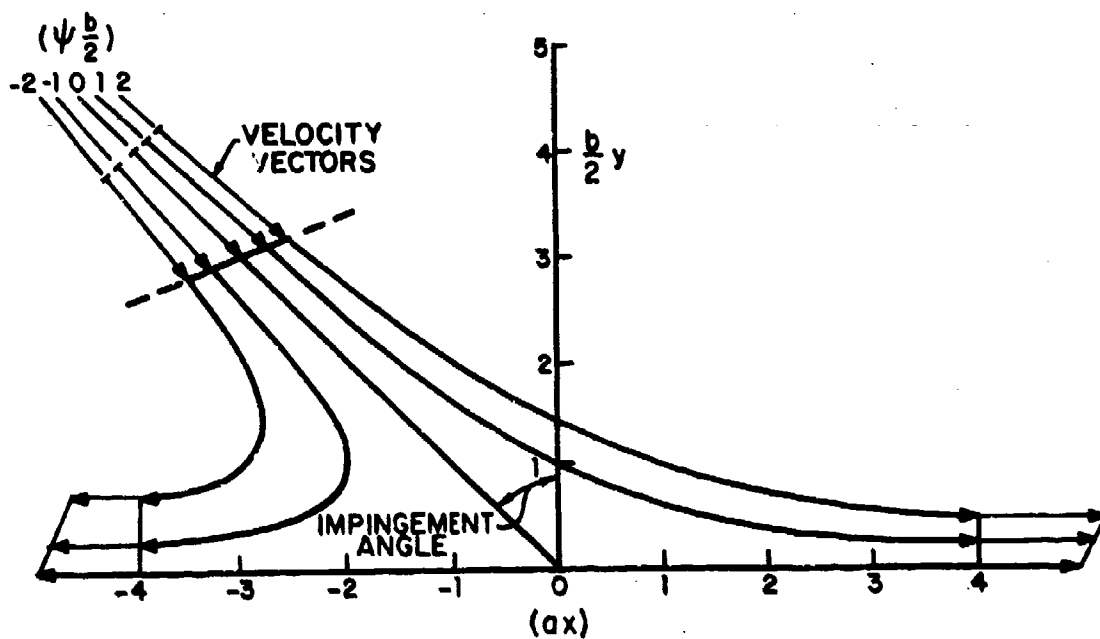


FIG. 89. STAGNATION-POINT FLOW WITH CONSTANT VORTICITY.

The fact that the flow impinges at an angle has a simple physical explanation. Shear flow has a velocity gradient; i.e., velocities are higher on the freestream side of a shear layer than on the cavity side. As the flow impinges on a wall, the streamlines must curve, which introduces centrifugal pressure forces. If the flow were symmetrical about the stagnation streamline, the opposing pressures would not balance because the velocity is higher on one side. However, if the streamline radii of curvature are made larger on the high velocity side and smaller on the low velocity side, then a balance can be achieved.

This conclusion has definite implications for the phenomena of cavity oscillations. In order to suppress oscillations, a steady flow must be physically possible. Figure 90a depicts the behavior of the shear layer in a conventional cavity configuration. Note that the information about the angle of the stagnation streamline near the rear bulkhead was incorporated into Fig. 90a, since this must be true in a steady flow. In order to meet this condition, a considerable curvature of the shear layer over the cavity mouth is required. This curvature will cause the freestream flow to produce static pressure variations over the cavity mouth that cannot be balanced by the pressure within the cavity, which is uniform to first approximation (recirculation velocities are much less than the freestream velocity). Hence, an unsteady motion of the shear layer will result. Alternatively, if the shear layer is assumed to be straight so that unbalanced pressures do not occur over the cavity mouth, the impingement angle for steady flow cannot be satisfied and the flow in the immediate vicinity of the rear stagnation point must be unsteady. This type of reasoning suggests that steady-flow configurations over conventional unmodified cavities are difficult, if not impossible, to achieve. When this basic tendency towards unsteadiness is combined with the ability of cavities to sustain a modal unsteady pressure field, which can be coupled to shear layer motion, it is easy to see why the suppression of pressure oscillations is so difficult.

When the portion of the trailing-edge bulkhead that interacts with the shear layer is slanted, a steady-flow solution is much easier to achieve. If the slant angle is properly chosen, the shear layer can remain essentially straight over the cavity mouth and satisfy the proper impingement angle as well. This is illustrated in Fig. 90b, which represents a physically possible steady-flow solution. However, once the major conditions are satisfied, details of the real flow structure may still preclude ever achieving a completely steady state. However, levels of unsteadiness may still be considerably reduced, as the experimental results indicate.

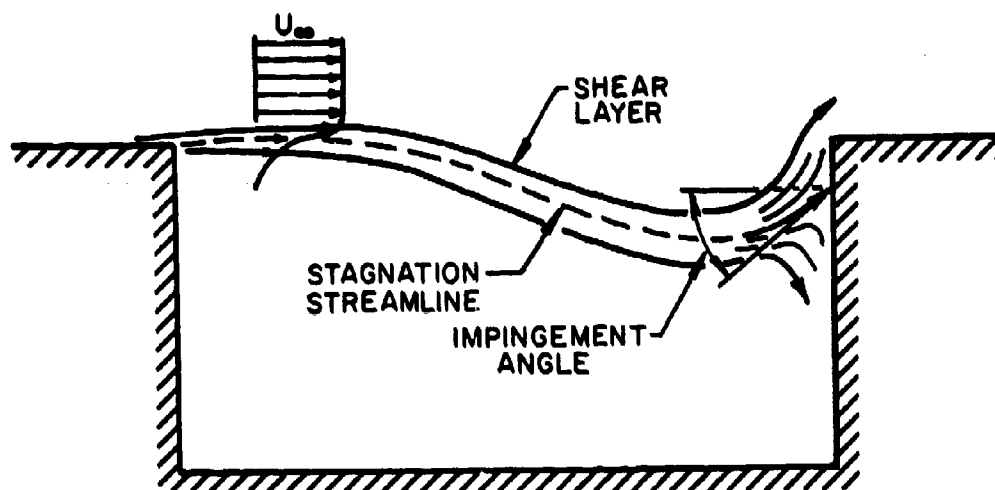


FIG. 90a. FLOW OVER A CONVENTIONAL CAVITY (this configuration cannot be a steady flow).

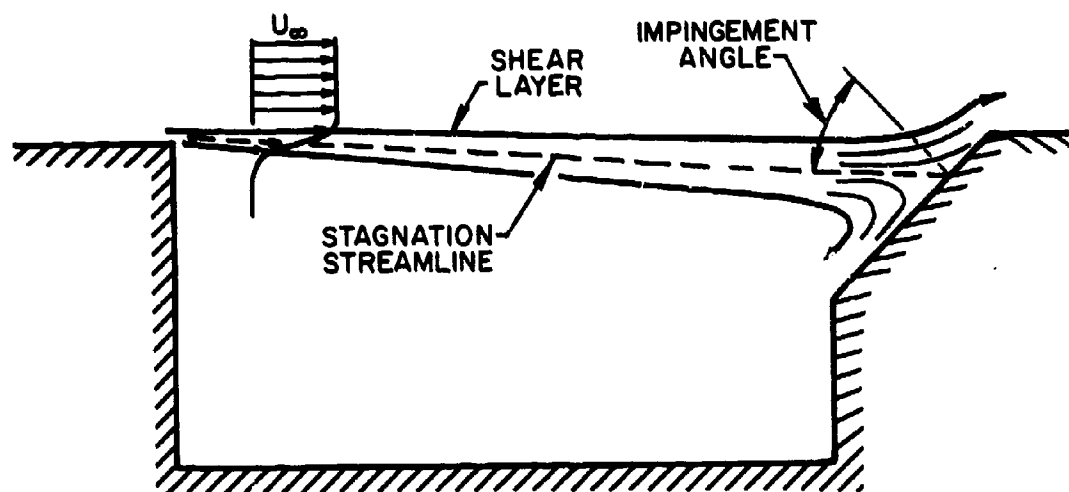


FIG. 90b. FLOW OVER A CAVITY WITH A SLANTED TRAILING EDGE (this configuration could be a steady flow).

Beyond the fact that a steady flow must be possible, the flow must also be stable to disturbances. Small vertical displacements of the shear layer do not strongly affect the impingement process, since the slanted edge has constant slope. This insensitivity should also considerably diminish the mass addition and removal processes that occur when the shear layer is deflected. The constant slope also allows the shear layer to find its own natural vertical level along the slanted edge. This level depends in a complex manner on the pressure and mass flow balances that must be maintained in the cavity. In contrast, a rounded edge has the correct slope for steady impingement at only one vertical height, which may not be the natural position for the shear layer. Furthermore, the geometric slope change, which is caused by a rounded edge when the shear layer is displaced vertically, is such that it adversely affects the stability.

Actual analytical determination of the optimum slant angle based on the mean-flow properties and characteristics of the shear layer is a complicated problem in fluid mechanics. A rough order of magnitude calculation was made which shows that the tangent of the slant angle is of order unity. This means that, typically, the slant angle will be a number like 45° (as opposed to numbers like 10° or 80°). In fact, the current experiments suggest that this number may be near 45° , at least for subsonic speeds. The length of the slanted portion must be large enough to accept the impingement of most of the shear layer thickness and to allow the shear layer to find its natural vertical level. Unfortunately, this factor may mean a fairly large slanted region at the trailing-edge bulkhead, particularly when the shear layer is turbulent. However, reductions in size may be possible by carefully testing the specific configurations.

APPENDIX D

FLOW STABILIZATION THROUGH DETACHED TRAILING-EDGE COWL

A detached cowl placed a small distance upstream of the trailing-edge bulkhead of a rectangular cavity has a stabilizing effect on the otherwise oscillating shear layer. To be effective, this cowl must have a curved surface that faces the flow. The water table flow visualization studies reveal that a half-cylindrical cowl stabilizes the flow under simulated supersonic flow conditions (Fig. 91). For the tests in air, an airfoil shape was used, as shown in Fig. 76.

We believe that stabilization is achieved by accelerating the shear layer over the curved surface; thus, an underpressure at the slot formed between the cowl trailing edge and the cavity bulkhead is created. This underpressure tends to suck fluid mass out of the cavity each time the shear layer attempts to inject mass into the cavity; thus, a cancellation effect is created. In this manner, the effective strength of the trailing-edge mass addition and removal process is greatly reduced.

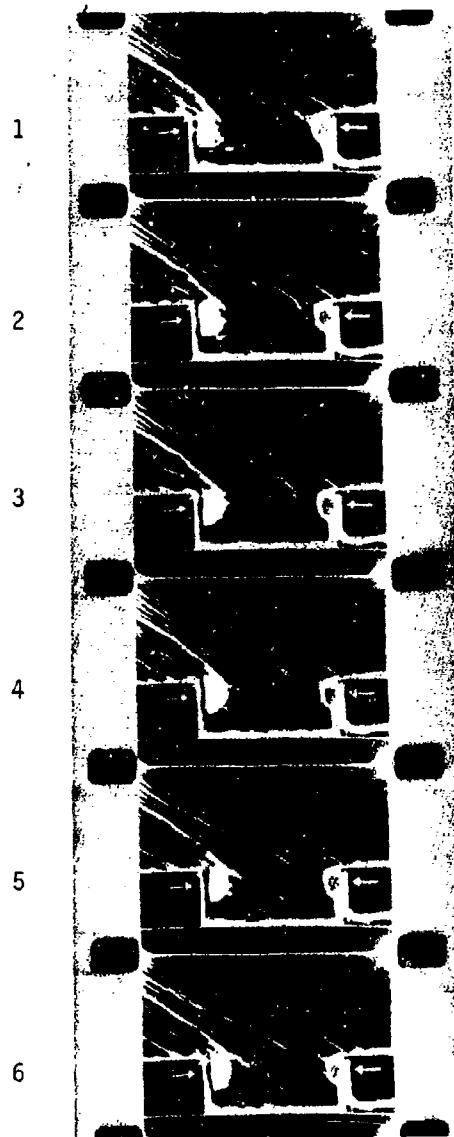


FIG. 91. WATER TABLE VISUALIZATION OF STABILIZED FLOW
THROUGH DETACHED TRAILING-EDGE COWL.

BIBLIOGRAPHY

- Bilanin, A.J. and Covert, E.E. (1973). "Estimation of Possible Excitation Frequencies for Shallow Rectangular Cavities," *AIAA J.* 11:347-351.
- Covert, E.E. (1970). "An Approximate Calculation of the Onset Velocity of Cavity Oscillations," *AIAA J.* 8 (12):2189-2194.
- East, L.F. (1966). "Aerodynamically Induced Resonance in Rectangular Cavities," *J. Sound Vib.* 3 (3).
- Ffowcs-Williams, J.E. and Hawkins, D.L. (1968). "Shallow Water Wave Generation by Unsteady Flow," *J. Fluid Mech.* 31:779-788.
- Gibson, J.E. (1958). "An Analysis of Supersonic Cavity Flow," MIT Aerophysics Lab., Tech. Rept. 299.
- Heller, H., Holmes, G., and Covert, E. (1970). "Flow-Induced Pressure Oscillations in Shallow Cavities," AFFDL-TR-70-104.
- Heller, H., Widnall, S., Jones, J. and Bliss, D. (1973). "Water-Table Visualization of Flow-Induced Pressure Oscillations in Shallow Cavities for Simulated Supersonic Flow Conditions," Paper Z13, presented at 86th Meeting, Acoustical Society of America.
- Ingard, U. and Dean, L.W. (1958). "Excitation of Acoustic Resonators by Flow," *Proc. 2nd Symp. Naval Hydrodynamics*:137-151.
- Karamacheti, K. (1955). "Acoustic Radiation from Two Dimensional Rectangular Cutouts in Aerodynamic Surfaces," NACA TM 3478.
- Leupold, M.J. and Baker, R.W. (1959). "A Report on Research Directed Toward the Design, Development, Construction and Testing of 'Aerodynamic Cavities'," MIT Aerophysics Lab. Tech. Rept. 417.
- Maurer, O. (1974). Oral Communication.

McGregor, O.W. (1969). "Aerodynamic Drag of Two-Dimensional Rectangular Notches in Transonic and Supersonic Turbulent Flow (with Emphasis on the Effects of Self-Induced Pressure Oscillations), Ph.D. Thesis, University of Illinois, Urbana, Illinois.

Plumlee, H.E., Gibson, J.S., and Lassiter, L.W. (1962). "A Theoretical and Experimental Investigation of the Acoustic Response of Cavities in an Aerodynamic Flow," Flight Dynamics Lab., Air Force Systems Command, Wright-Patterson AFB, Ohio, WADD-TR-61-75.

Powell, A. (1961). "On the Edgetone," *J. Acoust. Soc. Am.* 33(4).

Quinn, B. (1963). "Flow in the Orifice of a Resonant Cavity," *AIAA Student J.* 1(1).

Rossiter, J.E. (1966). "Wind Tunnel Experiments on the Flow Over Rectangular Cavities at Subsonic and Transonic Speeds," Royal Aircraft Establishment ARC R&M 3438.

Shaw, L.L., Smith, D.L., Talmadge, R.D. and Seely, D.E. (1974). "Aero-Acoustic Environment of Rectangular Cavities with Length-to-Depth Ratios of Four," AFFDL-TM-74-19-FYA.

Smith, D.L., Shaw, L.L., Talmadge, R.D. and Seely, D.C. (1974). "Aero-Acoustic Environment of Rectangular Cavities with Length-to-Depth Ratios of Five and Seven," AFFDL-TM-74-79-FYA.

Spee, B.M. (1966). "Wind Tunnel Experiments on Unsteady Cavity Flow at High Subsonic Speeds," *AGARD Conference Proc. No. 4, Separated Flows*, Pt. 2, MATA.

White, R.A. and McGregor, O.W. (1970). "Drag of Rectangular Cavities in Supersonic and Transonic Flow Including the Effects of Cavity Resonance," *AIAA J.* 8(11).

UNCLASSIFIED

SECURITY CLASSIFICATION OF THIS PAGE (When Data Entered)

REPORT DOCUMENTATION PAGE		READ INSTRUCTIONS BEFORE COMPLETING FORM
1. REPORT NUMBER AFFDL-TR-74-133	2. GOVT ACCESSION NO.	3. RECIPIENT'S CATALOG NUMBER
4. TITLE (and Subtitle) Aerodynamically Induced Pressure Oscillations in Cavities - Physical Mechanisms and Suppression Concepts		5. TYPE OF REPORT & PERIOD COVERED Final - April 1973 to November 1974
7. AUTHOR(s) Hanno H. Heller Donald B. Bliss		6. PERFORMING ORG. REPORT NUMBER BBN Report No. 2884
9. PERFORMING ORGANIZATION NAME AND ADDRESS Bolt, Beranek, and Newman, Inc. 50 Moulton Street Cambridge, Massachusetts 02138		8. CONTRACT OR GRANT NUMBER(s) F33615-73-C-3075
11. CONTROLLING OFFICE NAME AND ADDRESS Air Force Flight Dynamic Laboratory (AFFDL/FYA) Wright-Patterson AFB, Ohio 45433		10. PROGRAM ELEMENT, PROJECT, TASK AREA & WORK UNIT NUMBERS 147102
14. MONITORING AGENCY NAME & ADDRESS (if different from Controlling Office)		12. REPORT DATE February 1975
		13. NUMBER OF PAGES 212
		15. SECURITY CLASS. (of this report) Unclassified
		15a. DECLASSIFICATION/DOWNGRADING SCHEDULE
16. DISTRIBUTION STATEMENT (of this Report) Distribution limited to U.S. Government agencies only; test and evaluation; statement applied 7 November 1974. Other requests for this document must be referred to AF Flight Dynamics Laboratory, (FY), Wright-Patterson AFB, Ohio 45433.		
17. DISTRIBUTION STATEMENT (of the abstract entered in Block 20, if different from Report) Approved for Public Release; Distribution Unlimited		
18. SUPPLEMENTARY NOTES		
19. KEY WORDS (Continue on reverse side if necessary and identify by block number) Cavity Flow Cavity Oscillations Pressure Oscillations Oscillation Suppression		
20. ABSTRACT (Continue on reverse side if necessary and identify by block number) This report presents the results of an analytical and experimental research program to (1) improve the understanding of the physical mechanisms that control the occurrence of pressure fluctuations in long and shallow rectang- ular cavities, exposed to high-speed external flow, and (2) devise and eval- uate devices that would either substantially reduce the amplitude of such pressure fluctuations, or totally suppress the occurrence of pressure fluctuations.		

DD FORM 1 JAN 73 1473 EDITION OF 1 NOV 68 IS OBSOLETE

UNCLASSIFIED

SECURITY CLASSIFICATION OF THIS PAGE (When Data Entered)

UNCLASSIFIED

SECURITY CLASSIFICATION OF THIS PAGE(When Data Entered)

During this investigation, the understanding of the complex interaction of the external shear layer and the cavity internal fluid medium, which constitutes the generating mechanism of high-intensity periodic pressure fluctuations was substantially furthered. Both the analysis and investigation of the physical mechanisms were aided through extensive shallow-water flow-simulation experiments.

Large-scale experiments, using the NASA-Lewis Research Center 8 X 6 ft Supersonic Wind Tunnel were conducted to substantiate some of the analytical predictions and to study in detail the aeroacoustic behavior of cavities in the length-to-depth ratio range, L/D , of 2.3 to 5.5, and the Mach number range of 0.8 to 2.0. Detailed information was obtained on the normalized levels of the first three resonant modes in the cavity for a range of cavity length-to-depth ratios and freestream Mach numbers.

Several concepts for pressure oscillation suppression were developed and evaluated in wind tunnel experiments. The most promising concept utilizes a slanted trailing edge, which stabilizes the free shear flow above the cavity, thus effectively suppressing discrete-tone generation.

UNCLASSIFIED

SECURITY CLASSIFICATION OF THIS PAGE(When Data Entered)

4.0, and either 5.1 or 5.5. Not all of these data were reduced; however, all data, which were obtained through Sensor 3, were reduced and are available.

Signals from Sensor 3 were found to be close to those from Sensor 2 (on the leading-edge bulkhead); thus, Sensor 3 signals can be considered representative for the entire cavity internal leading-edge region. Figure 48 shows 1/3-octave band pressure level spectra, obtained through Sensor 3 for seven freestream Mach numbers and three L/D ratios. Levels are given in dB re $20 \mu\text{N/m}^2$. Each spectrum is composed of several discrete tones and a broadband noise floor. The discrete tones correspond to the various mode frequencies; in general, few modes with relatively high intensity appear in the deep cavity, and more modes with more evenly distributed intensity occur in the shallower cavities. In a 1/3-octave band representation, a discrete tone determines the band level. Hence, direct comparison of levels in each spectrum for corresponding modes is possible.

Following the L/D = 2.3 column, in Fig. 48 we can pursue the level and frequency change of the discrete peak at 250- to 315-Hz bands. This peak corresponds to a mode-2 oscillation (see Sec. 6.7). Levels reach a relative maximum at transonic Mach numbers. With increasing Mach numbers, the mode-1 oscillation in the 160-Hz band becomes significant. Clearly, most of the energy for such relatively deep cavities is in the discrete modes. For the shallower cavities, discrete tones are less pronounced, and relatively more energy is in the broadband portion. This figure is intended to give an overview of the spectral changes with the two most important parameters, i.e., Mach number and length-to-depth ratio. The levels would be those encountered by a cavity in an aircraft flying at the Mach number-dependent altitudes as shown in Fig. 28. Each altitude corresponds to a certain freestream dynamic pressure.

Since levels in the leading-edge bulkhead region are known to scale with freestream dynamic pressure, q_∞ (Smith *et al.*, 1974; Heller *et al.*, 1970), the ordinate scale of the Fig. 48 spectra can be converted into $20 \log (p_{rms}/q_\infty)$ by subtracting the numbers given in Table 1 from the fluctuating-pressure levels.